Development of an *In Vitro* whole cell Micronucleus Multiplex expansion assay:

Using DRAQ5™ and the DNA damage biomarkers ɣH2AX, P53, pH3 along with cell cycle relationships and the MN genotoxic endpoint to assess chemical Mode of Action on an imaging flow cytometry platform with template development.

Swansea University
Prifysgol Abertawe

Danielle Stephanie Gillien Harte

Submitted to Swansea University in fulfilment of the requirements for the Degree of Doctor of Philosophy

September 2020

Abstract

Genetic toxicity testing is the assessment of compounds, and their respective metabolites, potential to cause DNA damage either directly or indirectly. There are many genetic toxicology screening assays designed to assess the DNA damaging potential of chemicals in early drug development to help identify promising drugs that have a low risk potential of causing damage leading to cancer in humans. Despite this, *in vitro* tests generate a high number of miss-leading positives, the consequences of which lead to unnecessary animal testing and abandoning promising drug candidates. Understanding chemical Mode of Action (MoA) is vital in identifying true genotoxic potential of substances. Here I demonstrate a simple robust protocol for optimised staining of fixed human lymphoblast P53 proficient TK6 cells with the antibodies; Anti-ɣH2AX, Anti-P53 and Ant-pH3S28 along with DRAQ5™ DNA staining in a whole cell multiplex system that is suitable for analysis via microscopy or imaging flow cytometry. Use of the Amnis FlowSight® and ImageStream X Mark II® platform provided a high content high throughput acquisition platform with the sensitivity of flow cytometry and accuracy of image analysis. Using both optimal and suboptimal lasers for fluorophore excitation demonstrated that a multiplex system for DNA damage assessment including MN was possible in un-lysed cells. IDEAS 6.2 template generation allowed for batch processing of data samples extracting the following metrics: Cell Cycle, Micronucleus (MN), ɣH2AX, P53, PH3, G1 ɣH2AX, G1 P53, S ɣH2AX, S P53, G2 ɣH2AX, G2/M P53, Prophase, Metaphase, Anaphase and Abnormal mitosis. Furthermore, high content nature of the platform using imagery allows for identification of rare cellular event assessment particularly preliminary data on biomarker signal found within MN. The system found differences in the biomarker metric responses between the chemicals; MMS, Carbendazim, ARA-C, Vinblastine, Etoposide and Crizotinib suggesting potential for chemical MoA elucidation.

Declarations and Statements

DECLARATION

This work has not previously been accepted in substance for any degree and is not being concurrently submitted in candidature for any degree.

Signed .....  ..... (candidate)

Date .....30 Sep 2020.....

STATEMENT 1

This thesis is the result of my own investigations, except where otherwise stated. Where correction services have been used, the extent and nature of the correction is clearly marked in a footnote(s).

Other sources are acknowledged by footnotes giving explicit references. A bibliography is appended.

Signed .....  .... (candidate)

Date ..... 30 Sep 2020.....

STATEMENT 2

I hereby give consent for my thesis, if accepted, to be available for photocopying and for inter-library loan, and for the title and summary to be made available to outside organisations.

Signed .....  ..... (candidate)

Date ..... 30 Sep 2020.....

Contents

Title Page i
Abstract ii
Declaration and Statements iii
Contents iv
Acknowledgements ix
Abbreviations x
List of Figures xiii
List of Tables xix

Chapter 1 – Introduction 1-37
1.0. Background....1
1.0.1. Toxicology Terminology....2
1.1. DNA: Structure, Function, Damage and Repair....3
1.1.1. DNA Structure & Function....3
1.1.2. DNA Damage....6
1.1.2.1. Oxidative Damage....7
1.1.2.2. Base Alkylation....7
1.1.2.3. Abasic Sites....8
1.1.2.4. Bulky Adducts....8
1.1.2.5. DNA Crosslinking....8
1.1.2.6. DNA Strand Breakage....9
1.1.3. DNA Repair....9
1.1.3.1. Base Excision Repair....10
1.1.3.2. Nucleotide Excision Repair....10
1.1.3.3. Mismatch Repair....10
1.1.3.4. Double Strand Break Repair....11
1.1.3.4.1. Non Homologous End Joining....11
1.1.3.4.2. Homologous Recombination....12
1.2. Cell Cycle....13
1.3. Genetic Toxicology and Testing Strategy....15
1.3.1. Ames Assay....15
1.3.2. Mouse Lymphoma Assay....16
1.3.3. Comet....17
1.3.4. Micronucleus Test....17
1.3.4.1. *In Vivo*....18
1.3.4.2. *In Vitro*....18
1.3.5. Genetic Toxicology Summary....20
1.4. Biomarkers....20
1.4.1. P53....20

1.4.2. γH2AX....21
1.4.3. pH3....23
1.5. Micronucleus End Point....24
1.6. DNA Damaging Chemicals....26
1.6.1. Methyl Methane Sulfonate....27
1.6.2. Carbendazim....27
1.6.3. Etoposide....27
1.6.4. Crizotinib....27
1.6.5. Vinblastine....27
1.6.6. Cytosine β-Darabinofuranoside (ARA-C)....28
1.7. TK6 Cells....28
1.8. Confocal Microscopy....30
1.9. Imaging Flow Cytometry....32
1.9.1. AMNIS FlowSight® & AMNIS ImageStream X Mark II®....32
1.9.2. Workflow: Acquisition to analysis....34
1.9.3. IDEAS® Software....35
1.10. Summary....36
1.11. Aims....36

Chapter 2 – Materials & Methods 38-57

2.1. Materials....38
2.1.1. Equipment....38
2.1.2. Reagents....39
2.1.3. Chemicals....39
2.1.4. Antibodies and DNA stain....39
2.1.5. Computer Programs....39
2.2. Methods....40
2.2.1. Test Article Formulation....40
2.2.2. Cell Culture and Growth Media....40
2.2.2.1. Treatment of Cell Cultures....41
2.2.2.2. Cell Counts....41
2.2.2.3. Cytotoxicity....41
2.2.3. Cell Fixation and Staining....42
2.2.3.1. Antibody Staining....44
2.2.3.2. DNA Staining....44
2.2.4. Whole Cell Data Collection....45
2.2.4.1. Confocal Microscopy....45
2.2.4.1.1. Slide Preparation....45
2.2.4.1.2. ZEN Image Acquisition....45
2.2.4.1.3. ZEN Imaging Software....46
2.2.4.2. Imaging Flow Cytometry....46
2.2.4.2.1. AMNIS® FlowSight®....46
2.2.4.2.2. AMNIS® ImageStream X Mark II®....47
2.2.4.2.3. INSPIRE™....47

2.2.4.2.3.1. Template Set up....47
2.2.4.2.3.2. Laser Balancing....48
2.2.4.2.3.3. Compensation Matrix....51
2.2.5. Whole Cell Image Assessment....51
2.2.5.1. IDEAS®....51
2.2.5.1.1. Applied Compensation....51
2.2.5.1.2. Template Design....54
2.2.5.1.3. Mask Development and Feature Use....55
2.2.6. Data Assessment....56
2.2.6.1. Statistical Analysis....57

Chapter 3 – Results 1: Assay and IDEAS® Template Optimisation 58-116

3.1. Introduction....58
3.2. Materials & Methods....60
3.2.1. Test Article Formulation....60
3.2.2. Cell Culture and Growth Media....61
3.2.3. Treatment....61
3.2.3.1. Treatment Of Cell Cultures....61
3.2.4. Cell Fixation and Staining....61
3.2.5. Image Acquisition....61
3.2.6. Micronucleus Mask Accuracy....61
3.3. Results & Discussion....63
3.3.1. Confirmation of Antibody Binding and DNA Counterstaining....63
3.3.2. Gating: Placement and Boundary Cut Offs....65
3.3.2.1. Cell Cycle Assessment Gates....65
3.3.2.2. BV421 ɣH2AX Cut Offs....70
3.3.2.3. AF488 pH3 Cut Offs....74
3.3.2.4. PE P53 Cut Offs....85
3.3.2.5. Gating Strategy Overview and Final Gating Boundaries....90
3.3.3. Masks and Features....93
3.3.3.1. Cytoplasmic Mask and The Features That Use It....93
3.3.3.2. Nuclear Mask, The Features That Use It and Refining Biomarker Signal....100
3.3.3.2.1. Nuclear Mask 1....100
3.3.3.2.2. Nuclear Mask 2....103
3.3.3.2.3. Nuclear Mask 3....109
3.3.3.3. Micronucleus Mask and The Spot Count Feature....110
3.3.3.3.1. Complete Final Micronucleus Mask Accuracy Rate....114
3.3.3.4. Extracted Data Population....114
3.3.4. Template Overview....116

Chapter 4 – Results 2: Model Chemicals, Methyl Methanesulfonate and Carbendazim 117-146
4.1. Introduction....117
4.2. Materials & Methods....118
4.2.1. Test Article Formulation....118
4.2.2. Cell Culture and Growth Media....118
4.2.3. Treatment Of Cell Cultures....118
4.2.4. Preliminary....118
4.2.4.1. Cell Processing....118
4.2.4.2. Antibody and DNA Staining....118
4.2.4.3. Preliminary Data Acquisition FlowSight®....119
4.2.4.4. INSPIRE™ Compensation File Acquisition....119
4.2.4.5. Amnis IDEAS® v6.2 Template....120
4.2.4.6. Statistical Analysis....120
4.2.4.7. Positive Response Criteria....121
4.2.5. Optimised....121
4.2.5.1. Antibody and DNA Staining....121
4.2.5.2. Optimised Cell Processing....121
4.2.5.3. Optimised Data Acquisition ImageStream X Mark II®....122
4.2.5.3.1. Acquisition Error....122
4.2.5.4. INSPIRE™ Compensation File Acquisition....123
4.2.5.5. Amnis® IDEAS® v6.2 Template....123
4.2.5.6. Optimal Data Set Positive Response Criteria....124
4.3. Preliminary Results....124
4.3.1. Preliminary Dual Biomarker and MN Assessment....124
4.4. Optimal Results....128
4.4.1. Optimised Multiplex System: ɣH2AX, pH3, P53, MN and Cell Cycle Analysis....128
4.4.1.1. MMS: Optimal Staining Sub Optimal Laser Settings (Preliminary Response Data)....128
4.4.1.2. Carbendazim: Optimal Staining Sub Optimal Laser Settings (Preliminary Response Data)....135
4.5. Discussion....141
4.5.1. Preliminary Data Set: Dual Biomarker and MN Assessment....141
4.5.2. Optimal Staining Preliminary Data Set....141
4.5.3. Disparity Between FlowSight® and ImageStream X Mark II®....143
Chapter 5 – Results 3: ImageStream Micronucleus Expansion (ISMN-me) Assay: Optimal Staining and Laser Acquisition For The Chemicals ARA-C, Vinblastine, Etoposide and Crizotinib. 146-188
5.1. Introduction....146
5.2. Materials & Methods....148
5.2.1. Test Article Formulation....148

5.2.2. Cell Culture and Growth Media.....148
5.2.3. Treatment Of Cell Cultures.....148
5.2.4. ISMN-me Antibody and DNA staining.....148
5.2.5. ISMN-me Cell Processing.....148
5.2.5.1. ImageStream Flow Cytometry: ImageStream X Mark II®.....149
5.2.5.2. INSPIRE™ Compensation File Acquisition.....149
5.2.5.3. Amnis IDEAS® v6.2 Template.....150
5.2.5.4. MN Containing Biomarker Signal.....150
5.2.5.5. Data Assessment.....151
5.3. Results: ISMN-me Assay chemical assessment.....151
5.3.1. Etoposide.....151
5.3.2. Crizotinib.....158
5.3.3. Vinblastine.....164
5.3.4. ARA-C.....172
5.4. Discussion.....179
5.4.1. Etoposide.....179
5.4.2. Cizotinib.....180
5.4.3. Vinblastine.....181
5.4.4. ARA-C.....184
5.4.5. ISMN-me MoA Overview.....185

Chapter 6 – General Discussion 188-193
6.1. Thesis Overview.....188
6.1.1. Template Generation and Batch Processing.....188
6.1.2. FlowSight® and ImageStream X Mark II®.....188
6.1.3. ISMN-me Assay.....189
6.1.4. Position In Industry.....189
6.2. Conclusion.....191
6.2.1. Future Work and Developments.....192

References 194-210

Supplement 1

Supplement 2

Acknowledgements

I would like to thank my supervisor Dr George Johnson for providing me with the opportunity to obtain a PhD and the support he has given me throughout my time at Swansea University lending me a guiding hand. I would also like to thank Dr John Wills Cambridge fellow for his continued encouragement, expertise and invaluable advice on imaging and assay optimisation.

To Sally James, thank you for the lab technical support that enabled me to add an additional layer of robustness to my results.

Thank you to my Mum Paula and Dad Mike Harte who have continually supported me in all my endeavours.

Lastly, I have a deep gratitude and offer my everlasting thanks to my wife Chloe Harte who pushed me to get past the finish line of my research.

Abbreviations

’	Prime
µγ	Microgram
µλ	Microliter
µM	Micromolar
.cif	Compensated Image File
.daf	Data analysis File
.rif	Raw Image File
µm	Micron (Micrometer)
A	Adenine
AB	Antibody
AF	Auto fluorescence
AF488	AlexaFluor 488
ALK	Anaplastic Lymphoma Kinase
Ames	Bacterial Reverse Mutation Assay
AOP	Adverse Outcome Pathway
AP	Apurinic/Apyrimidinic
ARA-C	Cytosine β-Darabinofuranoside
AI	Artificial Intelligence
ATM	Ataxia-telangiectasia mutated kinase
ATR	Ataxia-telangiectasia and Rad3 related kinase
BER	Base Excision Repair
Bi	Binucleated
BTR	BLM helicase-TopoisomeraseIIIα-RMI1-RMI2
BV421	BrilliantViolet 421
C	Cytosine
CBMN	Cytokinesis Block Micronucleus Assay
CCD	Charged Coupled Detector
CFM	Complete Final Mask
Ch	Channel
Cis-Pt	Cisplatin
CM	Compensation matrix
CPD	Cyclobutane pyrimidine dimer
Crbz	Carbendazim
Crztib	Crizotinib
Cyto-B	Cytochalasin-B
Cdk	Cyclin dependant kinases
d(d)H2O	Distilled (deionized) water
D5	DRAQ5™
DDR	DNA Damage Repair
DMSO	Dimethyl sulfoxide
DNA	Deoxyribonucleic acid

DSB	Double Strand Break
DSBR	Double Strand Base Repair
DRAQ5™	Deep Red Anthraquinone 5
ECVAM	European Centre for the Validation of Alternative Methods
Etop	Etoposide
ECACC	European Collection of Cell Cultures
E.Coli	*Escherichia coli*
FISH	Fluorescence In Situ Hybridisation
G	Guanine
GG-NER	Global Genome Nucleotide Excision Repair
G1	Gap 1 stage of the cell cycle
G2	Gap 2 stage of the cell cycle
ɣH2AX/gH2AX	Phosphorylated Histone 2A variant X
HR	Homologous Recombination
Hrs	Hours
IDEAS®	Image Data Exploration and Analysis Software
ISMN-me	ImageStream MicroNucleus Multiplex expansion assay
ISXII	ImageStream®X Mark II
IVTG	*In Vitro* Toxicology Group
ICH	International Conference on Harmonisation
kDa	Kilo Dalton
LOGEL	Lowest Observed Genotoxic Effect Level
M phase	Mitotic stage of the cell cycle
MET	MNNG HOS Transfoming gene
mg	Milligram
min	Minutes
mL	Millilitre
MMC	mitomycin C
MLA	Mouse Lymphoma Assay
MMR	Mismatch Repair
MMS	Methyl methane sulfonate
MN	Micronucleus
MNT	Micronucleus Test
MoA	Mode of Action
Mono	Mononucleted
mRNA	Messenger RNA
NC3Rs	National Centre for the 3Rs
NER	Nucleotide Excision Repair
NHEJ	Non Homologous End Joining
NOGEL	No Observed Genotoxic Effect Level
OECD	Organisation for Economic Cooperation and Development
OGG1	8-Oxoguanine DNA glycosylase

·OH	Hydroxyl Radicals
P53	Tumor protein P53
PBS	Phosphate-Buffer Saline
PD	Population Doubling
pH3	Phosphorylated Histone 3
PMT	Photon Multiplier Tube
PCNA	Proliferating Cell Nuclear Antigen
RCG	Relative Cell Growth
RFC	Replication Factor C
RNA	Ribonucleic Acid
RMS	Root Mean Square
Rpm	Revolutions per minute
RSO	Reactive Oxygen Species
S phase	Synthesis stage of the cell cycle
SAC	Spindle Assembly Check Point
SDSA	Synthesis-Dependent Strand Annealing
SD	Standard Deviation
SDE	Spectral Decomposition Element
Ser	Serine
SSB	Single Strand Breaks
SP	Stained Peak
T	Thymine
Thymidine Kinase	TK
Topo	Topoisomerase
ToxPi	Toxicological Prioritization Index
TC-NER	Transcription Coupled Nucleotide Excision Repair
TFT	Trifluorothymidine
UP	Un-Stained peak
UV	Ultraviolet
Vblstn	Vinblastine
(6-4)PP	6–4 photoproduct
8-oxoG	8-oxo-7,8-dihydrogeanine

List of Figures

Chapter 1

Figure 1.1: Primary, secondary and tertiary stages of Deoxyribose Nucleic Acid (DNA) structure.

Figure 1.2: DNA damageing agents, DNA damage, resultant repair and outcomes.

Figure 1.3: Depicts the main stages of the cell cycle.

Figure 1.4: Demonstrating the role of phosphorylated H2AX known as gamma-H2AX (ɣH2AX) in the DNA damage repair pathway with regard to double strand breaks

Figure 1.5: Demonstrates the nucleosome consisting of histone octamer with DNA and the H3 tail along with the most well-known sites of post-translational covalent modifications

Figure 1.6: Simple diagrammatic representation of MN induction.

Figure 1.7: TK6 cell line phylogeny.

Figure 1.8: Overview of the confocal microscope LSM710 layout.

Figure 1.9: Overview of sample uptake to image output on INSPIRE software of AMNIS ImageStream®X MarkII and FlowSight®.

Figure 1.10: Schematic of file type workflow from the point of data acquisition on the imaging cytometer platform - Inspire software.

Figure 1.11: Showing IDEAS® software image analysis and work flow interface

Figure 1.12: Flow chart of thesis overview.

Chapter 2

Figure 2.1: Demonstrating a generalised overview of the method followed in this thesis.

Figure 2.2: Demonstrating example of intensity vs raw max pixel intensity on inspire software to aid laser power selection.

Figure 2.3: The graph was generated from collected compensated data as an example step. This being such means the DRAQ5™ signal was optimal for the system.

Figure 2.4: Example of how compensation removes signal overspill from incorrect channels prevents signal from being miss identified.

Figure 2.5: Overview of compensation matrix generation using IDEAS® and following the steps in the compensation wizard.

Figure 2.6: Opening window start up for IDEAS® software for analysis of rif files.

Chapter 3

Figure 3.1: Emission spectra of each of the fluorophores conjugated to each of the antibodies and DNA stain present in the multiplex system.

Figure 3.2: Example of plotted histogram from a population of healthy cells containing only one nucleus.

Figure 3.3: 1.6µg/mL Carbendazim dosed TK6 cells demonstrating linear unmixed 4 colour, stained sample at x63 magnification acquired on confocal microscope.

Figure 3.4: Graph 1a Population of H3 positively stained cells plotted on nuclear content histogram graph.

Figure 3.5: Nuclear content graphs of entire available cell population

Figure 3.6: DNA content graphs demonstrating G1 and G2 gate generation and use of region manager.

Figure 3.7: Demonstrating the final gate layout for cell cycle assessment based on DRAQ5™ staining of nuclear content.

Figure 3.8a: Demonstrating steps 1-6 of the BV421 ɣH2AX gating strategy

Figure 3.8b: Demonstrating steps 7-12 of the BV421 gating strategy

Figure 3.9: Z stack image taken on Zeiss confocal microscope x40 water lens objective.

Figure 3.10: Unstained vehicle control autofluorescence peak for generation of an average autofluorescence unstained DMSO peak gate.

Figure 3.11: Displayed histogram of AF488 stained DMSO sample.

Figure 3.12: Display of Crbz unstained AF488 histogram peak.

Figure 3.13: Demonstrating a-e steps leading to +veAF 488 (H3 gate) generation.

Figure 3.14: Demonstrating continued steps leading to +veAF 488 (H3 gate) generation.

Figure 3.15: Combined +veAF488 is now referred to +veAF488 (H3 gate).

Figure 3.16: Scatter graph of negative control DMSO demonstrating the gated populations of +ve Af488(H3) meaning positively stained for pH3 and -ve AF488 (H3) meaning no stain for H3 present above background AF.

Figure 3.17: Demonstrating top dose Carbendazim (1.6 µg/mL) scatter graph combined with image assessment for more accurate gating.

Figure 3.18: Refining pH3 populations to exclude AF and or off target binding.

Figure 3.19: P53 stepwise gating strategy

Figure 3.20: Demonstrates the stained PE peaks of negative vehicle DMSO and positive sample of the clastogen MMS and aneugen Carbendazim.

Figure 3.21: Demonstrating PE stained peaks of Carbendazim sample and secondary peak gating

Figure 3.22: Histogram demonstrating the generation of the ++PE (P53 gate).

Figure 3.23: Demonstrating generation of lower boundary of +PE (P53 gate).

Figure 3.24: Finalised gating cut off points for the biomarkers pH3, P53 and γH2AX.

Figure 3.25: Demonstrating the function rules used to designate brightfield image mask criteria.

Figure 3.26: Brightfield 1A (highlighted by red arrow) and Brightfield 1B (highlighted by green arrow) masks used to generate aspect ratio and area scatter graph, on the y and x axis respectively, for round and single cell assessment.

Figure 3.27: Example plot of the gating of single round cells with corresponding scatter point brightfield imagery that fall outside of the gated area, demonstrating correct population selection.

Figure 3.28: Generation of in focus cell population from single cell population.

Figure 3.29: Demonstrates the specific cytoplasmic mask generated when the nuclear mask based on DRAQ5™ signal is excluded from analysis.

Figure 3.30: Function use for P53 mask generation and P53 cytoplasmic mask generation.

Figure 3.31: Same cell demonstrating the different nuclear masks used in template feature generation.

Figure 3.32: Nuclear mask 1 generation.

Figure 3.33: Example graph showing the Healthy Cells gate in red that will select cells to be taken forward to the next stage of DNA content assessment (optimal master population).

Figure 3.34: Nuclear mask 2 generation.

Figure 3.35: Demonstrating mask combination using Boolean logic and nuclear mask 2 to generate “True Nuclear” signal masks.

Figure 3.36: Showing each graph used to generate the ɣH2AX response along with ɣH2AX response per each section of the cell cycle.

Figure 3.37: Graph demonstrating the separation of three phases of the mitosis cell cycle based on nuclear aspect ratio (how circular the DNA is) and spot count of nuclear bodies labelled Mitosis assessment that uses nuclear mask 1.

Figure 3.38: Demonstrating pH3 intensity plotted against ɣH2AX intensity as a scatter graph.

Figure 3.39: Application of the watershed function to Nuclear mask 2 allows for separation of the nuclear mask into multiple components

Figure 3.40: Showing use of the spot count feature to identify Mononucleated vs Bi-nucleated cells.

Figure 3.41: Demonstration of the basic principle of MN mask generated behind each of the three MN masks using IDEAS® 6.2 software

Figure 3.42: Complete final MN mask spot count for MN metric generations.

Figure 3.43: Demonstrating the population plotted on the scatter graph is the cells that fall within the DNA content gate of the cell cycle histogram.

Chapter 4

Figure 4.1: Demonstrating images obtained on Amnis FlowSight® at 20x magnification of sample dual stained with pH3 and ɣH2AX AB.

Figure 4.2: Demonstrating biomarker response of set 1 compared to the independent DRAQ5™ stained MN response of set 2 spanning similar dose ranges of MMS using the Amnis FlowSight®.

Figure 4.3: Demonstrating biomarker response of set 1 compared to the independent DRAQ5™ stained MN response of set 2 spanning similar dose ranges of Carbendazim using the Amnis FlowSight®.

Figure 4.4: Combination graph showing the square root of raw fold change values of the biomarker responses for ɣH2AX, pH3, P53 and the Micronucleus (MN) genotoxic endpoint in response to MMS doses.

Figure 4.5: Graph showing percentage of cells found in each portion of the cell cycle in relation to MMS concentration.

Figure 4.6: Line scatter graph visually displaying data in table 4.1a illustrating relationship of each biomarker and cell cycle stage for MMS dose.

Figure 4.7: Line scatter graph displaying the ratio of average fold change responses for MMS concentrations (data in table 4.1b). Allowing assessment of proportional changes of the different phases of mitosis to one another

Figure 4.8: Combination graph showing the square root of raw fold change values of the biomarker responses for ɣH2AX, pH3, P53 and the Micronucleus (MN) genotoxic endpoint in response to Carbendazim doses.

Figure 4.9: Graph showing percentage of cells found in each portion of the cell cycle in relation to Carbendazim concentration.

Figure 4.10: Line scatter graph visually displaying data in table 4.2a illustrating relationship of each biomarker and cell cycle stage for Carbendazim doses.

Figure 4.11: Line scatter graph displaying the ratio of average fold change responses for Carbendazim concentrations (data in table 4.2b). Allowing assessment of proportional changes of the different phases of mitosis to one another

Figure 4.12: Demonstrates the variation in spectrum detection between X20 FlowSight® machine and X40 ISXII.

Chapter 5

Figure 5.1: Images obtained at x40 magnification on Amnis ImageStream X mark II® demonstrating the combined platform.

Figure 5.2: Combination graph showing the square root of raw fold change values of the biomarker responses for γH2AX, pH3, P53 and the Micronucleus (MN) genotoxic endpoint in response to Etoposide doses.

Figure 5.3: Graph showing percentage of cells found in each portion of the cell cycle in relation to Etoposide concentration.

Figure 5.4: Line scatter graph visually displaying data in table 5a illustrating relationship of each biomarker and cell cycle stage for Etoposide.

Figure 5.5: Line scatter graph displaying the ratio of average fold change responses (data in table 5.1b) for Etoposide concentrations. Allowing assessment of proportional changes of the different phases of mitosis to one another.

Figure 5.6: Combination graph showing the square root of raw fold change values of the biomarker responses for γH2AX, pH3, P53 and the Micronucleus (MN) genotoxic endpoint in response to Crizotinib doses.

Figure 5.7: Graph showing percentage of cells found in each portion of the cell cycle in relation to Etoposide concentration

Figure 5.8: Line scatter graph visually displaying data in table 5.3a illustrating relationship of each biomarker and cell cycle stage for Crizotinib

Figure 5.9: Line scatter graph displaying the ratio of average fold change responses (data in table 5.3b) for Crizotinib. Allowing assessment of proportional changes of the different phases of mitosis to one another.

Figure 5.10: Combination graph showing the square root of raw fold change values of the biomarker responses for γH2AX, pH3, P53 and the Micronucleus (MN) genotoxic endpoint in response to Vinblastine doses.

Figure 5.11: Graph showing percentage of cells found in each portion of the cell cycle in relation to Vinblastine concentration.

Figure 5.12: Line scatter graph visually displaying data in table 5.5a, illustrating relationship of each biomarker and cell cycle stage for Vinblastine dose concentrations.

Figure 5.13: Line scatter graph displaying the ratio of average fold change responses (data in table 5.5b) for Vinblastine. Allowing assessment of proportional changes of the different phases of mitosis to one another.

Figure 5.14: Combination graph showing the square root of raw fold change values of the biomarker responses for γH2AX, pH3, P53 and the Micronucleus (MN) genotoxic endpoint in response to ARA-C doses.

Figure 5.15: Graph showing percentage of cells found in each portion of the cell cycle in relation to ARA-C concentration.

Figure 5.16: Line scatter graph visually displaying data in table 5.7a illustrating relationship of each biomarker and cell cycle stage for ARA-C.

Figure 5.17: Line scatter graph displaying the ratio of average fold change responses (data in table 5.7b) for ARA-C.

Figure 5.18: Demonstrating multinucleated cells and location within DNA histogram with cell cycle gates and rare events generated by Crizotinib.

Figure 5.19: Shows the G1 gH2AX response for Vinblastine at the 0.002µg/mL dose and corresponding apoptotic cell image.

Figure 5.20: Demonstrating qualitatively the overall visual differences of the different genotoxic chemicals assessed.

List of Tables

Chapter 2

Table 2.1: Summary of AB and associated fluorophores

Chapter 3

Table 3.1: Demonstrating the cell percentages that fall inside the boundaries of the +BV421(ɣH2AX) and ++BV421(ɣH2AX) gates for Carbendazim (Crbz), DMSO and MMS along with the fold change away from the solvent negative control

Table 3.2: Summary of the functions used to generate the three MN masks that make up the Complete final MN mask

Chapter 4

Table 4.1a: Fold change average of biomarkers ɣH2AX and P53 in direct relation to the phase of the cell cycle the cell population is in ±1SD for MMS doses.

Table 4.1b: Fold change average of the ratio of Prophase, Metaphase and Anaphase cells populations when compared to control for MMS doses

Table 4.2a: Fold change average of biomarkers ɣH2AX and P53 in direct relation to the phase of the cell cycle the cell population is in ±1SD for Carbendazim doses

Table 4.2b: Fold change average of the ratio of Prophase, Metaphase and Anaphase cells populations when compared to control for Carbendazim

Chapter 5

Table 5.1a: Fold change average of biomarkers ɣH2AX and P53 in direct relation to the phase of the cell cycle the cell population is in ±1SD for Etoposide

Table 5.1b: Fold change average of the ratio of Prophase, Metaphase and Anaphase cells populations when compared to control for Etoposide

Table 5.2: Etoposide 0.24µg/mL - Biomarker presence or absence in true MN microscope images obtained on ISXII

Table 5.3a: Fold change average of biomarkers ɣH2AX and P53 in direct relation to the phase of the cell cycle the cell population is in ±1SD for Crizotinib

Table 5.3b: Fold change average of the ratio of Prophase, Metaphase and Anaphase cells populations when compared to control for Crizotinib

Table 5.4: Crizotinib 4.51µg/mL - Biomarker presence or absence in true MN microscope images obtained on ISXII

Table 5.5a: Fold change average of biomarkers ɣH2AX and P53 in direct relation to the phase of the cell cycle the cell population is in ±1SD for Vinblastine

Table 5.5b: Fold change average of the ratio of Prophase metaphase and anaphase cells populations when compared to control for Vinblastine

Table 5.6: Vinblastine 0.002ug/mL - Biomarker presence or absence in true MN microscope images obtained on ISXII

Table 5.7a: Fold change average of biomarkers ɣH2AX and P53 in direct relation to the phase of the cell cycle the cell population is in ±1SD for ARA-C

Table 5.7b: Fold change average of the ratio of Prophase metaphase and anaphase cells populations when compared to control for ARA-C.

Table 5.8: ARA-C 0.05ug/mL - Biomarker presence or absence in true MN microscope images obtained on ISXII

Chapter 1 – Introduction

1.0 – Background

Genetic toxicity testing is the assessment of compounds, and their respective metabolites, potential to cause DNA damage either directly or indirectly. The Organisation for Economic Co-operation and Development (OECD) offers recommended regulatory guidance for genetic toxicology testing approaches in an attempt to unify assay standards across industry and academia world wide. One of the mandated tests for the assessment of chromosome damage, is the *in vitro* micronucleus (MN) assay, (OECD., 2014; Fenech *et al*., 2003). In this test, damage to the chromosomes (clastogenicity) and chromosomal segregation machinery (aneugenicity) can be evaluated via MN formation in cells that have undergone mitosis (Schmid., 1975). Typically, each cell type within the MN assay is identified using microscopy, via either manual scoring or semi-automated image classifiers, but more recently, flow cytometry approaches have been utilised. These approaches can be highly laborious or potentially lead to misleading positive or negative outputs, through over- and under-scoring respectively (Johnson *et al*., 2014; Verma *et al*., 2017). The main challenges with the *in vitro* tests, including the various incarnations of the MN assay, at this time, are related to the high number of misleading positives that are reported, especially when using mammalian cells (Fowler *et al.*, 2012). False positives in this context are found by subsequent animal tests which cannot confirm the genotoxicity reported with *in vitro* studies. The consequence of this situation results in unnecessary animal tests and or the abandonment of promising substances that otherwise are safe. Further testing is required to characterise the Mode of Action (MoA) that has driven the MN formation.

Conventionally, the presence or the absence of centromeric labels within the MN is used to discriminate between aneugenic or clastogenic Mode of Actions respectively (OECD., 2010). Recently, molecular markers have proven useful in identifying MoA, for example, the increase in phosphorylated Histone 3, linked to aneuploidy, and phosphorylated histone variant H2AX (ɣH2AX) linked with clastogenicity (Audebert *et al.*, 2010; Cheng *et al.*, 2015; Bryce *et al.*, 2016). Histones are proteins made up of two of each of the following sub-units, H2B, H2A, H3 and H4 in addition to a single H1 linker protein (Hans *et al.*, 2001). Post translational modifications of tail residues of these proteins, are responsible for a cells progression through the cell cycle and the condensing of chromosomes (Nowak *et al.*, 2004; Hans *et al*.,2001; Zhou *et al.*, 2006). The H2A histone is a highly conserved protein across many species, with the ɣH2AX foci occurring in a 1:1 ratio with regard to DNA damage (Hoeller *et al.*, 2009; Zhou *et al.*, 2006; Watters *et al.*, 2009). Phosphorylation of H2AX, on serine 139 of the SQEY tail, upon double strand breaks results in the activation of the DNA damage repair (Watters *et al.*, 2009). Chromosome condensation is accompanied by phosphorylation of the H3 protein, at two different serine residues, S10 and S28, to ensure movement through mitosis (Doerig *et al*., 2015; Hans *et al.*, 2001). Phosphorylation of H3 at the S28 position begins at prophase and by late anaphase has been completely dephosphorylated (Hans *et al.*, 2001). H3 phosphorylation is affected by the amount of DNA damage found within the cell as it passes through the cell cycle, especially by chemically induced DNA damage (Ozawa., 2008). These characteristics of pH3 and ɣH2AX, used in

combination with immunofluorescent antibodies (AB), enables the use of flowcytometry based platforms to determine the clastogenic/aneugenic potential of compounds (Smart *et al*., 2011; Bryce *et al*., 2016). Past the direct assessment of histone tail modifications additional biomarkers in combination with pH3 and ɣH2AX aid in MoA assessment of chemicals one such biomarker is the tumour suppressor protein P53. P53 often referred to as the guardian of the genome has multiple functions including but not limited to; Cell cycle progression and maintenance, DNA damage repair initiation and induction of apoptotic pathways (Lavin & Gueven., 2006). P53 response to DNA damage and cellular stresses is mediated by complex pathways and phosphorylation of different protein residues dependant on the mechanism of DNA damage induction (Lavin & Gueven., 2006). Due to P53 intrinsic nature related to DNA damage pathways regardless of aneugenicity or clastogenisity it offers a biomarker for overall assessment of DNA damage induction (Bryce *et al.*, 2016).

The following work attempts to build on work by Khoury *et al*., 2016 and Bryce *et al*., 2016 pH3 and pH2AX genotoxicity screening assay and MultiFlow® assay respectively using the Imaging flow cytometry platform for unlysed cell assessment of the Biomarkers ɣH2AX, pH3-S28, P53 (unphosphorylated) individually and in relation to the cell cycle combined with the genotoxic endpoint MN assessment.

1.0.1 – Toxicology Terminology

In terms of colloquial communications within genetic toxicology circles, the terms 'Mode' and 'Mechanism' as well as 'Endpoint' and 'Biomarker' are often used interchangeably.

Here 'Mode' in Mode of Action (MoA) refers to the overriding way in which a chemical has induced damage to the DNA. Direct physical breakage of the DNA is a Clastogenic MoA. DNA loss due to interactions with the cell division machinery is a Aneugenic MoA. The 'Mechanism' in terms of mechanism of action is referred to as the underlying detailed steps of the MoA, for example, a chemical has a clastogenic MoA caused by the mechanism of DNA alkylation. In short, the MoA is the effect and mechanism of action the how.

The term 'Endpoint' is the physical conclusion of the MoA. The MN is the conclusion of the MoA whether it be by clastogenic or aneugenic means. A biomarker here is referred to as a measurable transient signal that occurs along the biochemical pathway that allows for an indication of MoA. With the potential for allowing mechanistic assessment.

Understanding the MoA can help determine testing strategy within safety assessment whilst knowing mechanism can help make decision on compound progression through the drug development pipeline and impact of DNA damage repair pathways on a biological system resistance to mutation.

1.1 – DNA: Structure, Function, Damage and Repair

Deoxyribose Nucleic Acid (DNA) is the hereditary information of all living organisms, and it is found within the nucleus of mammalian cells and as a circular chromosome in bacteria. DNA is the biological molecule that contains the genetic blue print of life. This set of instructions is contained within every cell and is passed down from parents to offspring, in the case of mammals half from the father and half from the mother. The DNA fingerprint is specific to each individual because of this combining of hereditary information.

DNA was first isolated in 1869 by Swiss biochemist Freidrick Miescher but the structure and importance of this polymer was a relative mystery (Dahm, 2008). Not until James Watson and Francis Crick in 1953 pulling pieces of the puzzle together from other scientists was the true structure of DNA realised. Phoebus Levene in 1919 put forth the 'polynucleotide' model of nucleic acids, that they contained one of four nitrogen containing basis, a sugar molecule and phosphate group. Oswald Avery and his team in 1944 demonstrated that genes composed of DNA were the hereditary units. Erwin Chargaff a few years later published in 1950 that no matter the organism the basis (Adenine (A), Thymine (T), Guanine (G) and Cytosine (C)) of DNA remain the same and that A and T are found in similar ratios, likewise for C and G, this known as 'Chargaffs rule'(Chargaff, 1950; Avery, 1944). The final piece of the puzzle was provided by Rosalind Franklin (unbeknownst to her) in 1952 when her X-ray diffracted image of DNA, that showed the three dimensional structure of DNA to be a double helix, was shown to Watson and Crick. This information along with previously published knowledge of the structural chemistry of the basis allowed Watson and Crick to suggest the structure of two opposing strands of DNA wound in a right handed helical structure allowing for the base pairing of Purines with Pyrimidines and stabilised by hydrogen bonds.

Elucidation of the structure of DNA allowed for the understanding of DNA replication and the passing of hereditary events as well as potential impact of mutation.

1.1.1 – DNA Structure & Function

Whilst simple in design the structure and packaging of DNA can be thought of in three levels of increasing complexity: Primary, Secondary and Tertiary. Figure 1.1 demonstrates the three levels of structure the DNA macromolecule passes through to form a single condensed metaphase chromosome (Pierce, 2012).

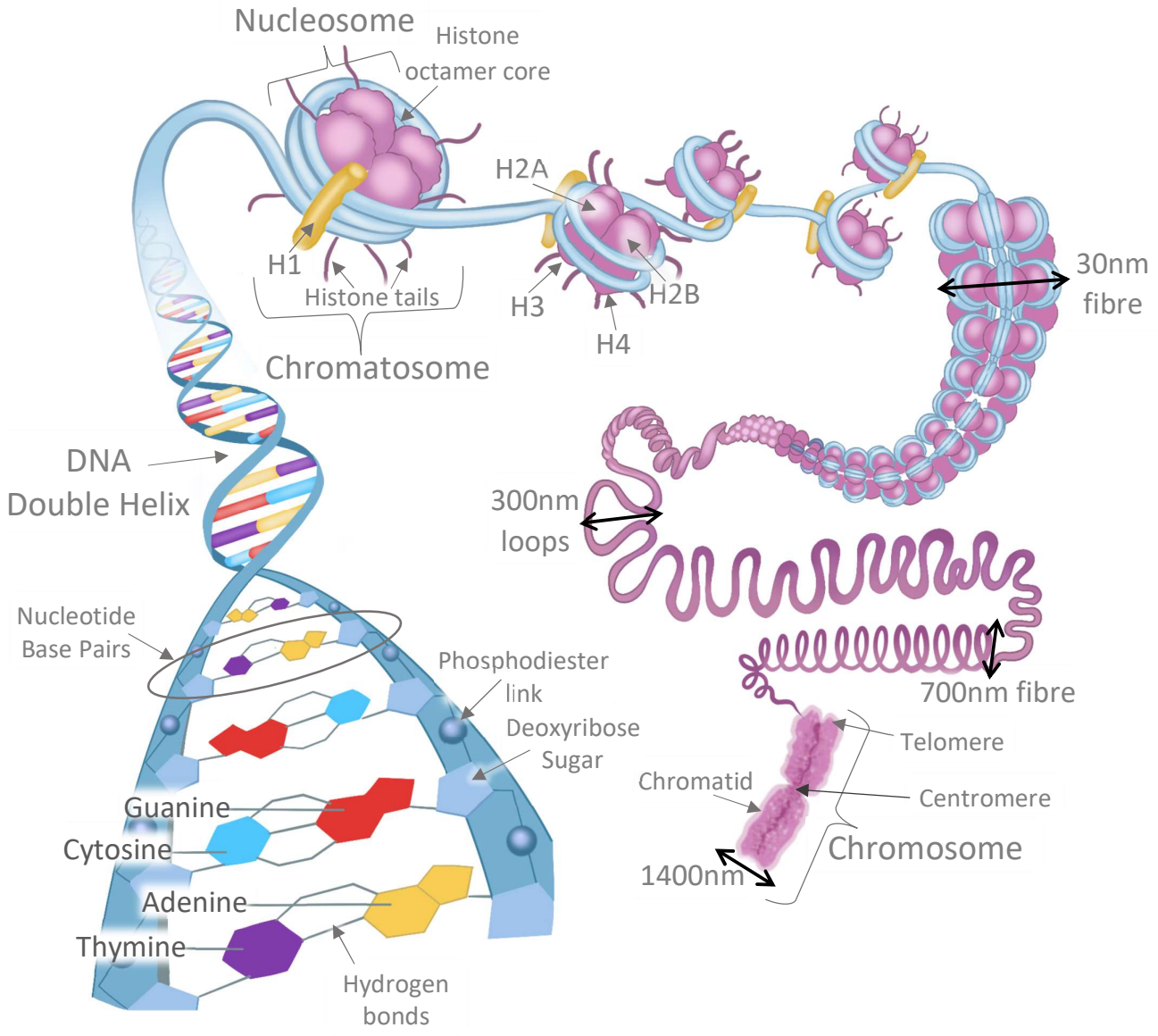

Figure 1.1: Primary, secondary and tertiary stages of Deoxyribose Nucleic Acid (DNA) structure. DNA is a polymer made up of a long sequence of deoxyribose nucleotide bases bound together by phosphodiester covalent bonds. Hydrogen bonds form between the specific base pairs Guanine:Cytosine and Thymine:Adenine stabilising the two strands of DNA into a helical structure referred to as a double helix (Watson & Crick, 1953; Chargaff, 1950; Pierce, 2012). DNA strands wrap 1.65 times around histone octamer protein core consisting of H2A, H2B, H3 and H4 dimmers, this is referred to as a nucleosome. H1 protein stabilises the structure and is known as a chromatosome, forming beads on a string (Carruthers *et al*., 1998; Pierce, 2012). Nucleosomes fold together to form a 30nm DNA and protein fibre. Further folding generates 300nm long loops that compact to 250nm wide coiling fibres that form 700nm wide chromatid arm (Lodish *et al*., 2000; Lodish et al., 2004 Dorigo *et al*., 2004; Pierce, 2012). The metaphase chromosome consists of two sister chromatids joined at the centromere, telomeres being at the very end of each chromatid arm, the chromosome is roughly 1400nm in width. Figure adapted from Pierce, Benjamin. Genetics: A Conceptual Approach, 4th edition.

DNA is a polymer made up of multiple repeating nucleotide units linked together to form a long molecule termed, a macromolecule. A single DNA macromolecule makes up one chromosome (Alberts *et al*., 2002; Pierce, 2012). The nucleotide monomers DNA is made up of are composed of the following:

- Pentose sugars composed of five carbons 1' through to 5' and has a hydrogen atom bound to the second carbon giving its name deoxyribose.
- Nitrogen containing base (nitrogenous base), which is either purine or pyrimidine. A and G are purines, they are formed of a six sided ring attached to a five sided ring and differ based on the positions of double bonds in the structure and adjacent groups. C and T are 6 sided pyrimidines that differ again based on double strand positioning and associated chemical groups. The nitrogenous base forms a covalent bond with the 1' carbon of the sugar.
- Phosphate group consisting of a phosphorus atom bound to four oxygen atoms, carrying a negative charge, and is bound to the 5' carbon of the sugar.

DNA nucleotides are properly known as deoxyribonucleotides and are the primary structure of DNA (Pierce, 2012).

The secondary structure refers to the 3D alpha double helix formed of two complimentary polynucleotide strands wound around one another, running anti parallel, with the sugar phosphates being on the outside fused to the neighbouring monomer by phosphodiester bond (Watson & Crick, 1953). At the 5' end of each strand there is a free phosphate and at the 3' end a free hydroxyl group. The associated bases of the structure are on the inside, like rungs on a ladder (Watson & Crick, 1953; Pierce, 2012). The structure is stabilised by the Watson and Crick base pairs C and G forming three hydrogen bonds with each other and A and T forming two hydrogen bonds, along with stacking forces between neighbouring bases (Watson & Crick, 1953; Chargaff, 1950; Pierce, 2012), refer to figure 1.1. These interactions whilst not as strong as covalent bonds have a purpose to their weakness. The frailty of the bonds and interactions allows for the separation of the strands by cellular machinery for DNA replication and transcription during Ribonucleic Acid (RNA) synthesis (Pierce, 2012; Alberts *et al*., 2002). As genetic information resides in the base sequence of DNA, transcription to RNA allows the code to be read and translated into amino acids that form proteins generating the cellular phenotype (Avery, 1944; Watson & Crick, 1953; Pierce, 2012). This is why when DNA is lost or mutated due to damage or error, the expression of genes and therefore proteins can be faulty or missing completely, in the case of loss of the protein P53 this can potentially result in initiation of cell malignancy.

The tertiary structure of DNA is a dynamic system, supercoiling between its most condensed chromosome state during mitosis and more relaxed chromatin state consisting of DNA and proteins during interphase where genes for transcription and translation need to be accessed and replication to occur (Li *et al*., 2007; Woodworth & Holloway, 2017; Pierce, 2012). This more relaxed state of active DNA access is referred to as euchromatin, heterochromatin is the more condensed form of chromatin and is mainly found at the centromeres and telomeres of chromosomes (Woodworth &

Holloway, 2017). Proteins in the chromatin are positively charged histones that attract the negatively charged DNA. There are five main histones; H1, H2A, H2B, H3 and H4. As seen in figure 1.1, DNA wraps around a octamer core consisting of H2A, H2B, H3 and H4 dimers forming a nucleosome (Luger *et al*., 1997). H1 stabilises the nucleosome structure. The core nucleosome combined with H1 is referred to as a chromatosome (Carruthers *et al.,* 1998; Pierce, 2012). Chromatosomes are connected to one another by linker DNA of about 30-40 base pairs forming beads on a string. Histone tails project out from the nucleosome core, and whilst offering a site for a number of modifications from initiation of gene transcription to the DNA repair pathway, they also interact with tails of neighbouring nucleosomes facilitating compaction (Bednar *et al*, 1998; Lodish, *et al*., 2000; Fischle *et al*., 2003; Pierce, 2012). This is a higher order of chromatin structure making a fibre about 30nm wide (Dorigo *et al*., 2004; Pierce, 2012). This fibre further compacts forming 300nm long loops anchored at their base by proteins. Additional folding and compressing occurs forming 250nm wide fibre that folds into the 700nm wide chromatid arm of the metaphase chromosome (Bednar *et al.*, 1998; Pierce, 2012). The metaphase chromosome consists of two sister chromatids held together at the centromere and a multiprotein complex termed the kinetochore at each chromatid centromere (Pierce, 2012). The kinetochore facilitates binding of the spindle fibres to the sister chromatids in preparation for the chromatid separation in anaphase of mitosis. It is during this process that aneuploidy or polyploidy may occur due to a nondisjunction event resulting in the miss segregation of chromosomes.

1.1.2 – DNA Damage

Consisting of 2.9 billion base pairs the human genome is simultaneously complex and simple (Venter *et al*, 2001). Simple in that its base components are only made up of 4 bases, complex in the packaging and maintenance mechanisms in place to preserve its integrity. Occurring at a rate of up to 10^5 lesions per cell per day both exogenous and endogenous agents can result in DNA damage (Lindahl, 1993). Exogenous (environmental) sources include ultraviolet (UV), radiation as well as chemicals introduced to a system. Whereas endogenous chemical genotoxins are as a result of normal metabolic activity, hydrolytic and oxidative reactions with water and reactive oxygen species (Chatterjee & Walker, 2017; Lindahl, 2000). It is predominantly these reactions that lead to spontaneous cancers and hereditary diseases (Chatterjee & Walker, 2017; Perrone *et al*., 2016). Predominantly DNA damage occurs at the primary level of DNA structure. These can result in bulky adducts and chemical bonds forming at the base level that disrupt the secondary helical structure of DNA. Due to the dynamic nature of DNAs' tertiary or 'superstructure' moving between heterochromatin and euchromatin for gene expression, this higher form of packaging does not confer additional protection from DNA damaging agents (Lodish *et al*., 2004). Damaging agents can cause harm to DNA in a number of ways, the most common of which are summarised in figure 1.2 along with the repair mechanisms and potential consequences): DNA strand breaks, both single and double; Oxidative; Base alkylation; Abasic site generation; Bulky adduct formation and DNA crosslinking (Hoeijmakers 2001; Chatterjee & Walker, 2017).

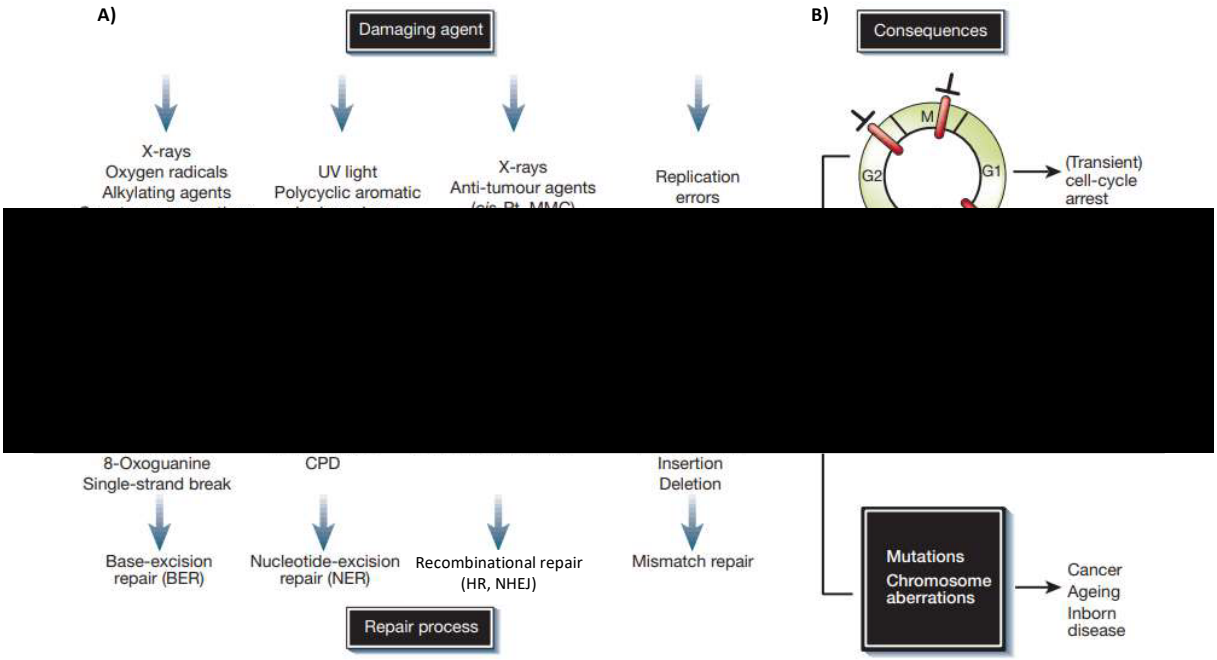

Figure 1.2: DNA damaging agents, DNA damage, resultant repair and outcomes. A) Top - Common DNA damaging agents; Middle - examples of DNA lesions induced by these agents. Cisplatin (cis-Pt) and mitomycin C (MMC) are crosslinking agents. 6–4 photoproduct ((6-4)PP) and cyclobutane pyrimidine dimer (CPD) are induced by UV; Bottom - most relevant DNA repair mechanism responsible for the removal of the lesions. There are two main types of recombinational repair that fix DNA double strand breaks, Homologous recombination (HR) and Non Homologous End Joining (NHEJ). B) DNA damage effects on cell-cycle progression, leading to G1, S, G2 and M phase arrest, resulting in inhibition of DNA processing. Consequences of DNA injury include permanent changes in the DNA sequence, mutation and chromosomal aberrations lead to biological effects such as cancer, ageing and hereditary diseases (Hoijmakers, 2001; Hoijmakers, 2009).

1.1.2.1 – Oxidative Damage

Reactive oxygen species (ROS) such as hydroxyl radicals (·OH) can be produced by ultraviolet (UV) and ionizing radiation or from metabolic reactions (Galano *et al*., 2018). Guanine is the most easily oxidised nucleic acid and reactions with ·OH forms 8-oxo-7,8-dihydrogeanine (8-oxoG). 8-oxoG is one of the most prevalent DNA lesions and is considered a biomarker for oxidative stress (Poetsch, 2020; Galano *et al*., 2018). Replication of DNA containing 8-oxoG results in the incorporation of Adenine opposite these modified Guanines. Upon conclusion of replication 8-oxoG is excised during DNA repair and Thymine used to replace it due to the A incorporation on the opposite strand resulting in a mutational event (Galano *et al*., 2018).

1.1.2.2 – Base Alkylation

Alkylating agents introduce legions that can be cytotoxic, mutagenic or neutral to the cell. Alkylating chemicals can modify any Oxygen and Nitrogen external to the rings

of the pyrimidine/purine structure as well as ring nitrogen's (Chatterjee & Walker, 2017; Eker *et al*., 2009). However, the amount of site modification depends on the alkylating agent and position of the DNA. Mutagenic lesions result in the miscoding of newly synthesised DNA, the most common modification of alkylation being methylation. The products formed include N7-methyl guanine, N3-methyladnenine and O6-methylguanine. Blocking of replication, interruption of transcription or apoptotic pathway activation are signs of cytotoxic legion induction (Eker *et al*., 2009). Base alterations also occur spontaneously such as the spontaneous deamination of 5-methylcytosines. These occur at varying rates dependant on the position in the DNA i.e., within a nucleosome turn or on linker DNA (Tomkova & Schuster-Bockler, 2018). Upon deamination cytosine converts to thymine resulting in a G to T. Both MMR and BER play a role in the correction of these errors (Poulos *et al*., 2017; Walsh & Xu, 2006).

1.1.2.3 – Abasic Sites

Abasic sites, apurinic/apyrimidinic (AP) sites are different terms for 'Base Loss'. AP sites are formed due to unstable hydrolysis of DNA. This is where neither a purine or pyrimidine base has been incorporated on one of the strands of the DNA leaving the opposing base without a partner (Lindahl, 1993; Lindahl & Barnes, 2000). This may happen spontaneously or be due to DNA damage. AP sites may also occur as a intermediate step in the Base Excision Repair (BER) pathway (Lindahl, 1993; Lindahl & Barnes, 2000). Abasic sites by nature are unstable and convert into single strand breaks (SSBs) due to targeting of 3' phosphodiester bond of the remaining deoxyribose by a β-elimination reaction (Bailly & Verly, 1988; Chan *et al*., 2013)

1.1.2.4 – Bulky Adducts

Biologically active chemicals may form covalent links with molecules such as DNA with molecules such as DNA, creating bulky adducts or appendages that branch off from the main molecule. Benzo[a]pyrene, a polycyclic aromatic hydrocarbon found in burnt meat and tobacco smoke, is one such chemical that when metabolically activated forms a epoxide that preferentially binds with Guanine residues to form a bulky adduct (Chatterjee & Walker, 2017; Wiencke, 2002). If this adduct is not repaired a Adenine base will be inserted opposite the adduct during replication. Excision of the bulky adduct after replication will result in a thymine insertion causing a G-T transversion mutation (Chatterjee & Walker, 2017). Additional examples of bulky adducts are Cyclobutane Pyrimidine Dimers (CPDs) and (6-4)Pyrimidine-pyrimidone photoproducts at dypyrimidine sites that form due to UV exposure (Besaratinia *et al*., 2005; Chatterjee & Walker, 2017).

1.1.2.5 – DNA Crosslinking

DNA crosslinking occurs when a reactive agent interacts with two nucleotides forming covalent link between them. This may happen on the same strand (intrastrand) or opposite strands (interstrand) (Chatterjee & Walker, 2017; Clauson

et al., 2013). DNA replication and transcription are often affected by these adducts. UV radiation can cause crosslinks to occur between pyrimidines and often neighbouring thymines, chemicals such as cisplatin and mitomycin C generate interstrand crosslinks often between guanine residues (Hoeijmakers, 2001; Clauson *et al*., 2013). These inter and intra strand adducts cause a kink to occur in the helical structure of DNA, if uncorrected inhibition of polymerases can occur causing misreading during transcription or replication and may lead to replication arrest (Hoeijmakers, 2001; Clauson *et al*., 2013). DNA intrastrand crosslinking is often fixed by Nuclear Excision Repair (NER) and interstrand crosslinks by Homologous recombination and Non homologous end joining (Hoeijmakers, 2001; Clauson *et al*., 2013).

1.1.2.6 - DNA Strand Breakage

Ionising radiation i.e. X-rays, due to high energy, can cause both single and double strand brakes directly. Chemicals that cause crosslinking of bases can also induce strand breakages if the damaged DNA undergoes replication (Hoeijmakers, 2001). During replication and transcription of DNA Topoisomerase (Topo) enzymes are used to relieve the helical tension, crosslinks cause Topo to stall remaining covalently bound to the DNA (Morimoto *et al*., 2019). This process, abortive catalysis, leads to the formation of single strand breaks in the case of Topo1 and double strand breaks in the case of Topo2. Generation of these breaks during transcription may help to signal DNA damage response pathway initiation (Morimoto *et al*., 2019; Hoeijmakers, 2001).

1.1.3 – DNA Repair

Eukaryotic cells have developed a series of mechanisms to preserve genome integrity, predominantly, DNA damage checkpoint activation and DNA damage repair (Chatterjee & Walker, 2017; Ding *et al*., 2020). In terms of DNA damage response two outcomes are prevalent, cells either undergo cell cycle arrest to allow damage repair and re-enter the cell cycle or the apoptosis (cell death) pathway is initiated (Ding *et al*., 2020; Hoeijmakers, 2001). Cell cycle progression and segregation of chromosomes into daughter cells is a highly regulated process and is separated into four distinct phases, multiple checkpoints are in place to ensure correct transition into each of the phases, see section 1.2 below. Upon incidence of DNA damage detection, the cell cycle is halted by cyclin-dependant kinase inhibitors (Ding *et al*., 2020). This is a complicated cascade with a series of downstream effects. DNA damage sensors in addition to blocking cell cycle progression are responsible for initiating repair pathways that are specific for each type of DNA damage (Ding *et al*., 2020; Hoeijmakers, 2001; Chatterjee & Walker, 2017). Single strands DNA breaks are repaired by Base Excision Repair (BER), Bulky adducts and crosslinks are repaired by Nucleotide Excision Repair (NER), smaller nucleotide mutations such as alkylation's are repaired by Mismatch Repair (MMR). Double strand breaks can be repaired by two different mechanisms; Non homologous End Joining (NHEJ) or Homologous Recombination (HR) (Chatterjee & Walker, 2017; Hoeijmakers, 2001).

1.1.3.1 – Base Excision Repair

Single strand breaks are repaired by the BER pathway as are oxidised bases. Oxidised bases are removed from the DNA by BER enzymes. The 8oxoG lesion is excised OGG1 (8-Oxoguanine DNA glycosylase) leaving a AP site. AP sites are then processed further, AP-endonuclease 1 nicks the backbone inducing a single strand break (Poetsch, 2020; Galano *et al*., 2018). This AP site can be repaired in one of two ways. The first is long patch base excision repair, the AP site along with additional bases are replaced by the activity of polymerase δ and ε with proliferating cell nuclear antigen (PCNA) (Poetsch, 2020). The old strand is removed by flap endonuclease one and ligase one reseals the backbone. The second is short patch BER, here Polymerase β replaces the single missing base, LigaseIII and X-ray repair cross complementing protein one complex sealing the backbone (Poetsch, 2020).

1.1.3.2 – Nucleotide Excision Repair

The NER process excises DNA fragments of 24 to 32 nucleotides long that contain the damage lesion with high accuracy. Then the undamaged strand is used as a template and repaired sequence ligated into the DNA, repairing the break that occurred as a result of the cross link/ bulky adduct damage excision (Petruseva, 2014; Hanawalt, 2002). Determined by initial type of damage recognition there are two potential NER routes. Global Genome Nucleotide Excision Repair (GG-NER) identifies and removes bulky lesions from the entire genome. Transcription Coupled Nucleotide Excision Repair (TC-NER) is initiated when damage to the DNA that is being transcribed inhibits RNA polymerase II transcription (Petruseva, 2014; Hanawalt, 2002). XPC-hHR23B protein identifies damage in GG-NER it is not required in TC-NER. After the initial detection of damage, the continued progression of the NER pathway is the same for both GG-NER and TC-NER (Petruseva, 2014; de Laat *et al*., 1999). Involved in RNA polymerase II activation, NER and cell cycle regulation TFIIH is a 9 subunit complex (de Laat *et al*., 1999). TFIIH bind the DNA near the site of the bulky addict creating a 10 to 20 nucleotide opening in the DNA complex. Additional proteins: RPA, XPG, XPA, ERCC1 are recruited to the site (Petruseva, 2014; Gillet & Schärer, 2006; Fousteri & Mullenders, 2008). XPA bind the damaged nucleotides, RPA to the undamaged strand (Shivji *et al*., 1995; de Laat *et al*., 1999). The repairasome is fully stabilised by XPG which makes the three prime incision on the DNA backbone. ERCC1-XPF makes the second incision on the five prime side of the lesion (Shivji *et al*., 1995; de Laat *et al*., 1999). Once the lesion has been removed proliferating cell nuclear antigen (PCNA) and Replication Factor C (RFC) aid polymerase δ to perform patch repair (Shivji *et al*., 1995). DNA ligase then re-seals the DNA backbone.

1.1.3.3 – Mismatch Repair

Mismatch repair helps maintain genome stability through correction of mismatched bases and modified bases such as alkylation. The major source of mismatch base pairs is replication error. The E-coli MMR machinery is able to identify the DNA template strand due to its methylated state compared to the new strand which is

unmethylated, it is possible that this also occurs in eukaryotes (Fukui, 2010). Post replicative MMR is performed by the long patch MMR mechanism, here a long portion of oligonucleotide is excised during repair removing the lesion. In eukaryotes mutSα and mutSβ identified the mismatch (Fukui, 2010). PCNA, RFC, mutLα and mutLγ perform the strand incision, RPA single stranded binding protein and Exo1 exonuclease excised the nucleotide sequence with the lesion (Fukui, 2010). DNA polymerase δ fills the gap and ligase repairs the backbone nicks (Fukui, 2010).

1.1.3.4 – Double Strand Break Repair

Induction of a Double Strand Break (DSB) in the DNA is a highly toxic lesion, and unresolved DSBs are linked to various cancers and human diseases (Jackson & Bartek, 2009). Non homologous end joining (NHEJ) and Homologous recombination (HR) are the two major pathways of DSB repair. The first step that signals DSB induction is chromatin modifications that trigger cascading events for recruitment of the DNA damage repair machinery, this include but are not limited to: Ataxia-telangiectasia mutated (ATM) kinase activation, H2AX phosphorylation, MDC1 recruitment along with 53BP1 and BRCA1 (Panier & Boulton, 2014; Liu *et al*., 2014; Chatterjee & Walker, 2017). Phosphorylation of serine 139 on the histone H2AX variant, referred to as γH2AX, through both direct and indirect mechanisms serves in both the NHEJ and HR pathways to aid in scaffold and retention of effector proteins (Cully & Xie, 2013; Chen *et al*., 2019; Collins *et al*., 2020). The NHEJ pathway for repair of DSBs can take place at any phase of the cell cycle whereas HR can only occur in the S and G2 phases of the cycle (Krajewska *et al*., 2015). NHEJ is the simplest and widest used mechanism of DSB repair, the process simply reseals the two broken ends regardless of base sequence homology, this means the process is error prone. In contrast HR is extremely accurate in maintaining sequence homology by predominantly using the sister chromatid as a template for repair (Krajewska *et al*., 2015; Hoijmakers *et al*., 2001). The two pathways compete to perform the repairs. The MRX complex, composed of MRE11/RAD50/XRS2 is recruited to the ends of the DNA DSB and plays a role in both NHEJ and HR (Decottignies, 2013).

1.1.3.4.1 – Non Homologous End Joining

For initiation into the NHEJ, Ku70/Ku80 heterodimer inhibits the 5'-3' exonuclease activity by binding the DNA ends, which prevents initiation of the HR pathway. The DNAPKcs, complexes with XRCC4 and binds to the Ku70/Ku80 stabilising the NHEJ complex and initiating recruitment of further proteins (Jackson, 2009; Panier & Boulton, 2014). This stabilising scaffolding complex allows Artemis, PNKP, APLF, WRN, APTX to initiates DNA end processing, this removes blocking groups and resecting the naked strands (Jackson, 2009; Chattergee & Walker, 2017; Panier & Boulton, 2014). The gaps left behind by resection are filled by specific polymerases (POLμ or POLλ) and DNA ligase IV joins and seals the ends (Panier & Boulton, 2014; Lieber, 2010). NHEJ low fidelity usually results in nucleotide deletions or insertions at the repair junction (Decottignies,2013; Chattergee & Walker, 2017).

1.1.3.4.2 – Homologous Recombination

Due to the lack of a sister chromatid in G1 the HR pathway is largely inhibited, not until the synthesis phase of the cell cycle where two copies of the DNA become available does HR become active (Johnson & Jasin, 2000; Krejci *et al*., 2012). HR does not have one unique mechanism but many potential routes: Synthesis-Dependent Strand Annealing (SDSA), double Holliday junction resolution (also known as Double Strand Base Repair (DSBR)) and single-strand annealing (SSA). The common theme in each of these mechanisms is the generation of single stranded DNA and can be classified into presynapsis, synapsis and postsynapsis (Chattergee & Walker, 2017; Li & Heyer, 2008). The presynapsis and synapsis stages are the same for SDSA, DSBR and SSA, it is not until postsynapsis that distinct divergence of mechanisms occurs (Li & Heyer, 2008).

The MRN complex consisting of MRE11/RAD50/NBS1 initiates HR where it recognises and binds to the DNA at the DSB site (Stracker & Petrini, 2011; Chatterjee & Walker, 2017). During presynapsis ATM and TIP60 are recruited to the DNA, TIP60 activates ATM which phosphorylates H2AX which provides anchoring for MDC1 across the DSB site (Riches *et al*., 2008; Panier & Boulton, 2013; Collins *et al*., 2020). Upon recruitment ATM phosphorylates MDC1 which acts as a scaffold for the ubiquitin E3 ligases RNF8 and RNF168. The E3 ligases are then able to ubiquitinate H2AX which then acts as a docking site for BRCA1 and 53BP1 (Riches *et al*., 2008; Altmeyer and Lukas, 2013; Panier & Boulton, 2013;) BRCA1 inhibits 53BP1 helping to commit the system to the HR pathway (Panier & Boulton, 2013). RPA and RAD51 join the scaffolding complex on the DNA and end resectioning occurs via the endonuclease activity of MRN and EXO1 or BLM where 5'-3' nucleolytic degradation results in 3' nucleotide overhangs, the system is now fully committed to the HR pathway (Chen *et al*., 2008; Nimonkar *et al*., 2011; Panier & Boulton, 2013; Chatterjee & Walker, 2017). The next step 'synapsis' is entered, and RPA is dislodged from the 3' overhang by RAD51 generating a nucleoprotein filament when combined with BRCA2 and PALB2 (Zhang *et al*., 2009; Holloman, 2011). This nucleoprotein filament then invades near by duplex DNA forming a D-loop (Krajewska *et al*., 2015; Li & Heyer, 2008).

After formation of the d-loop intermediate the HR pathway diverges commits to one of the three mechanisms during postsynapsis. A summary of the DSBR mechanism shall be focussed on here. On invasion of the template DNA RAD54 and 54B remove RAD51 allowing the 3'OH group to activate by Polymerases δ, κ and ν ready for synthesis (Li & Heyer, 2008; Mazin *et al*., 2010; Sebesta *et al*., 2013; Punatar *et al*., 2017). DNA synthesis occurs filling the gaps at which point second end capture occurs resulting in the formation of double Holliday junctions (Punatar *et al*., 2017). The BLM helicase-TopoisomeraseIIIα-RMI1-RMI2 (BTR) complex catalyses the dissolution of the Holliday junctions. GEN1 endonuclease, MUS81/EME1 and SLX1/SLX4 complexes may also process the

junctions (Cicca *et al*., 2008; Fekairi *et al*., 2009; Rass *et al*., 2010; Punatar *et al*., 2017).

1.2 – Cell cycle

The biomarkers ɣH2AX, pH3, P53 and genotoxic endpoint of micronucleus formation cannot be discussed without first having an understanding of the cell cycle and its checkpoints. This is because cellular and DNA damage responses are intrinsically linked with the cell cycle (figure 1.3).

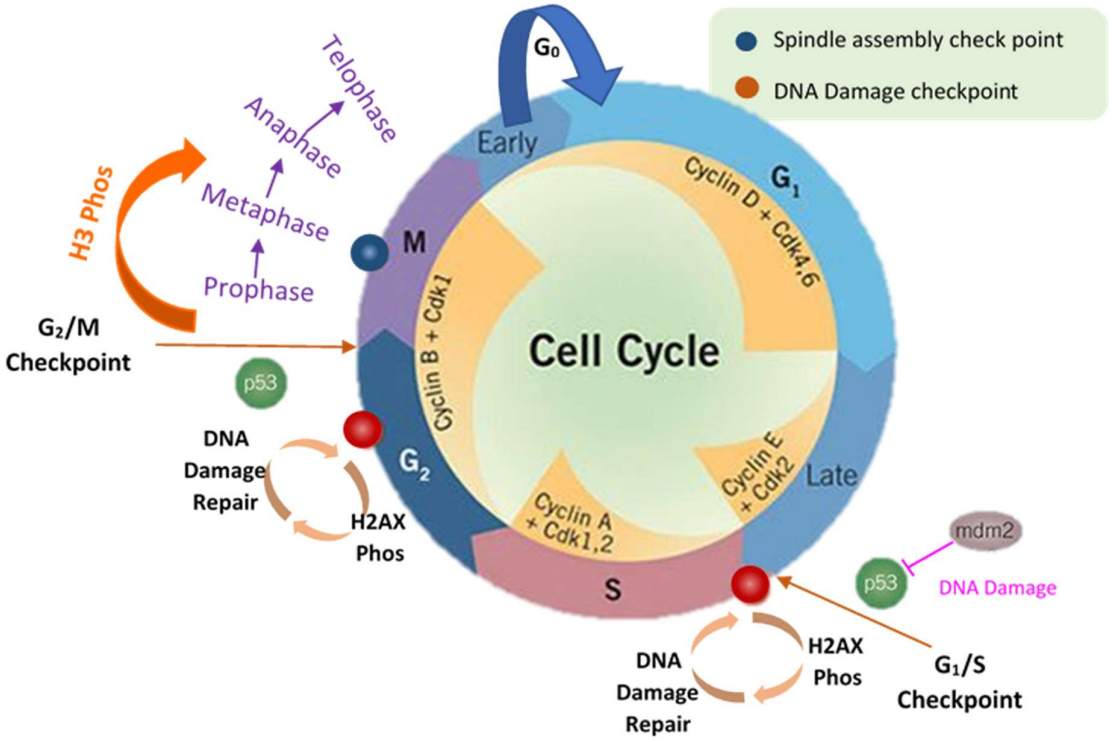

Figure 1.3: Depicts the main stages of the cell cycle; Interphase consisting of G1, S and G2. Mitosis consisting of: Prophase; condensing of chromosomes. Metaphase; Chromosomes aligned along metaphase plate. Anaphase; Cohesins binding chromatids are degraded spindles contract pulling chromatids apart and Telophase; Daughter nuclei begin to form and cell starts to divide (Tyson *et al.*, 2002). H2AX phosphorylation at checkpoints on the induction of SSBs and or DSBs result in DNA damage repair to occur, allowing the cell cycle to continue. Phosphorylation of H3 Serine residues signal prophase initiation, global phosphorylation at metaphase and progression into anaphase (Hans *et al*.,2001). Figure adapted from Tocris., 2015.

Cell cycle Interphase is split into G1, S and G2 stages. Mitosis is the last stage of the cell cycle and is split into: Prophase, Metaphase, Anaphase and Telophase contributing to an equal division of DNA into two daughter cells (Poehlmann *et al*., 2010). G1 (Gap phase 1) of the

cell cycle is characterised by increase of cell size through accumulation of proteins, energy, and nucleotides ready for nuclear content duplication (Schafer., 1998; Vermeulen *et al.*, 2003). The S (Synthesis) phase of the cell cycle immediately follows G1 and is named as such as DNA replication occurs during this phase of the cell cycle. Here centrosomes also duplicate. At the end of this phase the nuclear DNA will have doubled 1n to 2n (also referred to as 2n to 4n) (Schafer., 1998; Sclafani *et al.*, 2007). The second Gap (G2) phase, also referred to as the rest phase, the cell makes preparations to enter mitosis. Protein synthesis for chromosome manipulation and organelle duplication occurs here (Vermeulen *et al*., 2003; Norbury & Nurse., 1992). Once the cell is prepared it will enter mitosis. The first phase of mitosis is prophase, here chromosome condensation begins, spindle fibres start to develop from the centrosomes and the nuclear envelop disappears (Poehlmann *et al*., 2010). Prometaphase and metaphase stages consist of continuation of chromosome condensation microtubule and kinetochore assembly, centrosomes move to opposite poles. This is followed by chromosomes being lined up along the metaphase plate and full mitotic spindle assembly with centrosomes at opposite poles of the cell (Poehlmann *et al*., 2010; Cheeseman & Desai., 2008). At entry to anaphase the sister chromatids bound together at the centromere kinetochore complex, are completely attached to one spindle fibre emanating from opposite centromeres at the cell poles. Cohesin proteins connecting the centromere of the two sister chromatids break down and are separated by contracting microtubules at the kinetochore interface (Poehlmann *et al.*, 2010; Cheeseman & Desai., 2008). The newly defined chromosomes move to the cellular poles the cell lengthening and becoming oval in shape. Once chromosomes have arrived at the opposite poles the cell has entered telophase. The DNA structure begins to relax and the mitotic spindle breaks down, the nuclear envelope reforms. A cleavage furrow then separates the daughter cells before individual cytoplasmic membranes are formed generating two identical daughter cells (Poehlmann *et al*., 2010. Vermeulen *et al*., 2003). The mechanisms that aid mitosis include the epigenetic modifications of histone tails on histones such as Histone 3 and Histone 2A variant X (Ichijima *et al*., 2005). Daughter cells then enter Go phase, this is a holding pattern state where cells are inactive. External signals trigger the onset of G1 (Vermeulen *et al*, 2003; Foster., 2008).

During the G phase, S phase and G2/M phases of the cell cycle information is continually being collected to determine cellular readiness to pass into the next cell cycle stage (Norbury & Nurse., 1992). These are termed checkpoints. The main checkpoints are G1/S, Inter S phase, G2/M and Spindle Assembly Check Point (SAC) (Elledge., 1996; Tyson *et al*., 2002; Poehlmann *et al*., 2010). Checkpoint control is mediated through Cyclin dependant kinases (CdK) and Cyclins, the DNA either passes the checkpoint into the next phase or the cell cycle is arrested (Tyson *et al.*, 2002; Poehlmann *et al*., 2010; Otto *et al*., 2017). This occurs through induction of tumour suppressing factors such as P53 and DNA damage repair pathway mediators such as ATM kinases upon Double Strand Breaks (DSB) and Ataxia-telangiectasia and Rad3 related (ATR) Kinases on Single Strand Breaks (SSB) figure 1.3 (Tocris., 2015; Lord & Ashworth., 2012). The maintenance of these checkpoints, cyclin complexes and monitoring of the genome for DNA damage and therefore having a crucial role in genome maintenance, is P53 (Schafer., 1998; Lavin & Gueven., 2006). P53 signalling

pathways in turn lead to recruitment of DNA repair complexes signalled by epigenetic modifications of histones such as H2AX phosphorylation.

1.3 – Genetic Toxicology and testing strategy

Genotoxicity tests can be defined as *in vitro* and *in vivo* assays designed to detect compounds that induce genetic damage by various modes and mechanisms. These tests enable hazard identification with respect to damage done to DNA and potential risk (Dearfield *et al*., 2017; Hartwig *et al*., 2020; Thybaud *et al*., 2007). Genotoxic chemical compounds can be divided into 3 categories:

- Mutagens – Compounds that react with DNA causing mutation.
- Clastogens – Compounds that react directly or indirectly with the DNA resulting in DNA breaks.
- Aneugens – Compounds that disrupt the cell division apparatus leading to miss segregation of the chromosomes.

In terms of safety assessment for human exposure, genetic toxicology tests are used across several industries from chemical and environmental to fashion, food and pharmaceuticals. Within the drug development pipeline specifically there are approved guidance's available on appropriate testing strategies, namely International Conference on Harmonisation (ICH) S2(R1) and the various *in vitro* and *in vivo* Organisation for Economic Co-operation and Development (OECD) testing guidelines. A combination of assays, referred to as a test battery, are used to assess the potential for carcinogenesis due to the vast spectrum of genetic damage mechanisms (ICH S2(R1), 2011; OECD, 2017; MacGregor *et al*., 2000; Dearfield *et al*., 2017; Hartwig *et al*., 2020). The recommended tests focus predominantly on gene mutation and chromosome damage endpoints because they have been identified as molecular events that are critical in tumour initiation.

There are two predominant pathways suggested in the ICH and OECD guidelines for an appropriate battery of genetic toxicology good laboratory practice (GLP) package prior to first time in human that provide a robust platform for the identification of potential risk to the human population for promising drug candidates (ICH S2(R1), 2011; OECD, 2017). The first pathway consists of two *in vitro* assays, one being the bacterial reverse mutation assay ('Ames' test) the other a mammalian cell assay usually the Mouse lymphoma L5178Y cell *thymidine kinase* gene mutation assay (MLA) or Micronucleus Test/Assay (MNT). *The in vitro* assays may also include a +S9 arm in an attempt to mirror *in vivo* metabolism of the drug compound (ICH S2(R1), 2011; Kirkland *et al*., 2005) . These *in vitro* tests are followed by a single end point *in vivo* rodent micronucleus study using either peripheral blood or bone marrow. The second pathway again includes an Ames test but excludes the *in vitro* mammalian option for a dual endpoint *in vivo* study, taking samples for both micronucleus assessment and Comet analysis (ICH S2(R1), 2011; OECD, 2017; Kirkland *et al*., 2019).

1.3.1 – Ames assay

Salmonella typhimurium reverse mutation assay developed by Bruce Ames *et al*., 1973, which may be combined with the *Escherichia coli* (*E.Coli*) reverse mutation assay, Green

& Muriel, 1976, is colloquially referred to as 'The Ames Assay'. The assay detects gene mutations, specifically base pair substitutions and frameshift mutations, using bacterial test strains modified at specific *histidine* or *tryptophan* loci that may or may not contain a plasmid (Gatehouse, 2012):

- *Salmonella typhimurium* – TA1535, TA100, TA1538, TA98, TA1537, TA97, TA102

- *Escherichia coli* – WP2uvrA(pkm101), WP2uvrA

The *salmonella typhimurium* strains each differ in that they have a different mutation in the histidine operon (Ames, 1975; Maron, 1983). The *E.Coli* strain carries a AT base pair at the critical mutation site within the *trpE* gene blocking tryptophan biosynthesis (Bridges *et al*., 1967; Green & Muriel, 1976; Mortlemans & Roccio, 2000). These different mutations act as sensitive sites where reversion to the parent wild type for histidine/tryptophan synthesis are possible. These mutations in the amino acid synthesis genes make the bacteria auxotrophic, so they require the presence of the histidine and tryptophan amino acids to grow (Ames, 1975; Maron, 1983; Mortlemans & Zeiger, 2000; Gatehouse, 2012). In the presence of a genotoxic mutagen the bacteria will revert back to the wild type prototrophic strains, meaning they are able to grow in the absence of amino acids (Gatehouse, 2012). An increase of large bacterial colony growth compared to that of untreated controls identifies true revertants and a positive response indicating the test compound is a mutagen (Ames, 1975; Green & Muriel, 1976; 1967; Maron, 1983; Gatehouse, 2012). Not all treated bacterial strains may give a positive response and this is due to the sensitive sites in each of the different strains detect different types of mutation mechanism i.e. base pair substitution or frameshift (Maron, 1983; Wilcox *et al*. 1990; Yamada *et al*., 1995; Gatehouse, 2012). Different combinations of bacterial strains are used in an attempt to cover the array of potential mutations that may occur in the presence of a potentially genotoxic compound (Gatehouse, 2012).

1.3.2 – Mouse Lymphoma Assay

The MLA is a mammalian cell culture assay used to evaluate chemicals for their potential to induce genetic mutation and/or chromosomal damage which result in the formation of mutant colonies (i.e. it is a clonal mutation assay) (Lloyd & Kidd, 2012; Cole *et al*., 1983; Moore *et al*., 1985; Applegate *et al*., 1990). The *Thymidine Kinase (TK)* locus is used as a genetic biomarker of gene mutation and is an indicator of chemically induced mutagenesis in mammalian genome, the assay is performed using mouse lymphoma L5178 Y *(TK +/-)* cell line. TK is an enzyme involved in a salvage pathway for incorporating thymidine bases into DNA. TK converts free thymidine to thymidine monophosphate to be used in DNA synthesis (Lloyd & Kidd, 2012). Once cells have been incubated with the test compound and the inclusion of Trifluorothymidine (TFT) during plating, this allows for the identification of cells that have undergone a forward mutation to *TK -/-* due to cell colony survival (Moore-Brown, 1981; Cole, *et al*., 1983). TFT is a thymidine nucleoside analogue and is lethal to the cell when it becomes incorporated into the DNA in the presence of the active TK protein (Lloyd & Kidd, 2012). The premise of the assay is if a test compound results in a mutation at the *TK* locus or

damage to the chromosome resulting in conversion from a functional (*+*) gene to mutant (-), the cell will use an alternate pathway for the incorporation of thymidine monophosphate for DNA synthesis resulting in cell survival (Lloyd & Kidd, 2012; Cole *et al*., 1983; Moore *et al*., 1985). As L5178Y cells are negative for P53 activity there is reduced repair and apoptosis which results in the creation and survival of more mutant cells i.e. *TK-/-* cells. An increase of cell colony growth in treated cultures compared to that of untreated identifies potential mutagens and clastogens (Lloyd & Kidd, 2012; Cole *et al*., 1983; Moore *et al*., 1985). The assay is able to identify both through the size of the cell colonies, large colonies are indicative of small point mutations or deletions whereas smaller colonies are more likely to be as a result of larger chromosome rearrangements/deletion/breaks (Applegate *et al*., 1990; Moore *et al*., 1985).

1.3.3 – Comet

Physical DNA Breaks may be repaired (no effect), may be lethal (cell death), or may be fixed into a mutation (permanent damage). The Comet assay detects global DNA strand breaks (clastogenicity) in somatic tissues at that moment in time, it also has the potential to detect DNA crosslinking chemicals (Sasaki *et al*., 2000). Under alkaline conditions this assay detects single, double strand breaks as well as alkali-labile sites (Singh *et al*., 1998). Comet can be performed with any tissue sample that can be made into a single cell suspension, with minimal processing avoiding damage to cells (Singh *et al*., 1998; Sasaki *et al*., 2000). A cell suspension volume mixed with low melting point agarose, is placed on normal melting point agarose dipped slides. Once set, cells are lysed leaving the nuclear contents held within the agarose matrix, the slides are then electrophoresed (Fielder *et al*., 1992; Lovell *et al*., 1999; Hartman *et al*., 2003; Hartman *et al*., 2004]. Pieces of DNA that have become 'broken' move through the agarose from the negative terminal to the positive, given the negative charge of the DNA molecules, away from the main nuclear body 'head' creating a 'tail' (Olive *et al*., 1990; Singh *et al*., 1998). Slides are then stained before being visualised and quantified via microscope using specialised image analysis software. The assay measures DNA fragment migration following electrophoresis; the length of migration is proportional to the amount of DNA strand damage (Olive *et al*., 1990).

1.3.4 – Micronucleus Test

Use of MN as a measure of chromosomal damage was first suggested by Evans *et al* in 1959. However, MN were not used as a established genetic toxicology assay until after 1971 when Matter and Schmid developed the *in vivo* mouse bone marrow MN test. Following this in 1976 an *in vitro* version of the MN assay using cultured human lymphocytes for short term carcinogenicity testing was developed by Contryman & Heddle, 1976.

The Micronucleus Test (MNT) is a straightforward cytogenetic assay based on scoring small portions of DNA whether they be whole chromosomes, acentric chromatids or chromosome fragments that have not been incorporated into the daughter cells' nucleus during cell division. Micronuclei (MN) are produced when whole chromosomes

or DNA fragments are unable to attach to the spindle at mitosis appearing during the next interphase as small bodies adjacent to the daughter nucleus. The MNT assesses DNA loss in cells through either Clastogenicity (structural chromosomal changes – caused by DNA strand breaks, DNA adducts, or genome instability) or Aneugenicity (numerical chromosomal changes – caused by mitotic infidelity and/or genome instability) (Tsuchimoto, 1979; Yamamoto, 1980). In essence, MNT detects non-lethal gene mutations and structural chromosome damage in mammalian cells, using fluorescence whether that be microscopy or flow cytometry (Bryce *et al*., 2008; Diaz *et al*., 2007). This test can be performed *in vitro* or *in vivo* and is considered an important assay in the assessment of risk following the dogma 'one point of DNA damage results in one mutation that will then result in cancer'. There are multiple versions of the MNT, but one rule is the same for all, it must be performed in actively dividing cells i.e., a nuclear division must occur (OECD 474, 2016; OECD 487,2016).

1.3.4.1 – *In Vivo*

In vivo assessment of MN allows for the consideration of factors of *in vivo* absorption, distribution, metabolism, and excretion of drugs and also mammalian DNA-repair processes (OECD 474, 2016). The tissue most often assessed for frequency of micronuclei is bone marrow. The bone marrow is readily accessible to chemicals that are present in the blood. Peripheral blood using flow cytometry analysis can also be used to assess MN response (OECD 474, 2016; Richold *et al*, 1990). Due to the high proliferating nature of liver tissue when damaged, the liver MN assay can also be performed, however use of this version of the assay is rare.

For the bone marrow MN assessment animals (usually rats or mice) are dosed twice 24 hours apart and are sacrificed 24 hours later (OECD 474, 2016). The femur is removed, and bone marrow aspirated. The sample is smeared onto microscope slides and stained with acridine orange before being analysed by fluorescence microscopy (Schmid, 1975; Matter, 1976; Tsuchimoto & Matter 1979). The immature red blood cells, polychromatic erythrocytes, stain orange due to the RNA content whilst normochromatic (mature) erythrocytes stain green as the RNA content has been removed as the cell matures (Hayashi *et al*., 1990; Kasamoto *et al*.,2013). If DNA damage has occurred a small piece of DNA remains in the polychromatic or normochromatic erythrocytes after the main nuclear body has been expelled during erythropoiesis (MacGregor *et al*.,1980; Hayashi *et al*., 1990; Kasamoto *et al*.,2013). The nuclear content stains bright yellow. With all biological systems there is a background frequency of DNA damage, this is no different for the MN endpoint and therefore a positive response to a test compound is indicated by a increase of MN induction compared to control (normal) levels (OECD 474, 2016).

1.3.4.2 – *In Vitro*

The *in vitro* MNT is predominantly used to help identify MoA. The addition of cytogenetic staining techniques allows the differentiation between aneugenicity and clastogenicity to be made (Doherty *et al*., 1996; Lynch and Parry, 1993; Hoshimoto *et*

al., 2012). The *in vitro* assay can be performed on human peripheral blood lymphocytes and different mammalian cell lines including but not limited to; L5178Y ($TK^{+/-}$) Mouse Lymphoma cells, Human Lymphocyte TK6 cells, Chinese Hamster Cho-K1 cells and Human HepG2 hepatoma cell line. The *in vitro* MNT can include a number of treatment regimens (OECD,2016; Fowler *et al*., 2012; Hoshimoto *et al*., 2012; Doherty, 2012):

- long treatment (24 hours in the absence of S9-mix), with the option of a 12 hour recovery period
- short treatment (3 hours in the presence &/or absence of S9-mix)

The profile of treatments conducted usually depends on the information required from the compound being tested e.g., short acting genotoxin requiring metabolic activation would require a 3 hour treatment in the presence of S9 (OECD, 2016; Doherty, 2012). Whilst the time points of compound exposure may change, as well as the cell line used, the time it takes for a MN to be generated is roughly 1.5-2 cell cycles (OECD, 2016). There are two versions of the MN assay the Mononucleted (mono) and the Bi-nucleated (Bi) assay. The main difference between these two assays is the Bi-MNT requires the addition of Cytochlasin B (CytoB) (Fenech & Morley, 1986; OECD, 2016). CytoB is a actin inhibitor that prevents cytokinesis at the end of mitosis from occurring. As a result, a binucleate (a cell containing two distinct nuclei) is generated. This demonstrates the cell has divided when in the presence of the test compound and often makes it easier to identify MN as well as other nuclear abnormalities such as neoplasmic bridges (Fenech & Morley, 1986; Fenech, 2007; Fenech, 2020). In the Bi-MNT only micronuclei in cells with two nuclei are counted whereas in the Mono-MNT MN are only counted in cells with one nucleus.

In the event a test compound indicates a positive MN response, cytogenetic staining techniques such as Fluorescence In Situ Hybridisation (FISH) and Kinetochore staining have been traditionally used for the assessment of chemical MoA (Doherty *et al*., 1996; Lynch & Parry, 1993). Both these techniques allow for the assessment of whole chromosome presence. The idea being the presence of a centromere/kinetochore is indicative of a whole chromosome being present as it is unlikely that fragmentation of a chromosome would result in centromere/kinetochore loss from the nucleus. Therefore, it is reasonable to suggest that presence of a MN containing a centromere/kinetochore fluorescence signal would have likely occurred due to some nondisjunction event i.e., aneugenic MoA and lack of signal would imply a clastogenic MoA (Doherty *et al*., 1996; Lynch & Parry, 1993). The main difference between FISH and Kinetochore labelling is FISH allows specific chromosome identification due to fluorescently labelled DNA probes binding to unique DNA centromere sequences that are specific for each chromosome during a heating, denaturing, hybridisation process (Doherty, 2012; Hoshimoto *et al*., 2012). In binucleated cells this also allows for a more specific analysis of non disjunction events. Kinetochore staining indirectly assesses whole chromosome presence as a specific anti-kinetochore antibody binds to the

kinetochore protein. The antibody will bind to the kinetochore regardless of chromosome number i.e., chromosome 2 will stain the same as chromosome 11. Whilst kinetochore staining does not require the same denaturation and hybridisation protocol as FISH it is still an extra, time consuming processing step (Doherty, 2012; Hoshimoto *et al*., 2012).

1.3.5 – Genetic Toxicology Summary

Due to the Ames test concordance with rodent carcinogenicity study data (Zeiger, 1987; Ashby & Tennant, 1988) if a positive response is recorded for a compound using this assay it usually goes no further in the development process unless the compound is known to have specific bactericide properties (ICH, 2011). In the event of a *in vitro* mammalian positive, the pipeline may still continue but requires a dual endpoint *in vivo* study to confirm or overrule the *in vitro* mammalian positive result. The reasoning behind this flexibility is there is less concordance with *in vitro* mammalian assays and *in vivo* carcinogenicity data compared to that of Ames and is often overly sensitive i.e., the hazard does not often translate into risk *in vivo* (ICH S2(R1), 2011; OECD, 2017; Kirkland *et al*., 2019; Kirkland *et al*., 2014; Kirkland *et al*., 2008).

Whilst there may be weaknesses to *in vitro* GLP safety assessment, use of these assays as screening tools not only help mitigate hazard translating to risk in the human population and potential financial fall out due to late stage attrition but also reduce animal usage in line with the NC 3Rs principles (Kirkland *et al*., 2005; Kirkland *et al*., 2014). Screening assays provide the ability to reduce the pool of drug candidates down to the most promising options whilst having safety at the forefront of the strategy. Understanding the chemical Mode of Action leading to potential insights into the mechanism can aid in an informed decision process and understanding of threshold and point of departure metrics of dose responses (Dearfield *et al*., 2017; Hartwig *et al*., 2020). Providing more information prior to *in vivo* studies can help us understand the biological system capacity for tolerance and a threshold at which hazard translates to risk in a compounds potential for initiating tumorigenesis (Jenkins *et al*., 2010; Thomas *et al*., 2015; Chapman *et al*., 2021).

1.4 – Biomarkers

1.4.1 – P53

P53 is a tumour suppressor transcription factor that plays a vital role in both the regulation of cell cycle checkpoints and apoptotic induction. Due to the interlinked pathways of cell cycle maintenance and apoptosis, mutation and or loss of the *P53* gene can lead to cancer. The cell cycle consists of 4 main phases; Cell growth 1 (G1), DNA synthesis (S), Cell growth 2 (G2) and Mitosis (M). Each phase has a checkpoint of control that the cell is arrested at if DNA damage is detected to allow time for repair. The main checkpoints are; G1/S, G2/M, intra S-phase and Mitotic as shown in figure 1. P53 on the induction of DNA damage can halt the progression of the cell cycle into the next phase,

this allows time for DNA Damage Repair (DDR) pathways to be initiated and instigate any DNA adduct removal (Lord & Ashworth., 2012). If the damage at these checkpoints is excessive P53 will then upregulate the apoptotic pathway via transcription of apoptotic transcription factors which initiate the caspase cascade (King & Klidowski., 1998).

At the G1/S checkpoint active un-phosphorylated Cdc25A, dephosphorylates Cdk2-Cyclin E complex keeping it in its active form and phosphorylated CDK4-Cyclin D phosphorylates Rb (Retinablastoma protein) causing it to release E2F. The active Cdk2-Cyclin E and E2F drives the cell forward into S phase (Moll & Petrenko., 2003; Ma *et al*., 2015). Upon DNA damage ChK1/ChK2 phosphorylates Cdc25A inducing either its degradation or binds 14-3-3 and can activate the MPF pathway (Nag *et al*., 2013. Otto *et al*., 2017). BRCA1 binds Rb and E2F which recruits HDAC deacetylating histones causing nucleosome formation. P53 is phosphorylated on Ser-15 by BRCA1/BARD1 complex resulting in the release of MDM2 stabilising P53, P53 accumulation activates DNA damage repair (DDR) pathways and initiates arrest through upregulation of P21 suppressing Cdk2-Cyclin E and Cdk4-Cyclin D from phosphorylating Rb (Moll & Petrenko, 2003; Lavin & Gueven, 2006). At G2/M checkpoint dephosphorylation of Cdk1-CyclinB1 is the initiation for mitotic entry. A positive feedback loop of activated Cdk1-CyclinB1 activating Cdc25C pushes the cell cycle into mitosis (Otto *et al*., 2017). If DNA damage has occurred at this checkpoint P53 mediated activation of CHK1 results in phosphorylation of Cdc25 and dephosphorylating Cdk1 induces arrest, here P53 can also be activated by ChK1/ChK2 inducing P21 which prevents the CdK1-CyclinB1 complex forming. It is the arrest at this checkpoint that allows the DDR pathway to enter homologous repair (HR) (Lord & Ashworth, 2012; Lavin & Gueven, 2006). Loss of P53 and or BRCA1 function compromises P21 and Chk1 induction therefore checkpoint arrest would not occur and lack of nucleosome formation means transcription is no longer inhibited leading to continued proliferation (Hartwell & Kastan, 1994).

1.4.2 – γH2AX

At the cell cycle checkpoints it is the phosphorylation of H2AX on the induction of strand breaks that results in the activation of the DNA Damage repair mechanism (Watters *et al.*, 2009) (figure 1.4).

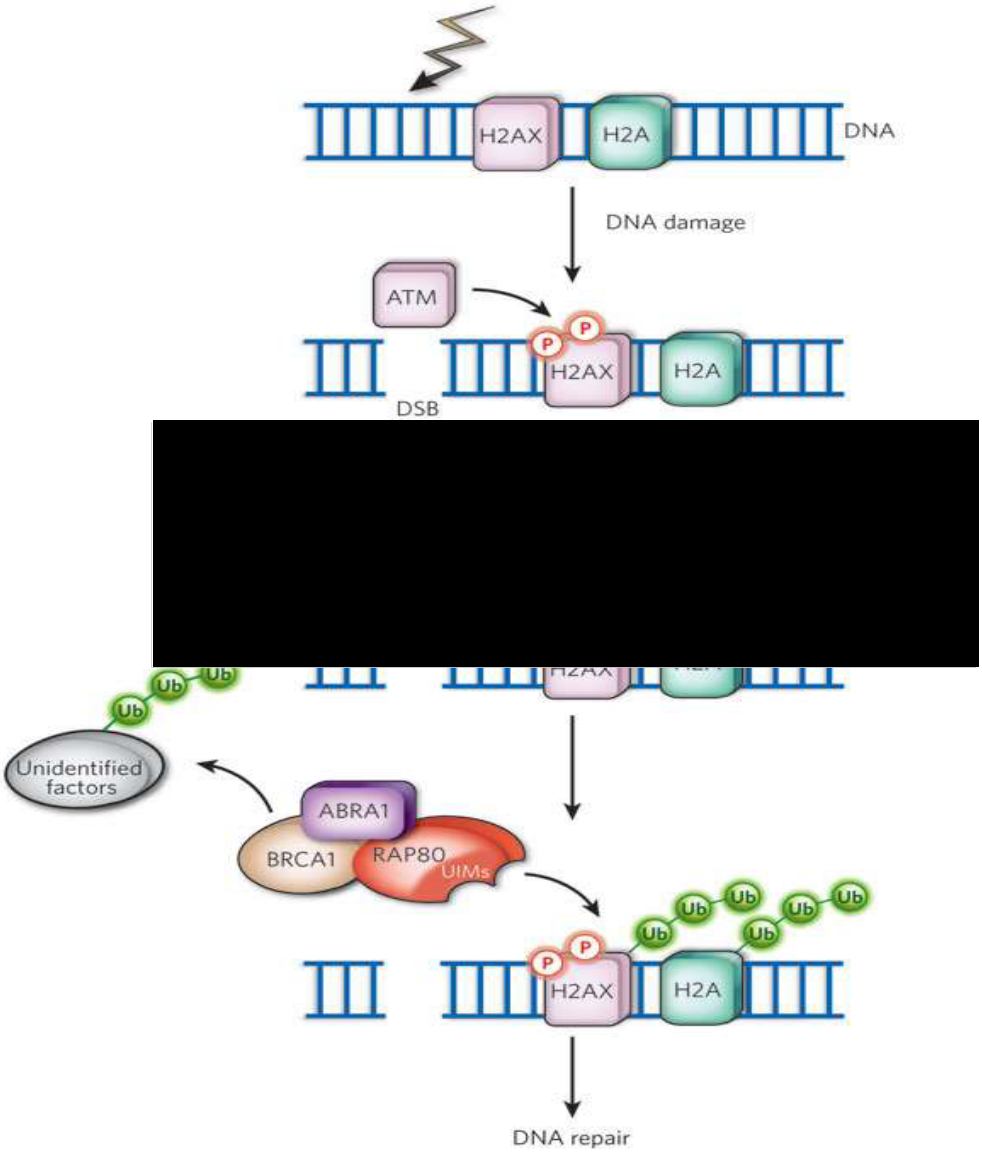

Figure 1.4: Demonstrating the role of phosphorylated H2AX known as gamma-H2AX (ɣH2AX) in the DNA damage repair pathway with regard to double strand breaks (Hoeller *et al*., 2009). The phosphorylation of serine-139 on the SQEY tail leads to the generation of ɣH2AX foci, and is a universal cellular response to DNA strand breaks, providing a scaffold and retention role aiding formation of repair DNA protein complexes (Zhou *et al.*, 2006; Watters *et al*., 2009)

The H2A histone is a highly conserved protein across species, the H2AX variant being a specific and sensitive biomarker for DNA damage repair and is very much in a 1:1 ratio with regard to DNA damage and ɣH2AX foci generation (Zhou *et al*., 2006; Watters *et al*., 2009). It is these qualities and the availability of ɣH2AX antibodies that enables the use of flow cytometry platforms. Positive results i.e., identifying potential clastogens, are

classed positive if ɣH2AX signal is above a 1.5 fold change over negative control levels (Smart *et al*., 2011).

Phosphorylation of the H2AX molecule is a useful biomarker in the identification of chemicals that cause physical strand breakage (Clastogens) through an increase of ɣH2AX levels in terms of fluorescence intensity over that of standard cell cycle and DNA maintenance ɣH2AX i.e., control 'normal' cells. However apoptotic cells have a widespread phosphorylation event, so it is important to identify true cellular DNA damage linked with the chemical rather than falsely identifying cytotoxicity with genotoxicity (Huang *et al*., 2006). Healthy mitotic cells also undergo pan nuclear phosphorylation of H2AX meaning a global phosphorylation of the variant ɣH2AX occurs during healthy mitosis alongside H3 serine 10 and serine 28 phosphorylation's (Ichijima *et al*., 2005). Use of the anti P53 antibody is one way to confirm true DNA damage has occurred in response to chemically induced strand breakage and presence of healthy mitotic cells can be confirmed by the presence of both ɣH2AX and pH3.

1.4.3 – pH3

During the mitotic phase of the cell cycle chromosome condensation is accompanied by phosphorylation of H3, occurring in a stepwise manner. During this global phosphorylation two different serine residues, S10 and S28, on the H3 tail (figure 1.5) occur to condense the chromosome and ensure movement through stages of mitosis (Doerig *et al*., 2015; Hans *et al*., 2001).

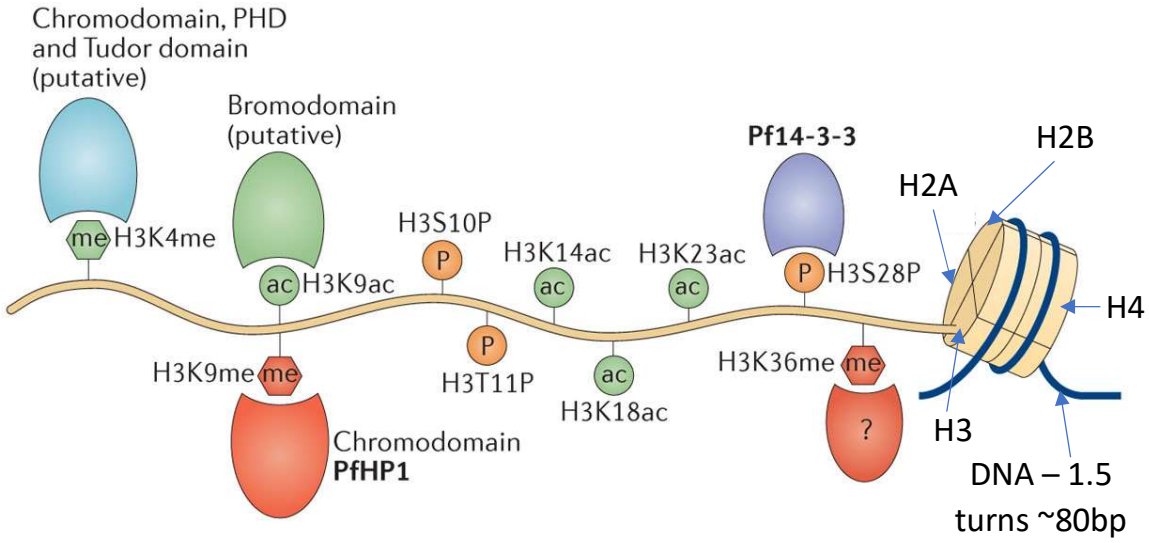

Figure 1.5: Demonstrates the nucleosome consisting of histone octamer with DNA and the H3 tail along with the most well-known sites of post-translational covalent modifications (Nowak *et al*., 2004; Hans *et al*., 2001). The kinase/phosphatase system is responsible for phosphorylation in mitosis and meiosis (Hans *et al*., 2001). Figure adapted from Doerig *et al*., 2015.

S10 H3 phosphorylation begins in late G2 phase in the pericentromeric and heterochromatin as the chromosomes begin to condense. This phosphorylation then

spreads through the whole chromosome continuing through prophase and maintained through metaphase, de-phosphorylation starts in anaphase (Hans *et al.*, 2001; Nowak *et al.*, 2004). Phosphorylation of H3 at the S28 position begins later than S10 phosphorylation, initiating at prophase maintained through metaphase and by late anaphase has been dephosphorylated (Hans *et al*., 2001). It has also been suggested that S28 phosphorylation is more prevalent in the rare H3.3 variant of histone 3 than S10 phosphorylation which is more heavily present in H3.1 and H3.2 variants, in these S28 phosphorylation is at much lower levels (Sun *et al*., 2007). Phosphorylation of H3 has been shown to be affected by amount of DNA damage found within the cell as it passes through the cell cycle (see figure 1.3) especially through chemically induced DNA damage (Ozawa., 2008). Due to the specificity of H3 phosphorylation to mitotic events it proves a good biomarker for both cell cycle and mechanistic information (Bryce *et al*., 2016) and highly specific antibodies for both S28 and S10 have been developed (Nowak *et al*., 2004) enabling assessment via flow cytometry platform.

1.5 – Micronucleus End Point

Within the pharmaceutical industry genetic toxicology plays a vital role in the safety stages of drug development. The regulatory guidelines require a minimum of two *in vitro* and one *in vivo* genotoxic assays to be negative before a compound can enter clinical trials (ICH., 2011). One of the gold standard assays in the assessment of a compounds impact on DNA is the micronucleus (MN) assay (OECD., 2014; Fenech *et al*., 2003). Generation of MN can occur through induction of direct DNA damage (clastogenic chemical), resulting in chromosome break. MN can also be induced by damage to cellular machinery (aneugenic chemical) resulting in chromosome loss (Schmid., 1975). The failure of the chromosome fragment or whole chromosome to move to either one of the poles during mitosis results in nuclear DNA being left outside the main nucleus when the nuclear membrane reforms. This small additional nuclear body distinct from the main nucleus is a what we call a MN (Schmid., 1975), (figure 1.6).

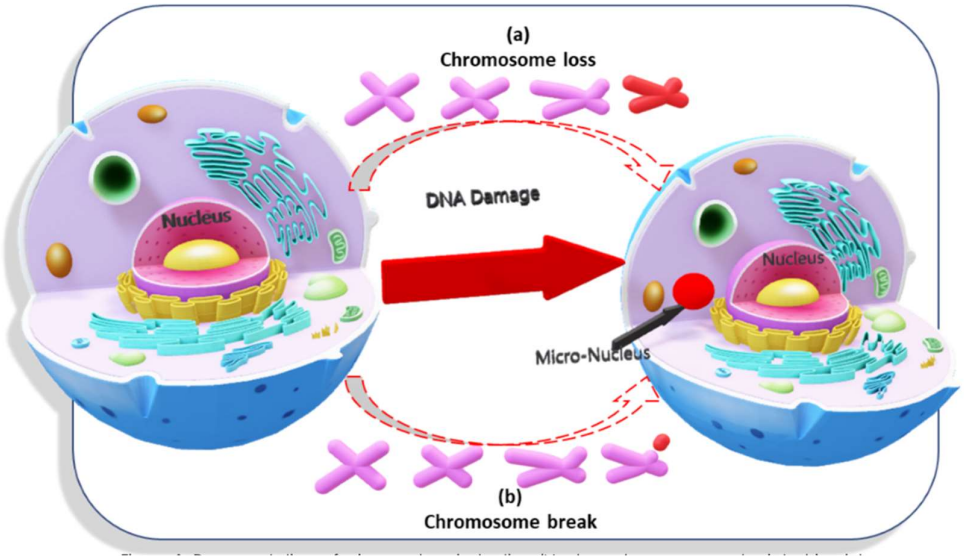

Figure 1.6: Simple diagrammatic representation of MN induction. If the DNA damaging agent is a clastogen, MN formation will take route (a) this implies the compound has directly interacted with the DNA resulting in a chromosome break. If the agent is a aneugen, MN will form via route (b), this means the compound has affected the metaphase machinery i.e. the centrosomes themselves, the spindle fibres or even the kinetochore protein. Thus, resulting in a lack of attachment of the spindle at the centromere equalling whole chromosome loss. Chromosome break or loss from a daughter cell nucleus results in a MN formation as the aforementioned DNA segments are not pulled to one pole or the other and thus remain in the cytoplasm when the main nuclear envelope reforms and cytokinesis occurs. An additional nuclear membrane forms around the DNA fragment that has remained outside the main nucleus (MN is depicted in red).

The frequency of MN induction induced by a chemical, as compared to that of control samples therefore assesses the genotoxic potential of a compound (OECD, 2014; Fenech *et al.*, 2003). Currently, this assessment can be carried out in three main ways: Firstly, the manual scoring assay; Dosed cells are lysed, dropped onto a microscope slide, fixed and stained, MN are then counted manually under a light or fluorescent microscope. Second, the Metafer™ system (MetaSystems™); Samples are prepared as in the manual assay but MN are counted automatically using a computer based imaging system. Third, MicroFlow™ assay; Cells are again lysed but are prepared in suspension before being run on a flow cytometer where front-scatter, side-scatter and fluorescence aids in the gating to assess the presence of MN (Verma *et al.*, 2017; OECD, 2014; Fenech *et al.*, 2003). Each of these methods for the assessment of MN induction, however, have their disadvantages. The manual assay, though accurate, is slow and labour intensive. The Metafer™ system although quicker, underscores MN due to program assessment parameters, therefore MN events often have to be double checked manually (Johnson *et al.*, 2014). The MicroFlow™ method is quick, high-throughput and high-content but over-scores MN events due to lack of its ability to assess if the multiple MN or nuclei have occurred within one cell or many (Johnson *et al.*, 2014).

Binucleate manual MN assessment, using the FlowSight® and ImageStream®X Mark II platform, has recently been validated by Verma *et al*., 2018 and has shown the platform to be a robust alternative to semi-automated microscopy and comparable to the gold standard manual scoring approach, with the addition of numerous advantages, including image collection and precision. Furthermore, use of image masking in binucleated MN has been shown by Rodriguez *et al.*, 2018 to be a possibility. Mononucleated MN assessment in the imaging flow cytometry platform via chemical induction, whilst shown to be possible, has been brief and in no great detail with very limited published data. Whilst assessment of mono MN is not necessarily the first choice in the Genetic toxicology world it does present some benefits. One major benefit is not adding the cytokinesis blocking chemical cytochalasin-B (cyto-B). Cyto-B works by inhibiting actin polymerase, allowing one nuclear division but preventing cell separation i.e., inhibits cell division (Fenech & Morley., 1985). Whilst this allows for easier phenotypic assessment of the cells and the likelihood that MN will be correctly identified the chemical adds additional stress to the cell and alters the true state of the cell cycle. This means attempts to assess additional biomarkers such as ɣH2AX, P53 and H3 that are mediated by cell cycle and cell stresses would be skewed. Furthermore, any cell cycle effect of the genotoxic chemical being tested may be lost. As a result the micronucleus assessment using the ImageStream X Mark II in multiplex with the biomarkers ɣH2AX, P53 and pH3 will take place in mononucleated cells. Multiplexing the *in vitro* MN assay with mechanistic information obtained from well characterised histone biomarkers ɣH2AX and phosphorylated H3 (Audbert *et al*., 2010; Khoury *et al*., 2016; Bryce *et al*., 2016) would provide additional confidence in MN scoring, while also reducing the need for follow up MoA testing.

1.6 – DNA Damaging Chemicals

The complex relationship of cell cycle monitoring proteins such as P53 along with DNA superstructure epigenetic modifications and specific cell cycle phase DNA replication and condensation demonstrate the challenges posed when assessing a chemicals MoA. Expanding the tool box of available assays for elucidation of chemical MoA especially *in vitro* is therefore crucial to reducing animal usage, time and money during the drug development process. To develop such assays however, chemicals with known MoA need to be assessed to determine effectiveness of assays in identifying misleading positive chemicals.

ECVAM (European Centre for the Validation of Alternative Methods) compounds are a set of 64 compounds that are often used to aid the validation of new *in vitro* assays (Kirkland *et al*., 2008; Kirkland *et al*., 2016). The compounds cover three chemical groupings; True positives (Group 1): DNA interactive compounds that are known to cause mutation *in vivo* and *in vitro*. True Negatives (Group 2): Non-DNA interactive compounds that are negative *in vivo* and *in vitro*. Misleading positives (Group 3): Non-DNA interactive compounds that are negative *in vivo* but have been shown to induce chromosome damage at concentrations of high cytotoxicity and/or at high concentrations *in vitro* (Kirkland *et al*., 2008; Kirkland *et al*., 2016).

Six well defined genotoxic chemicals were chosen based on the varying Mode and Mechanisms of action to assess the platforms' ability to distinguish between these different

chemicals and DNA damaging pathways. MMS, ARA-C and Etoposide work via a clastogenic Mode of Action and Carbendazim, Crizotinb, Vinblastine via a aneugenic Mode of Action. Whilst these chemicals may be grouped into either clastogenic or aneugenic Modes of Action, the mechanisms of these chemicals within the respective mode groupings differ.

1.6.1 – Methyl Methane Sulfonate

Methyl Methane Sulfonate (MMS) is a well characterised alkylating agent. MMS works by directly interacting with the DNA by alteration of the nucleotide bases guanine and adenine in the DNA structure. These physical changes to the DNA result in base mismatch and replication inhibition are most often repaired by base excision repair (BER) pathway and DNA alkyltransferases (Barreneck, 1990; Lindahl, 1999). Double strand breaks arise during BER when the replication fork encounter single strand breaks (Lord & Ashworth, 2012). Such types of DNA damage are referred to as being induced by a clastogenic Mode of Action.

1.6.2 – Carbendazim

Carbendazim is a antifungal compound that inhibits mitosis through potential interactions with tubulin and destabilisation of the microtubule spindle assembly (Hummelen *et al*., 1995). Carbendazim works primarily via a aneugenic Mode of Action.

1.6.3 – Etoposide

Extracted from mandrake root Etoposide is a Topoisomerase II inhibitor. Topoisomerase II acts by cutting both strands of the DNA to alleviate knots generated by the supercoiling of DNA structure (McClendon, 2007). Etoposide kills cells by stabilisation of cleavage complex which actively 'chops up' the genome induces permanent strand breakage leading to recombinant pathway DNA repair. These breaks can eventually overwhelm the cellular DDR pathways and result in cell death (Baldwin, 2005).

1.6.4 – Crizotinib

Crizotinib is a anti small lung cancer chemotherapy drug that works via Tyrosine Kinase inhibition more specifically its targeting of Anaplastic Lymphoma Kinase (ALK) and MET (*MNNG HOS* transforming gene) family (Megiorni *et al*., 2015; Zhang *et al*., 2018). Tyrosine Kinases are large protein families and aid in multiple cellular pathways including; activation of ATM, MDM2 regulation, Chromatin modulation DNA synthesis and repair such as non homologous end joining (NHEJ) as well as cell cycle G2/M arrest (Mahajan., 2015).

1.6.5 – Vinblastine

Vinblastine is a vinka alkaloid and works through a aneugenic MoA through the mechanism of binding to tubulin. This inhibition of microtubule formation and therefore abnormal mitotic spindle assembly at metaphase leads to cell cycle arrest (Gerson *et al*., 2018).

1.6.6 – Cytosine β-Darabinofuranoside (ARA-C)

Cytosine β-Darabinofuranoside also known as ARA-C or Cytarabine is a nucleoside analogue and whilst is can be found naturally in the cell and multiple food sources in higher concentrations it is used as a chemotherapeutic drug particularly looking at: acute non-lymphocytic leukaemia, acute lymphocytic leukaemia and blast phase of chronic myelocytic leukaemia (Momparler, 2013). When converted by cellular mechanisms ARA-C competes with the nucleotide Cytosine for incorporation into the DNA (Gerson *et al*., 2018). The altered sugar results in a 'rigid' DNA backbone that hinders structural movement affecting DNA replication the compound also inhibits DNA polymerase further reducing replication but also impacting DNA repair (Momparler, 2013; Gerson *et al*., 2018).

1.7 – TK6 Cells

The TK6 human lymphoblastoid nearly diploid cell line was originally generated for use in a human lymphoblastoid forward mutation assay, similar to that of the MLA, based on the heterozygous nature of its thymidine kinase gene ($TK^{+/-}$) (Skopek *et al*., 1981; Liber & Thilly, 1982). A USA patent was originally filed for this assay in 1979 and granted in 1981. The parent cell line of TK6 is the Epstein Barr virus transformed cell line, WI-L2 (WIL2), derived from the spleen of a 5 year old male with hereditary spherocytosis free from evidence of malignancy (Levy *et al*., 1968). The first isolated subclone from the WIL2 cell line by Henry Hoppe IV at MIT was the HH4 cell line, these cells were then mutated using ICR191 generating the heterozygous *TK* cell line H2BT more commonly known as TK6 cells (Skopek *et al*., 1978; Skopek *et al*., 1981; Liber & Thilly, 1982). Figure 1.7 demonstrates the phylogeny of the TK6 cell line.

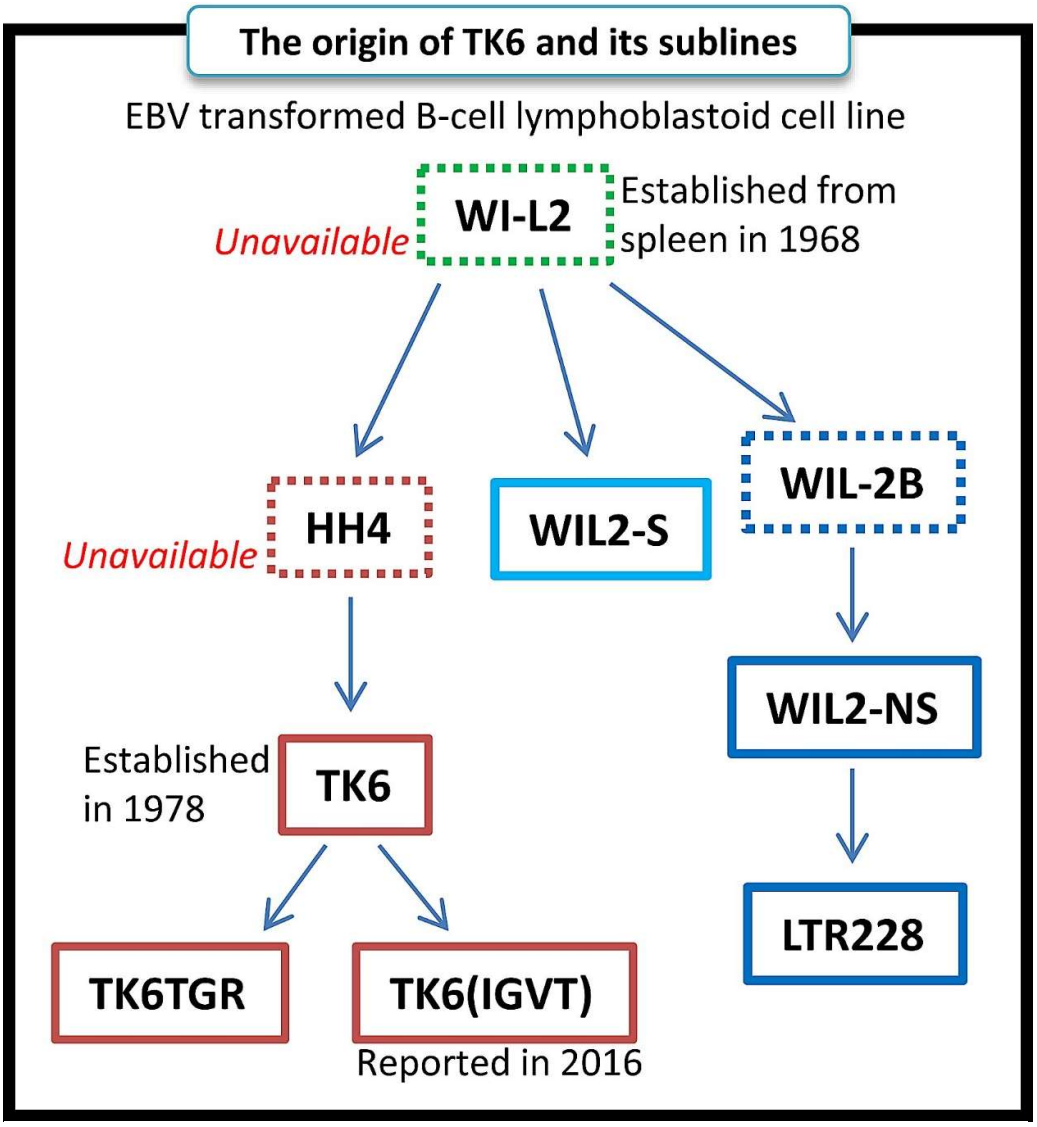

Figure 1.7: TK6 cell line phylogeny. Three different cell line lineages were developed from the spontaneous immortalized lymphoblast culture WIL2 in 1968. Whilst the commercially available cell lines TK6, WIL2-S, and WIL2-NS stem from the same parent cell line they are now distinct cell lines with different genomic profiles. The original parent cell line as well as HH4 and WIL-2B are no longer available for acquisition (Kasai *et al*., 2020).

Whilst the TK6 cell line was originally intended for use in a thymidine kinase mutation assay, within genetic toxicology they are often used in a multitude of assays. The reasoning behind this is TK6 are a human cell line with a near diploid karyotype and active DDR system that are easy to grow with a doubling time of roughly 16-18hours. TK6 have two alleles of the wild type *P53* gene meaning they are P53 proficient, and they also show low spontaneous chromosome and gene mutation frequencies however they are not metabolically active (Xia *et al*., 1995; Liber & Thilly, 1982; Jensen & Thilly, 1986). This wild type P53 activity is

important in potential reduction of misleading positive results when using a *in vitro* testing system (Kirkland *et al*., 2007; Fowler *et al*., 2012).

1.8 – Confocal Microscopy

One of the major challenges compared to that of traditional flow cytometry is the maintenance of cell integrity during DNA staining and the penetration of any antibody and associated fluorophore through both the cell membrane and nuclear membrane. Use of the Zeiss 710 LSM confocal microscope has been invoked to confirm both maintenance of cell integrity and antibody penetration of the nucleus has occurred therefore any fluorescence of antibody fluorophore observed on AMNIS FlowSight® is not just surface nuclear binding.

Zeiss 710 LSM confocal microscope is inverted meaning the Objective lens sits underneath the scanning stage and the Photon Multiplier Tube (PMT) detector sits on top of the microscope, see figure 1.8 (Zeiss., 2010). The objective lens (20X, 40X or 63X) is used to focus the lasers, 405/488/633/543/458/594nm, into the sample, the emitted fluorescence is then collected by the objected and directed to the PMT through the confocal aperture, also known as the 'Pinhole' (Zeiss., 2010; Abramowits *et al*., 2002).

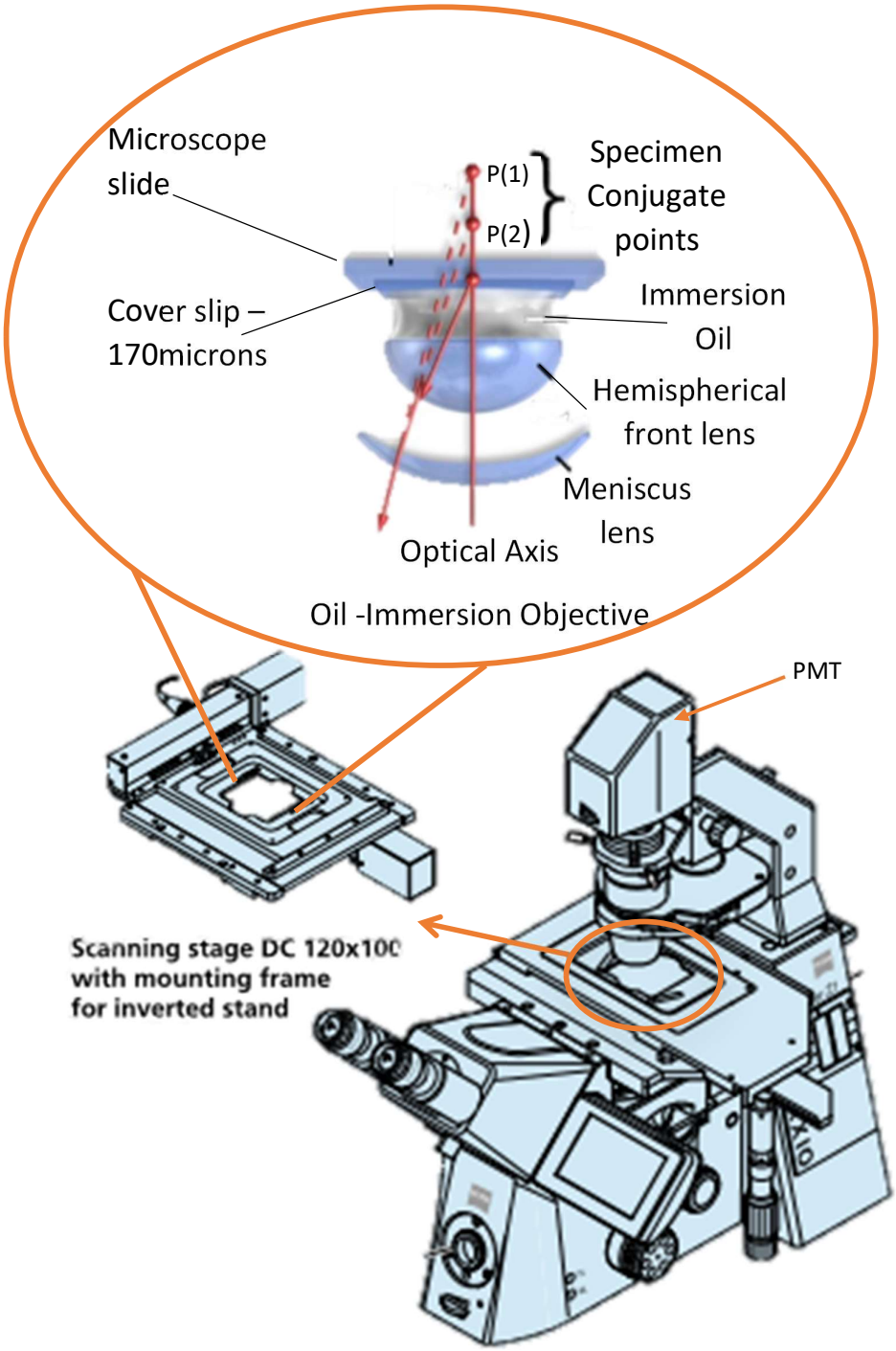

Figure 1.8: Overview of the confocal microscope LSM710 layout. Demonstrating scanning stage where sample slides are placed with objective lens closest to coverslip underneath the scanning stage, i.e. inverted. Oil immersion is only required for 40X and 63X magnification. Figure adapted from Zeiss., 2010 operation manual and Abramowits *et al.*, 2002.

The pinhole only allows fluorescence of a specific focal plane or 'slice' to pass to the PMT this results in a point by point assessment of fluorescent images in a scanning fashion. This

means that not only can multicolour fluorescence be separated sufficiently to be assessed simultaneously, but movement of the sample along the Z axis using fine focus results in multiple slices that can be assessed and viewed as a 3D image (Zeiss., 2010). This therefore allows the assessment of the cellular and nuclear penetration of fluorescent probes in multiplex. The collected coloured fluorescent images are actually collected in levels of grey known as 'bit depth' and colour artificially added, the more levels of grey there are the more detailed your acquired image: 8 bit; 256 levels of grey. 12 bit (recommended for quantitative analysis); 4096 levels of grey (Zeiss., 2010)

1.9 – Imaging Flow Cytometry

1.9.1 – AMNIS FlowSight® & AMNIS ImageStream X Mark II

Imaging Cytometry offers the speed, sensitivity and phenotyping abilities of flow cytometry, coupled to the detailed imagery and functional insights of microscopy. It therefore has high-throughput screening potential, with the added advantage that analysed cells do not need to be lysed. Figure 1.9 demonstrates the combination of FlowCytometry fluidics and microscopy components within the imaging cytometry platform. The FlowSight® and ImageStream®X MarkII (ISXII) have quantitative imaging sensitivity at 1 micron per pixel. This allows for determination of location and strength of fluorescence signals such as nuclear translocation, shape change for apoptosis and cell cycle analysis.

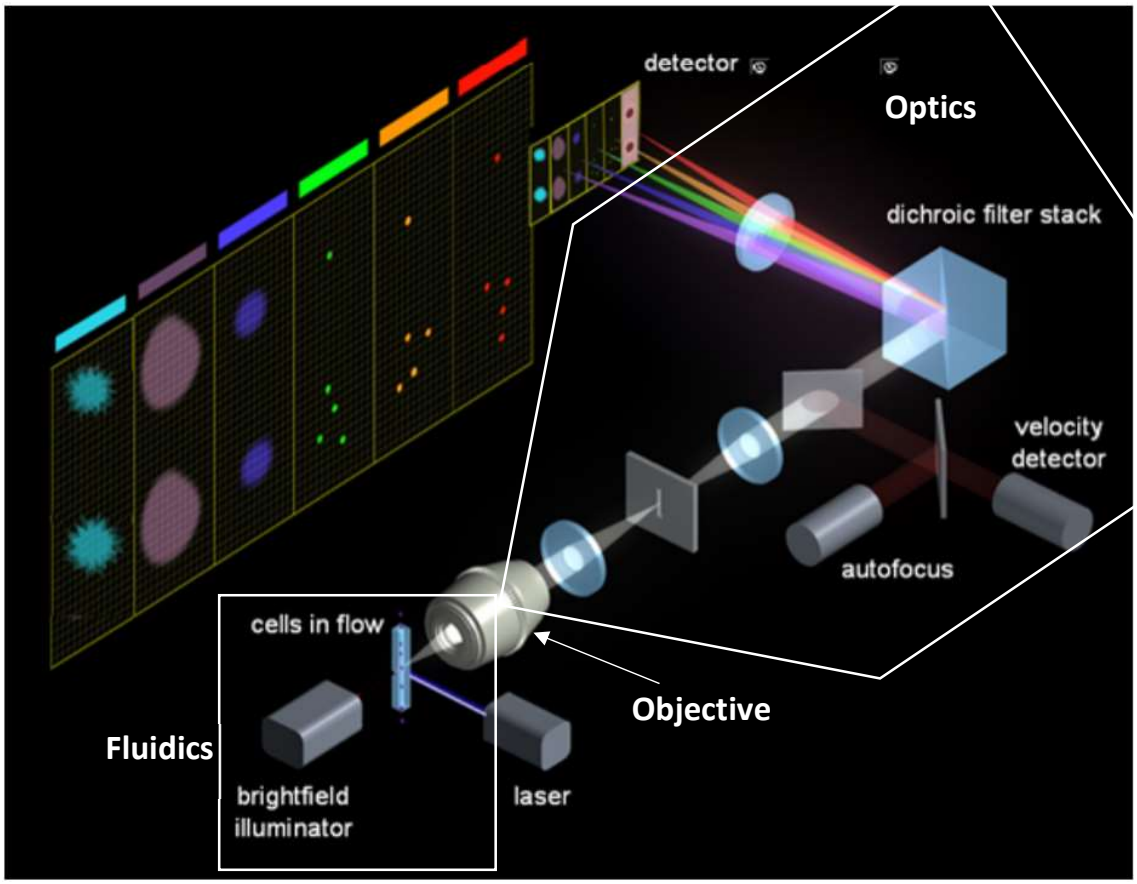

Figure 1.9: Overview of sample uptake to image output on INSPIRE software of AMNIS ImageStream®X MarkII and FlowSight®. Fluidics: Sample is organised into a single cell stream and exposed to brightfield and laser light. Scattered, fluorescence and transmitted light is collected by the objective lens. Optics: Pixelated light is focused, and velocity tracked in relation to the cell flow speed before being split into multispectral bands by the spectral decomposition element (SDE) resulting in the collection of 6 different wavelengths concordant with channel by the Charged Coupled Detector (CCD) camera. The Imagestream X Mark II has 2 CCD cameras 12 images per object can be collected, Camera 1 is channels 1-6 and camera 2 is 7-12. (Diagram adapted from Amnis IDEAS® 6.2 user manual , 2015; Zuba-Surma *et al*., 2007).

MN analysis approaches that lyse cells can introduce artefacts that may mask or interfere with the micronucleus analysis. Each event/cell is photographed and images stored for validation; other types of cytology can also be documented (apoptosis, mitotic stage) and flow gating strategies can be refined with precision based on the available cell image (Amnis®., 2020). Furthermore, this platform allows for multiple endpoints to be combined in a unlysed cell system. Litron laboratories have recently shown the combination of labels for pH3, γH2AX, P53 and polyploidy to provide extensive MoA and dose response information in lysed cell samples via standard cytometry (Khoury *et al*., 2016; Bryce *et al*., 2016; Dertinger *et al*., 2019).

1.9.2 – Workflow: Acquisition to analysis

Both the FlowSight® and ISXII use the acquisition software INSPIRE™ and image data analysis software IDEAS®. Figure 1.10 demonstrates the workflow of data and file generation from INSPIRE™ and into IDEAS® software. The Raw Image File (.rif) contains the raw data obtained during experimental acquisition, these store all the raw fluorescence, channel, and pixel data along with the settings used on the instrument at collection. The .rif files cannot be altered.

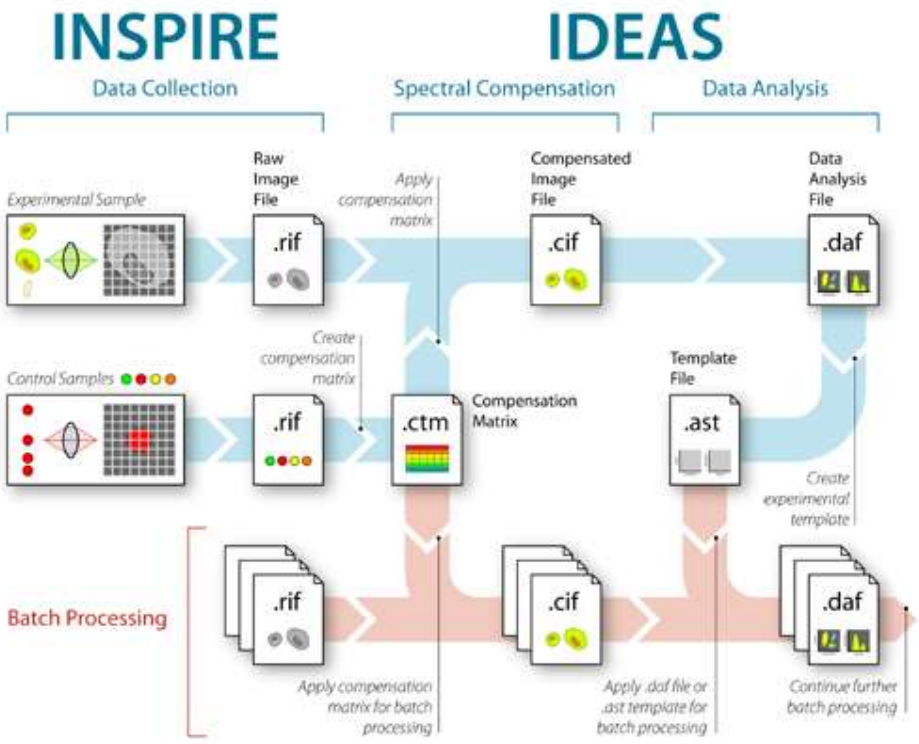

Figure 1.10: Schematic of file type workflow from the point of data acquisition on the imaging cytometer platform - Inspire software. Through to data analysis – IDEAS® software (Amnis®., 2015).

Compensated Image Files (.cif) are files automatically generated when .rif files are imported to the IDEAS® software regardless of presence of a compensation matrix a cif file is generated, this allows the generation of object identification and default mask generation. When no compensation matrix file (ctm) is selected the data that was collected at acquisition will be opened. When a ctm file is applied a pixel by pixel fluorescence compensation is performed 'correcting the images' removing fluorescence overlap, minimizing camera background and correcting for variability in flow speeds. Data Analysis File (.daf) is the IDEAS® file interface that allows analysis of the compensated image file, in other words this is the file format that opens in the IDEAS® software allowing direct interaction with the acquired cell images. This allows feature definitions, advanced masking options scatter and histogram generation, similar to that of conventional flow cytometry, display imagery and calculate response metrics. Daf files

also allow generation of template (.ast) files. Template files save features, graphs and masks used that have been determined, by the user, to be optimal for the data analysis. Template files allow for batch processing of data in a consistent manner aiding removal of user bias. Compensation matrix (.ctm) files are generated during acquisition separate from experimental analysis files, they are generated using control positively stained and negatively stained populations with brightfield and side scatter turned off. These files contain no object data and is created to be applied to collected data sets where multiple fluorophores are present.

1.9.3 – IDEAS® Software

IDEAS® stands for Image Data Exploration and Analysis Software. This is the analysis software that allows assessment of Raw Image Files by converting them to CIF and DAF files. It is on the data analysis files that population selection and metric extraction is performed. Figure 1.11 provides an overview of the work area layout.

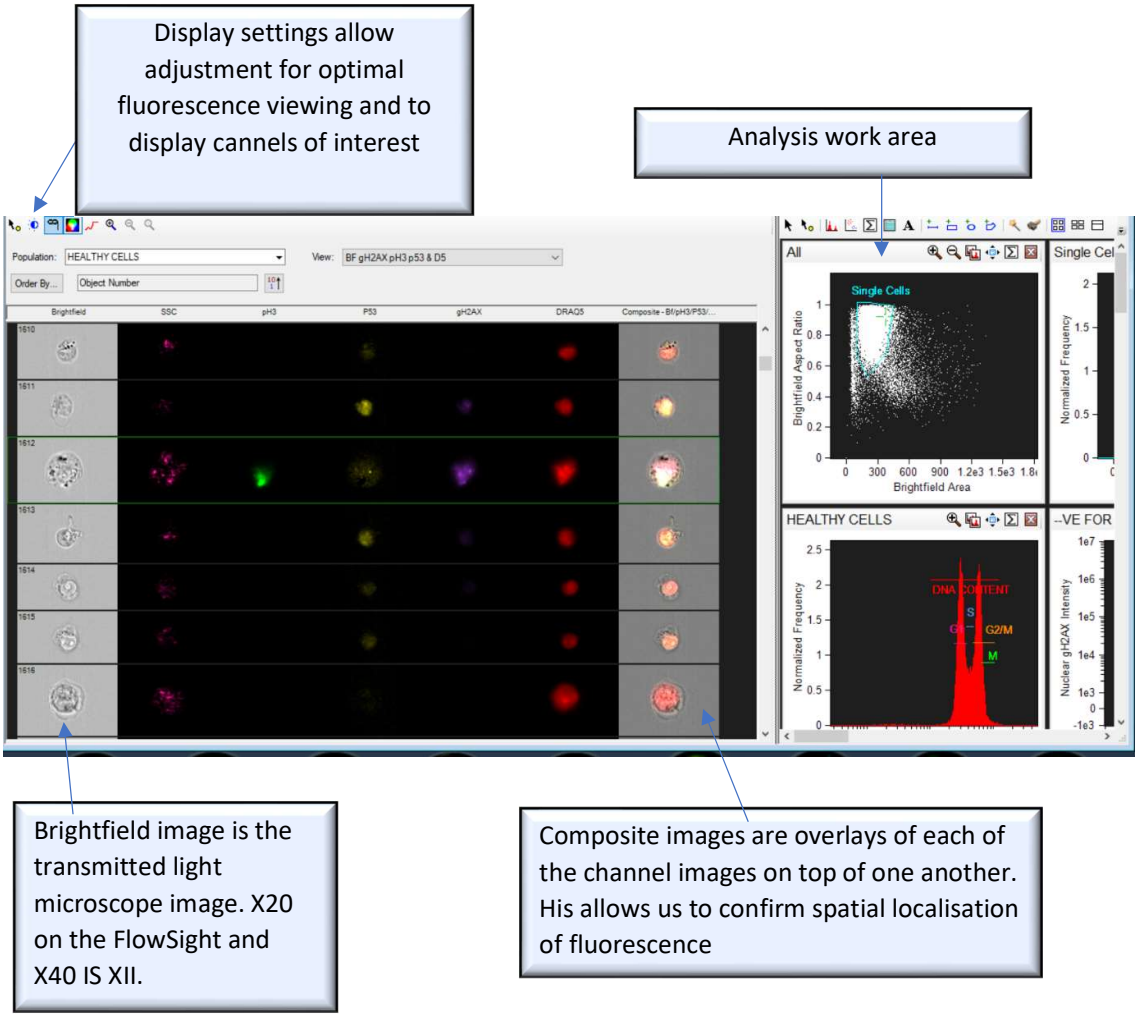

Figure 1.11: Showing IDEAS software image analysis and work flow interface. Channel numbers can be renamed in relation to signal of interest being looked at. pH3, P53, gH2AX and Draq5 are in channels 2,3,7 and 11 respectively. Brightfield images are collected and displayed in channels 1 and 9 and Dark field (or side scatter) is collected in channel 6.

1.10 – Summary

A summary work flow of processing and results generation is provided in the flow chart schematic below (figure 1.12).

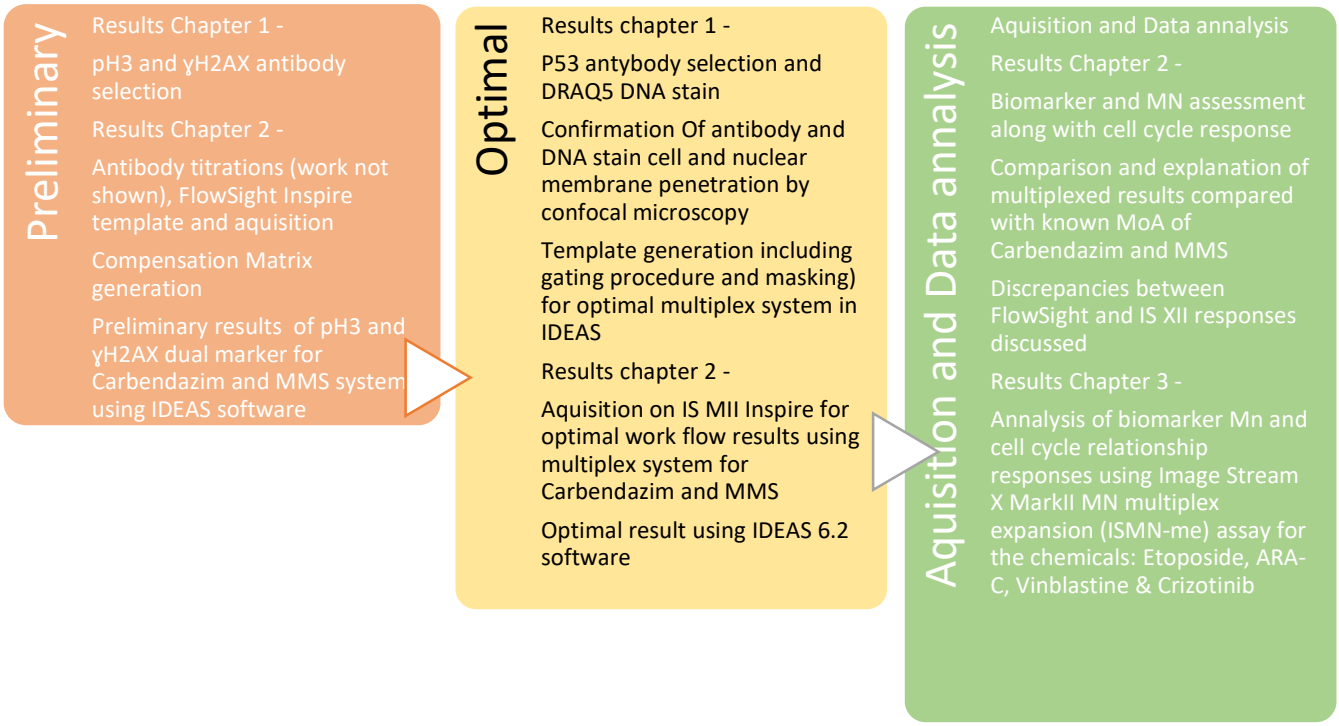

Figure 1.12: Flow chart of thesis overview. Focus on results chapters

1.11 – Aims

This thesis intends to build on the work from these labs by designing a multiplex assay in whole cells that can simultaneously measure cell cycle MN, γH2AX pH3 and P53 response using the imaging flow cytometry platform, and I therefore plan to multiplex these with the micronucleus assay.

Assess the feasibility of assessing γH2AX, P53, pH3 and MN response simultaneously in whole unlysed TK6 cells using the ImageStream platform. Optimise procedures to generate a automatically populated template using IDEAS® software that can be applied to multiple samples in a batch process system for consistent, minimally biased data providing a robust system for autofluorescence identification and implemented procedures to minimise AF effect. Assess if the multiplex system produces data that is in line with the current literature and dose response data for other platforms looking at MN, P53, pH3, and γH2AX responses of the model chemicals MMS and Carbendazim. Generate a novel approach for assessing cell cycle relationships of biomarker responses to uncover additional trends in MoA

identification of chemicals falling under the genotoxic headings: Aneugen, clastogen followed by subdivision into spindle poisons, topoisomerase II inhibitors and alkylating agents.

Chapter 2 – Materials & Methods

2.1 – Materials

2.1.2 – Equipment

Equipment	Supplier
FlowSight®	Luminex (Formerly Amnis®)
ImageStream X Mark II®	Luminex (Formerly Amnis®)
Centrifuge tubes (15ml/50ml)	Fisherbrand
Centrifuges: BIOFUGE fiesco Centrifuge 5810R Centrifuge Microfuge	 Heraeus Eppendorf Thermo Scientific Fisher Scientific
96 Well plate	Fisher Brand
CO_2 Air-Jacketed Incubators	Nuaire™
CELLview™ slide (Multi Chamber cover slip)	Greiner bio-one
Cryovials®	Elkay Laboratories
Freezeable Gel Packs	Various
Fridge (4°C)	Liebherr
Freezer (-20°C)	Proline
Fume Hood	Clean Air, Limited
Heat Block	Techne Di-Block
Hotplate & Stirrer	Jenway
Ice machine	Hoshizaki
Carl Zeiss™ Immersol™ Immersion Oil	Fisher Scientific
Microcentrifuge tubes	Eppendorf
Microscopes: Confocal LSM 710, AxioObserver Light Microscope	 Carl Zeiss Microscopy Olympus BX51
Milli-Q Integral Water Purification System	Millipore
Multipurpose Container (20ml)	Greiner bio-one
Pipettes	Gilson/ Eppendorf
Pipette tips	StarLAB
Pipettors	StarLAB/Fisherbrand
Platform Shaker (Innova™ 2100)	New Brunswick Scientific
Scales: LA 120S TE 3102S	 Sartorius Sartorius
Tissue Culture Flask ($25cm^2$/$75cm^2$/$175cm^2$)	Fisherbrand
Tissue Culture Hood	Scanlaf mars
Ultra Low Temperature Freezer (-80°C)	New Brunswick Scientific
Vortex	Fisons
Water baths: SUB Aqua 18	 Grant

The Belly Dancer® Hybridization water bath	Stovall Life Sciences Inc.
Z1 Coulter Particle Counter	Beckman Coulter Inc.

2.1.2 – Reagents

Reagents	Supplier
UltraComp eBeads™ Compensation Beads	ThermoFisher Scientific
Amnis® ImageStream SpeedBead calibration reagents	ThermoFisher Scientific
Cytochalasin B	Merck
Dimethyl sulfoxide (DMSO)	Fisher Scientific
Ethanol	Fisher Scientific
Heat Inactivated Horse serum	Gibco®
Phosphate saline buffer	Gibco®
Penicillin Streptomycin	ThermoFisher Scientific
BD FACS™ Lysing Solution	BD Biosciences
RPMI 1640 glutamax	Gibco®

2.1.2 – Chemicals

MMS	Sigma-Aldrich
Carbendazim	Sigma-Aldrich
Vinblastine	Sigma-Aldrich
Etoposide	Sigma-Aldrich
Crizotinib	Sigma-Aldrich
ARA-C	Sigma-Aldrich

2.1.3 – Antibodies and DNA stain

BV421 Anti-H2AX (pS139) Clone N1-431, Mouse BALB/c IgG1, κ	BD Biosciences
AF488 Anti-Histone H3-Phosphorylated (Ser28), Clone HTA28, Rat IgG2a, κ	BioLegend
PE anti-p53 Antibody, Clone DO-7, Mouse IgG2b	BioLegend
DRAQ5™	BD Biosciences

2.1.8 Computer Programs

Microsoft 3D paint

Swansea University Mutait.org web package

Graph Pad Prism 8, Version 8.4.3 (686)

Carl Zeiss Zen (2.3) Blue lite imaging software

Carl Zeiss Zen (2.3) Black lite imaging software

IDEAS® 6.2 software

INSPIRE acquisition software

ThermoFisher Fluorescence Spectra Viewer

2.2 – Methods

2.2.1 – Test Article Formulation

Master stock solutions for each chemical were made fresh on the day of the experiment. DMSO (Cas. No. 67-68-5) was the solvent used to generate the dose concentrations and was therefore used as vehicle control. In instances where the chemical would not go into solution gentle warming and vortexing was used.

Methyl Methanesulphonate (MMS), Cas no.: 66-27-3, Carbendazim, Cas no.: 10605-21-7, Crizotinib (Crztb) Cas no.: 877399-52-5, Etoposide (Etop) Cas no.: 33419-42-0, Cytosine β-Darabinofuranoside (ARA-C) Cas no.: 147-94-4 and Vinblastine (Vbstn) Cas no.: 143-67-9 all supplied from Sigma-Aldrich.

The working concentrations for MMS 0.00, 0.31, 0.63, 1.25, 2.50, 5.00 (µg/ml) and Carbendazim 0.00, 0.40, 0.60, 0.80, 1.20 and 1.60 (µg/ml) were selected based on the data produced by Verma *et al.*, 2017.

Working concentrations for the remaining chemicals were: Crizotinib, 0.00, 0.57, 1.31, 2.25, 4.51 (µg/ml); Etoposide 0.00, 0.01, 0.03, 0.06, 0.13 (µg/ml); ARA-C 0.00, 0.01, 0.03, 0.05, 0.21, 0.41 (µg/ml); Vinblastine, 0.0000, 0.0002, 0.0006, 0.0008, 0.0010, 0.0020 (µg/ml). Concentrations were selected based on relative cell growth responses along with suggested concentrations found in the literature, Doherty *et al*., 2013, Kirkland, 2010, Bryce *et al*., 2007, Cariou *et al*., 2012, and Dertinger *et al*., 2019.

2.2.2 – Cell Culture and Growth Media

Human, P53 competent, lymphoblastoid TK6 cells (Cat.No. 95111735, alternate collection no.: ATCC CRL 8015) were used in this study and obtained from European Collection of Cell Cultures (ECACC) Salisbury (Branda *et al*., 2001).

RPMI 1640 (Gibco) culture media supplemented with 1% penicillin streptomycin (pen strep) and 10% heat inactivated horse serum (Gibco) was used for TK6 cell culture. Cells were incubated at 37˚C in a humidified atmosphere of 5% (v/v) CO_2. TK6 cells doubled every 16-18hrs and once cells reached confluence sub-cultures were established. Each subculture did not exceed a confluence value of $1X10^6$ cells/mL as per ECACC/ATCC recommendations. Cell culture passage number did not exceed passage 20 for preliminary work and did not exceed passage 12 for optimised assay analysis.

2.2.2.1 – Treatment of Cell Cultures

$2x10^5$ TK6 cells/mL were placed in a series of sterile vented tissue culture flasks (Fisher brand) and treated with either MMS, Carbendazim, Crizotinib, Etoposide, ARA-C or Vinblastine for a 1.5 cell cycle period with no recovery. Dose volume to cell culture did not exceed 1% i.e., 100ul of dose was added to 9.9mL of cell suspension. Any precipitation or colour change was noted upon chemical addition to cell culture flask. All incubation steps occurred at 37˚C, 5% (v/v) CO_2± 0.5% in air. All experiments per chemical consisted of three replicates with the exception of ARA-C where two replicates were performed. Each replicate when performed on the same day were generated from cells of a different passage, when different chemicals were assessed on the same day the same cell passage was used.

After the treatment period, cell counts were taken for each culture using a Beckman coulter counter. Cell cultures were then transferred to 15mL centrifuge tubes and were centrifuged at 200 *xg* for 8 minutes, supernatant was discarded, and the pellet re-suspended in 5mL pre-warmed RPMI HIHS culture media. Subsequently, the RPMI media was removed via centrifugation at 200 *xg,* the pellet was re-suspended and wash step repeated with 5mL Phosphate-Buffered Saline (PBS).

The highest concentration tested is one that allows the maximum exposure up to 2000 µg/mL or 10mM for freely soluble test articles, or the limit of solubility or toxicity, whichever is lower (OECD., 2014).

If test article solubility in the test system is a limiting factor, the maximum concentration chosen for analysis will be the lowest concentration at which test article precipitation is observed by eye in treatment cultures at the end of the treatment period. If toxicity is a limiting factor, the maximum treatment concentration selected for analysis is that of relative cell growth at 30%.

2.2.2.2 – Cell Counts

Cells were counted automatically via Z1 Coulter Particle Counter. Cell counts were obtained by adding 100ul of cell suspensions to a beaker containing 10ml of isotone solution. The beaker was then placed on the counting platform of the Z1 coulter particle counter and the cell count per/ml was recorded.

2.2.2.3 – Cytotoxicity

Relative Cell Growth (RCG) was used to estimate cell death and cytotoxicity in treated samples. RCG was calculated as follows:

$$RCG = \frac{\text{No. of Cells/mL in treated cultures}}{\text{No. of Cells/mL in vehicle control}} \times 100$$

2.2.3 – Cell Fixation and Staining

Once the cell treatment period ended and cell wash steps performed to remove media containing the chemical dose, the cell pellet was resuspended in residual PBS and BD FACS Lyse was used to fix and permeabilise the cells. FACS Lyse solution is a proprietary buffered solution containing <15% formaldehyde and <50% diethylene glycol. BD FACS Lyse was diluted in a 1:10 ratio with distilled water (dH20) (1ml FACS Lyse:9mL dH2O). The solution was mixed thoroughly and 2mL of solution was added to each sample. Avoiding agitation after 12minute incubation time at room temperature the samples were spun on the centrifuge at 200xg for 5 minutes. Supernatant was discarded and the cell pellet gently resuspended in the remaining solution, PBS was added in excess (5mL) and samples returned to centrifuge for further 5 minutes, this wash step was repeated twice. Samples at this stage may be placed in the fridge and stained at a later date or stained immediately. Samples were stained with 300ul of antibody (AB) master mix for preliminary work and the optimal method. For preliminary work this consisted of BV421 Anti- ɣH2AX AB and AF488 Anti- pH3 AB in PBS agitated at room temperature for a minimum of 60 minutes. For optimal work this consisted of BV421 Anti- ɣH2AX AB, AF488 Anti- pH3 Ab and PE Anti-P53 AB in PBS at room temperature for minimum of 60 minutes and 100ul of DRAQ5™ diluted solution for minimum of 20 minutes. Further information on the antibody and DNA staining procedure can be found in section 2.2.3.1 below. After the staining period ended samples were centrifuged and washed in 5mL PBS. Figure 2.1 below provides an overview of the two main methods of TK6 cell processing.

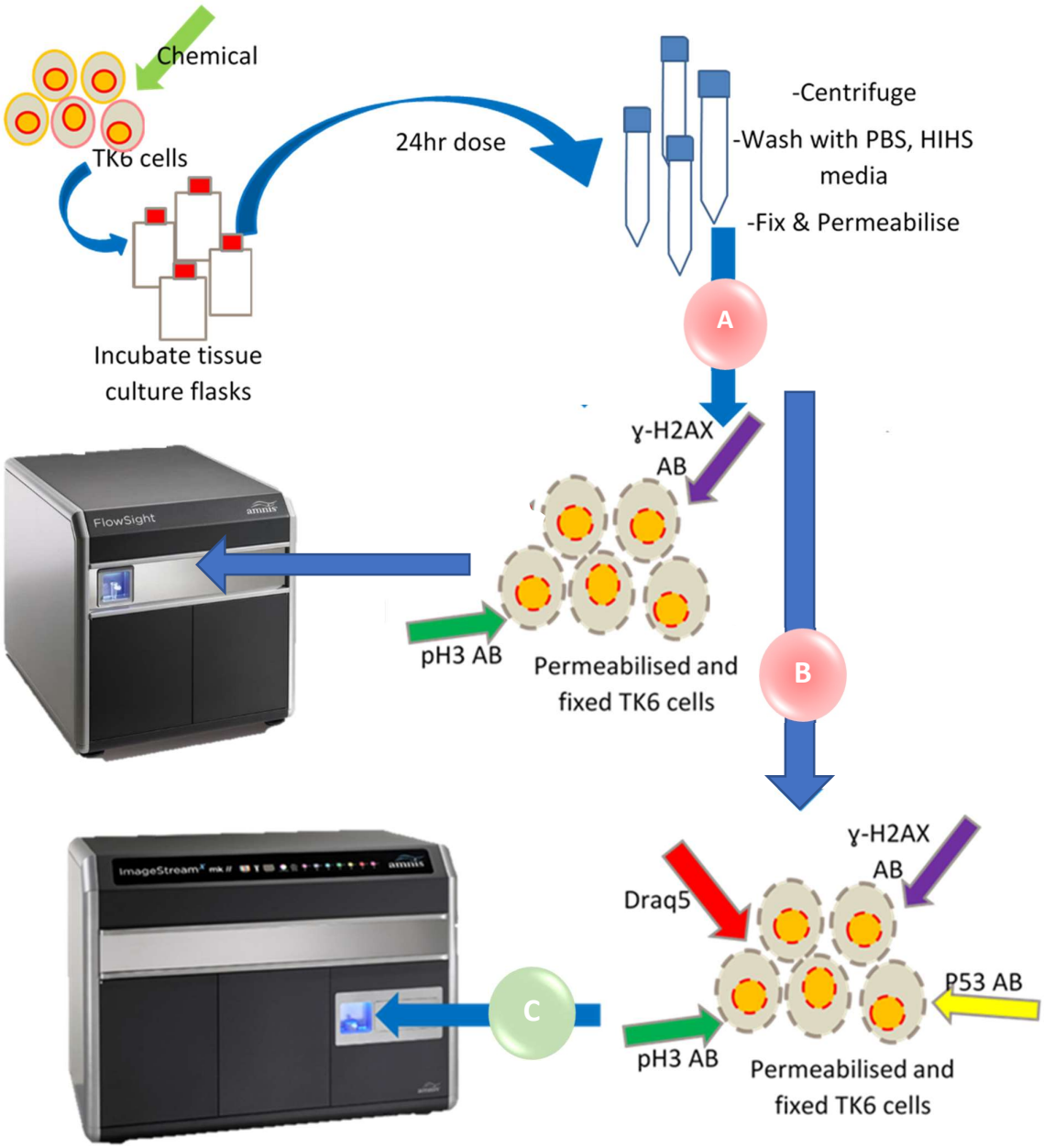

Figure 2.1: Demonstrating a generalised overview of the method followed in this thesis. Procedural steps were exactly the same prior to cell staining for both preliminary work and optimised work flow. Route A shows the preliminary work done on the FlowSight® and route B shows the optimal work flow. At point C analysis was either performed by manually imputing Eppendorf into the sample port or via 96 well plate sampling. Samples at point C may also be analysed on confocal microscope platform.

2.2.3.1 – Antibody Staining

Regardless of ratio of antibody in PBS solution the antibody incubation of permeabilised and fixed cell samples is a minimum of 60 minutes at room temperature under agitation.

For preliminary work (figure 2.1 route A) Immunofluorescence antibodies used were: Anti ɣH2AX Brilliant Violet 421 antibody (Cat. No. 564720) and Anti pH3 ser 28 AlexaFluor 488 antibody (Cat. No. 641003) in multiplex. Antibodies were supplied by Beckton Dickinson and Biolegend respectively. These antibodies generated a master stock solution, in the ratio 3µl of pH3: 5µl of ɣH2AX: 292 µl of PBS

For optimal workflow (figure 2.1 route B) Immunofluorescence antibodies used were: Anti ɣH2AX Brilliant Violet 421 antibody (Cat. No. 564720) supplied by Becton Dickinson Biosciences. Anti-phosphorylated Histone H3-ser28 AlexaFluor488 antibody (Cat. No. 641003) and anti P53 PE antibody (Cat.No. 645805) were both obtained from BioLegend. These antibodies generated a master stock solution, in the ratio 3µl of H3: 5µl of ɣH2AX: 6µl of P53: 286µl of PBS. 300ul of master antibody solution was added to each resuspended cell pellet. Cells were stained in multiplex at room temperature under agitation for a minimum of 60 minutes. Excitation and emission spectra of each antibody and its associated fluorophore is summarised in table 2.1 below.

Table 2.1: Summary of AB and associated fluorophores

Biomarker Targeted by AB	Associated Fluorophore	Excitation Laser wavelength (nm)	Emission Max wavelength (nm)
Phosphorylated serine 139, SQEY tail, H2AX (ɣH2AX)	Brilliant Violet 421	405 (Violet)	421
Phosphorylated serine 28, H3	AlexaFluor 488	488 (Blue)	525
N-Terminal P53	PE	488[1] (Blue)	574

[1]Suboptimal excitation.

2.2.3.2 – DNA Staining

DNA staining only occurred in multiplex for route B in figure 2.1 due to the lack of lasers available on the FlowSight® and the inability for sufficient spectral separation.

DRAQ5™ DNA stain (Cat. No. 564902 supplied from BD Biosciences, sub optimally excited by 488nm blue laser and optimally excited by 642nm red laser, was used to label nuclei and MN. 2ul DRAQ5™:98ul PBS was mixed, 100ul of the 1:49ratio stain solution added to each 300ul cell sample antibody solution making final staining

ratio of 1:199. Samples were counterstained with DRAQ5™ for a minimum of 20 minutes.

2.2.4 – Whole Cell Data Collection

Whilst predominantly work was performed on the ImageStream platform once the staining and wash steps were completed the samples were also viable for analysis via confocal microscopy. Use of the Confocal LSM 710, AxioObserver was used as a qualitative tool for the assessment of antibody penetration of the cellular and nuclear membrane. No quantitative analysis was performed using the confocal microscope. The confocal acquisition and analysis steps are outlined in section 2.2.4.1.

Samples that were analysed on the FlowSight® at Swansea University were either stained with antibody and processed immediately, stained placed in fridge protected from light and analysed no more than 48hrs later or stained up to 48hrs later followed by immediate analysis. The Flow sight acquisition and analysis steps can be found in section 2.2.4.2.1.

Samples that were analysed on the ImageStream X Mark II® at the Core Flow Facility, Newcastle University were done so by myself or Andrew Filby. Samples were stained immediately placed on frozen gel pack and shipped via DHL overnight. Samples were either analysed on day of arrival or 24hrs later. From point of being picked up by DHL the samples were not analysed any later than 48hrs after being stained. The ImageStream X Mark II® acquisition and analysis steps can be found in section 2.2.4.2.2.

2.2.4.1 – Confocal Microscopy

2.2.4.1.1 – Slide Preparation

Cells were processed as explained in section 2.2.3. No additional method steps were performed and a volume of 50ul was transferred to CELLview™ chamber slide from Greiner for analysis. Each one of the five samples were placed in a individual chamber of the chamber slide, each were as follows; 1) 5.0 µg/mL MMS dosed TK6 cells stained with only BV421 anti-ɣH2AX AB, 2) 1.6 µg/mL Carbendazim dosed TK6 Cells stained with only AF488 anti-pH3, 3) 1.6 µg/mL Carbendazim dosed TK6 Cells stained with only PE anti-P53 AB, 4) Negative control TK6 Cells stained with only DRAQ5™, 5) DMSO dosed TK6 Cells unstained 5) 1.6 ug/mL Carbendazim dosed TK6 Cells stained with all AB and DRAQ5™ stain. Please note no centrifugation or any other attempt to fix the cells to the coverslip glass was used.

2.2.4.1.2 – ZEN Image Acquisition

A compensation matrix file was generated using the same acquisition settings used for image collection using the individually stained and one unstained sample.

Three fluorophores AF488, BV421, PE and one DNA stain DRAQ5™ were assessed using the 405, 488 and 633 excitation wavelengths across 4 signal channels.

These signal channels were split onto two different tracks BV421 and PE were on Track 1 and AF488 and DRAQ5™ were on track 2. Use of two different tracks in this way was used to minimise signal cross talk between the channels as the excitation spectra of AF488 and PE are close together (see figure 3.1) in section 3.2.4. Image collection occurred using the Plan-Apochromat 63X/1.40 Oil DIC M27 objective, the pinhole was set to 51µm for both track 1 and track2, a 8 bit depth was selected. Light source balancing was performed for each sample exhibiting strongest signal for optimal intensity and gain settings. These same settings were used for the generation of a compensation file and collection of images.

2.2.4.1.3 – ZEN Imaging Software

Zen black and blue were used to assess images and perform pre-processing steps. The compensation file generated was applied to the Raw image file to allow linear unmixing to be performed. This step helped remove/minimise potential signal cross talk so signal observed could be trusted to be true signal in relation to the biomarker presence. Imaging software was then used to project the 3D image of Z stack generated files and available fluorescence pixel signal squeezed/expanded for optimal viewing of fluorescence signal.

Images acquired for the confirmation of cell sample staining can be found in section 3.3.1.

2.2.4.2 – Imaging Flow Cytometry

Acquisition of samples as described in the following methods followed the recommended procedures stated in the Amnis® FlowSight® Imaging Flow Cytometer User Manual and INSPIRE™ ImageStream®X System Software User's Manual

2.2.4.2.1 – AMNIS® FlowSight®

Upon initiation of the FlowSight® and Inspire software click ‘StartUp’. This opens ASSIST. Once focus and fluidics stabilised (buttons greyed out became active) ASSIST prompts loading calibration beads onto the sample port of the FlowSight®. When the beads are running and appear central in the channel image viewing area and in focus all calibrations and tests are performed by clicking ‘Start all calibrations”. All calibration tests are passed when they turn green and the ASSIST window is closed. Calibrations were performed at least once before use and sample collection was only performed once all calibration tests were passed.

Sample is loaded into the sample pump, a minimum of 50µl of sample is uploaded, and a new template or a saved template from previous experimental acquisition can be loaded. Each sample collection can be appropriately labelled and saved for export to IDEAS® analysis software.

Only chemicals Carbendazim and MMS were assessed on the FlowSight® for optimal staining and preliminary work. Carbendazim and MMS were selected for the well characterised nature, with clear MoA's. This allowed me to assess the expected results against the response provided by my assay and adjust the methodology accordingly.

2.2.4.2.2 – AMNIS® ImageStream®X Mark II

Having switched on the ImageStream X Mark II® and launched inspire software, SpeedBead calibration beads are loaded onto the specific bead port. Unlike the FlowSight® the ISXII continually mixes and loads beads for more accurate velocity and image tracking. 'StartUp' is clicked, and beads are automatically loaded and focus, and fluidics are established. The option to run ASSIST immediately after fluidics and focus stabilisation was unticked to allow manual positioning of the core flow centre if required. Once focus and positioning of beads were confirmed 'Start All Calibrations and Tests' was selected. When all calibration tests were passed the ASSIST progress light turns green. ASSIST window can then be closed. As with the FlowSight® only once all calibrations were passed was sample acquisition performed.

Sample is loaded into the sample pump, a minimum of 50µl of sample is uploaded, and a new template or a saved template from previous experimental acquisition can be loaded. Each sample collection can be appropriately labelled and saved for export to IDEAS® analysis software.

Replicates 1 and 2 of the chemicals MMS, Carbendazim and ARA-C were manually loaded onto the ISXII sample port and acquired. All other chemicals (Etoposide, Vinblastine and Crizotinib) were acquired using 96 well plate and autosampler procedure for unattended acquisitions.

2.2.4.2.3 – INSPIRE™

INSPIRE™ is the acquisition software associated with the Amnis® imaging cytometer platform. Once samples are loaded on the imaging cytometer prior to sample image collection a template can be generated that best fits the experimental design and are explained below. Display settings of the Image gallery can be adjusted for optimal sample viewing to confirm populations being collected are single, in focus with exclusion of debris. This also allows a confirmation that the population of cells being collected are actually the population of interest. For all sample collections a acquisition speed of low was selected to acquire samples with the highest sensitivity. The FlowSight® collected images at X20 magnification and IS XII collected images at X40 magnification.

2.2.4.2.3.1 – Template Set up

Cell sample acquisition using INSPIRE™ for FlowSight® and INSPIRE™ for ImageStream X Mark II® is the same process other than calibration beads are used alongside image acquisition on the ISXII for more accurate camera and

velocity tracking of cell samples. When acquiring samples collection is best for single and in focus cell population. The brightfield (microscope image) were plotted on a scatter graph aspect ratio plotted on the y axis and area of the cell plotted on the x axis. A gate was drawn around the single and round cell population based on cell density heat map, this population for TK6 cells usually sits between 1 and 0.6 of aspect ratio and above 70 but below 600 on the area axis, this allows debris to be excluded from sample collection. This single cell population is then plotted on a histogram using gradient RMS to select cells that are most in focus a gate is then drawn across the histogram peak. Whilst this gate is usually based on the histogram peak the lowest gate value is never placed below 50 on the gradient RMS axis. Cells that are within this focussed gate are deemed to be sufficiently in focus for acquisition. This is the population of cells that will be used for laser balancing procedures and then collected.

2.2.4.2.3.2 – Laser Balancing

When dealing with samples that contain multiple fluorophores it is important to balance the different lasers you are using, especially if the fluorophores have excitation wavelengths that can be activated by the same laser. Whilst this won't completely eliminate fluorescence spill over it will allow compensation matrices to be most effective at removing fluorescence that is not in the correct channel.

Prior to cell image collection laser intensities need to be balanced for optimal fluorescence image collection. Based on the single in focus cell population selected a scatter graph with channel intensity plotted on the x axis and raw max pixel channel intensity plotted on the y axis see figure 2.2.

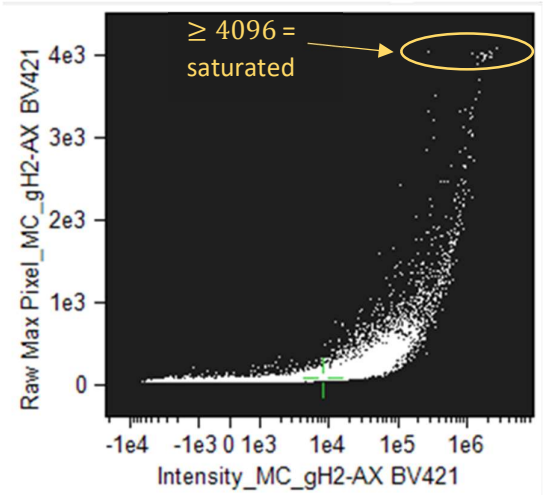

Figure 2.2: Demonstrating example of intensity vs raw max pixel intensity on inspire software to aid laser power selection. 4096 is the maximum pixel intensity the system can read before the image becomes saturated.

This was done for each channel of interest. Each channel that has cells with saturated pixel fluorescence need to be decreased in number to as low as possible, preferably zero, but not so low that signal separation is sacrificed, and that lower level signal is missed. This was done by starting the laser power off higher to induce saturation and then decrease laser power till saturated cells are minimal. This is repeated for each channel relative to the laser that excites them; AF488 is in channel 2, PE is in channel 3 both excited by laser 488nm. BV421 is present in channel 7 excited by laser 405nm. DRAQ5™ has a presence in channel 5 but is dominant in channel 11 is excited by laser 488nm and 642nm. If a laser is being used for more than one fluorophore it is important to have high enough fluorescence for one to be discernible from background autofluorescence but low enough so as not to induce large amounts of saturation. This is the case with AF488 and suboptimal excitation of PE with the 488nm laser. Once the laser values have then been set based on saturation, channel overlap is assessed, this is important when a fluorophore is either excited by more than one laser or has a distinct channel overlap. DRAQ5™ is excited sub-optimally by laser 488nm causing signal to be detected in channel 5 and optimally by 642nm for detection in channel 11. By plotting an intensity scatter graph of Ch5 (488nm blue laser) on y axis and Ch11 (642nm red laser) on x axis keeping laser intensities the same as determined by minimizing pixel saturation the balance of which channel the DRAQ5™ signal is most dominant in can be plotted, figure 2.3 is an example graph used during laser balancing for optimising signal to the correct ImageStream channel.

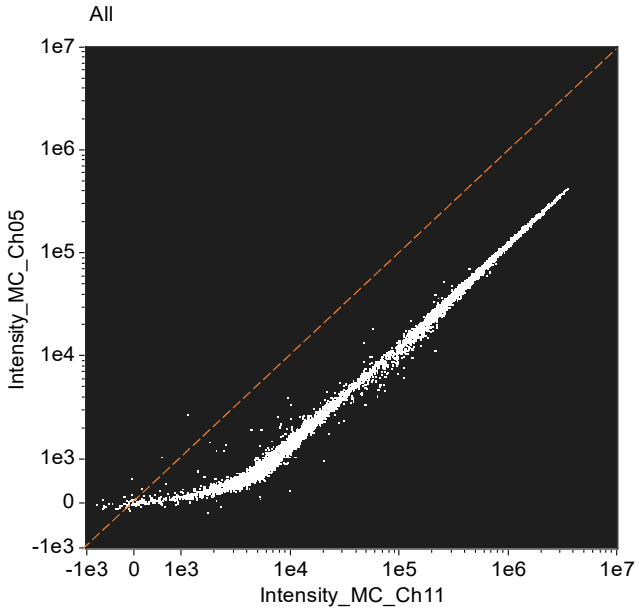

Figure 2.3: The graph was generated from collected compensated data as an example step. This being such means the Draq5 signal was optimal for the system. The cell population falls below the imagined orange line that passes through the graph's origin. This means the laser was balanced with the 488nm laser so that the DRAQ5 signal was dominantly picked up in the desired channel 11.

The orange line on figure 2.3 demonstrates an imagined line that passes through the origin of the graph if during laser balancing procedure the cell population signal for D5 sat above the line this would imply the DRAQ5™ signal was more dominant in channel 5 so the power of the 488nm laser would need to be decreased for the DRAQ5™ signal to become dominant in Ch11. This would also happen in the reverse, if the 642nm laser intensity was too low the signal would be dominant in channel 5 (cells above the line) and the intensity would need to be increased. This same process was performed for each of the main channels used (plotted on x axis) and compared against all other channels to confirm the dominant signal fell more below the origin line (in the correct channel) than above the line. This also minimalizes the risk of overcompensation when generating a compensation matrix.

Once these steps were complete acquisition of cell images took place and a collection value of; 15,000-20,000 events were acquired on the FlowSight® and 30,000 events were collected for samples stained with the 4 fluorophores on the ImageStream X Mark II®.

The optimal laser settings for the FlowSight® for the dual marker stain was 2mw for laser 488nm and 10mw for laser 405nm. The optimal laser settings

for the ISXMII four colour system were 120mw for laser 405nm, 90mw for laser 488nm and 80mw for laser 642nm.

These laser settings for experimental acquisition were then used to generate the compensation matrix.

2.2.4.2.3.3 – Compensation Matrix

UltraComp eBeads™ Compensation Beads (Cas no:01-2222-41) from thermofisher scientific were used for compensation in relation to BV421, AF488 and PE signal. A cell stained sample containing true population (stained with D5) and a negative population not stained. Compensation files are then generated by either following the INSPIRE™ compensation wizard or performing manual collection.

For both options side scatter laser and brightfield collection is turned off. All lasers that are used in the experiment are set at the same acquisition power as the experimental collection settings. One file is collected per fluorophore only the laser that is used to excite that specific fluorophore is turned on per file. The active fluorescence channel is selected and 500-1000 cells/beads that are classed as positive events are collected for each fluorophore. Signal that is then found in other channels i.e., not the active fluorescence channel is determined to be fluorescence overspill. Each compensation file can then be combined (if using the wizard this is done automatically) in IDEAS® software to generate a compensation matrix. All samples were collected with no compensation applied.

2.2.5 – Whole Cell Image Assessment

2.2.5.1 – IDEAS®

Image Data Exploration and Analysis Software allows for the quantitative analysis of the Raw Image Files (rif.) collected on the FlowSight® and ISXII machines. The following gives steps taken towards compensation matrix generation followed by a generalised method overview of template design and batch processing. In detail descriptions of the optimal template design can be found in in chapter 3, results section 1. Additional information and in-depth explanations of the features used in the IDEAS® software can be found in the v6.2 User's Manual, Version 6.2.

2.2.5.1.1 – Applied Compensation

The removal of signal overspill from incorrect channels prevents signal from being miss identified as true signal and minimises compounding of true and false fluorescence to give a increase of biomarker signal that may not be there or be the difference between a positive and negative biomarker response. A visual representation of this is shown below, figure 2.4.

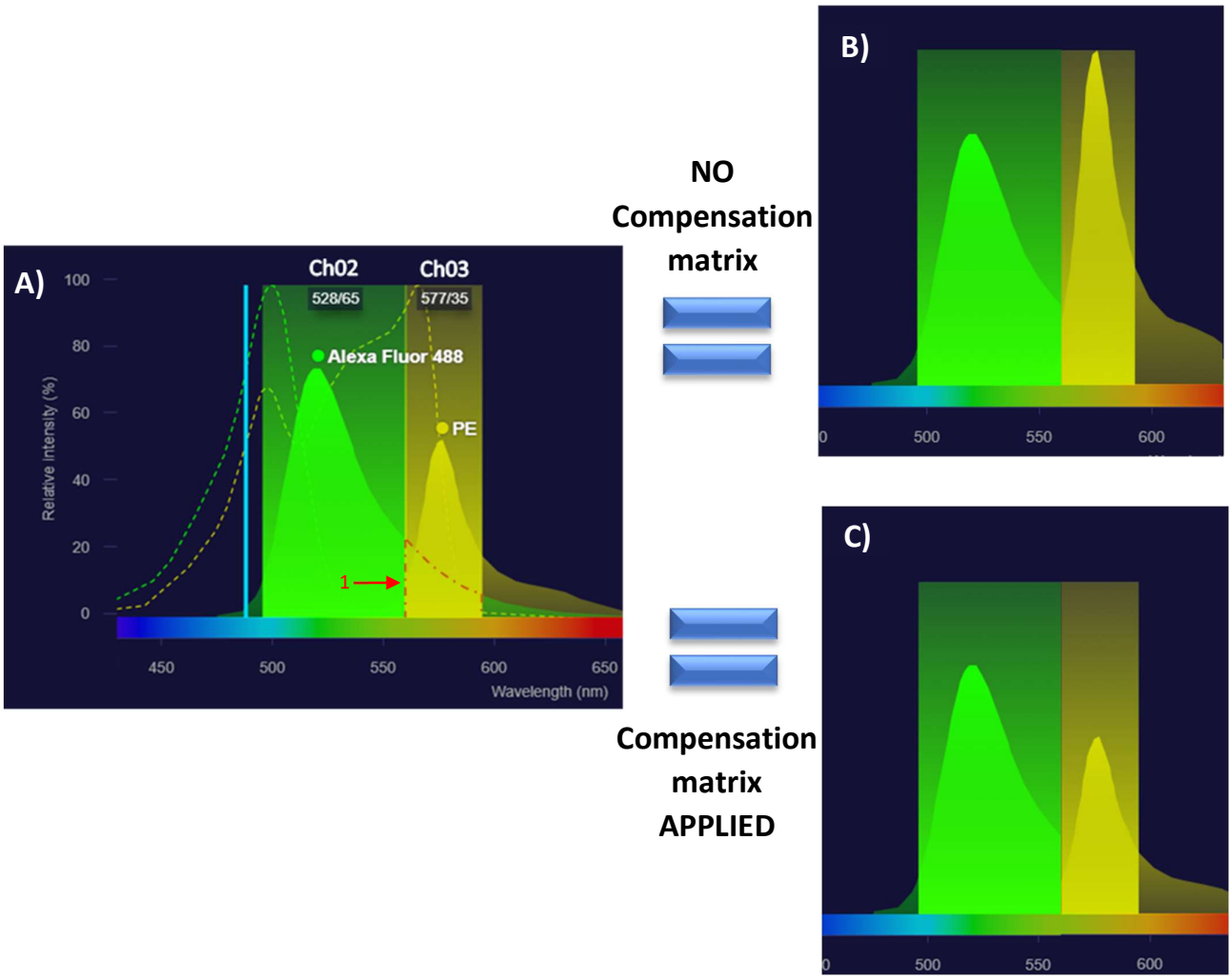

Figure 2.4: Example of how compensation removes signal overspill from incorrect channels prevents signal from being miss identified. Histograms show effect on fluorescence overspill of AlexaFluor488 from Channel 2 into PE Channel 3 with and without compensation matrix applied. A) Shows the excitation and the normalised emission spectrum of AlexaFluor488 and PE to the 488nm laser. The band passes are also displayed giving demonstrating the wavelength (nm) covered for Channel 2 and Channel 3. The Area under the dashed red line (highlighted by arrow 1) highlights the overspill of the AF488 emission spectra into Ch03. B) Shows the accumulative effect of fluorescence overspill from Ch02 into Ch03. Without compensation to remove the overspill of fluorescence signal this increases the fluorescence intensity seen in CH03 by the IDEAS software resulting in a false intensity reading. C) Shows that with a compensation matrix applied the overlapping signal from AF488 has been removed from the PE signal in Ch03 leaving only true fluorescence intensity to be analysed by the software. Spectral histograms were obtained using the ThermoFisher spectral viewer software.

Compensation files with no bright field and side scatter collected are uploaded to the IDEAS® 6.2 compensation wizard. All files for each fluorophore used in the experiments are uploaded to the compensation wizard. Active fluorescence channels that the experimental fluorescence signal is found in are selected. A coefficient table is then generated. The coefficient table shows all 12 channels. The compensation matrix coefficient table demonstrated in figure 2.5 display the

channel overlap of fluorescence signal. Values of 1 refer to the location of 100% signal i.e., Ch02 column, Ch02 Row is 1 so 100% of signal is in Ch02. All other values refer to the percentage of signal overspill from the active fluorescence channel into a neighbouring/suboptimal channel of collection i.e. active fluorescence channel 2 (fluorophore AF488) has a 1.3% signal overspill into channel 5. This means that 1.3% of AF488 signal that is not supposed to be in Ch05 will be removed.

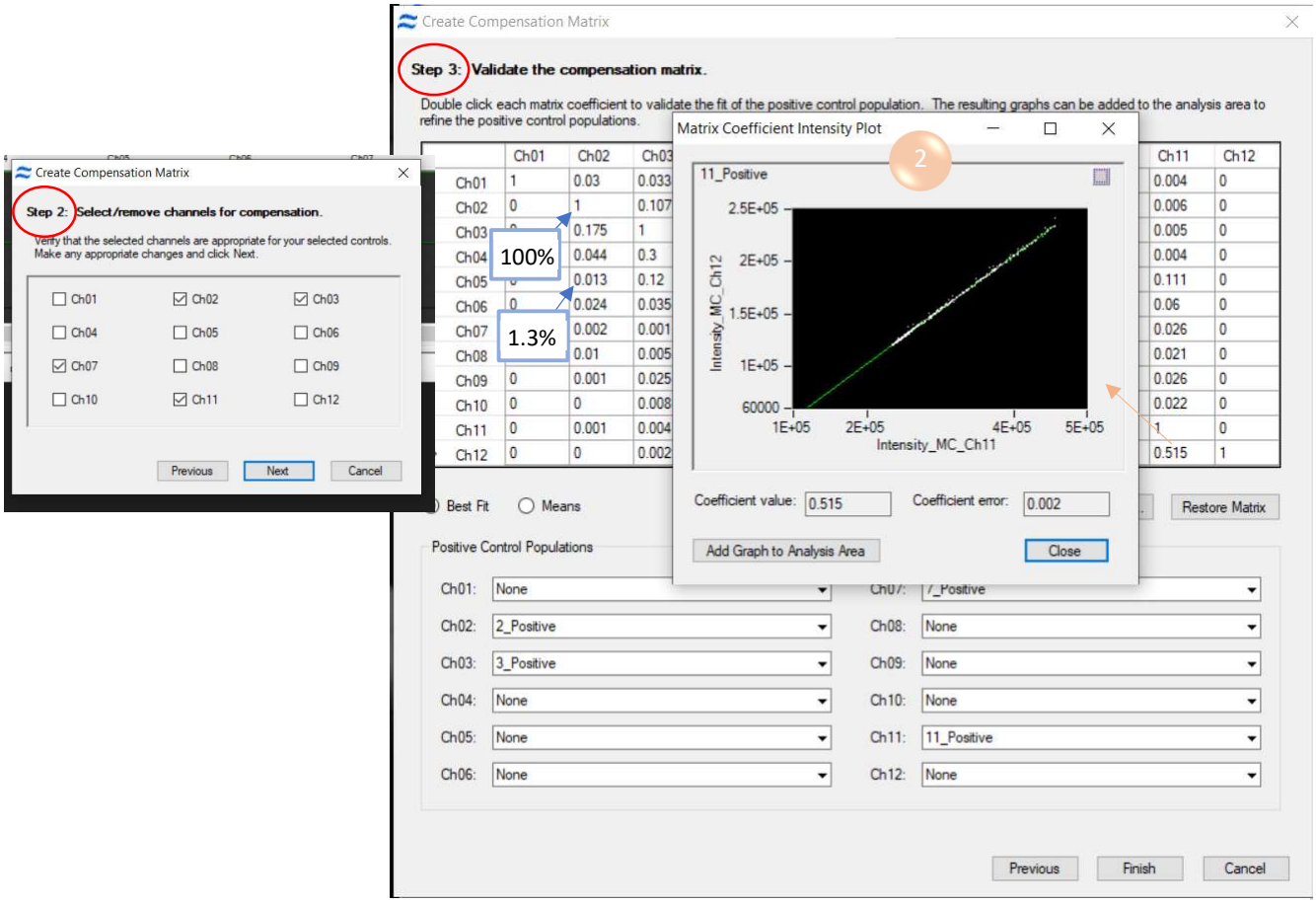

Figure 2.5: Overview of compensation matrix generation using IDEAS® and following the steps in the compensation wizard. Compensation wizard allows you to select the active fluorescence channels for the experiment. The third step is assessing the generated coefficients based on the uploaded files and selected channels. Label 2 is an example of how coefficient accuracy can be assessed by clicking on values in the table.

Best fit or mean selection may be used. Best fit tends to be used for cells that have varying intensities present but beads you could use mean as the variability is minimal. If values in the compensation matrix are red this implies the coefficient variations away from the line of best fit is more than 1% and the coefficient needs to be adjusted. This can be done by double clicking the concerning value, this will generate a coefficient graph, see label 2 in figure 2.5. Label 2 shows a linear relationship of cell population with the line of best fit

passing through the origin, this implies the coefficient is accurate. If the cell population were skewed the population falling excessively above or below the line of best fit i.e., not a liner relationship the compensation matrix would not work correctly resulting in under or overcompensation. To clean up the sample population the coefficient graph can be added to the analysis area and a new positive population for that channel generated via drawing a new gate. A new coefficient can be generated based on the new population selected and the linearity of cell population confirmed. This checking of each coefficient was performed on each of the coefficient values regardless of a greater than 1% variation away from the line of best fit to confirm accurate coefficients and therefore matrix has been generated. This mainly helps reduce overcompensation which would result in the removal of true signal skewing any data generated.

The compensation matrix can then be saved and applied to the raw data files prior to analysis and template based assessment. Per experimental run a new compensation matrix was generated and applied to the relevant files.

2.2.5.1.2 – Template Design

The IDEAS® 6.2 software can be used to generate a template that can then be used to batch process all experimental file with the same template. To generate a daf (data analysis file) the rif. (raw image file) is selected and at this stage either a new compensation matrix can be generated or a compensation matrix that has already been saved can be applied. Figure 2.6 shows the layout of IDEAS® software start up to generate a cif (Compensated image file) and daf file.

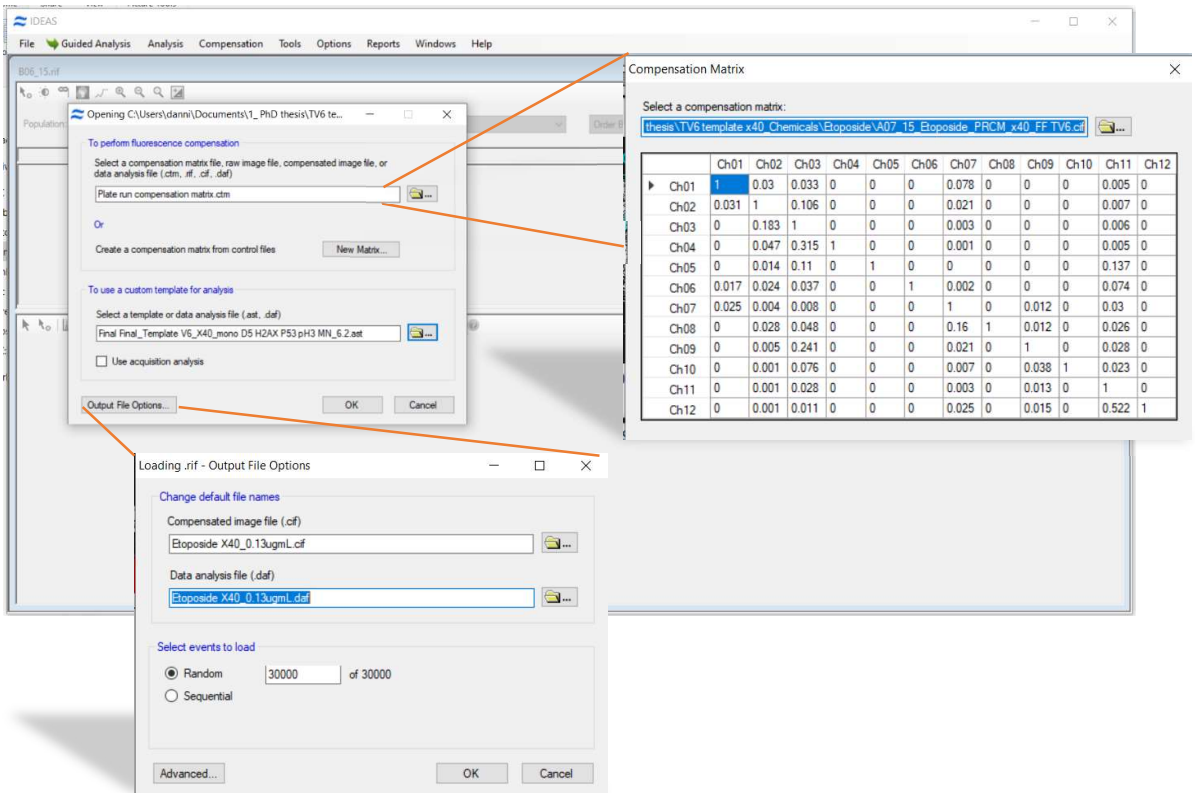

Figure 2.6: Opening window start up for IDEAS® software for analysis of rif files. Cif and daf files are generated by applying the compensation matrix generated for the experiment and a template if available, the file name can be adjusted. If a analysis template is available it can be used to automatically populate the analysis area.

All templates were generated based on compensated fluorescence data. There were two templates generated, one for preliminary data set and one for the optimal data set.

For the preliminary data the template generated was simple and the parameters assessed were based on single and in focused cell population. pH3 signal and ɣH2AX signal intensity, the H3 positive signal cell population were excluded from ɣH2AX assessment.

2.2.5.1.3 – Mask Development and Feature Use

Masking is the process by which imaging software, in this case IDEAS® 6.2, identify pixels of interest. IDEAS® software uses default masks to based on available fluorescence signal, using the mask manager more specific masks can be generated based on the criteria that needs to be assessed. These user defined function masks can be generated using a limited number of functions that when combined create a set of rules/criteria that can then be used to assess different features based on size, shape, texture, comparison and location. These masks once defined can be combined using Boolean logic (AND, OR, NOT etc.) to add or subtract criteria to generate a new specific mask.

For the preliminary work performed on the FlowSight® imaging cytometer the default IDEAS® masks were used for ɣH2AX and pH3 analysis.

For the optimal work flow and templates set up the following final masks were generated: Brightfield 1A, Brightfield 1B, Cytoplasm, Nuclear Mask 1, Nuclear Mask 2, Nuclear Mask 3, gH2AX mask, Nuclear gH2AX mask, pH3 Mask, Nuclear pH3 Mask, P53 Mask, P53 Cytoplasmic Mask, P53 Nuclear mask and MN Complete Final Mask (CFM). The functions in various combinations used to generate these masks were morphology, adaptive erode, threshold, range, dilate, intensity, spot, watershed and level set. The masks and functions used are demonstrated in depth in section 3.3.3.

Features in the IDEAS® system are mathematical expressions that assess, within the image, quantitative and spatial information. These allow for the generation of histograms and scatter graphs in the analysis area for cell population responses to be assessed. The features used were: Aspect ratio and Area assess circularity and singularity respectively, contrast Gradient Root Mean Square (RMS) assesses in focus objects to generate the most appropriate cell population for biomarker and MN analysis. Intensity, Similarity, and spot count features were used to automatically populate and extract biomarker and MN data. Aspect ratio, area, Gradient RMS and Intensity were also used in preliminary work template analysis using the systems default masks.

The finalised template generated can be saved as a ast file and used on all rif files in combination with the appropriate compensation matrix. This was done by selecting the batch data files option in the tools menu of the IDEAS® software. All the rif. files per chemical were grouped together in batches and given an appropriate name to be saved under. Once files were loaded either the preliminary or optimal template ast. file was selected and compensation matrix ctm. files were also applied. These batches were then run generating cif. and daf. Files for each individual sample data set and automatically saved. Data tables were generated for each daf. File and the population response data was exported to excel for formatting, graph and table generation.

The mask development and features used were based on the recommendations within the IDEAS® 6.2 user manual 2015, the publication Imaging Flow Cytometry: Methods and Protocols 2016 and literature Rodriguez *et al.*, 2018, Verma *et al*., 2018, Filby *et al*., 2016, Patterson *et al*, 2015.

2.2.6 – Data Assessment

All tables and graphs were generated using Excel Microsoft. Unless otherwise stated data displayed in tables and plotted in graphs for biomarker and MN metrics are presented in raw response fold change that has been square-rooted to normalise responses. Cell cycle data is presented as raw response cell percentages.

Fold change cut offs were also applied to graphical data. These cut offs were applied in line with industry standards whereby fold change over a certain amount are considered a biologically relevant response. For pH3 this was 1.3 fold change increase and 0.7 fold change decrease as suggested by Khoury *et al*., 2016. For ɣH2AX fold change increase was 1.5 as per Smart *et al*., 2011. Whilst P53 is a popular marker for DNA damage assessment a fold change cut off can't be easily identified from the literature. As P53 is induced by a DNA damage response, one could assume the fold change response is proportional to that of ɣH2AX biomarker response when assessing clastogens. It is therefore reasonable to suggest the same fold change cut off used for ɣH2AX may be used for P53 response. Whilst there is limited literature referring to a definitive industry standard of fold change for P53, the use of 1.5 fold change cut off is illuded to (Dertinger *et al*., 2019).

As all raw fold change values were square rooted the fold change cut off values were also square rooted giving the square root cut off values of: 1.2 for ɣH2AX and P53 and 1.1 for pH3 for increase in signal and 0.8 for decrease in signal.

The MN response was considered positive based on a statistically significant response ($P<0.05$) compared to that of DMSO control (Johnson *et al*., 2014). Where statistical significance was not achieved the MN response was considered positive based on a greater than 2 fold increase compared to control (Takeiri *et al*., 2019; Shi *et al*, 2010). As data is displayed in square root fold change, the fold change cut off value for the MN response will be 1.4. A genotoxic response is considered positive when the mean response relative to control exceeds the fold change cut off or is statistically significant. Where both MN and biomarker response exceed fold change cut offs and/or are statistically significant a indication of MoA may be inferred (Bryce *et al*., 2017; Dertinger *et al*., 2019).

2.2.6.1 - Statistical Analysis

All data sets distributions were tested for homogeneity and normality using the Brown forsythe/Bartletts test and D'Agnostino-pearson omnibus (K2)/Shapiro Wilk test respectively. If datasets proved both normal and homogenous a one way ANOVA Dunnets test was performed to identify significance (p value<0.05) of data response. If data was found to be either not normal and or heterogenous the data was either Log or Square root transformed and distribution retested. In the event the transformed data failed distribution tests the non-parametric Dunns Kruskal Wallis test was performed on the raw response data. This procedure is as recommended by Johnson *et al*., 2014. Presence of statistical significance was used to identify the no- and the lowest- observed genotoxic effect levels (NOGEL, LOGEL). This procedure is as recommended by Johnson *et al*., 2014; Verma *et al*., 2018. All statistics were prepared using Mutait.org or Graph Pad statistical software.

Note: The transformation of data for statistical analysis was log unless raw data value was <1 then square root was used to avoid negative values.

Chapter 3 – Results 1: Assay and IDEAS® Template Optimisation

3.1 – Introduction

The ImageStream platform provides high content, high throughput, whole cell microscopic analysis. The system provides the speed of flowcytometry with the spatial localisation information that comes with image based analysis. The ImageStream® MN multiplex expansion (ISMN-me) assay allows for the assessment of the well defined biomarkers P53, ɣH2AX and pH3-S28 along with cell cycle and MN analysis using the nuclear stain DRAQ5™ in whole (not lysed) cells.

Selection of the antibodies and DNA stain used in the development of the ISMN-me assay were based on a few factors.

Work previously done at Swansea University within the *In Vitro* Toxicology Group (IVTG) and published by Verma *et al* demonstrated that DRAQ5™ both sub-optimally at 488nm and optimally at 642nm generated sufficient DNA staining and crispness to identify MN in binucleated cells. Using the IDEAS® software masking system, MN can be automatically identified when stained with DRAQ5™ (Rodriguez., 2018; Rodriguez *et al*., 2018). The far-red emission spectra of DRAQ5™ provides a distinct profile separate from the other fluorophores used in this multiplexed assay.

The anti-ɣH2AX-Ser139 antibody has been used in numerous studies and publications, Bryce *et al*., 2016, Khoury *et al*., 2016, Smart *et al*., 2011, Cheung *et al*., 2015 and Wilson *et al*., 2021 to name a few, it is a truly well defined biomarker associated with DNA damage directly in the form of strand breakage and of the DNA damage response pathway (Podhorecka *et al*., 2010). Selection of the ɣH2AX antibody conjugated to the BV421 fluorophore was mainly chosen as it is excited by the 405nm laser which was available on the FlowSight® used at Swansea University for preliminary optimisation and work. Furthermore, BV421 signal is not as strong as the AF488 signal when excited by optimal lasers, as pH3 events are so much lower in frequency than the ɣH2AX response it was felt the pH3 detection sensitivity would benefit from having a more definitive fluorophore.

In most instances the preferred antibody used in the literature for detection of Histone 3 phosphorylation is Anti-pH3 Ser10. This antibody binds to H3 when phosphorylation at Serine 10 of the histone 3 tail occurs allowing for mitosis evaluation. However, H3 is normally phosphorylated at Ser10 in generic chromatin and is modulated by HMGN1 to aid gene expression and access of DNA damage repair proteins to DNA lesions (Huang *et al*., 2006; Juan *et al*., 1998; Lim *et al*., 2004). This implies there is potential for the pH3 antibody to bind to these normally phosphorylated Ser 10 sites outside of mitosis, the Ser 10 phosphorylation also occurs earlier in the cell cycle than mitosis being initiated throughout G2 phase (Hans & Dimitrov, 2001). As a result, the antibody selected for mitosis assessment as part of this multiplexing platform was Anti-pH3 Ser28. Phosphorylation of H3 at serine 28 has only been observed at the end of G2/beginning prophase and end of anaphase/early telophase therefore this biomarker is more specific for mitosis response (Hans & Dimitrov., 2001; Goto *et al*., 2002). The AlexaFluor488 Anti-pH3 Ser28 antibody was chosen for mitotic

assessment due to its strong signal when excited with the 488nm laser available on the FlowSight® at Swansea University.

For the assessment of P53 the antibody selected was specific to N-terminal linear epitope aa 20-25 of the P53 protein not any specific phosphorylation. Whilst use of the N-terminal P53 antibody may be considered generic and not specific enough to confirm the true translocation of stabilised P53 to the nucleus. Not using a phosphor P53 antibody allows the overall assessment of P53 within the cell and the corresponding increases/decreases to all types of damage induced by the various chemicals being assessed. For instance, a P53 antibody used that binds to phosphorylated serine 15 on the P53 protein is directly related to the damage induced by double strand breakage (Lavin & Geuven., 2006). Therefore, chemicals such as MMS that induce DNA breakages would have a corresponding increase of ɣH2AX response with pP53 Ser15 levels. However, when looking at a chemical that is not known for inducing strand breakage such as Carbendazim, there would be a lack of response in relation to phosphorylated P53 on serine15. Thus, not using a phospo-P53 antibody allows for the detection of stabilized P53 molecules in relation to various types of DNA damage and assessment in combination with other biomarkers should aid in identifying chemical Mode of Action. The PE fluorophore conjugated P53 antibody was chosen as the PE emission spectra was distinct from the DRAQ5™, AF488 and BV421 emission spectra and the PE fluorophore is sub-optimally excited by the 488nm laser enabling staining optimisation on the FlowSight® and combination assessment in the optimal ImageStream X Mark II® system.

Spectra for each of the conjugated antibodies and DNA stain, along with the associated channels on the IS XII and FlowSight® can be found in figure 3.1 below. Ch07 collects fluorescence emitted by BV421 associated with ɣH2AX. Ch02 collects fluorescence emitted by AF488 associated with pH3. Ch03 collects fluorescence emitted by the PE fluorophore associated with P53 and Ch11 collects the fluorescence associated with DRAQ5™ DNA stain.

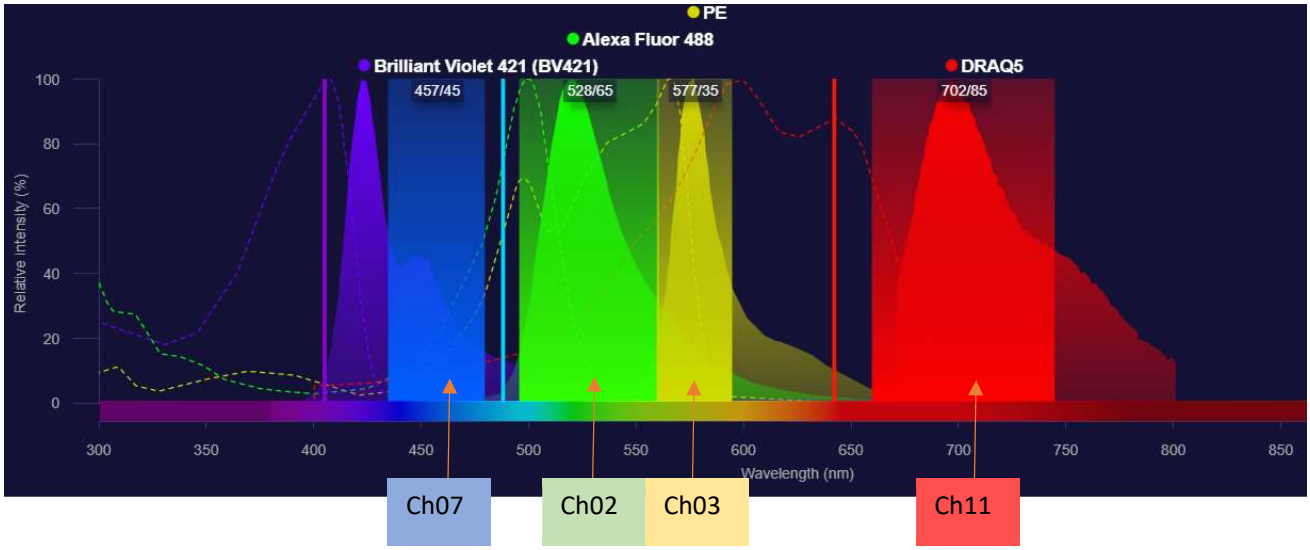

Figure 3.1: Emission spectra of each of the fluorophores conjugated to each of the antibodies and DNA stain present in the multiplex system. The band-passes demonstrate each of the channels the emission spectra associate with in both the IS XII and FlowSight®. The purple solid line represents the 405nm laser. The sky-blue solid line represents the 488nm laser and the Red solid line represent the 642 lasers. Spectral histogram was generated from ThermoFisher spectral viewer, and the band passes applied for each channel were taken from Amnis® Spectral Imaging Channels and Corresponding Fluorophores table.

This system provides the ability to compare these biomarker and MN responses directly to one another in the same cell. The system also allows us to confirm these relationships by looking at the associated generated cell brightfield image. Whilst this provides us with a vast pool of data, being able to sift through the large quantity of information poses a challenge, not only of identifying relevant data to analyse but also display and making sure the fluorescence associated with a specific biomarker is 'true'. This chapter attempts to address these challenges through demonstrating the steps taken to: Use gating and masking strategies to minimise potential autofluorescence/of target binding assessment, generate a standardised template that can be used to display and extract metrics of interest whilst minimising bias when assessing cell populations of interest, automating cell image analysis. This was done by combining flow cytometry fluorescence analysis and microscopy methods.

3.2 – Materials & Methods

3.2.1 – Test Article Formulation

Methyl Methanesulphonate (MMS), Cas no.: 66-27-3, and Carbendazim, Cas no.: 10605-21-7 supplied from Sigma-Aldrich. The working concentrations for confirmation of antibody penetration and gating assessment are as follows, MMS 2.50, 5.00 (µg/ml) and Carbendazim 1.20, 1.60 (µg/ml) and vehicle control DMSO.

The working concentrations for the assessment of MN mask accuracy are: Crizotinib, 4.51 (µg/ml); Etoposide, 0.13 (µg/ml); ARA-C, 0.05 (µg/ml) and Vinblastine, 0.0020 (µg/ml).

3.2.2 - Cell Culture and Growth Media

Cell culture prepared as in section 2.2.2.

3.2.3 – Treatment

3.2.3.1 - Treatment Of Cell Cultures

$2x10^5$ TK6 cells/mL were placed in a series of sterile vented tissue culture flasks (Fisher brand) and treated with MMS, Carbendazim, Crizotinib, Etoposide, ARA-C or Vinblastine for a 1.5-2 cell cycle period with no recovery. All incubation steps occurred at 37˚C, 5% (v/v) CO_2± 0.5% in air. Cell cultures were washed at the end of the treatment period as per section 2.2.2.1.

3.2.4 – Cell Fixation and Staining

Cell samples having been sufficiently fixed and permeabilised by FACSLyse solution in a 1:10 ratio with dH2O samples were stained with a maser antibody mix. The antibody master mix was made up fresh on the day of the experiment. The master mix consisted of anti ɣH2AX Brilliant Violet 421 antibody, anti pH3 ser 28 AlexaFluor 488 antibody, anti P53 PE antibody and PBS. DRAQ5™ DNA stain was added to each sample during antibody incubation. Refer to general material and methods in section 2 for full staining procedure.

3.2.5 – Image Acquisition

Stained samples were washed with PBS and transferred to appropriately labelled Eppendorf's and subsequently acquired on the ImageStream®X MarkII imaging platform. Cell samples were also looked at on the Confocal LSM 710, AxioObserver microscope platform to confirm antibody nuclear penetration and specific binding. Full acquisition details can be found in section 2.2.4.

3.2.6 – Micronucleus Mask Accuracy

To assess the effectiveness of the MN mask generated (see section 3.3.3.3) two metrics were assessed based on the MN populations of compounds, Crizotinib, Etoposide, Vinblastine and ARA-C.

The first, percentage accuracy (%Accuracy); Of the cell population Identified by the MN mask as containing MN what percentage were true, this was confirmed by inspecting each saved cell image by eye. %Accuracy was calculated as follows:

$$\%\text{Accuracy} = \frac{\text{Total True MN identified by mask}}{\text{Total cells with MN identified by mask}} \times 100$$

The second, percentage miss rate (%miss rate) required a defined cell population where the binned images could be assessed both by eye and using the MN mask. This population was selected by plotting healthy mononucleated cell population histogram using the Gradient RMS feature on the DNA content. A small gate termed DNA Focus was drawn to the right of the central peak (figure 3.2).

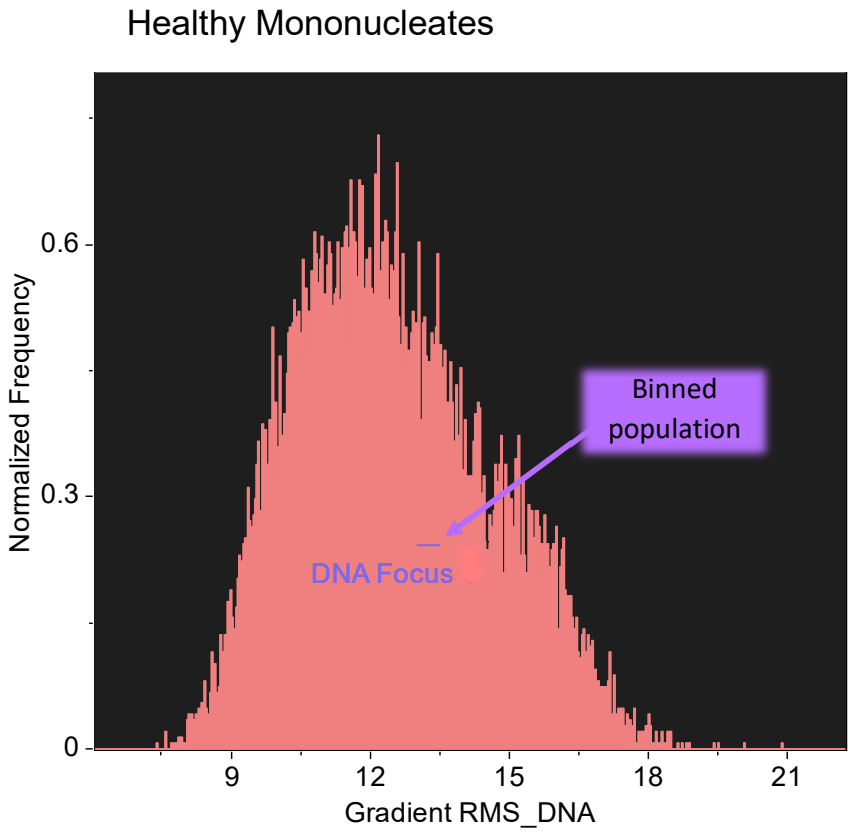

Figure 3.2: Example of plotted histogram from a population of healthy cells containing only one nucleus. Gradient RMS plotted along the x axis assesses how in focus the DRAQ5 stained DNA is, 0 indicating the least in focus. The DNA Focus gate contains the binned population to be analysed for MN mask %Miss Rate.

The binned population taken forward provided cells with clear crisp nuclei staining, giving the MN mask the best chance of identifying all MN, whilst randomly selecting cells to help minimize technician population bias and still being representative of the whole cell population. The total number of cells assessed were 1000-1500.

%Miss Rate was calculated as follows:

$$\%\text{Miss Rate} = \frac{\text{Total True MN identified by mask}}{\text{Total True MN identified manually}} \times 100$$

3.3 – Results & Discussion

Due to the optimisation nature of this chapter, the following results and discussion section is formatted in such a way to demonstrate the reasoning process behind the optimisation steps taken and generation of the IDEAS® template. This is in line with standard practise in the journals within the field of genetic toxicology.

3.3.1 – Confirmation of Antibody Binding and DNA Counterstaining

The confocal imagery in figure 3.3 below confirms that the antibody and DNA staining of permeabilised fixed cell samples sufficiently penetrated the cellular and nuclear membrane. The Z-Stack image also demonstrates that the antibodies have not just bound to the surface of the nucleus but have permeated through the depth of the nuclei. Details of confocal image acquisition can be found in section 2.2.4.1.

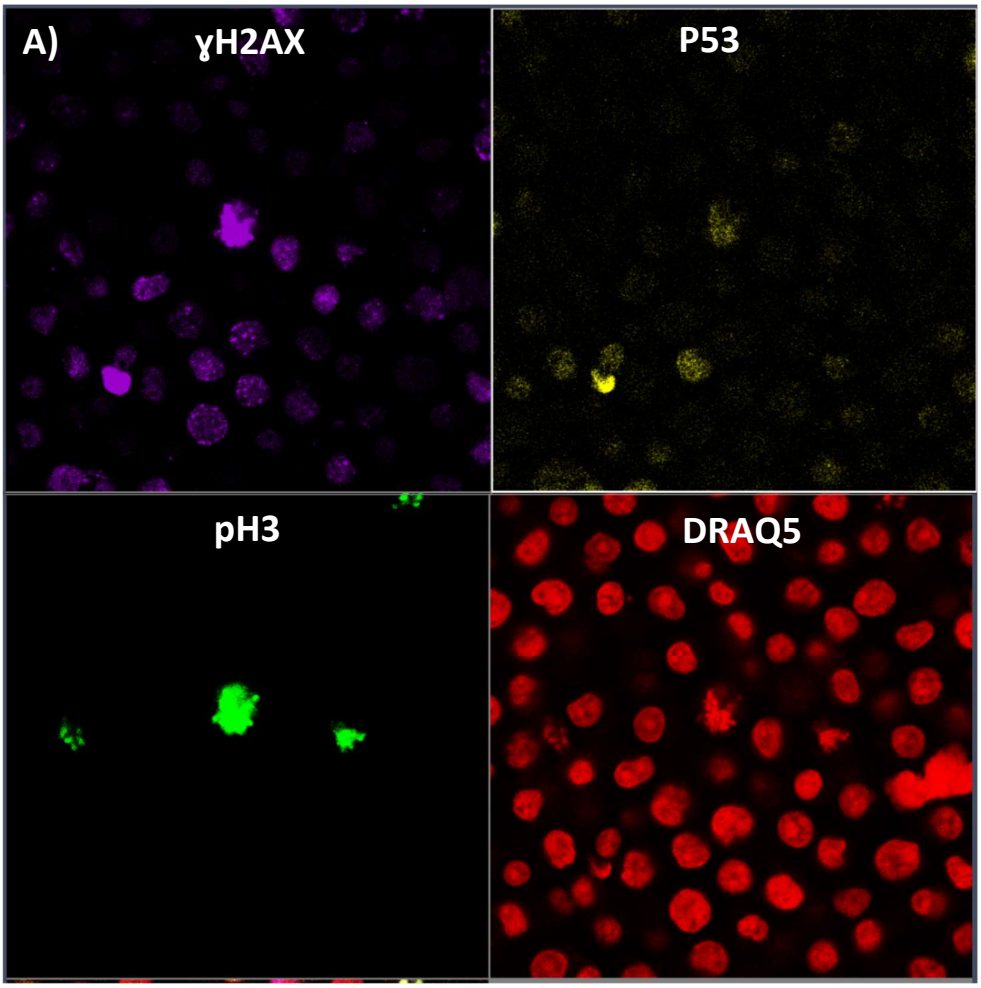

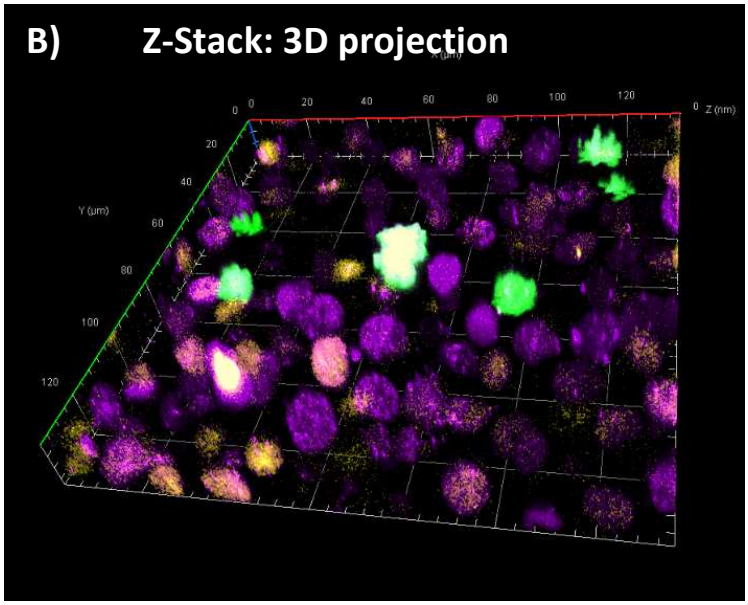

Figure 3.3: 1.6µg/mL Carbendazim dosed TK6 cells demonstrating linear unmixed 4 colour, stained sample at x63 magnification acquired on confocal microscope. A) Shows the individual channels associated with BV421 gH2AX, PE P53, AF488 pH3 and DRAQ5 DNA stain. B) Shows a z-stack of the same region of cells as in A confirming the penetration of the antibodies throughout the nuclei.

3.3.2 - Gating: Placement and Boundary Cut Offs

Gate boundary cut offs have been a constant debate within the scientific community. From assessing population by eye to allowing software to automatically set gates, the process is a subjective art. Subjectivity is never ideal when it comes to scientific practice, so for the assessment of my data it was necessary to generate a standardised method for generating gates and cut offs on my data. This was approached through the use of fixed unstained cells dosed with the solvent DMSO, MMS and Carbendazim, compared with DMSO, MMS and Carbendazim treated stained cells. The stains used were DRAQ5™, BV421, PE, AF488, appropriate compensation matrix was also applied to each of the assessed files prior to gate generation.

Assessment of solvent treated and compound treated cells with no stain is a crucial step when it comes to assessing gate boundaries and establishing auto fluorescent cut offs. This is crucial during genetic toxicology assessments at combined autofluorescence with biomarker signal could be the difference between generating a misleading positive and true negative especially when it comes to borderline genotoxic chemicals.

Trying to define finite gating cut-offs in a standardised manor is essential for compound analysis and has required definitive rules that can be applied to different chemicals especially if they exhibit more than 'background' autofluorescence of solvent treated cells. Populations of cells that were used for assessing the gating boundaries simply needed to meet the criteria of being single and in focus.

3.3.2.1 - Cell Cycle Assessment Gates

Cells cycle assessment gates were determined through initial assessment of pH3 signal (a marker of mitosis) and multiplying the nuclear DNA peak (n=1) location by 1.8-2. Gating of pH3 mitotic cells was plotted on DNA histogram of control sample see figure 3.4.

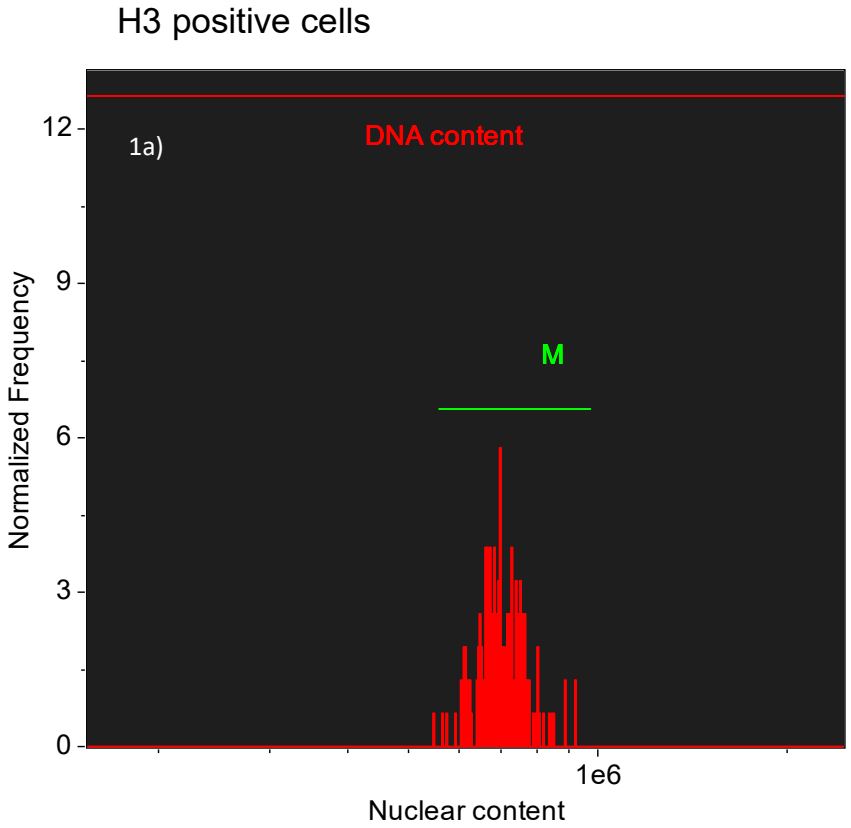

Figure 3.4: Graph 1a Population of H3 positively stained cells plotted on nuclear content histogram graph. Nuclear content assessed by presence of DRAQ5 DNA stain. This peak was then gated and determined mitotic (M) region of the cell cycle.

The whole available cell sample population was then plotted on nuclear content histogram graph and the Mitotic (M) gate from graph 1a was applied, see figure 3.5

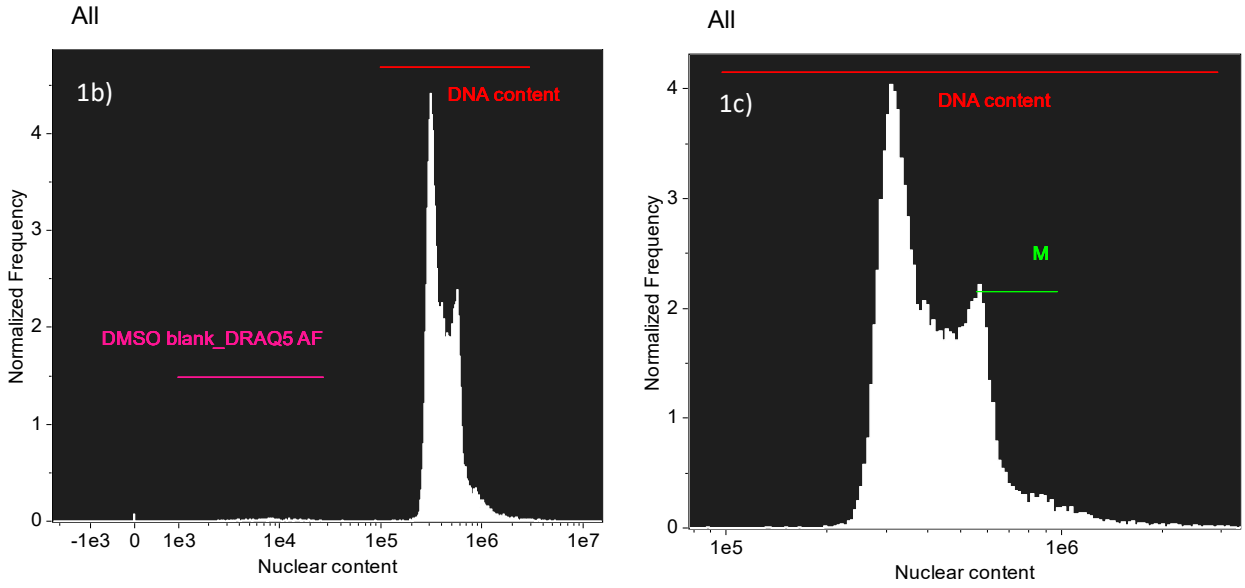

Figure 3.5: Nuclear content graphs of entire available cell population. Graph 1b demonstrates the entire cell sample population and the DNA content of those cells based on DRAQ5 DNA stain. The DRAQ5 channel AF (Auto Fluorescence) demonstrating the DNA content peaks are above background AF. The M gate from graph 1a was then applied to graph 1b generating graph 1c.

The major cell cycle phases, G1, S and G2/M were then applied to graph 1c. Starting with the G1 gate generating graph 1d) then the G2 gate by applying a times 1.8-2 greater than G1, graph 1e), figure 3.6.

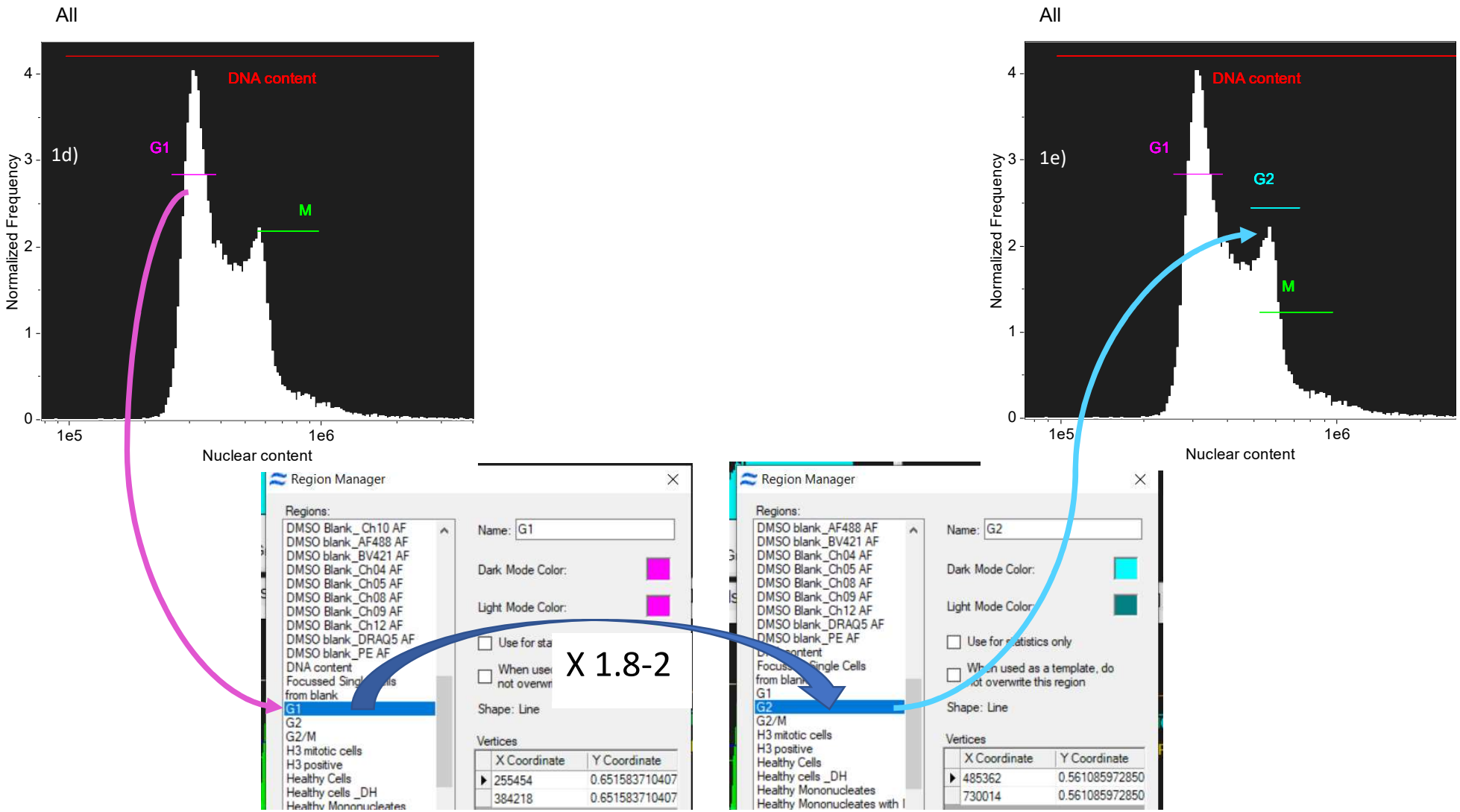

Figure 3.6: DNA content graphs demonstrating G1 and G2 gate generation and use of region manager. Graph 1d) demonstrates the gated G1 peak, nuclear content n=1. The gate upper and lower cut offs were then multiplied independently by 1.8 and 2 to generate the G2 gate nuclear content n=2. (255454 – 384218 x2 = 510908 – 768436. 255454 – 384218 x1.8 = 459817 – 691592). An average of these two n=2 upper and lower bound gate cut offs was then taken. Generating G2 gate (485362 – 730014) of graph 1e).

The G2 and M phase gates were then combined due to their overlapping nature generating G2/M gate. S then filled the gap between G1 and G2/M gate as demonstrated by figure 3.7.

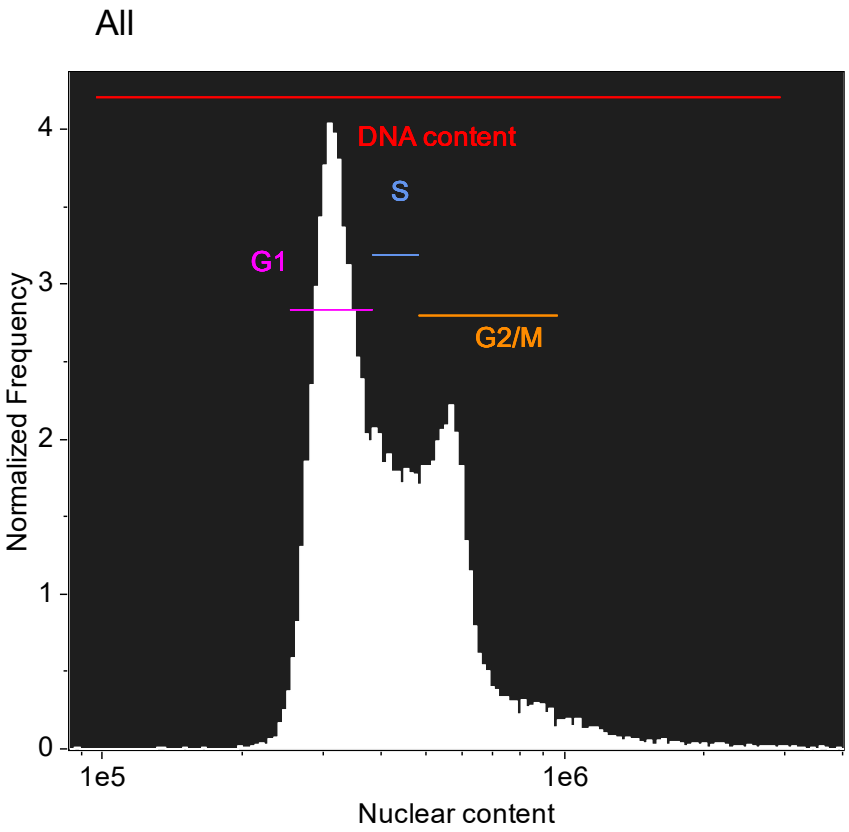

Figure 3.7: Demonstrating the final gate layout for cell cycle assessment based on DRAQ5 staining of nuclear content.

Between sample sets for the same compound and dose there can be variation due to sample preparation differences, fluctuation in timings, ambient temperature variation, stain adherence to DNA, compound AF and cell orientation as the cell passes through the detector. This can be a potential problem when trying to generate a templated based approach to sample analysis using the IDEAS® software. However due to the presence of phosphorylated H3 as a mitotic marker I use this as a 'anchor' point on any DNA histogram and then position the other cell cycle gates based on the M gate position.

This initial gating process was performed on the whole available sample i.e., included apoptotic/necrotic cells to try and avoid unconscious bias. The apoptotic and necrotic cell populations i.e., unhealthy cells were removed from the whole sample meaning the final cell population assessed were termed 'Healthy' based on nuclear content and brightfield contrast. Identification of this 'Healthy' population is demonstrated in section 3.3.3.

Despite consistent DRAQ5™ staining methodology with all things biological there is variability. Variability can be due to multiple factors: Environmental i.e. humidity, temperature; Technical; Variation between cells, cell cultures and replicates. These variations result in variability of DRAQ5™ staining meaning the G1, S and G2/M gate placement is the rate limiting step when it comes to template approach and batch processing of data sets because of subtle shifts of the DNA content histogram up and down the x axis. To counteract this effect the same method described in this section was used per dose per chemical. For each replicate of the same dose and chemical the same gate x co-ordinates for G1, S and G2/M were used. Where a distinct G1 peak was not present cells that were positive for pH3 staining were used to set the G2/M gate and then the S and G1 gates based on G2/M placement.

3.3.2.2 - BV421 ɣH2AX Cut Offs

To assess ɣH2AX response a step wise gating procedure was developed to help exclude any autofluorescence and determine a finite gating boundary cut off where background ɣH2AX levels are excluded from ɣH2AX metric generation and only ɣH2AX levels over a certain intensity are counted as being induced due to chemical related damage. Figure 3.8a and 3.8b shows the 12 steps taken to generate the lower gate and upper gate for ɣH2AX signal induction a stepwise description follows that relates to each graph within figure 3.8a and 22b.

1- MMS unstained autofluorescence (AF) graph. Full AF peak gated to the point where histogram cell 'bins' reach less than 2 cells consistently. X co-ordinates: 3210-32006. The lowest gate boundary needs to be higher than 32006, the highest point of AF.
2- Unstained peak (UP) gating based on the centralisation of gates over the AF peak drawn by eye at three different positions on the histogram peak. X co-ordinates: 1_MMS UP; 4917-21375, 2_MMS UP; 5168 – 19836; 3_MMS UP; 4678-23614
3- Average of these three X coordinates was then taken to generate the Average_MMS unstained peak X coordinates:4921-21608
4- MMS multiplexed (all biomarkers and DNA stain) cell sample. The stained distinct peak (SP) was assessed. The same process used as explained in step 2) i.e., 3 gates drawn by eye. However, the lowest x point of the three does not drop below the 32006 x axis value as determined by step 1 by more than 10%. X coordinates: 1_MMS SP; 37170-108428; 2_MMS SP; 32850 – 117736; 3_MMS SP; 29033 – 117736
5- Average of the 3 gates in step 4 was taken, X coordinates; Average_MMS SP; 33017-114633. The lowest x intercept is greater than the highest X point of the MMS AF peak
6- Demonstrating the Average_MMS UP gate and Average_MMS SP gate.
7- Working with the 10fold principle used as standard practice in flow cytometry. The x intercept coordinates of Average_MMS UP gate were multiplied by 10 generating the Average_MMS UP 10fold gate. 4921-21608 →X10→ 49210 – 216080

8- An average was then taken of these two gates from the two different methods (above AF and 10 fold) generating a Combined average MMS peak gate. X coordinates: Combined Average;41113-165357.

The combination of these two methods was used to provide a robust gate cut off with reduced subjectivity. The lowest X intercept 41113, will be the lowest gate cut off for ɣH2AX assessment and fulfils the requirements of: being greater than the highest MMS AF peak gate X intercept and does so by no more than 10%. This lowest gate will initially be referred to as; +BV421(gH2AX gate).

9- Due to the nature of ɣH2AX the use of only one gate cannot be used to identify strand break induction due to DNA damage over that of a healthy cell system. This can be achieved by assessing the difference in intensity of; the solvent DMSO control stained sample BV421 peak and the MMS induced BV421 peak. Therefore, an average of 3 gates centralised of the solvent (DMSO) only stained sample peak was given: 1_DMSO SP: 29127-70422, 2_DMSO SP; 27662 – 72924, 3_DMSO SP; 24734 – 82930. Average_DMSO SP; 27174-75425
10- Accepting that the lowest X coordinate for the +BV421(ɣH2AX gate) is equal to the lowest X coordinate of the combined average MMS peak averaged with the lowest x co-ordinate of the Average_DMSO stained peak. Thus, the upper gate boundary of +BV421 (gH2AX) should be the higher X intercept of the Average_DMSO stained peak. This allows us to assume that the cells within this gate are healthy and are experiencing 'normal' ɣH2AX cell cycle responses and that anything greater than this X intercept could be considered critically damaged as a result of induced DNA Damage.
11- MMS lowest gate intercept, 41113 combined with the highest Average_DMSO SP x axis intercept. This gives us +BV421 (ɣH2AX gate) lower and upper intercepts.
12- Anything greater than 75425 x intercept can then be considered ++BV421(ɣH2AX) and allow for the assessment of induced DNA damage based on compound interaction having taken into account any potential chemical AF. An upper x intercept cut off for ++BV421(ɣH2AX) was given at $1X10^6$ intensity units.

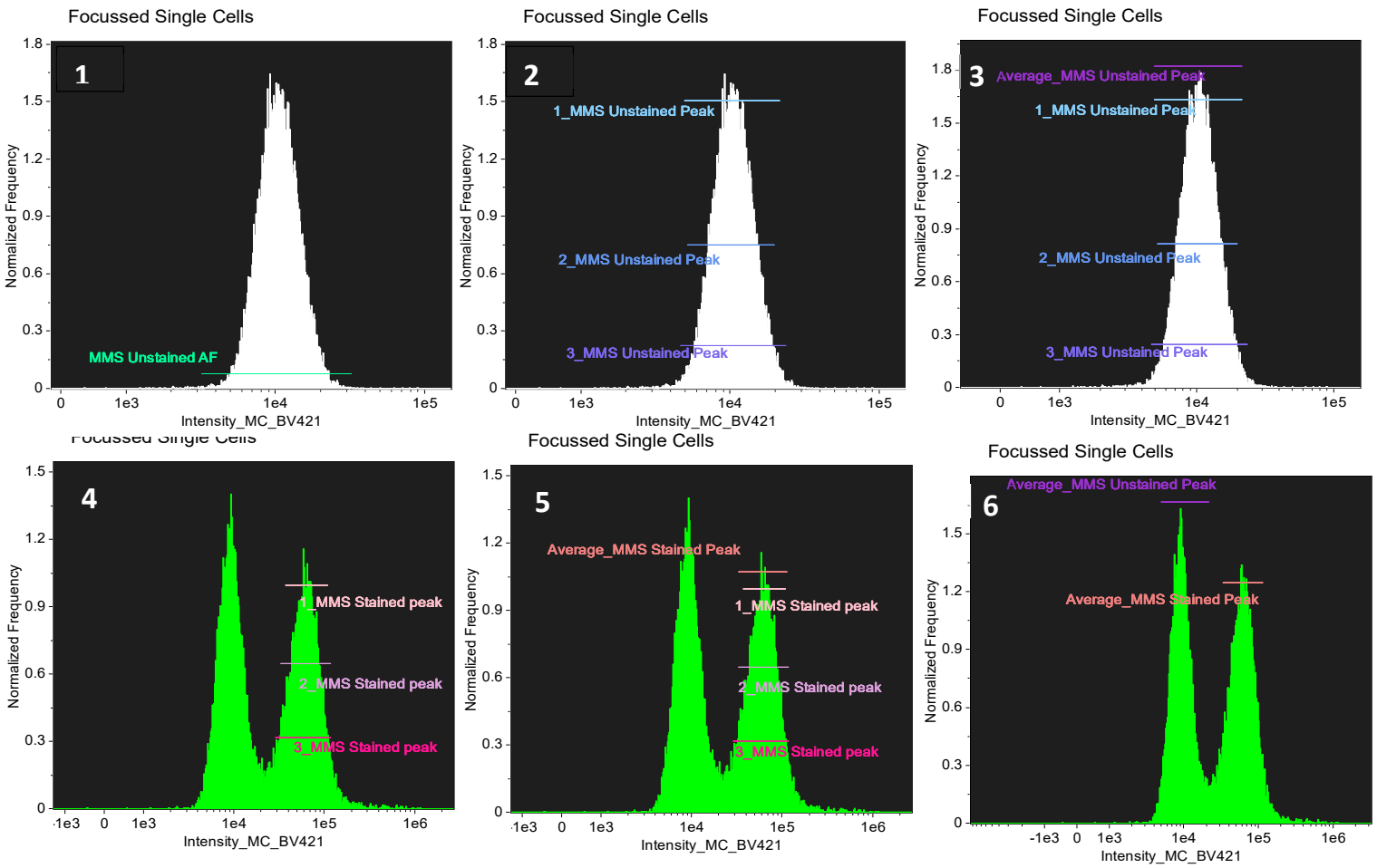

Figure 3.8a: Demonstrating steps 1-6 of the BV421 ɣH2AX gating strategy

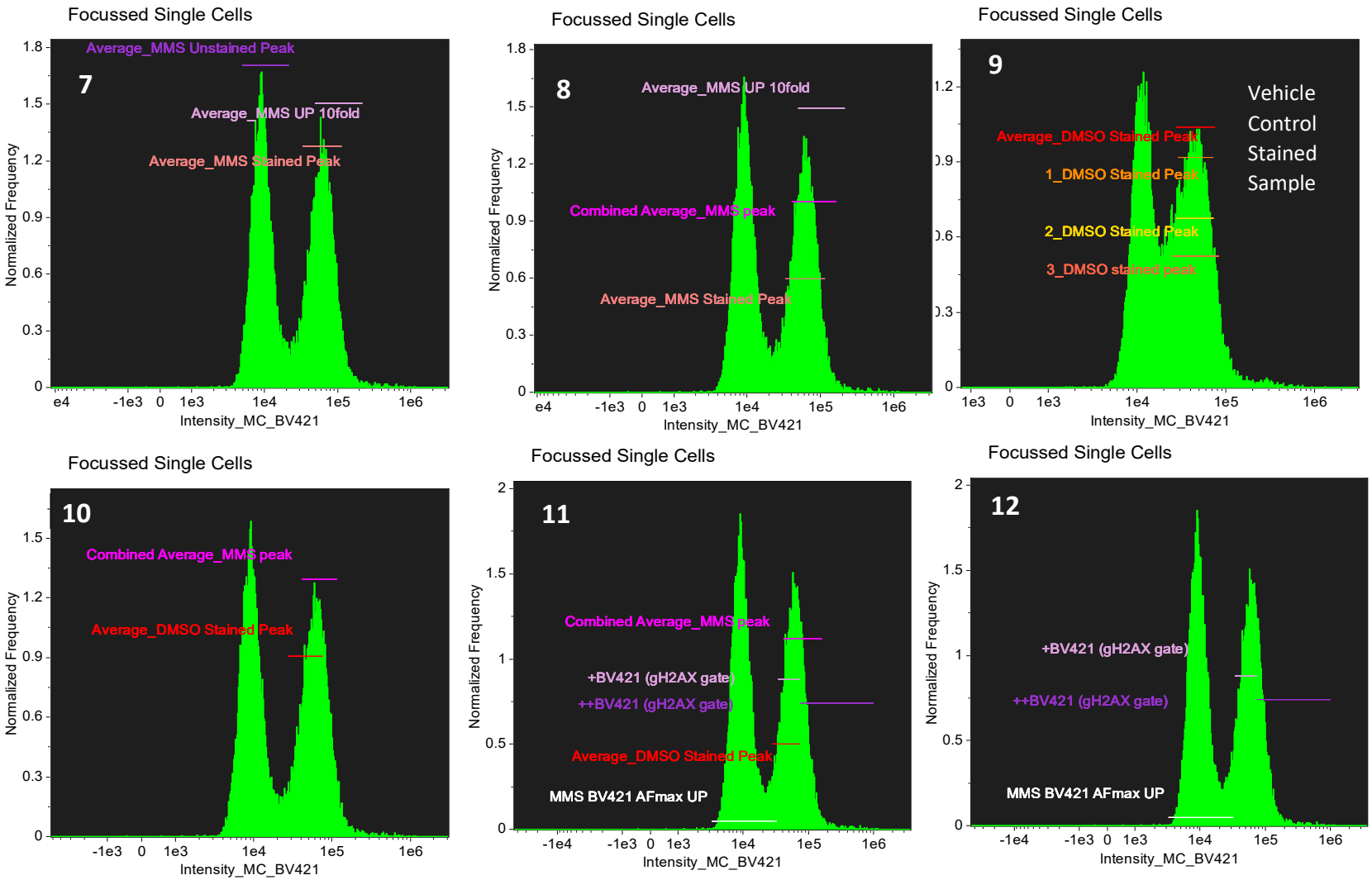

Figure 3.8b: Demonstrating steps 7-12 of the BV421 gating strategy

Applying these gates (+BV421(gH2AX) and ++BV421(gH2AX)) to the solvent control, known clastogen at 2.5µg/mL MMS and known aneugen 1.2µg/mL Carbendazim provides a snapshot of ɣH2AX response percentages of the two gates and are displayed in table 3.1. This data was assessed on the entire available ɣH2AX signal without assessing cell cycle (i.e., initially ignoring the DNA stain) and not gating out apoptotic and mitotic cells.

Table 3.1: Demonstrating the cell percentages that fall inside the boundaries of the +BV421(ɣH2AX) and ++BV421(ɣH2AX) gates for Carbendazim (Crbz), DMSO and MMS along with the fold change away from the solvent negative control

	Crbz	DMSO	MMS
Fold change	0.61		1.08
+BV421 (ɣH2AX)	15.2	25	27.1
++ BV421 (ɣH2AX)	7.06	6.72	15.1
Fold change	1.05		2.34

At this stage although mitotic and apoptotic populations have not been excluded from the ɣH2AX assessment. This demonstrates a difference between known aneugen, clastogen and control that is consistent with the current literature. These numbers will now be refined through population narrowing that will exclude ɣH2AX events that are not due to DNA damage but are induced as a result of mitosis and cell death.

3.3.2.3 - AF488 pH3 Cut Offs

The fluorophore AF488 is a brightly fluorescent fluorophore that is excited using the 488nm (blue laser). The emission spectrum in the ImageStream system is visualised in channel 2 of the 12 available channels. Initially Alexafluor488 fluorophore was chosen in association with the anti ɣH2AX antibody. However due to the available fluorophores that were commercially available with the antiH2AX antibody compared to Anti pH3 antibodies and the low levels of H3 signal available AF 488 was considered more appropriate for picking up pH3 signal. The z stack from confocal microscope demonstrated in figure 3.9 Shows the antibody has bound the phosphorylated H3 proteins available in mitosis generating the distinctive fingers associated with the condensation of chromosomes in the nucleus.

Whilst initial optimisation of the antibody (as with ɣH2AX antibody) was performed on the Amnis FlowSight® the now described gating strategy was used on data obtained on an Amnis® ImageStream X Mark II® at x40 magnification. This methodology was then followed and applied for data generated at x20 and x60 magnification on both the FlowSight® and ImageStream X Mark II®.

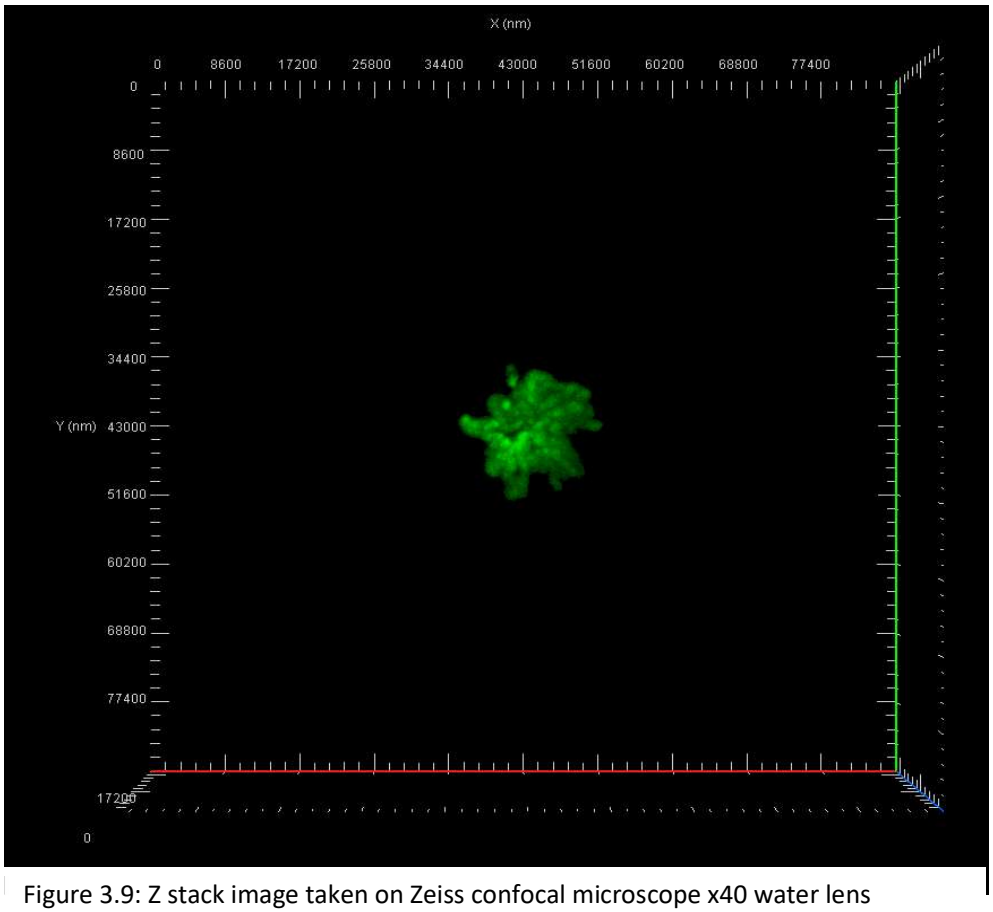

Figure 3.9: Z stack image taken on Zeiss confocal microscope x40 water lens objective. Demonstrates the penetration of the Anti H3 antibody throughout the entirety of the nucleus and not simply surface nuclear membrane binding.

The AlexaFluor (AF) 488 conjugated H3 Antibody specifically binds to the Serine (S) 28 residue when it has been phosphorylated. Due to the nature of Phosphorylated (p)H3 only occurring in late G2 and early mitosis phase of the cell cycle there is less subjectivity when compared to the transient nature of ɣH2AX when it comes to gating. This means the +ve pH3 gate simply needed to sit above/within 10% of the maximum autofluorescence of the cell sample. However, for consistency the methodology used to generate the ɣH2AX gates was applied to AF488 pH3 gate generation and adapted accordingly when needed. The population assessed was simply single in focus and circular, this helps to eliminate unconscious bias during the gating process.

The following graphs show a step wise process of how the +ve pH3 gate was generated. For a unstained DMSO sample, collected with all lasers set for optimal fluorescence acquisition of a stained sample, AF488 fluorescence intensity was plotted on the x axis as a histogram (Figure 3.10). A maximum unstained (US) peak gate for DMSO negative control was generated (Figure 3.10a) followed by averaging

the upper and lower x intercepts at three portions of the DMSO US histogram (Figure 3.10b).

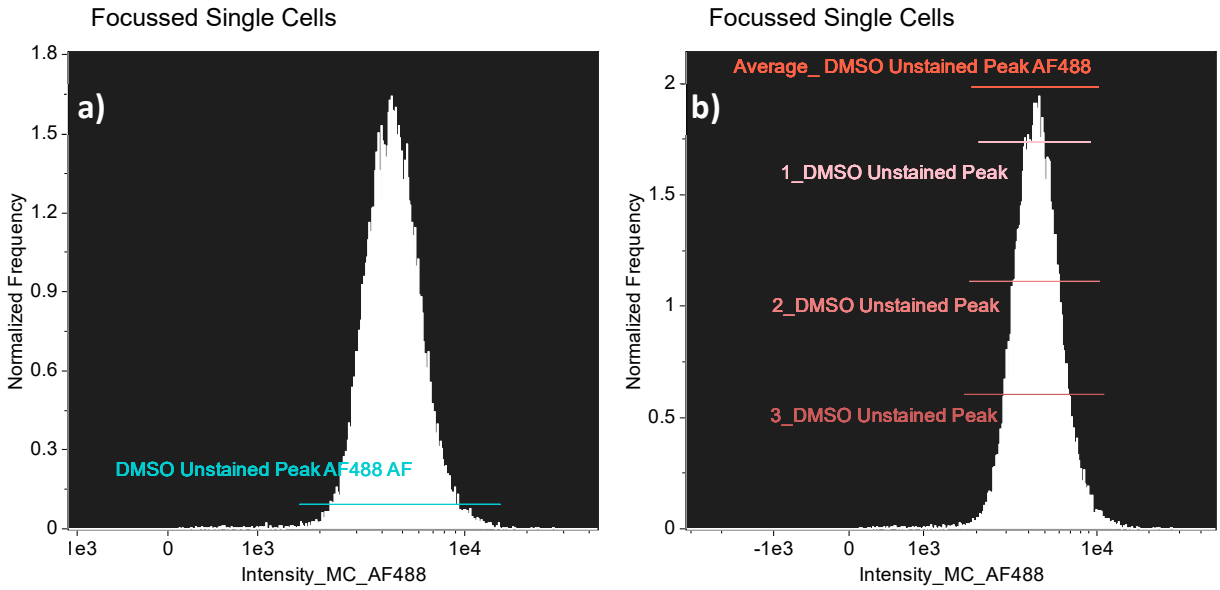

Figure 3.10: Unstained vehicle control autofluorescence peak for generation of an average autofluorescence unstained DMSO peak gate. a) Maximum DMSO autofluorescence gate. b) Average of the upper and lower intercepts at lower middle and top portions of the main US peak.

The Average_DMSO Unstained Peak AF488 now termed Average_DMSO UP AF488 was applied to acquired data for DMSO vehicle stained with the AF488 conjugated antibody. With AF488 intensity plotted along the X axis the histogram generated in figure 3.11 shows a primary peak that sits within the Average_DMSO UP AF488 gate (generated as per figure 3.10). This identifies cells that did not positively stain with the AF488 antibody despite its presence within the sample and that background autofluorescence in vehicle control samples is unaffected by antibody presence. The smaller secondary peak, zoomed in section of figure 3.11, are those cells positively stained with the AF488 pH3 antibody and DMSO stained AF488 Peak gate was applied.

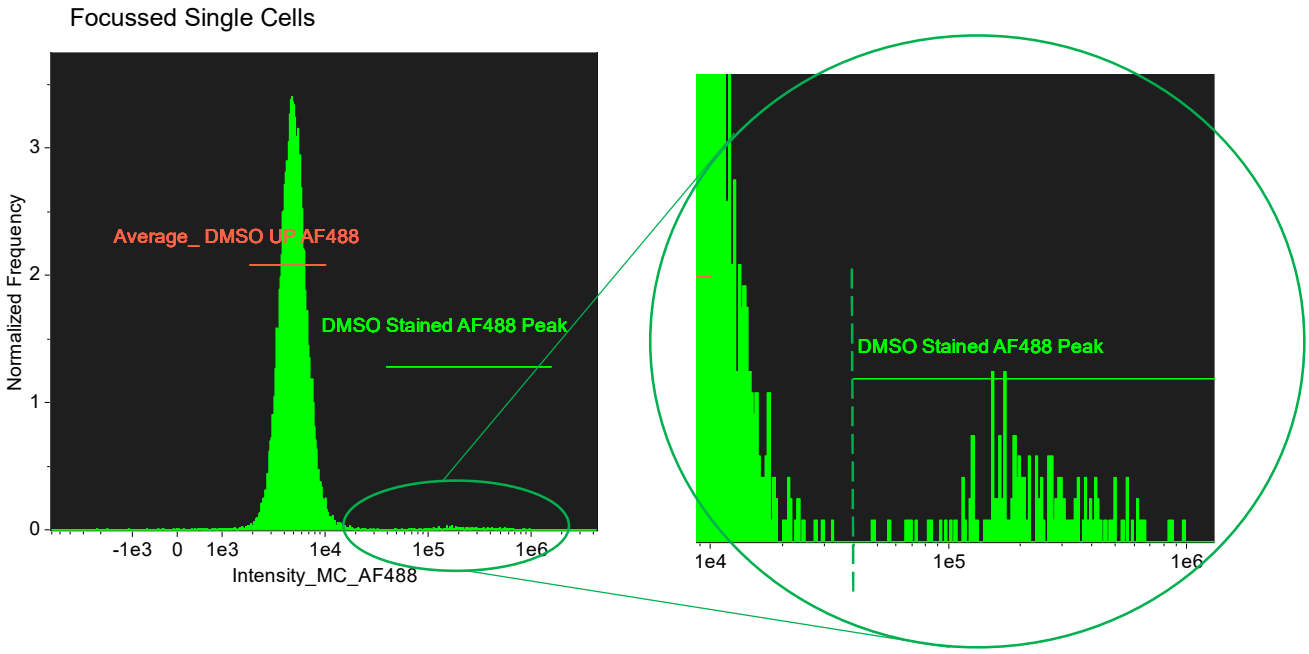

Figure 3.11: Displayed histogram of AF488 stained DMSO sample. The true fluorescence peak was determined through a break in the primary peak and the smaller secondary peak termed DMSO stained AF488 Peak.

The next step was to assess this initial AF488 gate on a sample of data known to induce a positive response in pH3 and therefore increased fluorescence availability of AF488 signal. As such a unstained Crbz sample was looked at without compensation to assess background autofluorescence (AF), see figure 3.12. This showed a higher level of AF than that of the vehicle control as demonstrated by figure 3.12b. To confirm this shift in autofluorescence was appropriately accounted for the compensated file of the stained Crbz sample and AF peak was assessed, Figure 3.12c.

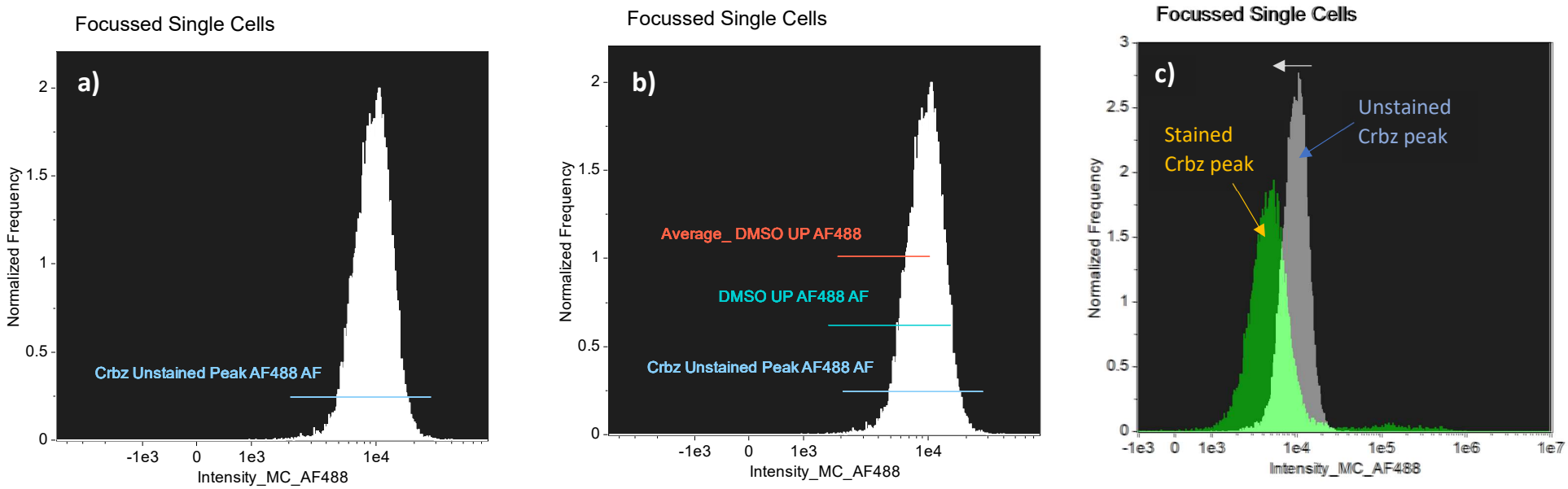

Figure 3.12: Display of Crbz unstained AF488 histogram peak. a) Shows the maximum AF of US Carbendazim following two cell bin rule. b) Demonstrates where the maximum AF DMSO gates from figure 3.10a and average DMSO UP gate from figure 3.10b sits on the unstained Carbendazim histogram. c) Showing the shift of the US Crbz peak to the stained Crbz peak

Upon application of compensation matrix to stained Crbz sample the AF peak shifts down to the left and falls within the Average_DMSO UP AF488 gate. i.e., the main AF peak fell to vehicle control AF levels, see figure 3.12c below. As a result, an average of the unstained peak of Crbz was not strictly needed. However, due to the minimal presence of a secondary AF488 true stain peak average of the stained peak could not be generated so an average of the US crbz peak was still taken and therefore a 10fold gate for US Carbendazim was generated, figure 3.13.

The following graphs in figures 3.13 – 3.14 demonstrate the 10 fold gate generation of estimated DMSO stained secondary peak and 10 fold estimated Crbz stained secondary peak. The 10 fold DMSO gate and stained AF488 DMSO gate (as seen in figure 3.11) lower

boundary overlap, shown by yellow R9, were then averaged to demonstrate DMSO 10F + AF488 stained gate. The R10 region combines the Crbz AF488 10fold lowest boundary and DMSO stained 10fold gate lowest boundary generating the combined +ve AF488 gate.

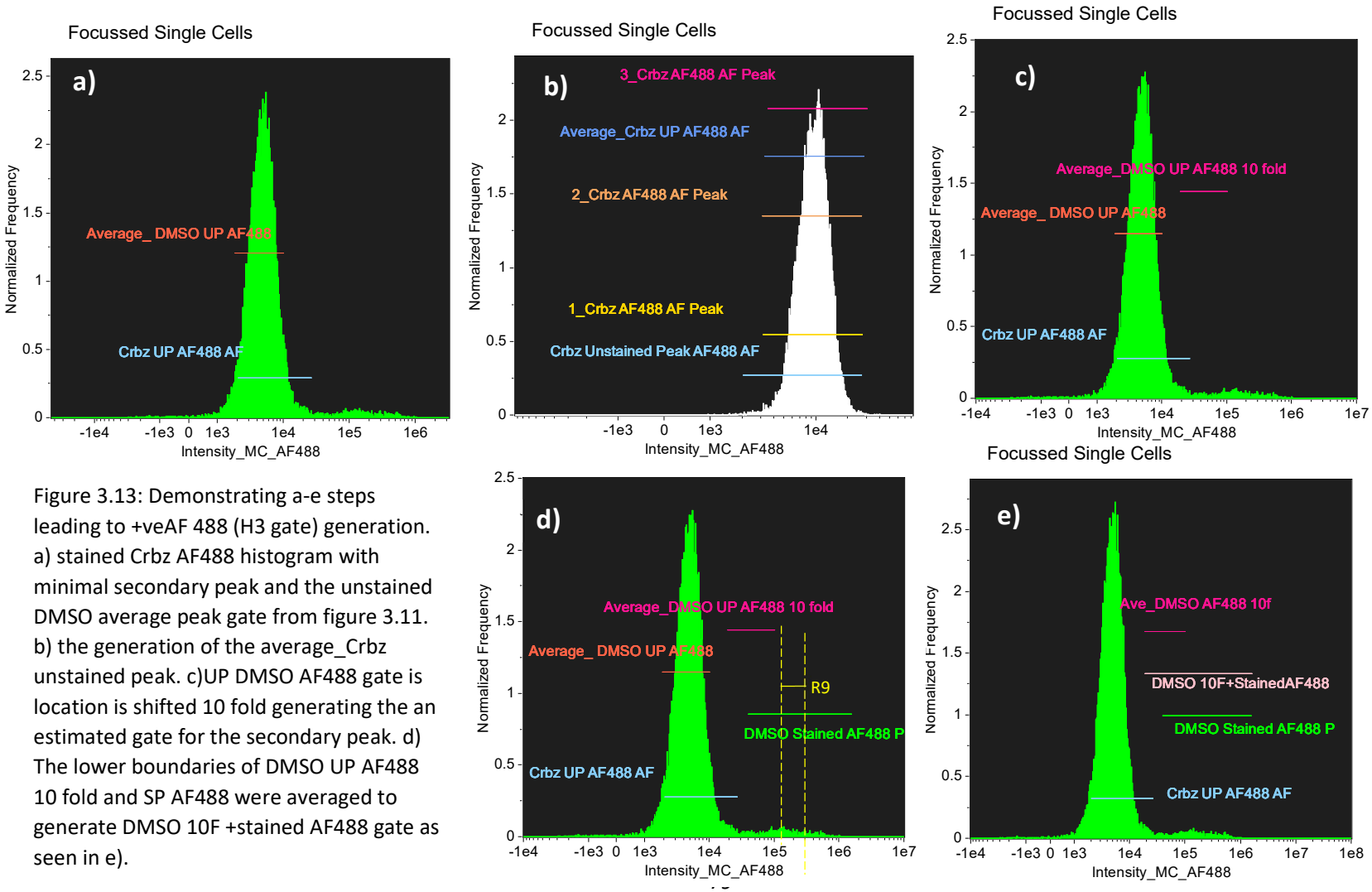

Figure 3.13: Demonstrating a-e steps leading to +veAF 488 (H3 gate) generation. a) stained Crbz AF488 histogram with minimal secondary peak and the unstained DMSO average peak gate from figure 3.11. b) the generation of the average_Crbz unstained peak. c)UP DMSO AF488 gate is location is shifted 10 fold generating the an estimated gate for the secondary peak. d) The lower boundaries of DMSO UP AF488 10 fold and SP AF488 were averaged to generate DMSO 10F +stained AF488 gate as seen in e).

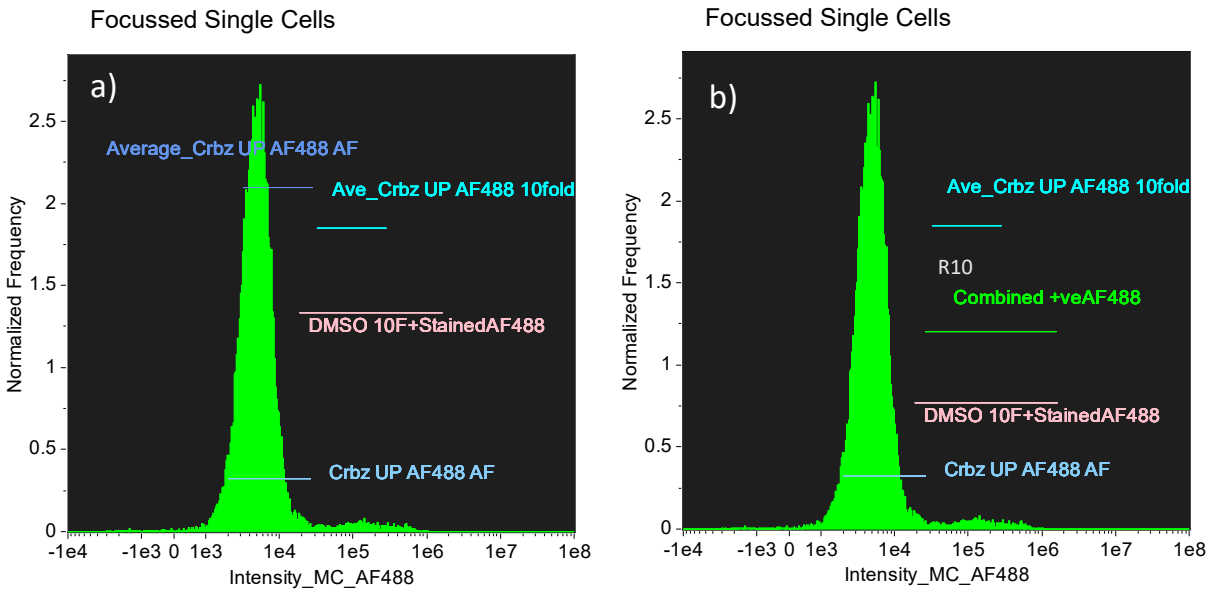

Figure 3.14: Demonstrating continued steps leading to +veAF 488 (H3 gate) generation. a) Showing the 10 fold increase of average unstained DMSO and Crbz peaks. b) R10 demonstrates the averaging of the lower cut off values of the two 10 fold gates to generate the combined +veAF488 gate.

The graphs in figure 3.15 show the +veAF488 (H3 gate) in histogram form and that there is some overlap with the maximum crbz AF demonstrated by the region R11. However, when this is plotted as a scatter graph the R11 AF overlap is diminished by the nuclear content and cell positions in the cell cycle see figure 3.16.

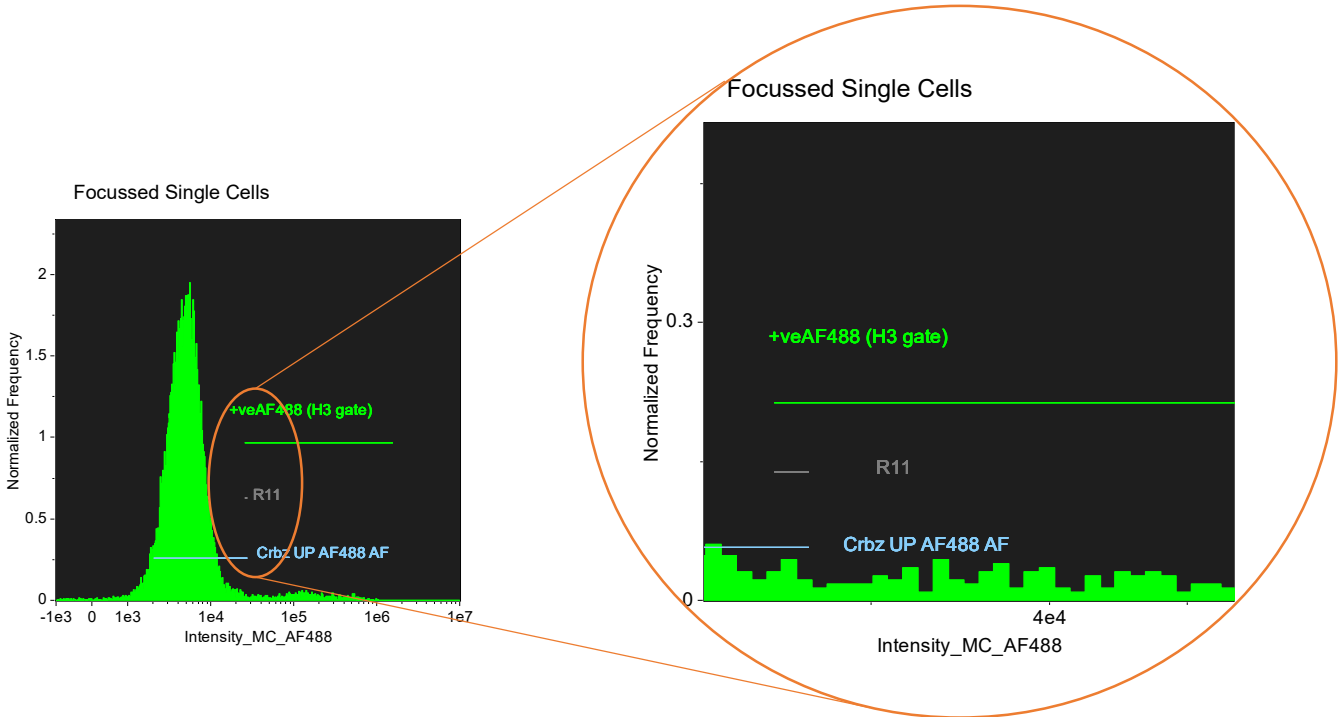

Figure 3.15: Combined +veAF488 is now referred to +veAF488 (H3 gate). R11 showing the overlap between +veAF488 (H3 gate) and Carbendazim autofluorescence gate.

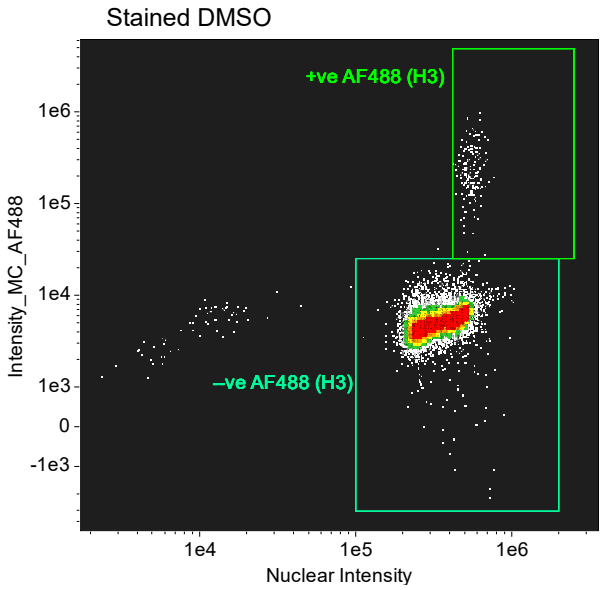

Figure 3.16: Scatter graph of negative control DMSO demonstrating the gated populations of +ve Af488(H3) meaning positively stained for pH3 and -ve AF488 (H3) meaning no stain for H3 present above background AF.

Figure 3.17 demonstrates that (example in orange bubble) off target binding or AF falls outside of the gates based on the secondary characterisation of DNA stain and the cell population separating into the distinctive G1, S and G2/M phases of the cell cycle as described in section 3.3.2.1 above allowing by the definition of biology to be excluded as 'True' pH3 events due to them sitting in the G1 phase of the cell cycle. Though the gates are robust there are some examples of AF/ potential off target binding events occurring (example in green bubble of 3.17). To help make sure the data is normalised and what is being observed/detected is true pH3 events in the G2/M section of the cell cycle. Ideas software provides a feature termed similarity of morphology o help determine localisation of a stain/probe within the cell i.e., the likelihood of it being in the cytoplasm or the nucleus. It does this by creating a mask of the nucleus i.e., DNA stain and overlaying this with the biomarker of choice (in this case pH3) and then seeing how similar in location these pixels are two one another (figure 3.18). A value of 1 and above indicates the pH3 pixels are most similar to the nuclear stain i.e., are in the nucleus rather than the cytoplasm. Below zero means the signal is most likely in the cytoplasm so these are the pixels that are least similar to the nucleus. The values between 0 and 1 are intermediates this means that, most likely, due to the orientation of the cell as it passed through the camera on the ImageStream was partially in and out of focus, so a portion of the signal has fallen outside the focal plane the camera was trained on during collection. As a result, for anything that was above zero the H3 signal was determined to be sufficiently 'similar' to the nucleus that the recorded result was not as a result of off target binding or AF. The use of this feature attempts to compensate for the lack of z stacking as available with confocal microscopy which provides the user with the

ability to definitively determine a probe/stain location. Though this feature does not provide definitive location of the biomarker it does lend confidence and allows for some assessment of the fluorescence spatially and not wholly relying on fluorescence intensity as with standard flow cytometry techniques.

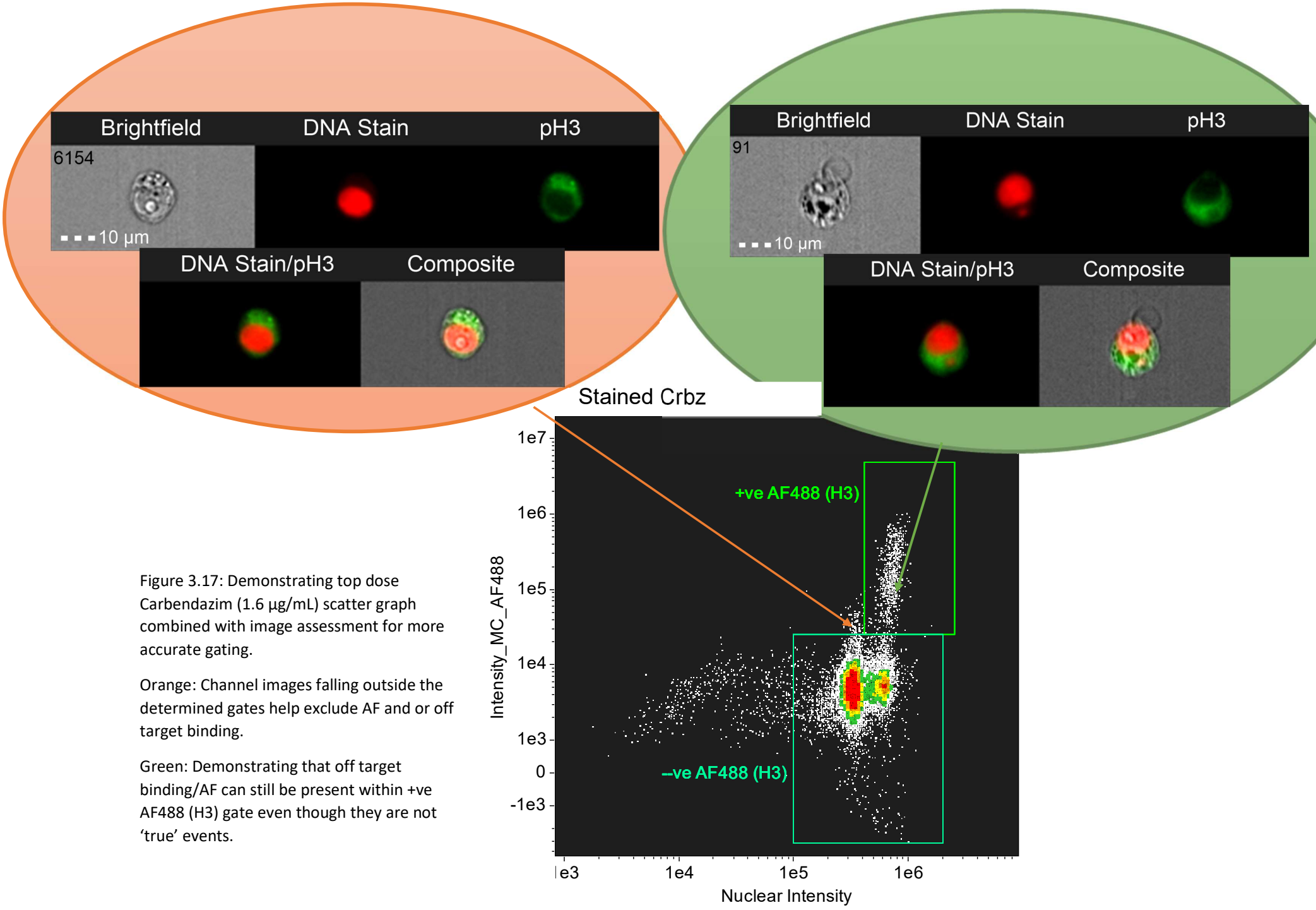

Figure 3.17: Demonstrating top dose Carbendazim (1.6 µg/mL) scatter graph combined with image assessment for more accurate gating.

Orange: Channel images falling outside the determined gates help exclude AF and or off target binding.

Green: Demonstrating that off target binding/AF can still be present within +ve AF488 (H3) gate even though they are not 'true' events.

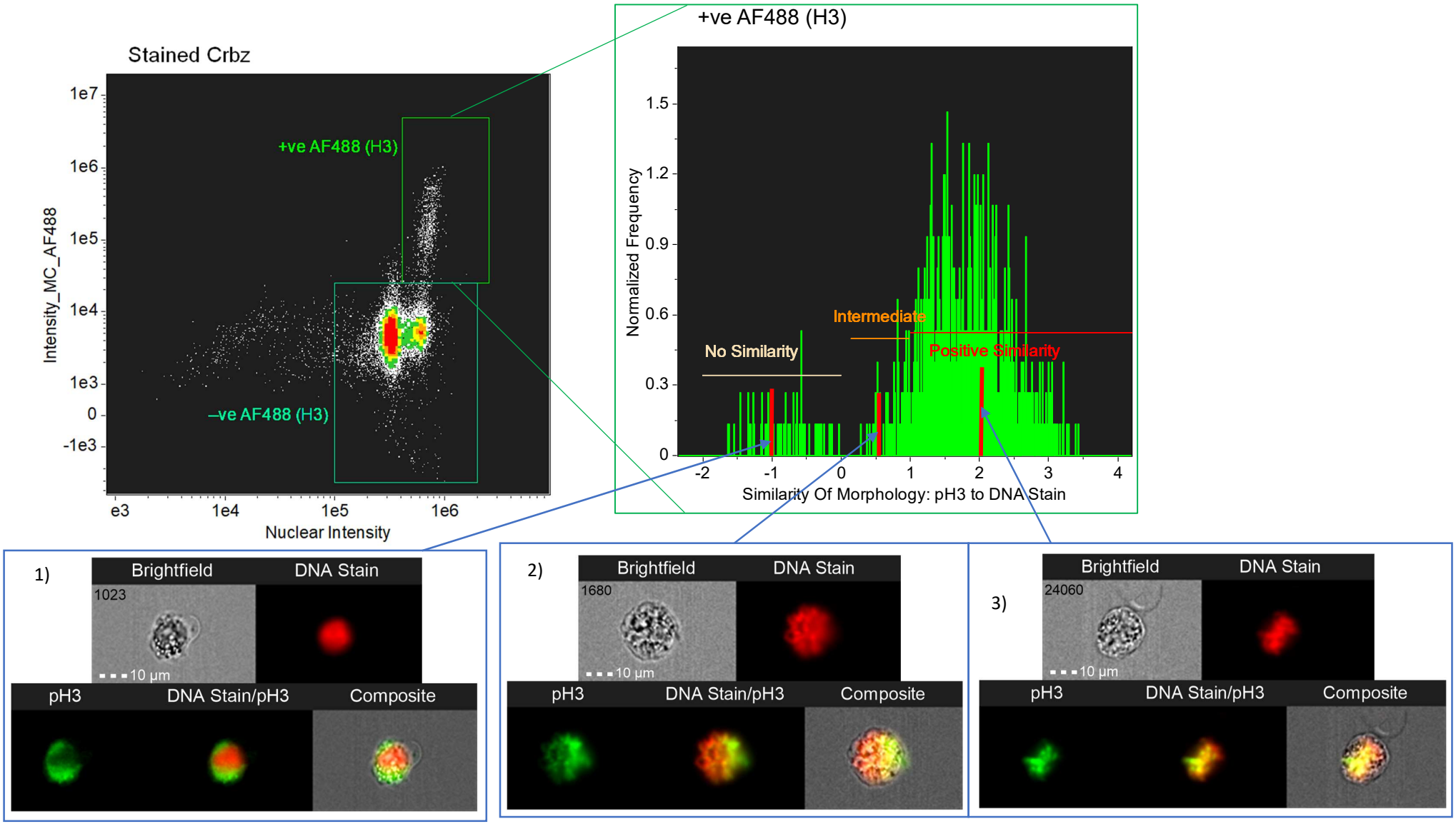

Figure 3.18: Refining pH3 populations to exclude AF and or off target binding. The use of an additional feature within the IDEAS® software termed 'Similarity' generates a histogram of a chosen population and plots how similar pH3 presence pixel location is to DNA stain pixel location. 1) Shows an example where pH3 signal appears to be present in the cytoplasm. 2) An example of partial similarity of pixel location, termed intermediate. 3) Giving an example of a cell with H3 signal that is most 'similar' to that of the nuclear stain.

Unlike in other assays where pH3 has been looked at the mitotic phase was not boosted by any additional chemical incubation i.e., with Colcemid as performed in Bryce *et al* 2007 for the assessment of hypo and hyper diploid metaphase cells. This means in control samples H3% is ~1-2%, for a more complete view of the mitotic portion of the cell cycle especially with the important role of phosphorylation and dephosphorylation of serine residues, other than the phosphorylation of the Serine28 looked at here, would identify cells in the later stages of mitosis after H3 S28 has been phosphorylated. This would not only provide a more comprehensive view of cells in the different phases of mitosis it would be interesting to see if chemical with different modes of action influence these different phosphorylation/acetylation etc events occurring during mitosis.

3.3.2.4 - PE P53 Cut Offs

The PE fluorophore is associated with an antibody that is specific for the N terminal of the P53 amino acid chain i.e., not the phosphorylated form of the tumour suppressing protein.

Maintaining methodology for gate generation has been kept as consistent as possible. However due to the less than optimal excitation of PE using the 488nm laser the separation of the emission spectrum is not as distinct as BV421 ɣH2AX and AF488 pH3 emission spectrum. After the compensation matrix was applied, the cell population used was deemed single and in focus but no other criteria was used to maintain as much of the cell population as possible to provide the best autofluorescence profile of each sample. The population was plotted on a histogram graph based on the intensity of available pixels found in channel three i.e., the channel the emission spectrum of the fluorophore PE falls in. The X axis is therefore labelled as Intensity_MC_PE displayed in log scale. The unstained peaks were averaged and 10fold increase gates were generated as per the BV421 ɣH2AX gating method. However, as a result of the reduced peak separation, unlike with BV421 ɣH2AX, only the Crbz stained peak was able to be averaged.

Figure 3.19a below demonstrates the maximum autofluorescence (AF) available of unstained samples exposed to the same laser intensities as the stained samples. These unstained samples provide a base line unstained (US) AF peak. A maximum autofluorescence gate was generated through assessment of cell bins found within the histogram, once these 'bin' populations dropped below two cells this was determined as the upper and lower boundary of the gate. Three smaller gates covering the main curve of the US peak were centralised at the base middle and top of the peak and averaged. This was performed on both Carbendazim and vehicle control DMSO US peak. The process was not performed on the MMS US peak as the AF was within the AF max unstained peak of Crbz as shown in graph e) of figure 3.19.

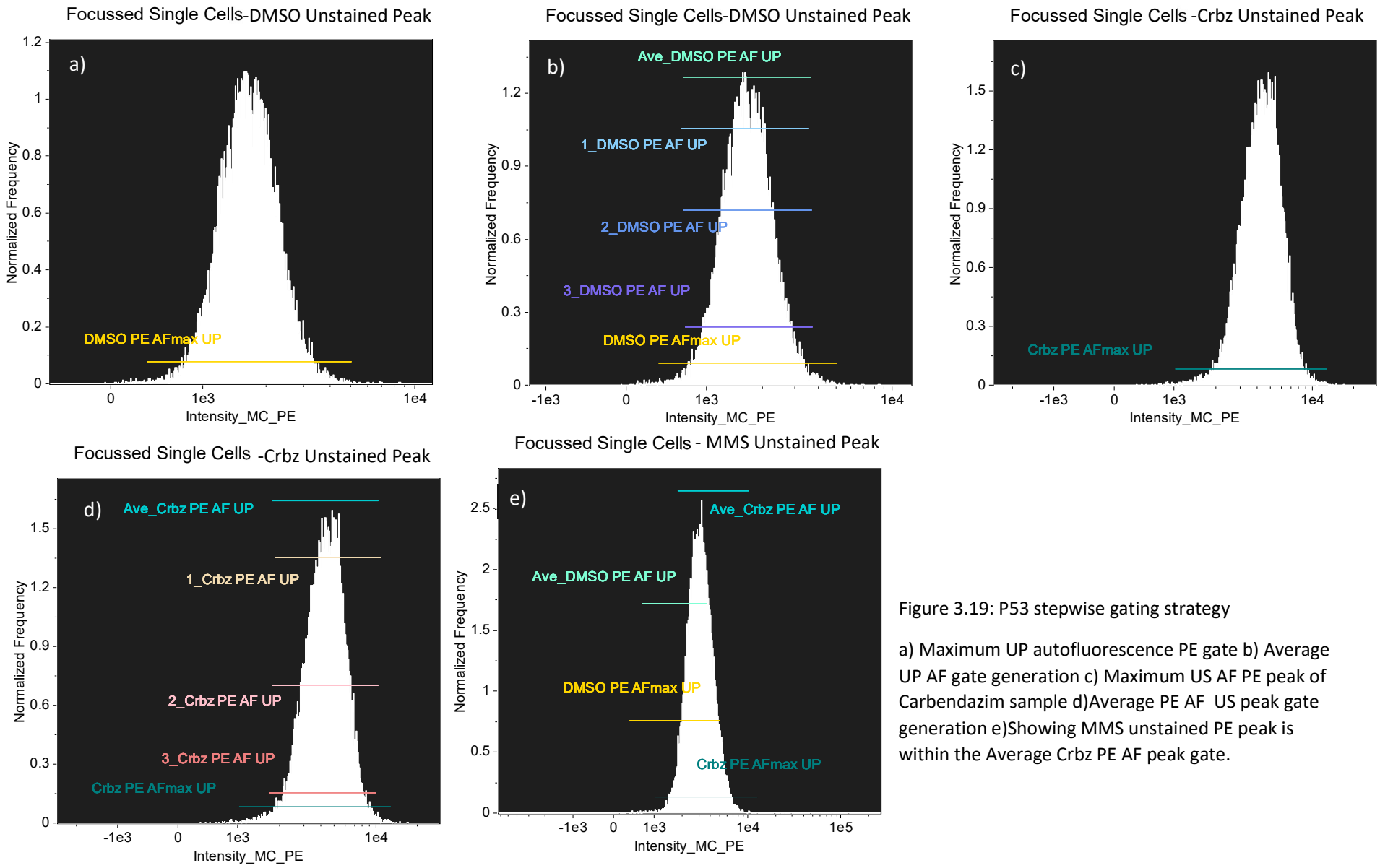

Figure 3.19: P53 stepwise gating strategy

a) Maximum UP autofluorescence PE gate b) Average UP AF gate generation c) Maximum US AF PE peak of Carbendazim sample d)Average PE AF US peak gate generation e)Showing MMS unstained PE peak is within the Average Crbz PE AF peak gate.

The stained histogram peaks of PE is displayed in figure 3.20. below. These histograms demonstrate the lack of a distinctly separate PE peak with both MMS and DMSO stained samples. The highlighted red area on graph 34a) identifies an area of the PE MMS primary peak that lies outside the PE DMSO primary peak, this being said the region is not distinct enough to qualify as a secondary peak. Development of the PE gates were therefore focused on the unstained DMSO and Carbendazim samples and the stained Carbendazim sample.

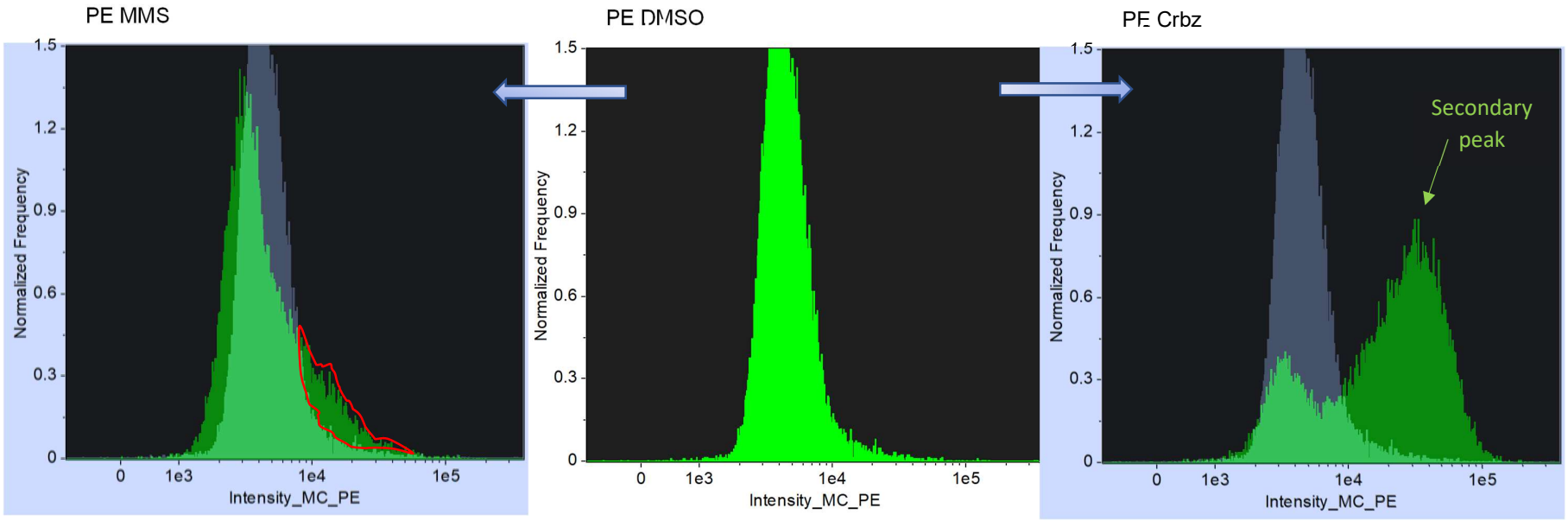

Figure 3.20: Demonstrates the stained PE peaks of negative vehicle DMSO and positive sample of the clastogen MMS and aneugen Carbendazim. The blue translucent peak is an overlay of the DMSO PE peak b) onto a) MMS stained peak and c) Carbendazim stained peak both in green. This demonstrates the lack of a distinct secondary peak in both a) and b) but a distinct secondary peak is present in c). The red drawn area on the MMS graph highlights the area that is outside the DMSO primary peak.

Having identified the average Carbendazim PE autofluorescence unstained peak (Ave_Crbz PE AF UP) in figure 3.19d) the lower and upper boundaries of the gate were multiplied by 10 to give the Carbendazim PE unstained peak 10 fold gate (Crbz PE UP 10F) as demonstrated in figure 3.21 graph a). The distinctive secondary peak of the stained Carbendazim sample was then averaged in a similar fashion as described for BV421 ɣH2AX making sure the lowest point was above the DMSO PE AFmax as demonstrated in figure 3.22.

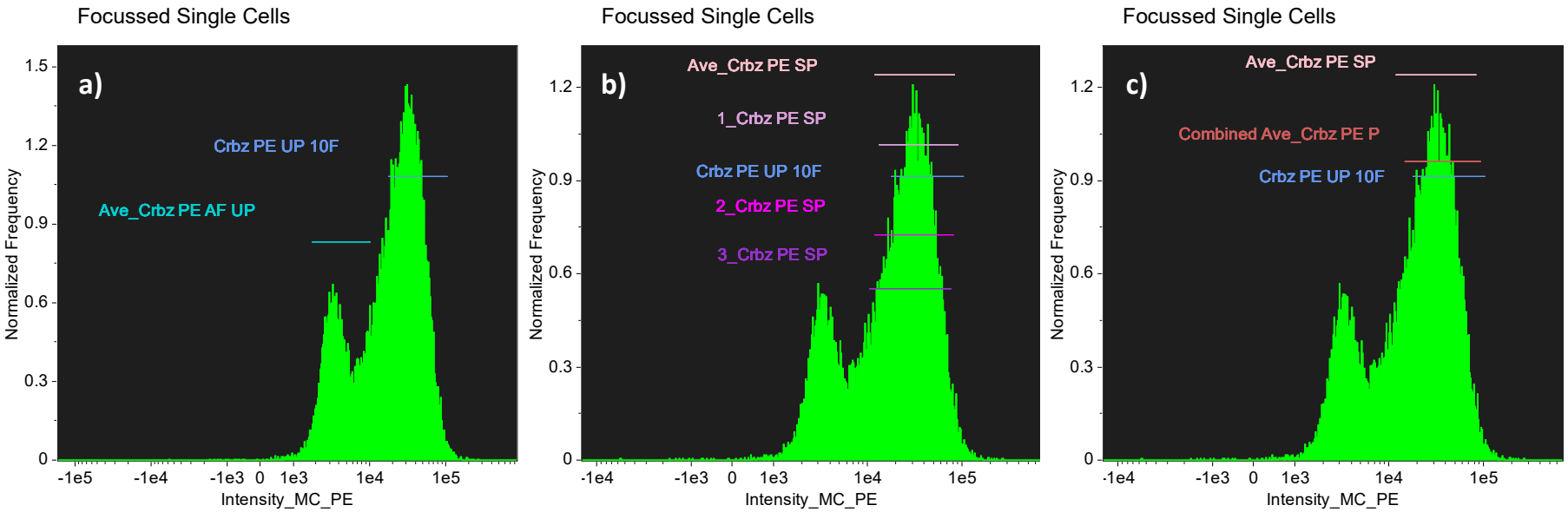

Figure 3.21: Demonstrating PE stained peaks of Carbendazim sample and secondary peak gating. a) 10 fold increase of Ave_Crbz PE AF UP; lower X boundary and Upper X boundary generating Crbz PE UP 10F gate. b) The three gates 1_/2_/3_ Crbz PE SP (Stained Peak) upper and lower X boundaries were added together and averaged to generate Ave_Crbz PE SP. c) Crbz PE UP 10F from a) was added to Ave_Crbz PE SP from b) and averaged as per section 3.2.5.2 and was termed Combined Ave_Crbz PE peak.

The Combined Ave_Crbz PE P gate takes into account both the estimated fluorescence of the Crbz PE UP 10F and the true stained fluorescence peak Ave_Crbz PE SP. At this point the value of the upper x boundary of this gate is irrelevant and it is the generation of the intermediate gate boundary and the lower x intercept boundary. Previously with BV421 ɣH2AX intermediate gate boundary this was determined using an combined average of DMSO stained and 10 fold gates and the overlap of these gates. As there is an absence of the distinct secondary peak for DMSO vehicle control PE stain the intermediate gate boundary was generated using and averaged of the lower X intercept of Combined Ave_ Crbz PE P gate and the upper X intercept of DMSO PE UP 10F gate as demonstrated by figure 3.22 graphs a) through c). This generated the lowest x intercept of the gate termed ++PE(P53 gate) this x intercept also becomes the upper x intercept of the gate termed +PE(P53 gate).

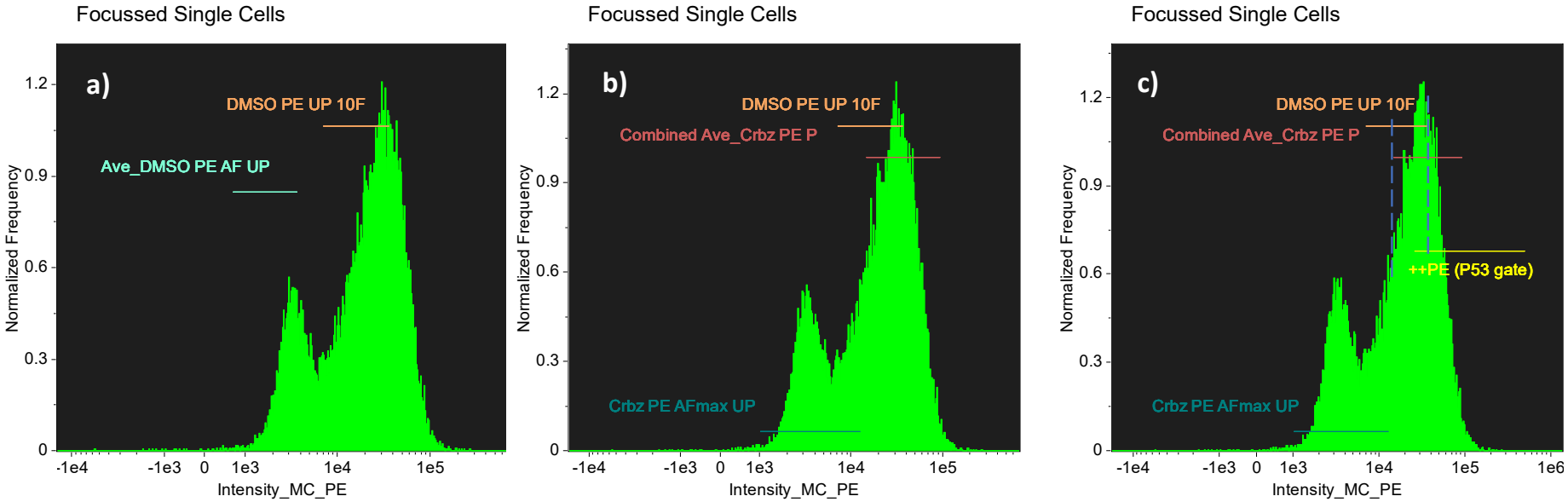

Figure 3.22: Histogram demonstrating the generation of the ++PE (P53 gate). a) The upper and lower bound x intercepts of the Ave_DMSO PE AF UP gate multiplied by 10 gives the DMSO PE UP 10F gate as an estimation of the true fluorescence of PE. b) Intermediate graph demonstrating the DMSO PE UP 10F gate and the Combined Ave_Crbz PE P gate. c) The dashes blue lines highlight the overlap between the Combined Ave and DMSO 10F gates. The lower x intercept of the former and upper x intercept of the latter were averaged to generate the lowest boundary of ++PE(P53 gate) .

To determine the lowest boundary of the +PE (P53 gate) in lou of having a secondary true fluorescence peak available for DMSO a value of 10% less than the Crbz Pe AFmax UP upper x intercept, this is demonstrated in figure 3.23 below.

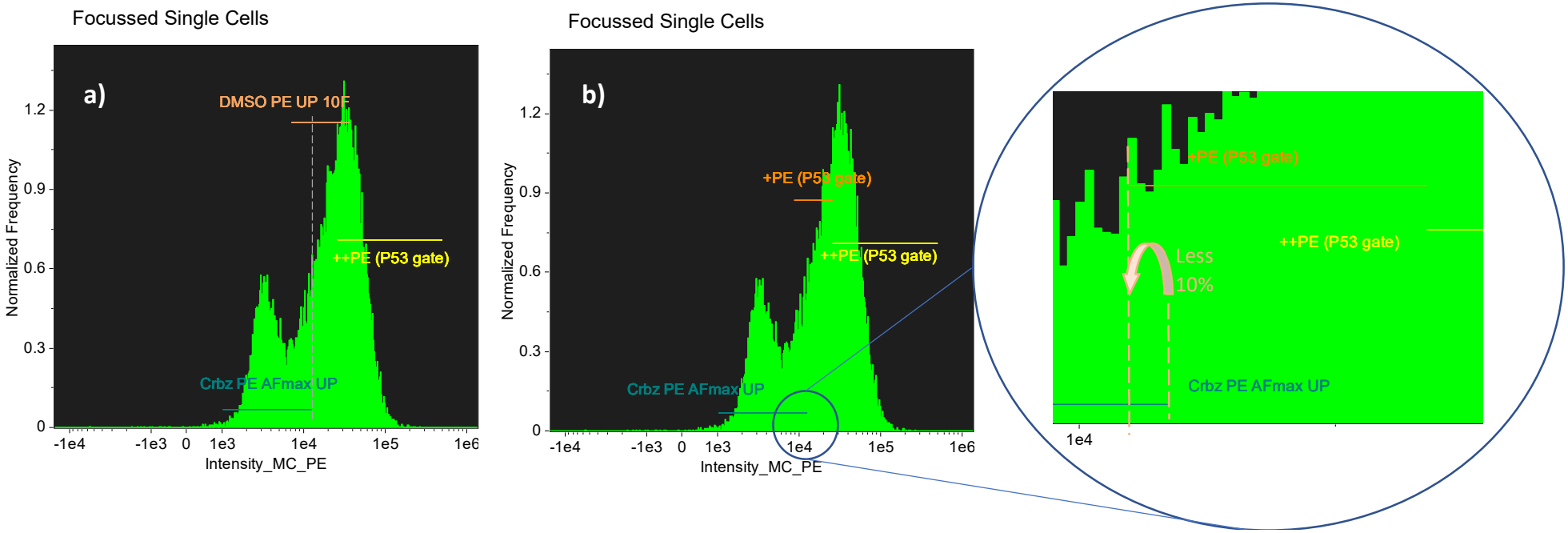

Figure 3.23: Demonstrating generation of lower boundary of +PE (P53 gate). a) Graph demonstrating the overlap of the Crbz PE AFmax UP and DMSO 10F gate. b) Demonstrates the removal of 10% of the upper Crbz PE AFmax UP boundary to generate the lower +PE(P53 gate) boundary.

3.3.2.5 – Gating Strategy Overview and Final Gating Boundaries

Flow Chart overview: Gating procedure

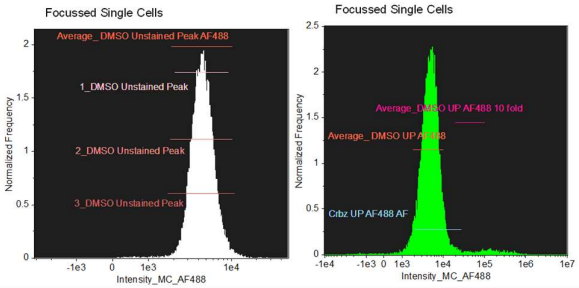

- Average autofluorescence of unstained peak assessed
- Gate multiplied by 10 generating 10fold gate of estimated fluorescence

The unstained sample is important to help identify true fluorescence over background autofluorescence. This helps minimise scoring of false signal which can become important when chemicals are borderline positive/negative.

Use of averaging allows for variability across samples.

Using the 10 fold gate helps mitigate potential unconscious bias

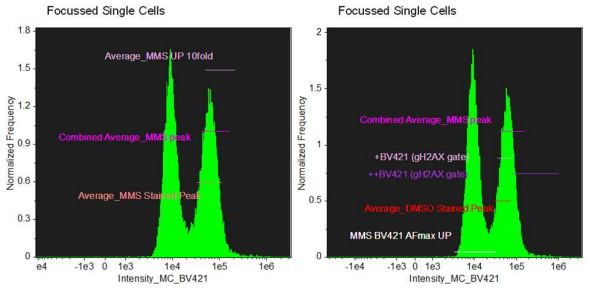

- Where a distinct secondary peak of positively stained cells available
  - Average of stained peak generated
- Where applicable a combined average gate of true fluorescence stained peak and 10 fold estimated fluorescence is generated
- Overlap of vehicle control and positive control gates are used to determine intermediate and lower gate boundaries

Through combining vehicle control and positive control samples in generating the gates this allows for excluding as much background fluorescence as possible whilst still trying to include the lower/weaker available true fluorescence signal.

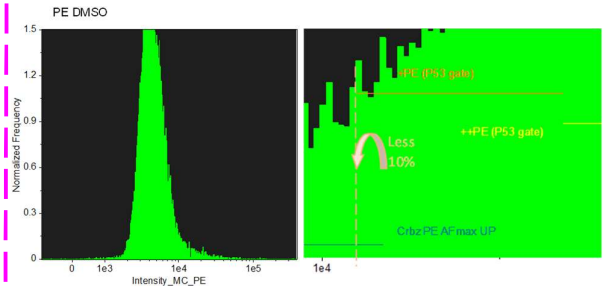

- In the absence of a distinct secondary true fluorescence stained peak to identify the lowest gate boundary
- 10% lower than the AFmax upper boundary is used

In the absence of a distinct secondary peak 10% of the upper x intercept of the AFmax provides a similar role as the combining of the vehicle control and positive control gates. i.e. Excluding as much background fluorescence as possible whilst still trying to include the lower/weaker available true fluorescence signal.

Regardless of the lowest boundary cut off generation method, this boundary should be ≥ 10% higher than the upper boundary of the average unstained autofluorescence peak

For the sake of robustness and to minimise inclusion of background fluorescence that may still be included using this gating method. When markers are known biologically to only be found in the nucleus use of similarity morphology feature is employed. This allows for removal of cells from the positively gated population where fluorescence is detected in the cytoplasm, the criteria of these cells is falls below zero.

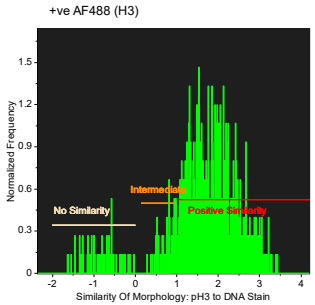

The above process demonstrates how for each parameter (pH3, ɣH2AX and P53) the gating boundary cut offs were determined. These X coordinates of +Bv421, ++BV421, +PE, ++PE and +veAf488 were applied to scatter graphs on the Y axis, the X axis coordinates were then chosen based on the DNA content histogram. These gates were then termed +Bv421 = gH2AX+, ++BV421 = gH2AX++, +PE = P53+, ++PE = P53++ and +veAf488 = pH3 +VE. The applied gates and their coordinates are shown in figure 3.24.

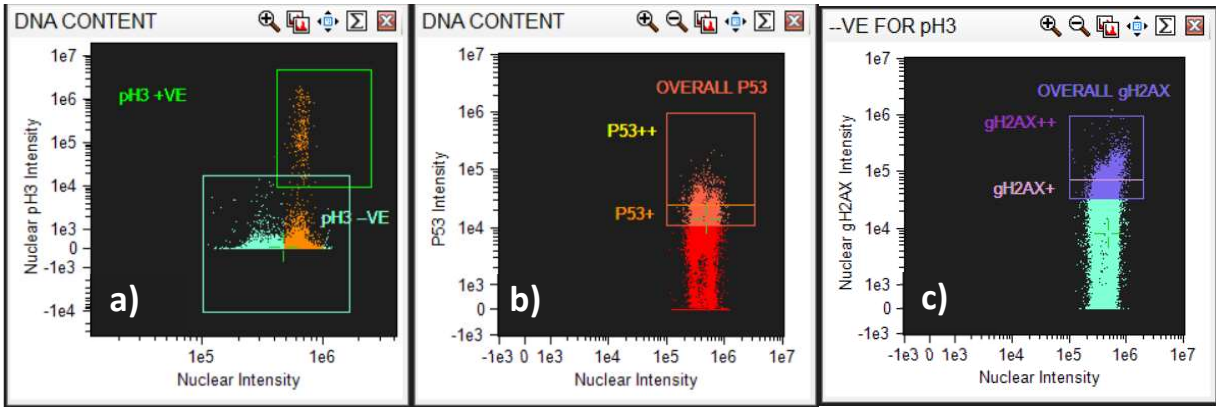

Figure 3.24: Finalised gating cut off points for the biomarkers pH3, P53 and ɣH2AX. a) pH3+VE (Green Gate) : Upper left (x) 4.2^5, (y) 5^6, upper right (x) 2.5^6, (y) 5^6, lower left (x) 4.2^5, (y) 1^4, Lower right (x) 2.5^6, (y) 1^4. pH3+VE gated population was used to generate pH3 response data and to assess proportion of cells in mitosis phases. b) P53+ (Orange gate): Lower left (x) 1^5, (y) 1.14^4, Lower right (x) 3.19^6, (y) 1.14^4. Upper left (x)1^5 (y)2.56^4. Upper right (x)3.19^6 (y)2.56^4. P53++ (Yellow gate) Lower left (x) 1^5, (y) 2.56^4. Lower right (x) 3.19^6, (y) 2.56^4. Upper left (x)1^5 (y)1^6. Upper right (x)3.19^6 (y)1^6. OVERALL P53 (Coral gate) uses the upper coordinates of P53++ and lower coordinates of P53+. The overall gate for P53 was used to generate the cell response results for P53. c) gH2AX+ (pink gate): Lower left (x) 1^5, (y) 3.41^4, Lower right (x) 2^6, (y) 3.41^4. Upper left (x)1^5 (y)7.54^4. Upper right (x)3.19^6 (y)7.54^4. gH2AX++ (Purple gate) Lower left (x)1^5 (y)7.54^4. Lower right (x)2^6 (y)7.54^4. Upper left (x)1^5 (y)2.5^6. Upper right (x)2^6 (y)2.5^6. OVERALL gH2AX (Lilac gate) uses the upper coordinates of gH2AX++ and lower coordinates of gH2AX+. The population used to generate H2AX response was gH2AX++ gate. The population used to assess the H2AX response is the pH3 -VE cell population gated in light blue on graph a).

The described gates were applied to all graphs that looked at biomarker fluorescence intensity, the gating boundaries maintained across all graphs and all chemicals that were tested using the ‘optimal’ ISMN multiplex expansion assay method obtained on the ImageStream® X Mark II. To generate the features displayed on the x and y axis’ in figure a series of defined masks and features for fluorescence analysis were used to set up a template based approach for chemical assessment.

3.3.3 - Masks and Features

The IDEAS® 6.2 software relies on a system of masking pixels and then measuring a series of morphology intensity shape and texture features within those masks to generate graphs to generate data not only based on fluorescence intensity but also spatial location. The masks that the system automatically applies to each of the 12 channels are generic but specific to any emission that falls within those channels. These masks can be refined to generate more accurate data sets relevant to the biology of the response being looked at whilst removing background from potential debris. The following describes the steps taken to generate specific masks for cytoplasm, nuclear DNA, ɣH2AX, pH3 and P53 signal based on the stain DRAQ5™ (signal collected in channel 11) Brilliant violet 421 (Signal collected in channel 7) Alexa Fluor488 (signal collected in channel 2) and PE (signal collected in channel 3).

The two masks generated for nuclear and cytoplasmic assessment provide the basis for refining the biomarker populations by making the selection process for pixels assessed by the system more robust. This is done through the mask manager and 'Defining mask function' in the IDEAS® software. Once the mask input meets the criteria for your assessment, whether that be texture, shape, intensity, spot counting etc you can then layer the masks using Boolean logic i.e., 'this AND this BUT NOT this' 'this Or this AND this'. System features can then be generated based on your designated masks to make your analysis more sensitive and specific.

Masks can be complex or simple. When a biomarker such as ɣH2AX and pH3 are known only to be located in relation to nuclear DNA both masks can be as direct as ɣH2AX and DRAQ5™ but not Cytoplasm the same logic can also be used for pH3. These masks are basically saying that the fluorescence intensity of interest is that which is directly associated with the pixels of the DRAQ5™ stain. This helps reduce the potential for identifying off-target antibody binding and including it in the data analysis populations. The steps for how both these masks were generated, and the ensuing features used to help build the overall IDEAS® template are outlined below in figures 3.25 through to 3.43.

3.3.3.1 - Cytoplasmic Mask and The Features That Use It

New masks can be added in the Define Mask function and from these masks the rest of the data analysis features can be derived. The first mask to be refined is the brightfield mask. Criteria in this mask will then be used to separate out cell population that are single, round and in focus

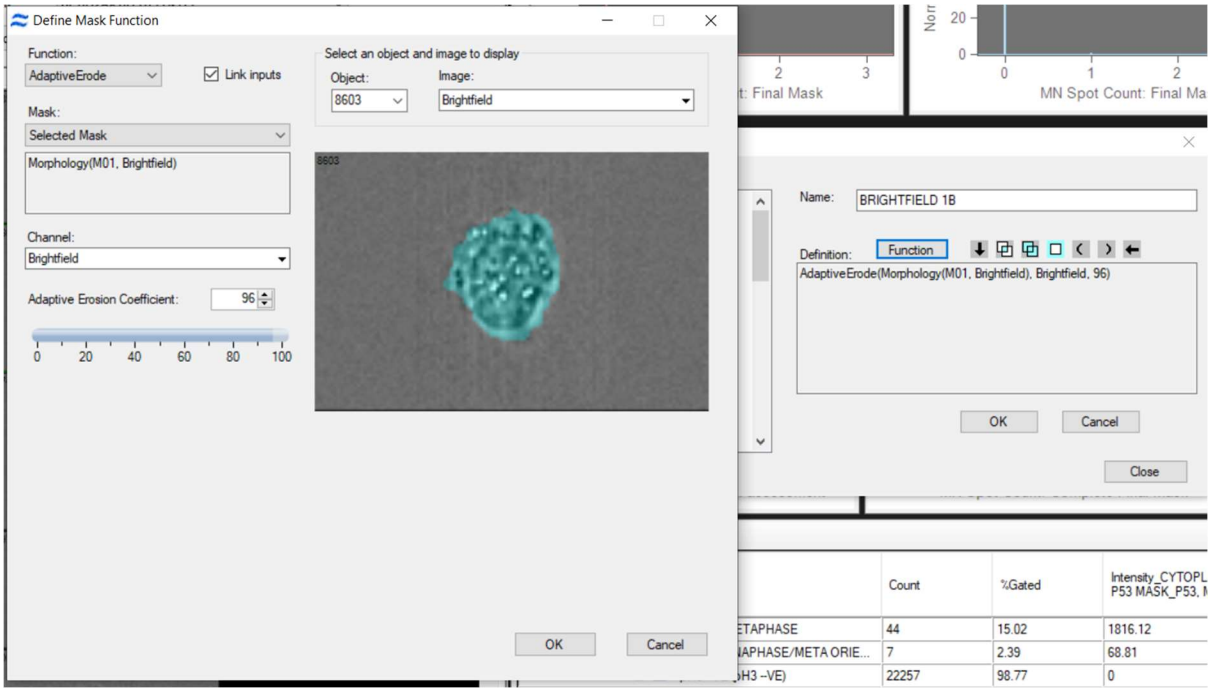

Figure 3.25: Demonstrating the function rules used to designate brightfield image mask criteria.

Use of the morphology function includes pixels at the outer most edge of the image and is recommended by IDEAS® manual when shape is an important aspect to be taken into account. This combined with the adaptive erode function further taking shape into account removes pixels from the boundary of the morphology input. This refines the mask morphology to be more consistent with the brightfield image as shown in figure 3.25 above. The more similar the brightfield mask to the actual shape of the cell image the more effective the ensuing features used in the IDEAS® template will be.

Brightfield masks 1A and 1B use the same mask function inputs, figure 3.26. Separate masks are required when using multiple area and texture features for the same mask in an individual channel otherwise the system will not auto populate, and population acquisition will be incorrect.

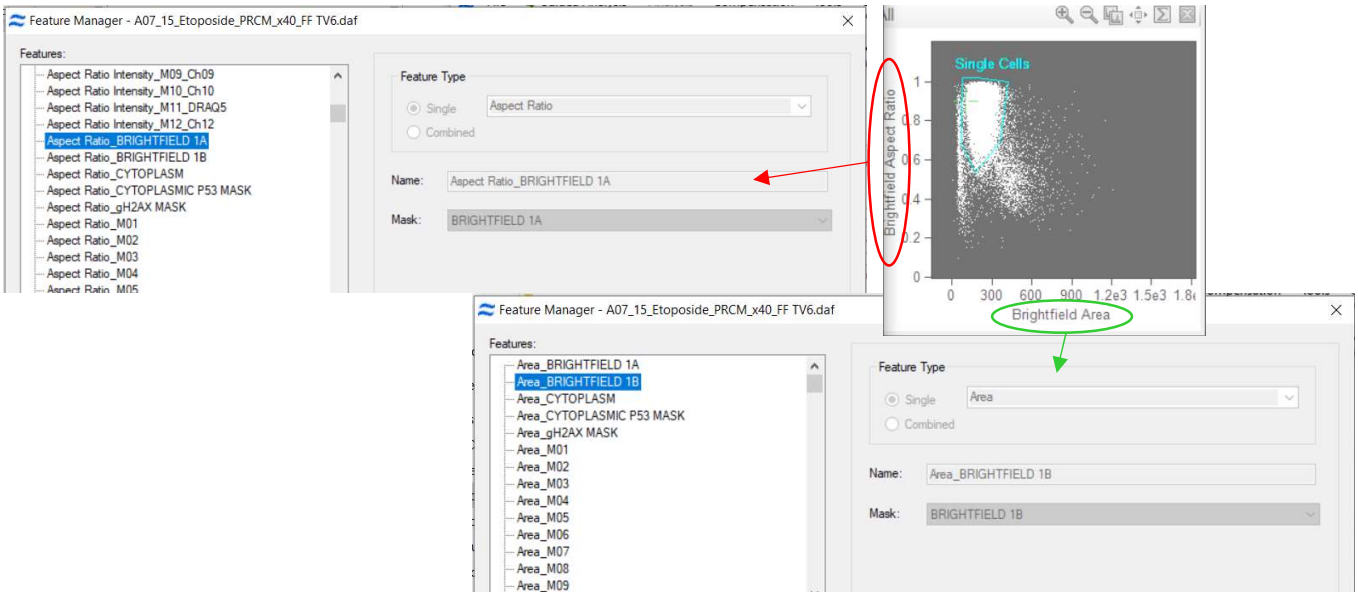

Figure 3.26: Brightfield 1A (highlighted by red arrow) and Brightfield 1B (highlighted by green arrow) masks used to generate aspect ratio and area scatter graph, on the y and x axis respectively, for round and single cell assessment.

Aspect Ratio feature tells us how round an object is, and area tells us how large the object is i.e., the combination of the two features will give us a single cell reasonable round population. This is displayed in figure 3.27 below. Cells that are in the gated blue area are termed single cells and meet the criteria of having a aspect ratio of >~0.6 and brightfield area of >~70 but <~450 this is consistent with other ImageStream analysis settings in literature (Verma *et al*., 2018; Rodriguez *et al*., 2018; Filby *et al*., 2016). This single round cell population is then taken forward to assess focus.

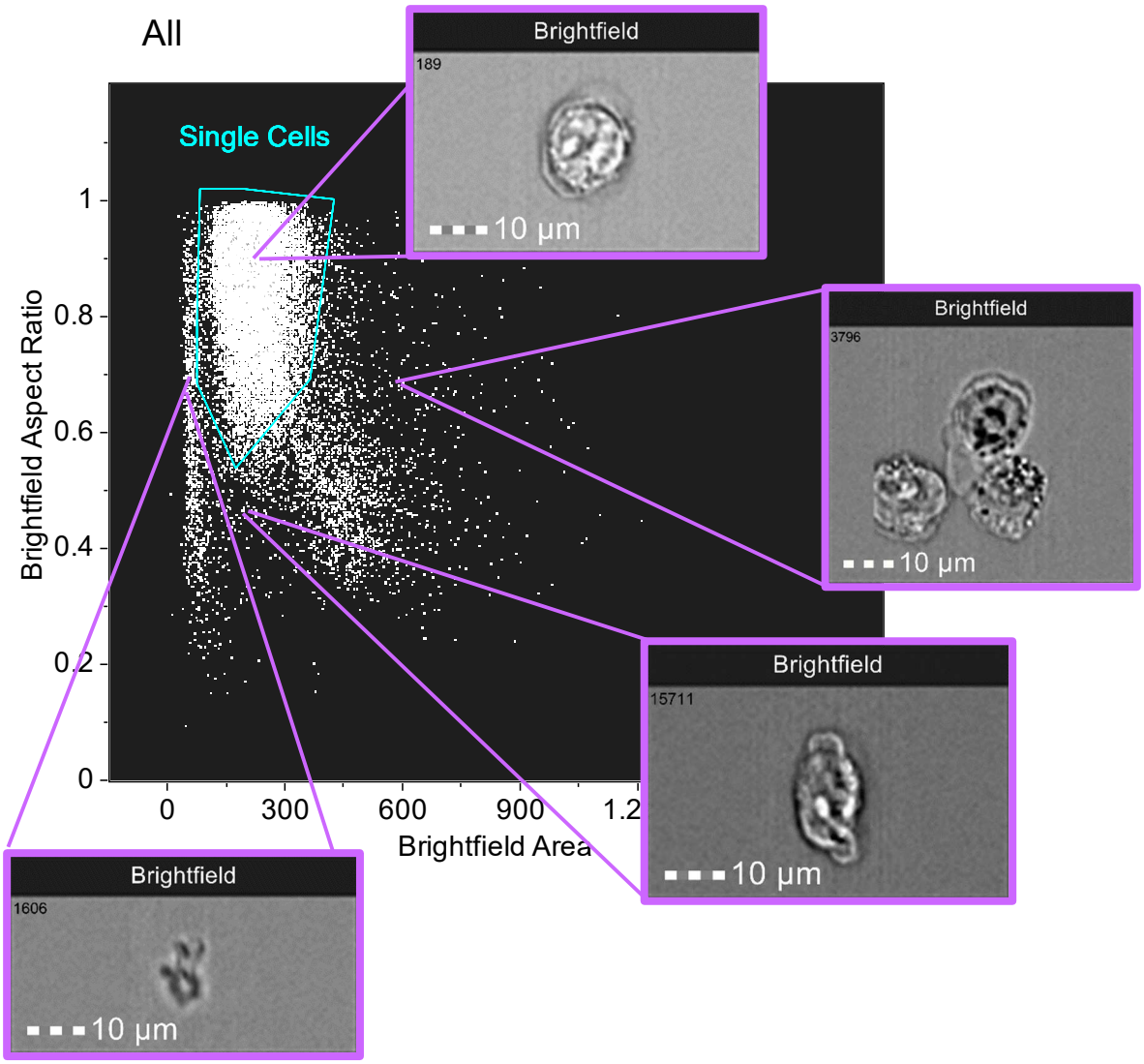

Figure 3.27: Example plot of the gating of single round cells with corresponding scatter point brightfield imagery that fall outside of the gated area, demonstrating correct population selection.

The next step to get to the working population for analysis is assessing image focus. The more focus the population the better the masks and features work. Using the same Brightfield 1A mask use of the gradient Root Mean Square (RMS) feature generates a histogram. A gate is then applied to the graph designating a single in focus cell population. This is demonstrated in Figure 3.28.

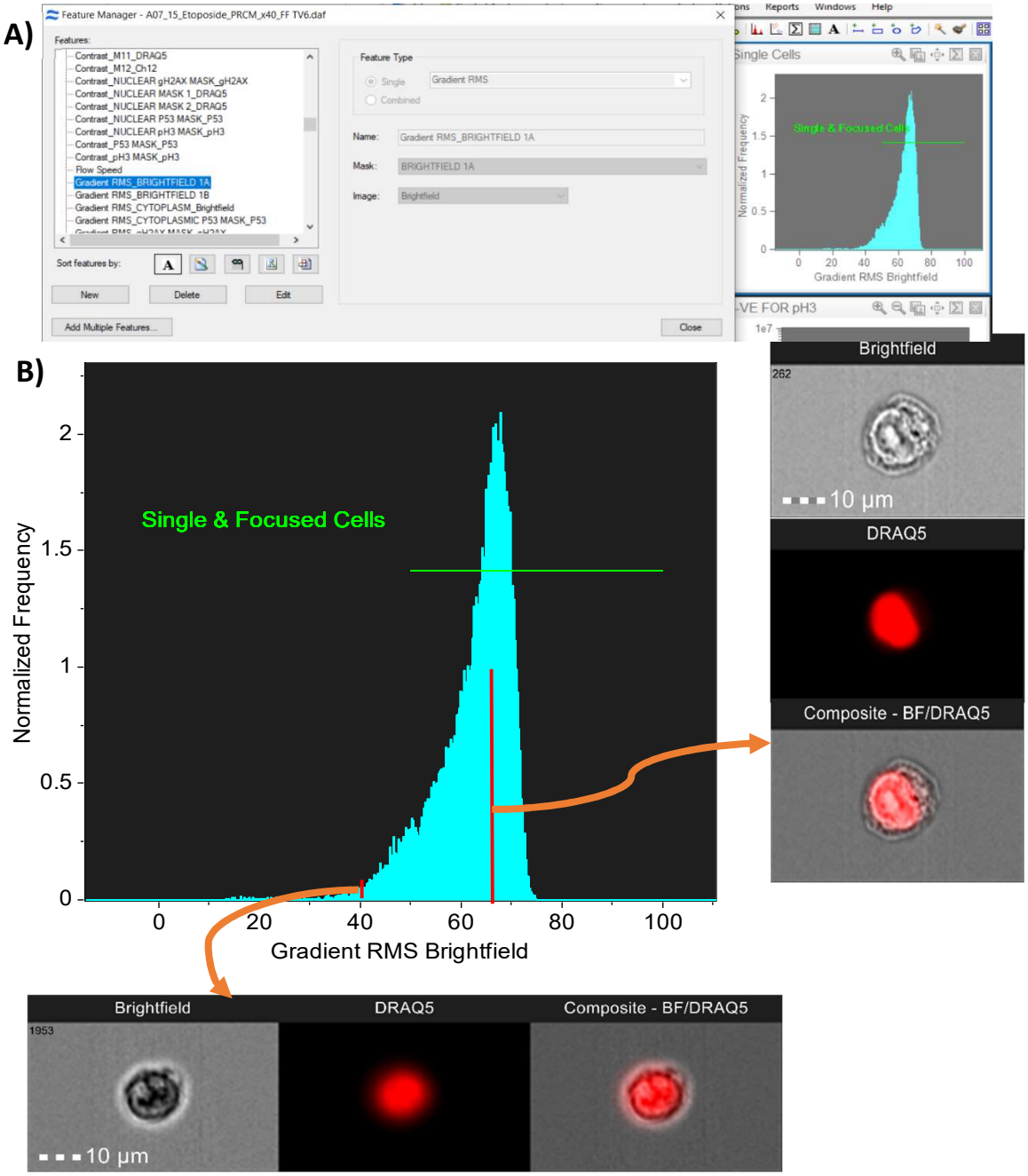

Figure 3.28: Generation of in focus cell population from single cell population. A) shows the feature selection to generate the 'in focus histogram. B) Example of the focus histogram and corresponding images found in the selected 'bin'. The higher the gradient RMS the more in focus the object image. Anything less than 50 was considered too out of focus for assessment. The highlighted red bins indicate the cell grouping the images displayed were taken from showing the differences between in focus and out

The single in focus cell population was then used to determine health of cells being analysed this was done by generating a cytoplasmic mask and following the feature steps used in the apoptosis wizard. The cytoplasmic mask was generated by using the

same mask functions as Brightfield 1A/B as described above combined with a nuclear mask using Boolean logic (Figure 3.29). Nuclear mask 2 that was used to generate this cytoplasmic mask is explained in section 3.3.3.2.2 below.

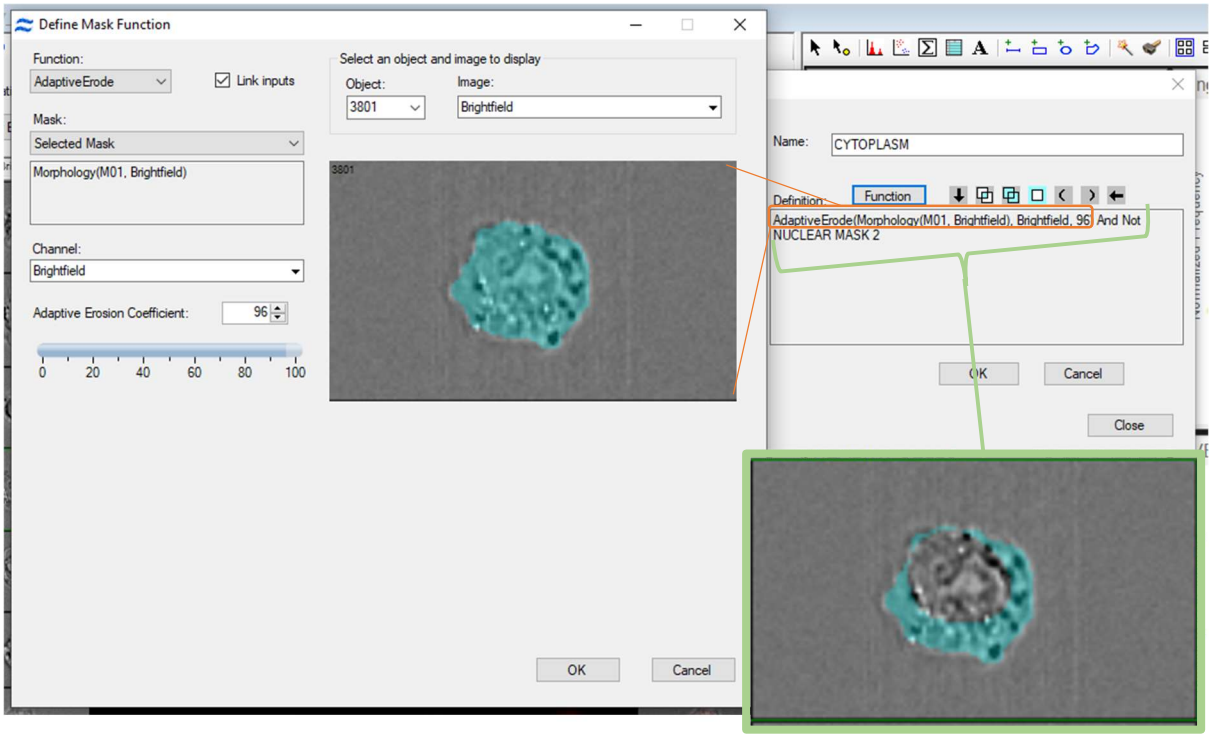

Figure 3.29: Demonstrates the specific cytoplasmic mask generated when the nuclear mask based on DRAQ5 signal is excluded from analysis.

Use of the Contrast feature with the cytoplasmic mask. This is a texture feature that assess sharpness quality. The higher the contrast the more likely the cell is to be unhealthy assessment of cytoplasmic contrast is a feature commonly used in manual microscopy to assess cell health. Further explanation of the generation of the healthy cell population will continue in the nuclear mask section below. Due to the nature of the P53 antibody being used for these experiments' detection of stabilised P53 in the cytoplasm is possible. This is due as explained above to the antibody binding to the N terminal of P53 protein rather than in response to its phosphorylation. The cytoplasmic P53 mask was generated as shown in figure 3.30.

A)

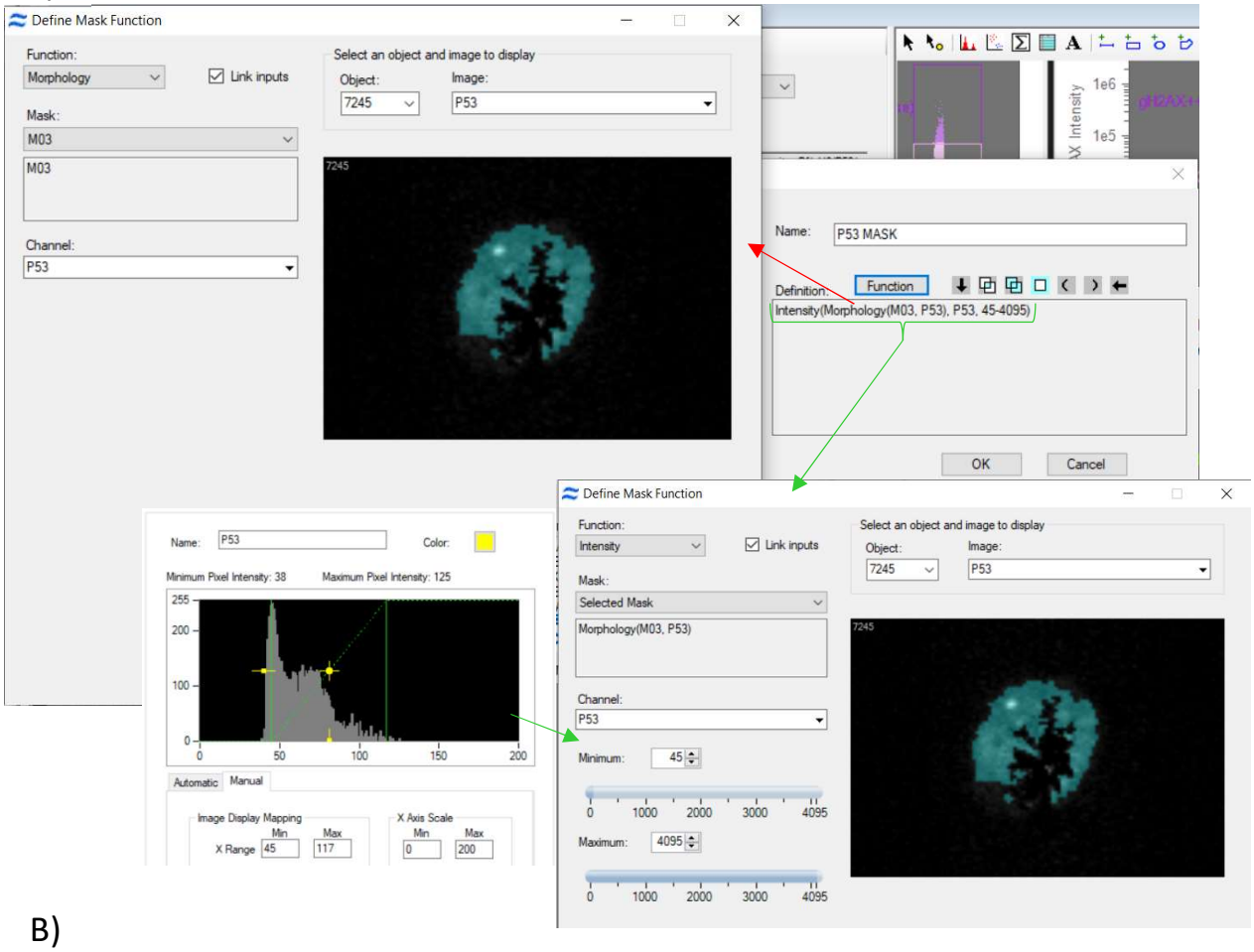

B)

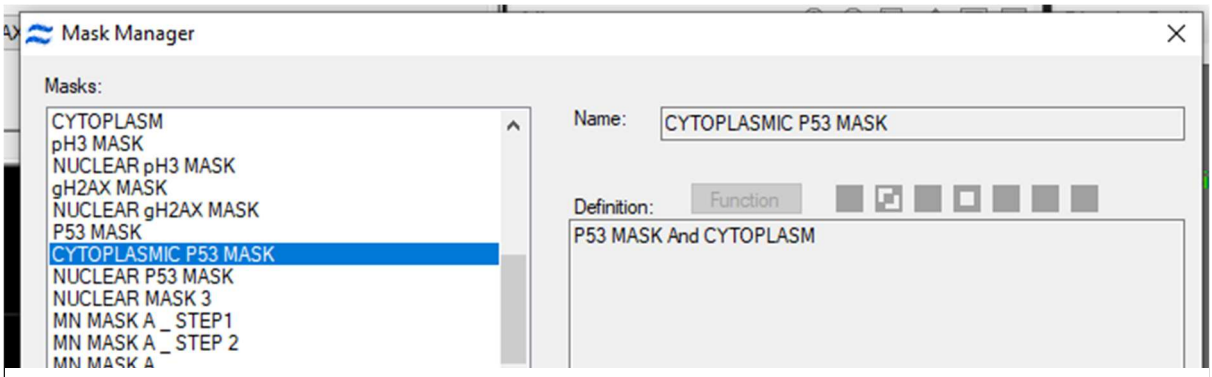

Figure 3.30: Function use for P53 mask generation and P53 cytoplasmic mask generation. A) Morphology mask (identified by red arrow) was used to identify shape of P53 fluorescence and intensity (green arrows) was used to exclude potential background. Use of the P53 pixel intensity histogram allowed the minimum pixel intensity to be selected. B) Using Boolean logic, the P53 mask was combined with the cytoplasmic mask. This allowed for specific location assessment of P53.

For P53 mask generation the morphology feature was used to assess the shape/spatial location of P53 this combined with intensity range of 45 – 4206 relative fluorescent units of pixel intensity generates the P53 mask based on shape and intensity. The lowest value of 45 was chosen as anything less than 30-40 pixel intensity units is not considered true fluorescence rather just background noise (Filby *et al*., 2016; Patterson *et al*., 2015). Using the P53 mask combined with the Cytoplasm mask the Cytoplasmic P53 mask is generated and can be used to assess P53 fluorescence in the cytoplasm. Whilst this feature has been applied in the template to assess cytoplasmic P53 compared to nuclear P53 giving the ability to assess P53 intensity ratios based on translocated vs untranslated this metric has not been assessed as part of this thesis.

3.3.3.2 - Nuclear Mask, The Features That Use It and Refining Biomarker Signal

Three different nuclear masks were used in the processing of the collected data sets. The masks were termed Nuclear Mask 1, Nuclear Mask 2 and Nuclear Mask 3, an example of the masks is displayed in figure 3.31 below.

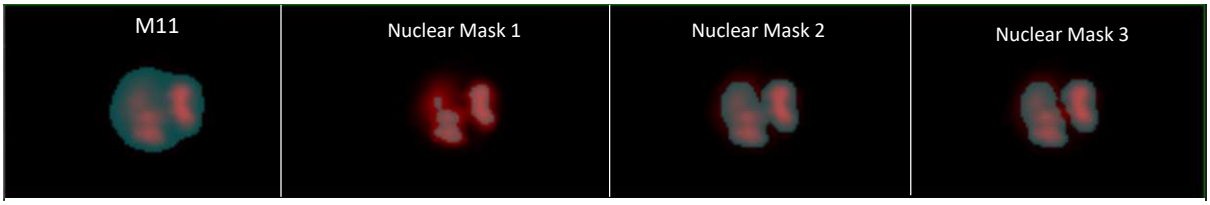

Figure 3.31: Same cell demonstrating the different nuclear masks used in template feature generation. Captured in channel 11 the Draq5 nuclear stain of a single cell is displayed. Each column shows the exact same cell the differences being the criteria the system is looking at in various relationships of size shape and intensities, demonstrated as a blue overlay. M11 merely shows the generic default mask used to detect signal by the system. The mask differences between nuclear mask 1, 2 and 3 allow for different features to be assessed. Nuclear Mask 1 was used to help determine 'Healthy' cell population. Nuclear Mask 2 was the predominant mask used for cell cycle and similarity assessment as it best matches the generalised overall shape of the nuclear staining. Nuclear mask 3 was used to help identify potential binucleates for assessment of mononucleate MN and mitotic stage analysis.

3.3.3.2.1 - Nuclear Mask 1

The first termed Nuclear Mask 1 was used to help identify the Healthy Cell population i.e., non-apoptotic/necrotic. This mask uses a 50% threshold feature that only allows the system to look at the top 50% of the highest intensity pixels. Whilst this is the same mask that is generated by IDEAS® software 'Apoptosis Wizard' this mask also includes a range feature that excludes nuclear bodies with less than 50 pixels (12um) from being looked at, this was to try and prevent MN events being excluded from the healthy population as being identified as apoptotic (figure 3.32).

a)

b)

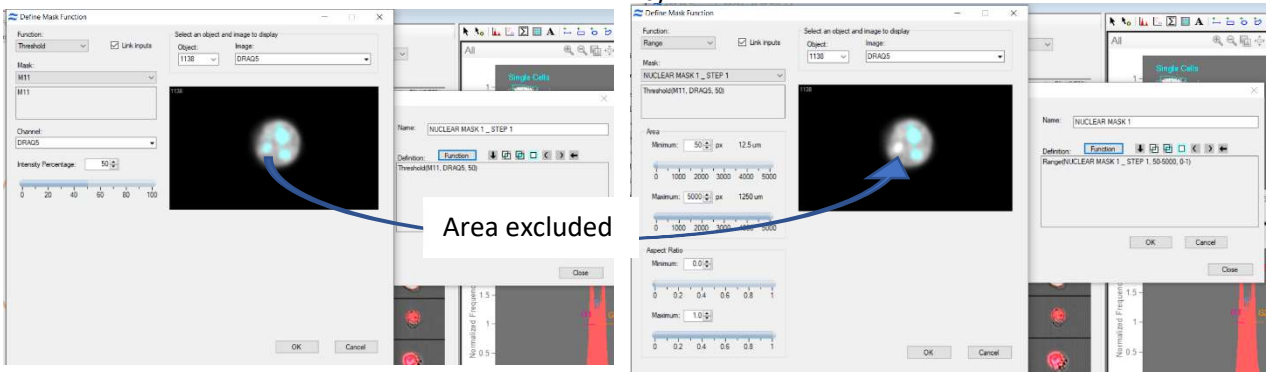

Figure 3.32: Nuclear mask 1 generation. a) Shows the 50% threshold mask that demonstrates the nuclear stain as being contrasting and only certain pixels meet the 50% highest intensity criteria. b) Using a minimum area of 50pixels (equivalent to 12.5um) a area of staining that were it outside be counted as a MN is removed from the apoptotic assessment so healthy MN cells are not removed from the analysis population.

Combining nuclear area of the Nuclear 1 Mask with the cytoplasmic contrast feature as explained in section 3.3.3.1 Above allows the assessment of a healthy cell population as recommended by the IDEAS® manual and in experimental literature that healthy cells have a high nuclear area with pixels that meet the 50% threshold intensity and low cytoplasmic contrast (Rodriguez *et al*., 2018; Rodriguez., 2018; Filby *et al*., 2011; Filby *et al*.,2016). Figure 3.33 below shows the relative cell brightfield and corresponding DNA staining in relation to scatter points that either fall within the 'Healthy Cells' gate or outside it. Whilst it could be considered that a larger nuclear area above say 150 on the scale could be so dispersed that the nucleus has degraded and is dispersing, due to the large area of cellular nuclei when in mitosis the higher nuclear area cells were kept in the population taken forward.

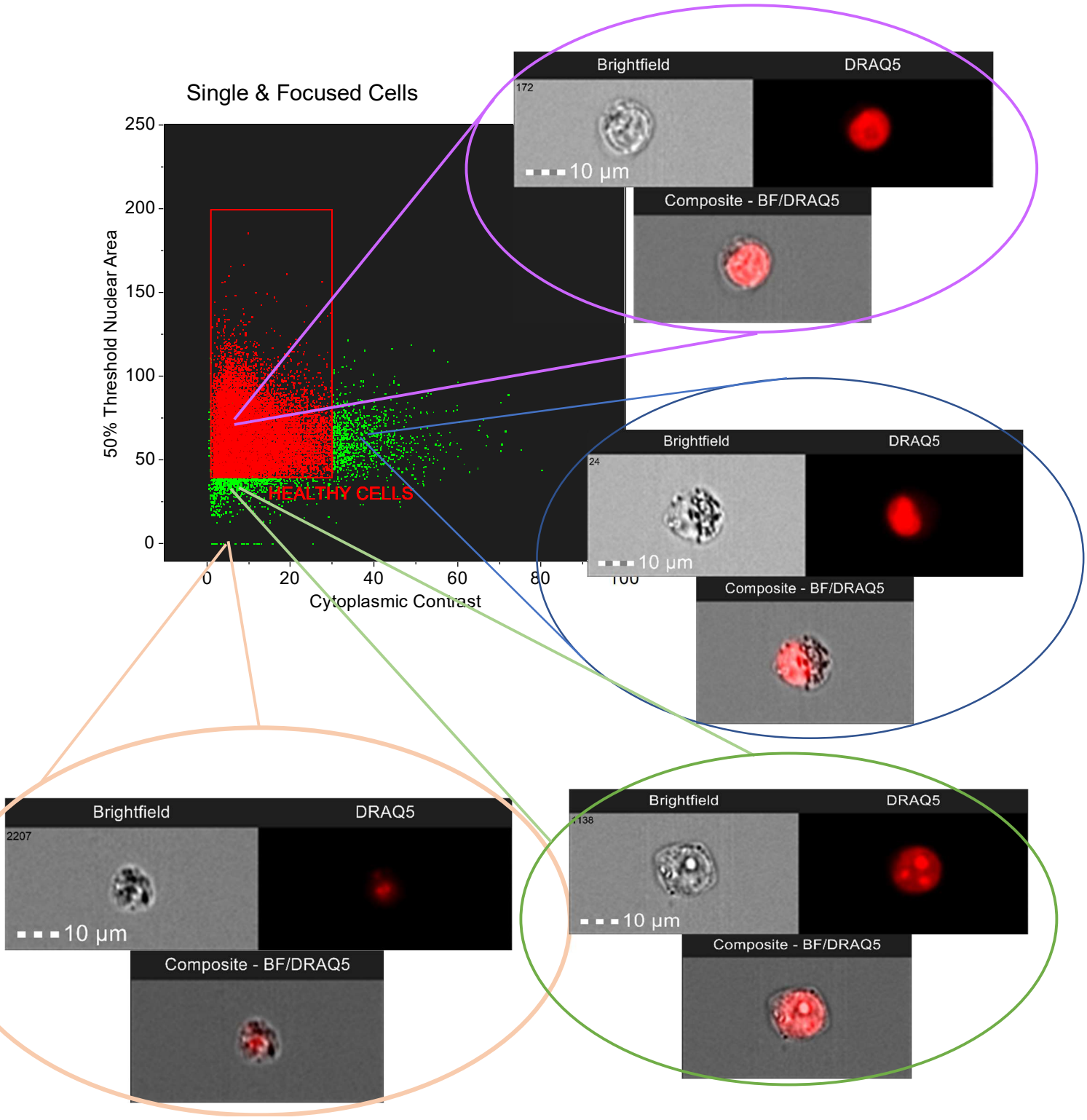

Figure 3.33: Example graph showing the Healthy Cells gate in red that will select cells to be taken forward to the next stage of DNA content assessment (optimal master population). A scatter point location at the main points outside of the gate show examples of the main type of cell that is able to be excluded as not healthy from the cell population.

Cells therefore that have a nuclear intensity (DRAQ5™ stained) area of greater than 40 when looking at the top 50% of pixel intensity but a cytoplasmic contrast of less than 30 are gated as 'Healthy Cells'. Without the use of additional viability stains or using a cleaved PARP indicator to identify apoptosis activation there cannot be a 100% certainty that all apoptotic/necrotic cells are excluded from analysis, it does remove the most distinctly compromised cells.

Nuclear mask 1 is also used in combination with a spot count and nuclear aspect ratio to assess mitosis stage of positive pH3 cells.

3.3.3.2.2 - Nuclear Mask 2

The second nuclear mask, the template attempts to match the morphology of the DRAQ5™ stain as closely as possible

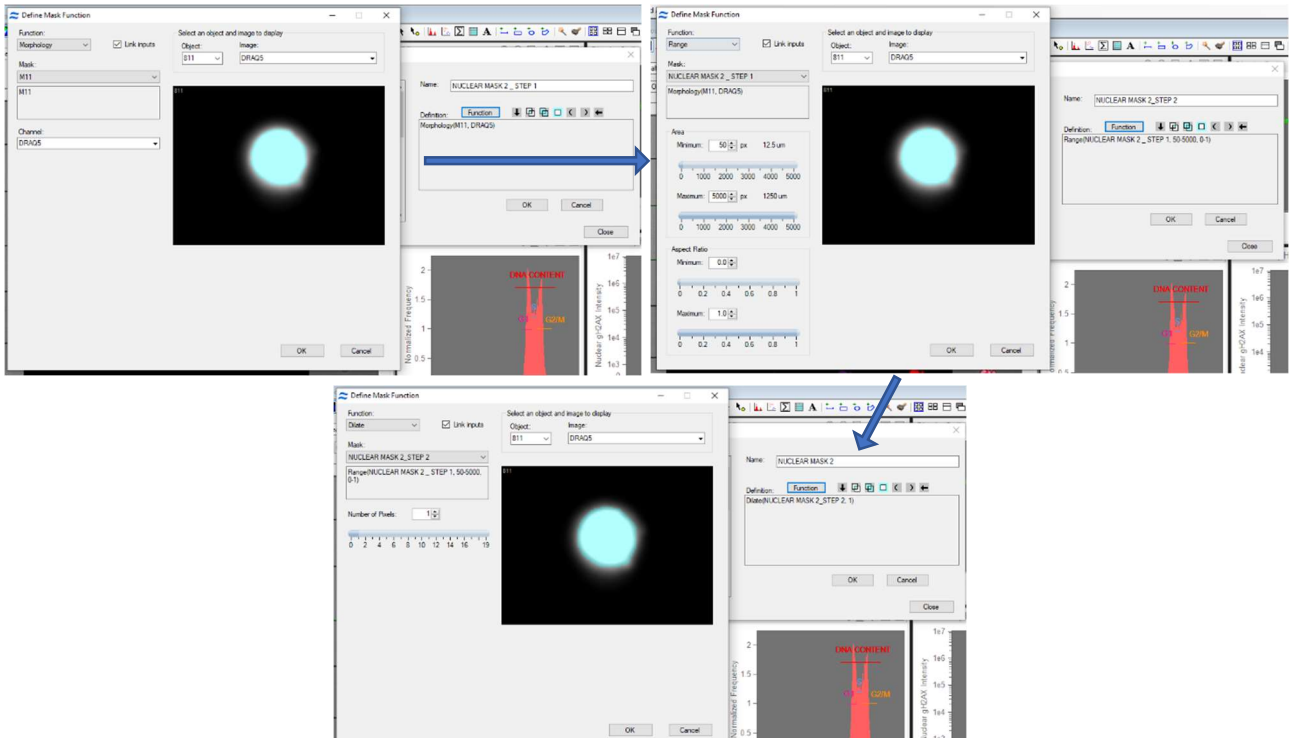

Figure 3.34: Nuclear mask 2 generation. Morphology function combined with range function allows for the shape of the nucleus to be mapped whist excluding smaller sized pixels that may also have DRAQ5 stain so only the main nucleus is looked at. Dilation of the mask proportionally expands the morphology input mask by 1 pixel allowing for lower intensity DRAQ5™ signal on the edges of the nuclear image to be taken into account whilst maintaining close nuclear morphology.

The main feature used in combination with the mask is intensity for the master population of cells that will be assessed for MN, ɣH2AX P53 and pH3. DNA content cell cycle assessment (figure 3.7 in section 3.3.2), generation of the cytoplasm mask

as demonstrated in section 3.3.3.1, generation of ɣH2AX and pH3 masks (figure 3.35A and 3.35B) and confirmation of biomarker location using the similarity feature see gating optimisation section.

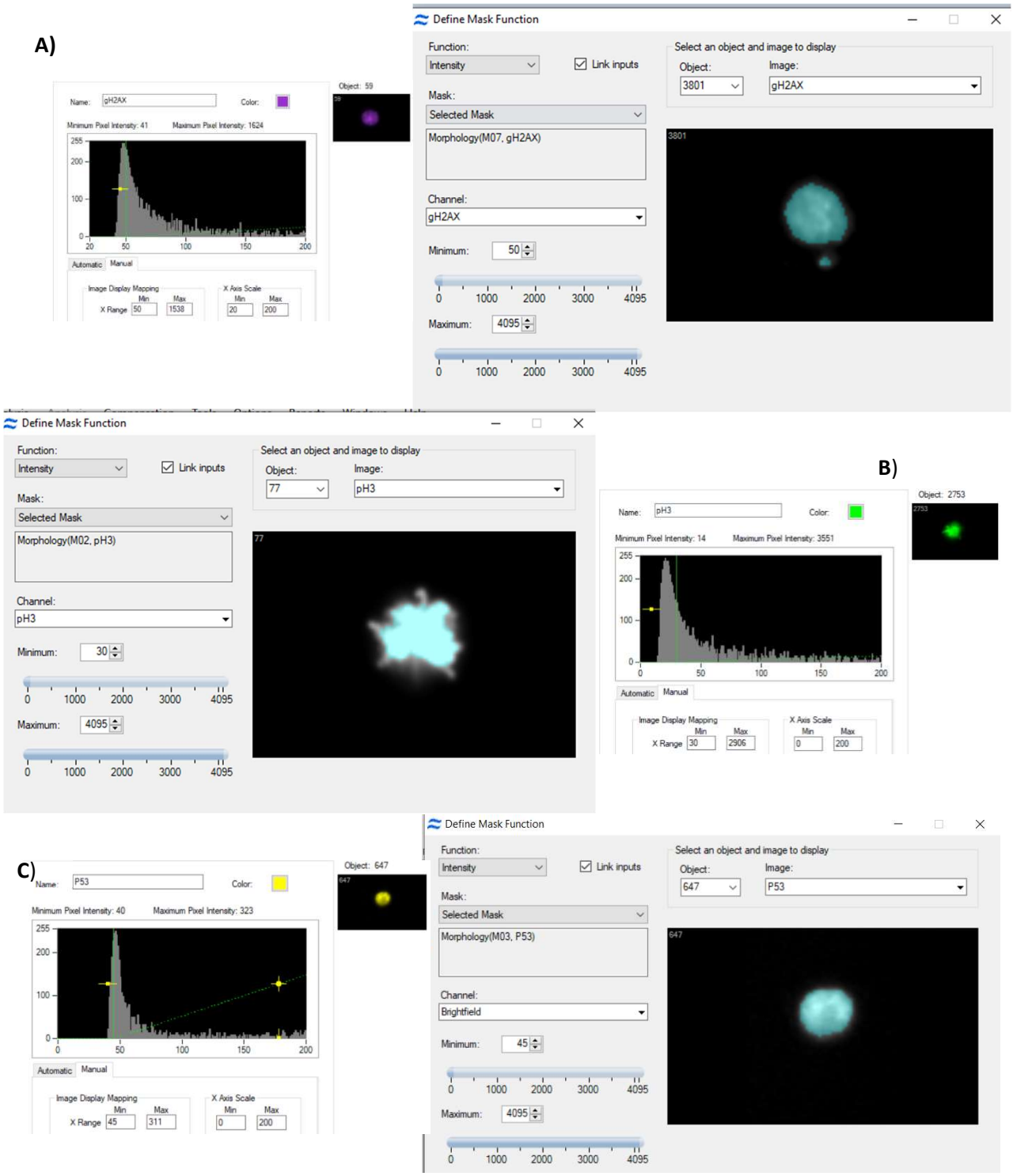

Figure 3.35: Demonstrating mask combination using Boolean logic and nuclear mask 2 to generate "True Nuclear" signal masks. A) γH2AX nuclear mask that all γH2AX metrics are generated from. B) pH3 nuclear mask that all pH3 metrics are generated from C) P53 nuclear mask that P53 metrics are generated from. All masks use the functions: Morphology that matches the shape of the signal and intensity that only looks at pixels with intensity of 30-50 and above, this removes background signal from assessment.

Using boolean logic the nuclear mask 2 is combined with the gH2AX mask (gH2AX MASK And NUCLEAR MASK 2) this helps minimise assessment of cells that may have above average autofluorescence or off target binding. Figure 3.36 Shows the graphs used to assess the ɣH2AX populations. This process was the same for P53 and pH3 signal, the differences being; the master population assessed was based on the entire DNA content profile so histogram gating step 4 as seen in figure 3.36 did not happen. P53 intensity was based on over all intensity assessed using just the P53 mask due to its potential for presence also being in the cytoplasm as well as the nucleus.

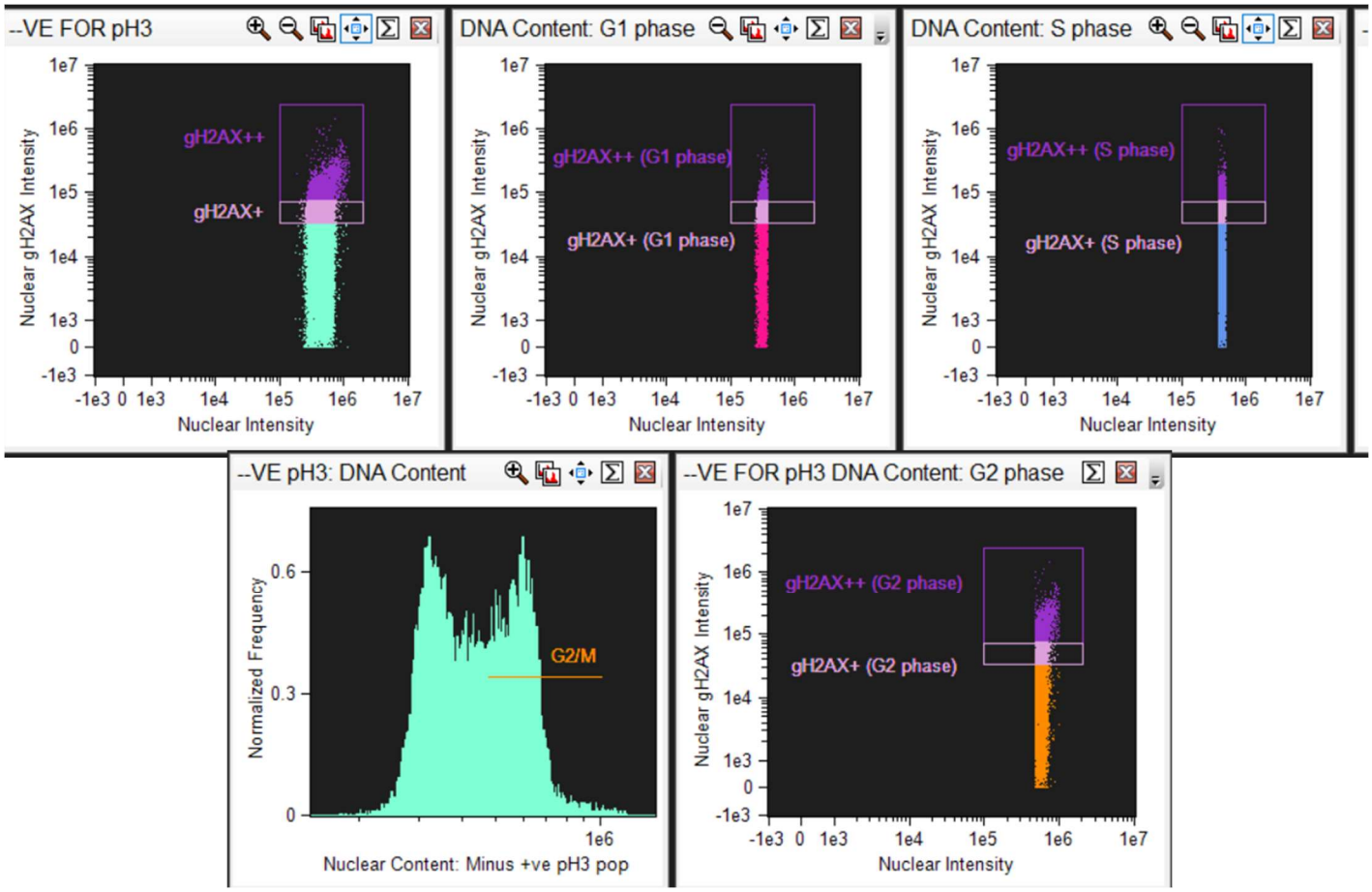

Figure 3.36: Showing each graph used to generate the ɣH2AX response along with ɣH2AX response per each section of the cell cycle. gH2AX++ and gH2AX+ gate coordinates as developed in 3.2.5 applied on the Y axis, Nuclear gH2AX intensity. The x coordinates of each of the gates covered the DNA content range and were applied to the Nuclear intensity. Unlike with pH3 and P53 populations, for the G2 assessment of H2AX cells stained positively with AF488 pH3 were excluded from the assessment.

Passed just Bv421 ɣH2AX, AF488 pH3 and PE P53 assessment, these biomarkers were assessed in direct relationship with the portion of the cell cycle they each fell into. These 'sub population' gates, taken from the DNA content histogram, G1 S and G2M were plotted on a intensity graph for each of the biomarkers as demonstrated in figure 3.36 above. The same gating boundaries as: pH3 +VE, pH3-VE, gH2AX ++, gH2AX +, P53+ and P53++ as developed in section 3.3.2.5 were used and labelled accordingly. The G2 assessment of ɣH2AX was based on the population of cells that fell within the G2M gate boundary of the histogram that was negative for cells with H3 staining.

The population of BV421 ɣH2AX ++, + and overall signal and AF488 pH3 were then further refined and confirmed using the similarity feature. The similarity feature in the IDEAS® software is usually used to assess the likelihood that a signal has been translocated into the nucleus or an overall move of a signal towards being translocated. This can be done by following the steps of the "Nuclear Localisation Wizard". The graph generated rates each of the pixels within the mask search criteria by assigning a + or – number to each pixel based on how similar pixels containing your signal of interest are in spatial location to your DNA stained pixel signal. The programme does this mathematically by plotting the log transformed pearsman coeffeicient correlation relationship of the DNA stain and signal (IDEAS® user manual 6.2, 2015). The system then places a gate of greater than or equal to +1 on a graph and plots the available cell population as a histogram. Cells that are above +1 can be described as; there is a high probability that you are most likely to find the chosen signal in the nucleus rather than outside it i.e., in the cytoplasm. Any signal that is found to be less than zero i.e., negative are the cells that the signal is the least similar to the nucleus, the signal is in the cytoplasm. In terms of signal that is transient you can say that the majority of the cell population has signal that translocated to the nucleus. Whilst the similarity feature is mostly used to identify how translocated a signal into the nucleus is it can also be used to confirm that the signal of a biomarker is actually coming from the area of the cell its supposed to, therefore be able to assess any off-target binding or exclude autofluorescence in cells. This was the rationale behind its use, in combination with specific pH3 and ɣH2AX signal masks it will help reduce counting signal that is unrelated to true antibody binding. Demonstration of use of the similarity feature in the above described manner can be found in in the gating section 3.3.2 figure 3.18. Combination of the intermediate gate and positive similarity gate generates the population of 'True nuclear pH3' and 'True Nuclear ɣH2AX' these are the cell populations that were used to calculate the percentage cell response.

As H3 phosphorylation on Ser28 only occurs in prophase metaphase and anaphase, the known features of these phases and microscopy assessment can be used to

identify cells in these various stages based on shape and pH3 presence. This is demonstrated in figure 3.37 below.

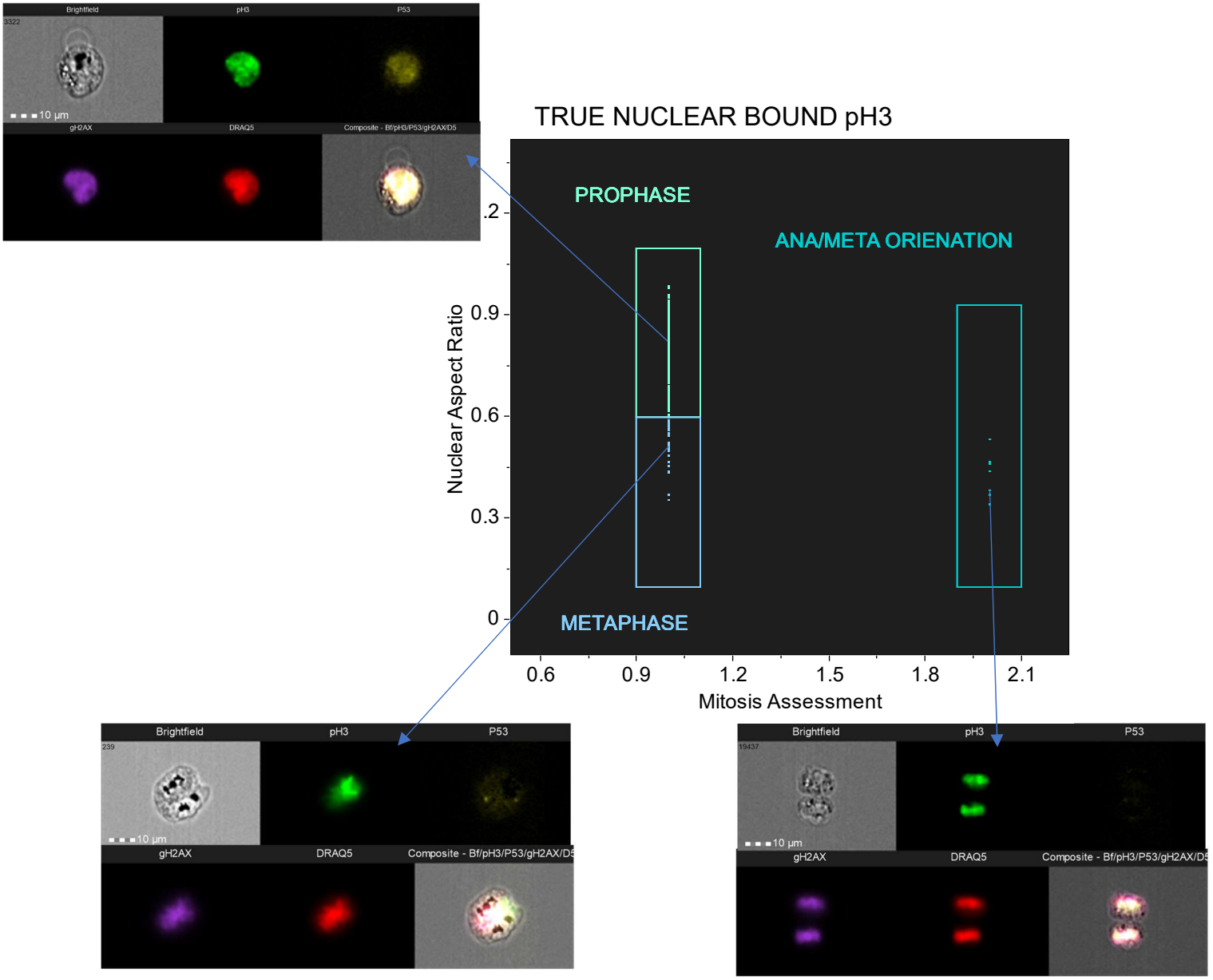

Figure 3.37: Graph demonstrating the separation of three phases of the mitosis cell cycle based on nuclear aspect ratio (how circular the DNA is) and spot count of nuclear bodies labelled Mitosis assessment that uses nuclear mask 1. An example image of the scatter points gated and their location in each of the mitosis phases is also highlighted. Population highlighted prophase is determined by its singular nucleus and relatively circular formation. Metaphase population is determined by it single nuclear content, the nuclear DNA being elongated as the chromosomes line up along the metaphase plate. Ana/meta orientation demonstrates the anaphase population based on the presence of two nuclei as the DNA content gets pulled towards opposite poles. The 'meta orientation' portion of this gate title refers to the potential of the cells, that fall into this gate, of actually being metaphase and are only classed as anaphase due to the orientation the cell image was captured in. The graphing and gating strategy used here was based on work done by, Filby *et al.*, 2011; Filby *et al.*, 2016.

The final biomarker related graph looks directly at the relationship of the true nuclear ɣH2AX and the True Nuclear pH3 response. Whilst the biology of cells in mitosis has a phosphorylation of PH3 at the same time there is a global phosphorylation of ɣH2AX signal. As demonstrated in the optimised gating step above the H3+ve population can be excluded from ɣH2AX analysis so as to avoid classing a healthy 'normal' cell response as a result of DNA damage. Whilst this is important to take into account during analysis it is also reasonable to assume that cells exposed to a chemical that affects the mitotic phase of the cell cycle in some way would in turn affect the direct relationship of H3 and H2AX phosphorylation. This allows us to assess another parameter that could be a potentially useful clastogenic/aneugenic flag by looking at the percentage of cells that are positive for H3 but negative for ɣH2AX. This was simply done by plotting the nuclear ɣH2AX intensity against the nuclear H3 intensity and reusing the gating boundary cut offs determined in section 3.3.2.5. Example of the graph is shown in figure 3.38.

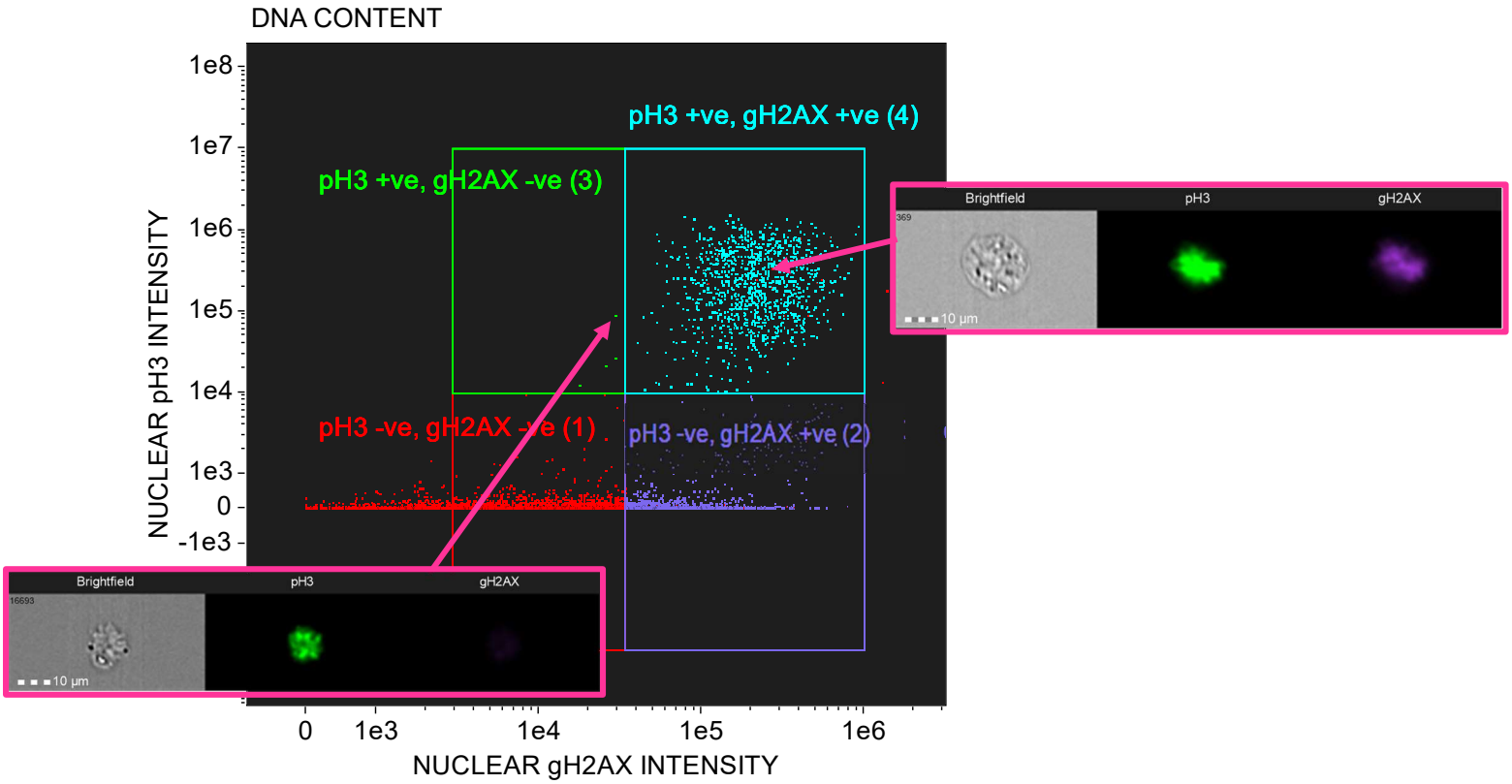

Figure 3.38: Demonstrating pH3 intensity plotted against ɣH2AX intensity as a scatter graph. Images show a ɣH2AX negative (abnormal) mitotic cell compared to a ɣH2AX positive (normal) mitotic cell.

3.3.3.2.3 - Nuclear Mask 3

Nuclear mask three was used to determine mononucleated cells from binucleated cells through the use of the spot count feature. Nuclear mask 3 uses the input mask of nuclear mask 2 which assesses shape, the 'watershed function (figure 3.39) is then applied which allows a mask to be divided into multiple components by removing a portion of the mask between areas of higher intensities.

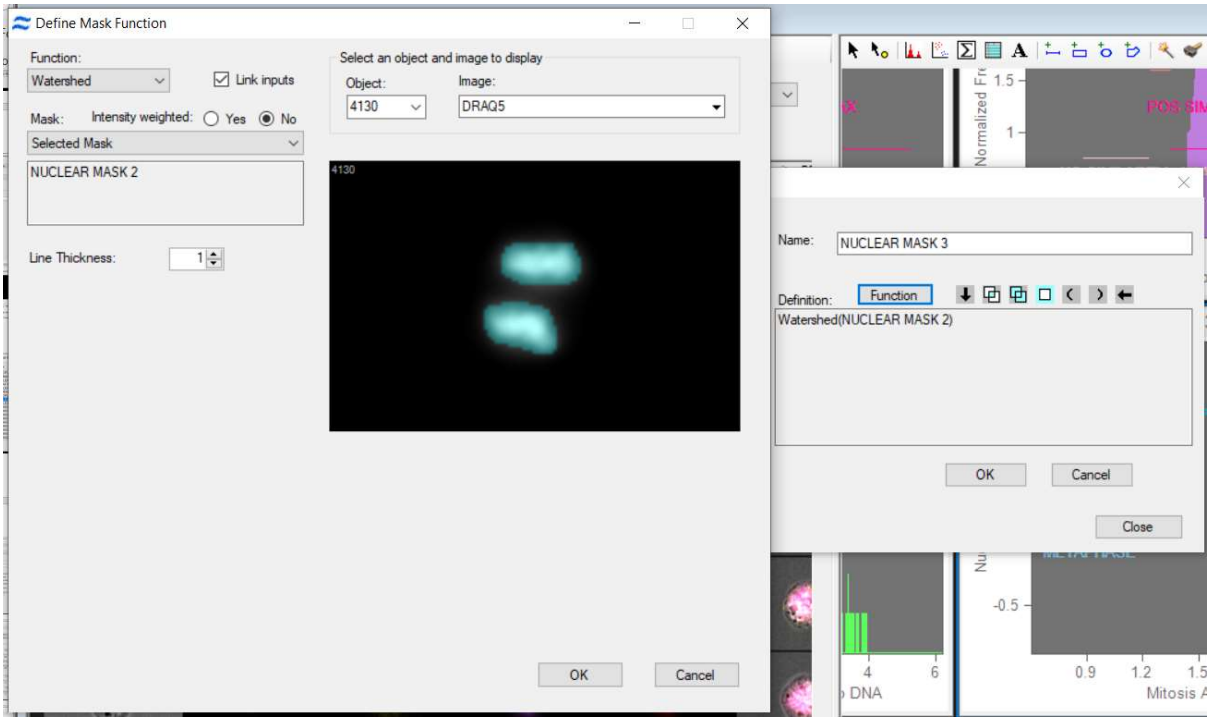

Figure 3.39: Application of the watershed function to Nuclear mask 2 allows for separation of the nuclear mask into multiple components. Not weighting the intensity of the watershed function allows the system to input a break in the area with least signal this minimises function basing the mask break on varying intensity levels.

Based on this mask the spot count feature can be used, this counts the number of individual components generated by the mask and plots them as a histogram values cells that sit in the histogram bar at one indicate there is only one component, in this case nucleus, present. Figure 3.40 below demonstrates the feature being selected and the graph generated. The gate termed healthy mononucleates is the population that will be assessed for MN presences.

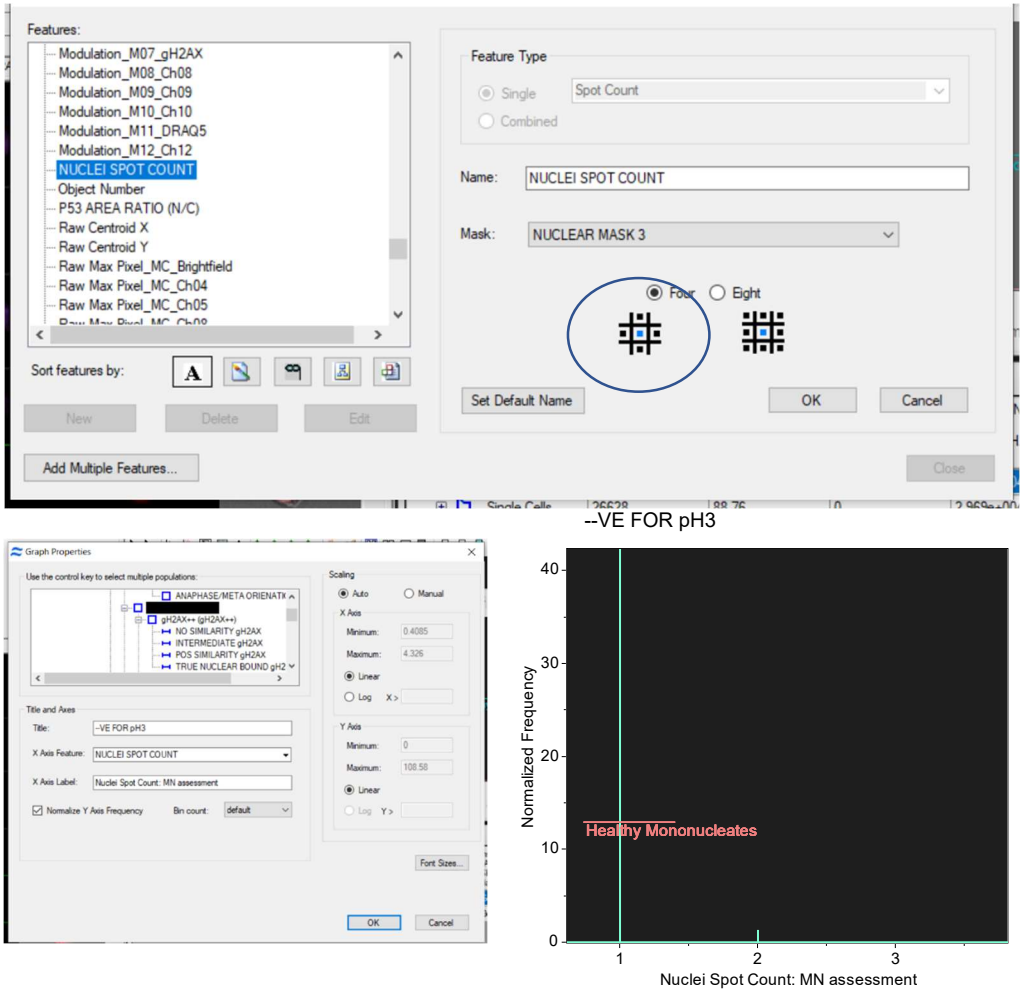

Figure 3.40: Showing use of the spot count feature to identify Mononucleated vs Bi-nucleated cells. The connectivity option circled in blue means the system only looks vertically and horizontally at the pixels next to the determined masked area of pixels to determine count.

3.3.3.3 - Micronucleus Mask and The Spot Count Feature

MN mask 1 which can be summarised as simply as Cytoplasm And MN but Not Nucleus. For MN Mask 2 whilst follows the methodology of MN mask generation by Rodriguez *et al* the variations that have been allowed try to take into account the variable nature of what constitutes a "true" MN. For example, the Rodriguez mask focusses on events that are round, completely distinct from the nucleus generated from a very specific population set. However as per Fenech *et al* this does not account for all MN. MN may be touching the nucleus or may be kidney shaped and these may be excluded from the analysis due to population exclusion or the mask being too specific. A third MN mask was also generated with slight variations on size range of MN looked at and main

nuclear shape to further account for variability in the populations. By combining all three masks and the cytoplasm presence addition the mask is trying to take into account variation of MN found in a cell population. A lack of refining the population that the spot count feature looks at based on this mask is trying to limit unconscious biasing of the data. The individual steps taken to generate the Complete Final MN mask are covered by table 3.2 and figure 3.41 and 3.42.

To generate each different MN mask two main functions are used. The spot count function and range function. For the assessment of bright points such as MN stained with sufficient DRAQ5™ the spot feature selects bright spots by simply eroding the selected bright detail from the image and removing this background from the total fluorescence image leaving the mask to identify only the bright spots. This is controlled by adjusting the spot to background ratio, minimum and maximum area of the bright spots. The range function then further enables refinement of the bright spot criteria through filtering of area size and how round that area is. Table 3.2 displays the sequence of functions each of the three individual MN masks use

Table 3.2: Summary of the functions used to generate the three MN masks that make up the Complete final MN mask

	Overall mask function combinations
MN Mask 1	(Range(Spot(Threshold(M11, Draq5,90)Bright, 3,6,1)5-100, 0.4-1) AND NOT (Range(Dilate(LevelSet (M11, Draq5, Middle, 3) 1) 100-5000, 0.2-1)
MN Mask 2	Range ((Threshold (Spot (M11, Draq5, Bright 2,5,2) Draq5 88) AND NOT (Range (Level Set (M11, Draq5, middle, 5) 90 -5000, 0-1) 10-80, 0.4-1)
MN Mask 3	Range ((Threshold (Spot (M11, Draq5, Bright 2,6,2) Draq5 88) AND NOT (Dilate (Morphology (M11, Draq5) 1) 10-80, 0.4-1)

The overall mask function combinations shows what the IDEAS® software reads to identify each different type of MN. In practice these sequences were divided up into stages and then each step was combined with the last, these steps can be seen in supplement 1. The three MN masks are variations on a theme, figure 3.41:

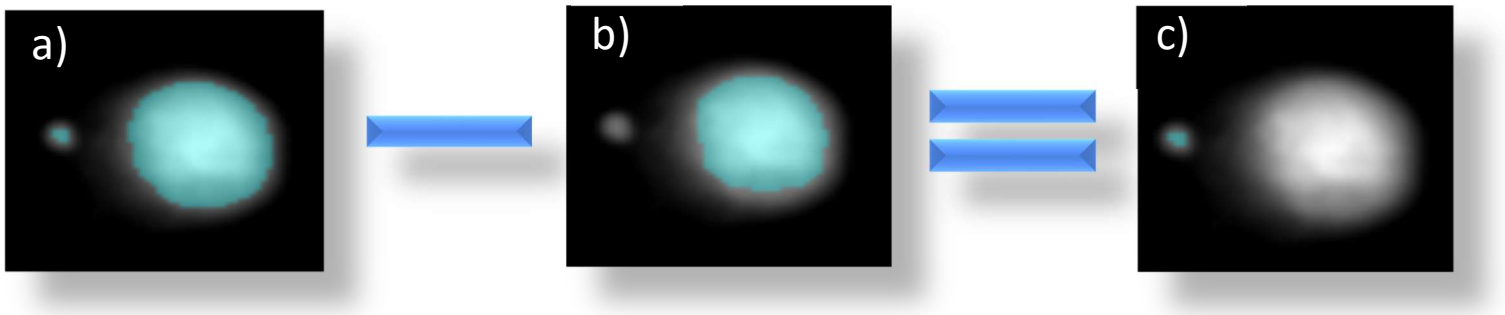

Figure 3.41: Demonstration of the basic principle of MN mask generated behind each of the three MN masks using IDEAS 6.2 software. a) Identification of DRAQ5 signal indicating nuclear content b) Removal of identified main nuclear pixels c) Remaining nuclear pixels above and below a specified size and roundness is classed as a MN.

Combination of these masks using the term OR means the system will take each of the criteria into account when looking for MN spots. Collectively the mask will be looking for bright spots that meet the criteria of having an area of 1.25-25 microns and be reasonably round. Combining this with AND cytoplasm means as long as a portion of the bright spot is inside the cytoplasmic boundary but not within the larger nucleus it will be masked. This is why the variations of nuclear masks are also used to make these three different MN masks, the variations allow the system to look at MN that may be touching or that are distinct from the main nucleus. An overview of the complete final MN mask and associated imagery along with the spot count feature and mask can be found in figure 3.42.

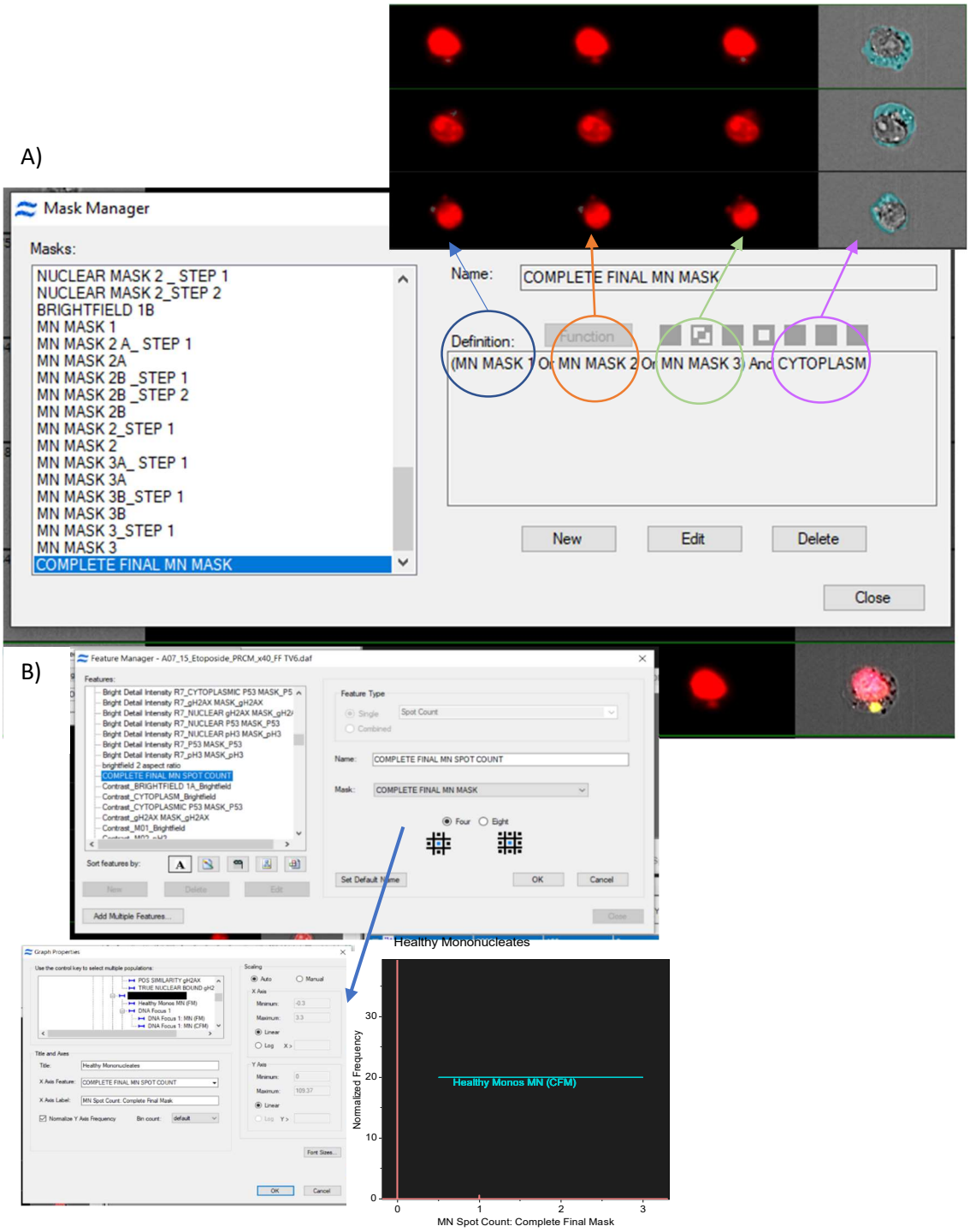

Figure 3.42: Complete final MN mask spot count for MN metric generations. A) Demonstrating the overall rule for the final MN mask and the corresponding masks assessed. B) Complete final MN mask is used to generate the spot count feature and corresponding graph. The MN gate is then used to extract the cells that contain MN.

3.3.3.3.1 - Complete Final Micronucleus Mask Accuracy Rate

Use of the IDEAS® mask in the IDEAS® software allows for the automation of MN assessment through use of the spot count feature, as explained in section 3.3.3.3 above. Over 10,000 cells can be assessed based on the population of cells being single, round, reasonably in focus, healthy DNA stained mononucleates with no pH3 staining. Due to the limited combinations of masks through Boolean logic processing all the variations and nuances that could be picked up by an experienced technician may be missed by the system. To assess the accuracy of the used MN mask a population of roughly 1000 cells were looked at manually to assess if any MN were not identified by the system termed %Miss Rate, followed by assessment of %Accuracy (see section 3.2.6 for details).

Based on the assessment of four top dose compounds known to induce MN the %Accuracy and %Miss rates are as follows:

- Crizotinib showed 72% accuracy and 52% miss rate
- Etoposide showed 57% accuracy 73% miss rate
- Vinblastine showed 64% accuracy with a 3% miss rate.
- ARA-C showed a 35%accuracy with 52%miss rate

Whilst the numbers are highly variable and therefore not ideal, it does imply that different chemicals generate different MN types that the mask is better or worse at identifying. On average the complete final MN mask is 57% accurate with a 44-45% miss rate

Based on the assumption that the system will consistently be ~57% accurate the dose response is relevant. The system will consistently miss the same types of MN within the population which ends up being balanced by the mask false identification rate. Use of the mask can be used to identify a general trend of MN fold change response of the assessed samples. It provides a quick overview snapshot of the potential MN within your sample whilst simultaneously providing a classic genotoxic endpoint that can be directly associated with DNA damage markers such as P53 and ɣH2AX levels.

3.3.3.4 - Extracted Data Populations

The population of cells that most of the analysis is based on is the healthy cells with DNA content of intensity greater than $1X10^5$. The percentage cell response data that has been reported as square root fold change in sections 4 and 5 below was generated by the generic rule (cell count with marker of interest/total cell master population analysed) X100. The IDEAS® software uses a waterfall style system to calculate the percentage cell response i.e., the system takes the gated population of cells plotted on a

new graph as the master population which is then reported in a statistics table, see figure 3.43 below which can then be exported as a statistics report.

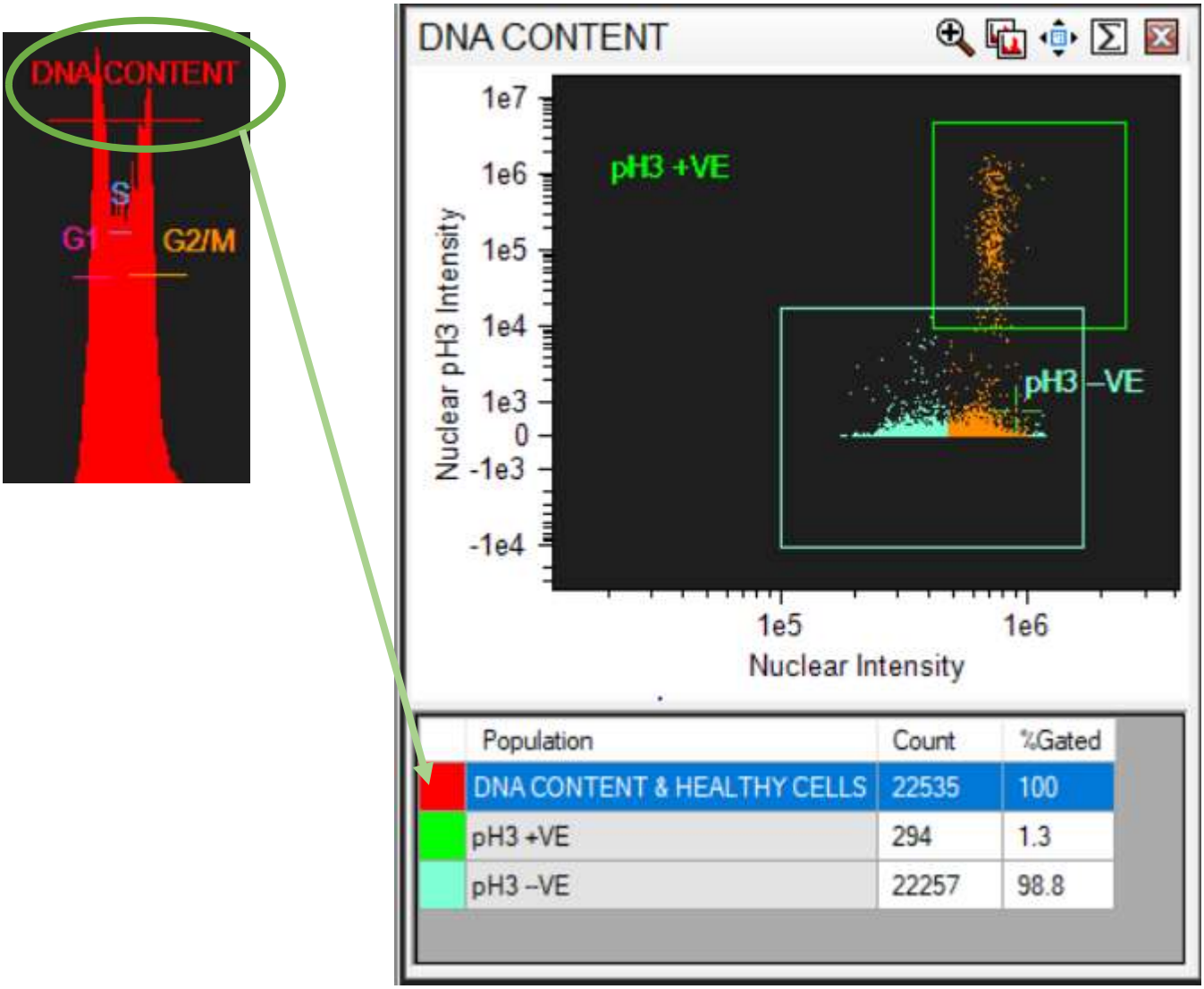

Figure 3.43: Demonstrating the population plotted on the scatter graph is the cells that fall within the DNA content gate of the cell cycle histogram. In this instance the DNA content count is the master population and the pH3+ve population is a proportion of the DNA content cell population.

Whilst these percentage calculations are calculated by the system and are able to be directly exported into excel, the master population to calculate the response of the signal is not necessarily the right population relevant for the analysis as a result the raw cell counts by the system for the relevant metric looked at were used to calculate the more accurate response using the correct master population cell count.

3.3.4 – Template overview

Template generation allows for the batch processing of analysis files using the IDEAS® platform. This provides a easily extractable data set containing the specific feature assessment of: Single in focus, healthy cell population with corresponding cell cycle information. Fluorescence intensity assessment of ɣH2AX, P53 and pH3 with defined gating cut offs allows for the assessment of biomarker response in a un bias dose dependant manner allowing for elucidation of biologically relevant fold change responses whilst simultaneously excluding potential autofluorescence/camera background/off target binding skewing of results. The template as is, allows for direct comparison of cell cycle stage biomarker relationships and automatic acquisition of MN data, all achieved per cell. However, lack of a automated cell cycle analysis artificial intelligence feature for cell cycle assessment total user bias and subjectivity cannot be removed due to the need to interactively adjust cell cycle gates due to sample variability. Whilst the MN mask and spot count feature provides a trend of MN response as the systems miss rate and inaccuracy scoring are proportional the template identifies limits to the software. Due to the limited nature of Boolean logic masking combinations the IDEAS® system does not have the finesse or sensitivity to account for all potential variations of MN generated by the various DNA damaging chemicals (Rodrigues et al., 2018; Rodrigues et al., 2021).

Whilst the template system is not perfect it provides a robust system for quick and efficient data extraction with minimal user interference creating relatively unbiased data to be used in chemical MoA assessment (see supplement 2 for the user interface profile of the finalised template generated).

Chapter 4 – Results 2: Model Chemicals, Methyl Methanesulfonate and Carbendazim

4.1 – Introduction

Identification and scoring of MN using the ImageStream has been achieved by various labs specifically focussing on the bi-nucleated MN cytome assay (Verma *et al*., 2018; Rodriguez *et al.*, 20; Wills *et al*., 2021) using DNA stains such as DAPI, Hoesht and DRAQ5™. However, dose response data has not been presented for the mononucleate assessment of MN nor has multiplexing of the biomarkers ɣH2AX, pH3, P53 using the FlowSight® or ImageStream X Mark II® (with the exception of Padalino *et al*., 2021 where data not used as part of this thesis was published). Use of the Amnis® Imaging flow cytometry platform, FlowSight® and ImageStream X Mark II®, combines the high throughput acquisition of data, typical to flow cytometry, whilst using un-lysed cells allows for the high content information collection and archiving capabilities supplied by automated microscopy (Amnis®., 2015). This system also allows for increased confidence in flow cytometry gating and the development of imaging classifiers, through the availability of collecting cellular images, which subsequently can significantly improve scoring precision. The use of said images can be used to refine and validate gating approaches as well as support image scoring as discussed in chapter 3.

This initial assessment looks at the feasibility of using the two imaging flow cytometry machines, FlowSight® and ImageStream X Mark II®, for detection of a dose response for the DNA damage markers ɣH2AX, pH3, P53 and MN. Usage in the first instance with the biomarkers ɣH2AX, pH3 compared to a second sample set of MN on the FlowSight® using mononucleated cells (without Cyto-B). In the second instance, also in mononucleated cells, a single sample set assessing dose response of ɣH2AX, pH3, P53 and MN on the ImageStream X Mark II®.

Given the highly characterised nature of MMS and Carbendazim respective MoA's (Kirkland et al., 2008; Kirkland *et al.,* 2016; Sarrif *et al*., 1994; Van Hummelen *et al.,* 1995) these two chemicals were used to initially assess the known expected responses of these chemicals in relation to ɣH2AX, pH3, P53 and MN response (Bryce *et al.,* 2014; Khoury *et al.*, 2016; Smart *et al.*, 2011; Verma *et al.,* 2017 ; Watters *et al*., 2009) versus the actual achieved responses of these biomarkers using the ImageStream platform.

This chapter, using the model clastogen MMS and aneugen Carbendazim, demonstrates how the *in vitro* MN assay performed on the FlowSight®, can be directly compared with ɣH2AX and phosphorylated H3 combined assay, providing both assessment of chromosome damage and underlying MoA. Furthermore, this chapter shows the progression and feasibility of multiplexing the ɣH2AX, pH3, P53 and MN damage identifiers using the ImageStream X Mark II®.

4.2 – Materials & Methods

4.2.1 - Test Article Formulation

Methyl methanesulphonate (MMS), Cas no.: 66-27-3, and Carbendazim, Cas no.: 10605-21-7 supplied from Sigma-Aldrich. The working concentrations, MMS 0.00, 0.31, 0.63, 1.25, 2.50, 5.00 (µg/mL) and Carbendazim 0.00, 0.40, 0.60, 0.80, 1.20 and 1.60 (µg/mL) were selected based on the data produced by Verma *et al*., 2017. Vehicle control was dimethyl sulfoxide (DMSO).

4.2.2 - Cell Culture and Growth Media

Refer to general material and methods section 2.2.2.

4.2.3 - Treatment Of Cell Cultures

TK6 at $2x10^5$ cells/mL were placed in a series of sterile vented tissue culture flasks and treated with MMS or Carbendazim for a 1.5 cell cycle period with no recovery. All incubation steps occurred at 37˚C, 5% (v/v) CO2± 0.5% in air.

4.2.4 - Preliminary

4.2.4.1 - Cell Processing

Approximately 2x105 TK6 cells/mL were placed in a series of sterile vented tissue culture flasks (Fisher brand) and treated with MMS and Carbendazim for a 1.5 cell cycle period with no recovery. All incubation steps occurred at 37˚C, 5% (v/v) CO2± 0.5% in air.

After the treatment period, cultures were centrifuged at 200 x g for 8 minutes, supernatant was discarded, and the pellet re-suspended in pre-warmed phosphate-buffered saline (PBS). Subsequently, the PBS was removed via centrifugation at 200 x g and the pellet was re-suspended in BD FACS lysis solution enabling cell fixation and membrane permeabilization. Post fixation, cultures were centrifuged for 5 minutes at 200 x g, supernatant discarded and subsequently stained either ɣH2AX, pH3, PBS AB solution or DRAQ5™ and agitated at room temperature for a minimum of 1 hour for the former and 20 minutes for the latter then washed with PBS. Stained cells were then transferred to appropriately labelled Eppendorfs and subsequently acquired on the FlowSight® imaging platform.

4.2.4.2 - Antibody and DNA Staining

Samples stained with only the antibody master mix will be referred to as experimental set 1 and samples counterstained with just DRAQ5™ will be referred to as experimental set 2.

Experimental set 1, 300µL of freshly made antibody master mix, containing Immunofluorescence antibodies anti ɣH2AX Brilliant Violet 421 antibody (Cat. No. 564720) and Anti Histone pH3 AlexaFluor 488 antibody (Cat. No. 641003), was added to each sample and incubated under agitation protected from light at room temperature for a minimum of 60 minutes.

Experimental set 2 stained with DRAQ5™ DNA was used to label nuclei and MN in a ratio of 1:99 of PBS due to DRAQ5™ suboptimal excitation on the FlowSight® using laser 488nm. Samples were incubated for a minimum of 20 minutes.

Additional information on the full staining procedure can be found in section 2.

4.2.4.3 – Preliminary Data Acquisition FlowSight®

Samples were analysed on an Amnis FlowSight® imaging flow cytometer using Amnis INSPIRE® software version 6.2 (Merck Millipore, Nottingham UK). Prior to experimental analysis, following the manufacturers instructions for appropriate Amnis FlowSight® set up and quality control procedures, all system calibrations performed and passed using Amnis® ImageStream SpeedBead calibration reagents (Cat. No. 400041). 75µL aliquots of cell suspension at a concentration of ~$7x10^5$ and no less than ~$4x10^5$ cells/mL were prepared in 1.5mL Eppendorf's and loaded on the sample port. All samples were excited using 405nm and 488nm lasers. An INSPIRE® template was set up for in focus and single cellular event gating, using Aspect Ratio and Root Mean Square (RMS) features, to enable sample data acquisition, ensuring collected cells were sufficiently circular and in focus. Once established, data was acquired at a low velocity, resulting in 15,000 – 20,000 single cellular events being collected in approximately 45 seconds, and subsequently automatically saved for each experimental replicate. Experimental set 1 acquisition of images for ɣH2AX and pH3 combined assay assessment occurred in: Channel 1, bright field; channel 2 and 7 fluorescence. Acquisition of images for experimental set 2 of mononucleated MN events, stained with DRAQ5™ DNA stain occurred in: Channel 1, bright field and channel 5 fluorescence.

Once data has been collected for all samples, the acquired raw image files (.RIF) data files were analysed using IDEAS® v 6.2 software, compensation matrix and template applied and subsequent, .CIF (compensated image files) and .DAF (Data Analysis Files) were generated.

4.2.4.4 - INSPIRE® Compensation File Acquisition

Compensation sample files were acquired using the INSPIRE® acquisition compensation wizard. Acquisition of correct compensation samples was performed without the presence of brightfield or side scatter, but both 488nm and 405nm lasers were utilised at the same intensity value as used during the experimental setup. 500-1000 cells were acquired for MMS (5.0 µg/mL) dosed TK6 cells stained with the anti-ɣH2AX antibody BV421, and Carbendazim (1.6 µg/mL) TK6 cells stained with the anti-pH3 antibody AlexaFlour 488. 50µL of each stained sample was combined with 50 µL of unstained untreated cells. Acquired files formed compensation matrices in AMNIS IDEAS® 6.2

software. Compensation file acquisition was not required for DNA stained only set 2 samples.

4.2.4.5 - Amnis IDEAS® v6.2 Template

Data analysis was conducted using Amnis IDEAS® software version 6.2 (Merck Millipore, Nottingham, UK). Prior to signal assessment RIF files were converted to compensated image files (CIF) and data analysis files (DAF).

For the assessment of BV421 ɣH2AX and AF 488 H3 signal of experimental set 1, an additional gate was included for analysis to exclude cells that were considered saturated, using the Raw Max Pixel function to exclude cells with saturation pixel count of >1 and raw max pixel function of 4095≤ (Amnis 2015). Composite images of combined bright field, BV421 ɣH2AX and AF488 H3 were generated to visually confirm signal was within the cytoplasmic boundary and assess the viability of the cells. The single, in-focused unsaturated cells were then used to assess ɣH2AX and H3 presence. Fluorescence signal positivity was determined through the use of visual assessment of cell images allowing the extraction of positive and negative populations with regard to H3 and γH2AX signal intensity by comparison of control samples and top dose of aneugenic/clastogenic compound, thus a subsequent gate was established. Once these parameters were established the CIF files were batch processed via the use of an IDEAS® template. A total of 15000 cells were assessed to obtain the ɣH2AX and phosphorylated H3 dose response. For full details on template and gate generation steps see general methods and section 3.3.2 respectively.

For the preliminary assessment of mononucleated MN cells using experimental set 2, an overlay of DRAQ5™/Bright field (Composite) images was created in IDEAS® by combining images of DRAQ5™ (nuclear stain) stained nuclei/MN collected with bright field images of cells (Verma *et al*, 2018). The composite images were manually assessed to classify cells based on their morphology as mono's, bi and tri nucleates with and without micronuclei present (Verma *et al*, 2018). MN scoring within the mononucleated cells was carried out by adopting the criteria designed for slide based scoring (Fenech *et al*., 2003). Therefore, the MN that were DRAQ5™ positively labelled were accepted for scoring were, circular/oval, 1/3-1/16 the size of the main nuclei and resided within the cytoplasmic boundary (Verma *et al*, 2018). A total of 6000 mononucleated cells were assessed per dose to obtain the MN dose response. Please note no mask for automated MN assessment was used for this data nor was cell cycle data generated.

4.2.4.6 - Statistical Analysis

Preliminary data experimental set 1, distributions were tested for homogeneity and normality using the Brown forsythe/Bartletts test and D'Agnostino-pearson omnibus (K2)/Shapiro-Wilk test respectively. If datasets proved both normal and homogenous a one way ANOVA Dunnett's test was performed to identify significance (p value<0.05) of

data response. If data did not pass these trend tests the data was either Log or square rout transformed and distribution retested. In the event the transformed data failed distribution tests the non-parametric 1 sided Dunns Kruskal Wallis test was performed on the raw response data. Presence of statistical significance was used to identify the no- and the lowest- observed genotoxic effect levels (NOGEL, LOGEL). This procedure is as recommended by Johnson *et al*., 2014; Verma *et al*., 2018.

For preliminary data experimental set 2 no statistical analysis was performed as experimental repeats were n=1.

4.2.4.7 - Positive Response Criteria

With regards to histone signal, here a >1.5 fold increase over that of control values, for either histone signal, to be classed as a biologically relevant positive result as per industry standards (Smart *et al*., 2011). A positive decrease was defined as a <0.7 change, in respect to control values, based on criteria proposed by Khoury *et al*., 2016. A result was considered equivocal if the fold change was equal to either, exactly a 1.5 increase or 0.7 decrease. Values that fall <1.5 fold but >0.7 fold are considered negative. Based on available literature such as Smart *et al*., 2011, Bryce *et al*., 2016, Khoury *et al*., 2016 with regards to industry defined fold change cut offs for ɣH2ax and pH3 is a 1.3-1.5 fold increase and a 0.7 fold decrease as being biologically relevant. A positive response criterion for the preliminary MN response was considered to be a greater than 2 fold change induction compared to control (Takeiri *et al*., 2019; Shi *et al*., 2010).

For the preliminary data set the data was not transformed and is reported in normal fold change.

4.2.5 - Optimised

4.2.5.1 - Antibody and DNA Staining

Immunofluorescence antibodies used were: Anti ɣH2AX Brilliant Violet 421 antibody (Cat. No. 564720) supplied by Becton Dickinson Biosciences. Anti-Histone pH3 AlexaFluor488 antibody (Cat. No. 641003) and anti P53 PE antibody (Cat.No. 645805) were both obtained from Biolegend. These antibodies generated a mass stock solution, in the ratio 3µl of pH3: 5µl of ɣH2AX: 6µl of P53, with 286µl of PBS. Cells were stained in multiplex at room temperature under agitation for a minimum of 60 minutes.

DRAQ5™ DNA (Cat. No. 564902 supplied from BD Biosciences) was used to label nuclei and MN in a ratio of 1:199 of PBS. Samples were incubation time for DRAQ5™ was a minimum of 20 minutes.

4.2.5.2 - Optimised Cell Processing

After the treatment period, cultures were centrifuged at 200 x g for 8 minutes, supernatant was discarded, and the pellet re-suspended in pre-warmed phosphate-

buffered saline (PBS). Subsequently, the PBS was removed via centrifugation at 200 x g and the pellet was re-suspended in BD FACS lysis solution enabling cell fixation and membrane permeabilization. Post fixation, cultures were centrifuged for 5 minutes at 200 *x g*. Supernatant discarded and subsequently stained with ɣH2AX, pH3 and P53 antibody solution and agitated at room temperature for a minimum of 1 hour followed by the addition of DRAQ5™ nuclear stain for a minimum of 20 minutes then washed with PBS. Stained cells were then transferred to appropriately labelled Eppendorfs and shipped on ice via DHL to: *Newcastle Flow Cytometry Core Facility (FCCF), William Leech Building (2nd floor Room M2.099), Newcastle University, NE1 7RU*, for subsequently acquisition on the ImageStream X Mark II® imaging platform.

4.2.5.3 – Optimised Data Acquisition ImageStream X Mark II®

Samples were analysed on a Amnis® ImageStream X Mark II® imaging flow cytometer using Amnis INSPIRE® software version 6.2 (Merck Millipore, Nottingham UK). Prior to experimental analysis, following the manufacturer's instructions for appropriate ImageStream X Mark II® set up and quality control procedures, all system calibrations performed and passed using ImageStream X Mark II® SpeedBead calibration reagents (Cat. No. 400041). 100µL aliquots of cell suspension at a concentration of ~$7x10^5$ and no less than ~$4x10^5$ cells/mL were prepared in 1.5mL Eppendorf's for shipment upon arrival at the FCCF facility, samples either remained in the Eppendorf's or were transferred to a 96 well plate and loaded on the sample port. All samples were excited using 405nm, 488nm 642nm lasers at 120mw, 90mw, 80mw respectively. Laser 785nm was used for side scatter at laser power 5mw. An INSPIRE® template was set up for in focus and single cellular event gating, using Aspect Ratio and Root Mean Square (RMS) features, ensuring collected cells were sufficiently circular and in focus. Once established, data was acquired at a low velocity 66.0(mm/sec), resulting in 15,000 – 30,000 single cellular events being collected in approximately 45 seconds, and subsequently automatically saved for each experimental replicate. Acquisition of images for ɣH2AX pH3, P53 and DRAQ5™ assessment occurred in: Channel 1, bright field; channel 2, 3, 7 and 11 fluorescence; Channel 6 side scatter. Whilst these channels were of main interest data was acquired for all 12 channels.

Once data has been collected for all samples, the acquired raw image files (.RIF) data files were analysed using IDEAS® v 6.2 software, compensation matrix and template applied and subsequent, .CIF (compensated image files) and .DAF (Data Analysis Files) were generated.

4.2.5.3.1 - Acquisition Error

Due to an acquisition error and laser malfunction experimental repeats 1 and 2 for both Carbendazim and MMS had no side scatter laser and a reduced 405nm (BV421 ɣH2AX excitation laser) laser power of 20mw. To account for this, the optimal gate

positioning discussed in section 3.3.2 for template analysis, was shifted down by a factor of 6, proportional to the laser power reduction. Historical data (not shown) of vehicle control response, 1.2 µg/mL Carbendazim and 2.5 µg/mL MMS using optimal power settings as described in section 4.2.5.3, were used to confirm the suboptimal BV421 collection and adjusted gating parameters were reasonable adjustments to confirm response consistencies despite acquisition error. Laser powers for 488nm and 642nm were 100 and 90mw respectively. As these laser powers were only 10% different from optimal acquisition setting the pH3+ve gates and P53 gate was not adjusted. Experimental repeats 3 for both chemicals had the laser powers as described in section 4.2.5.3.

4.2.5.4 - INSPIRE® Compensation File Acquisition

Compensation sample files were acquired using the INSPIRE® acquisition compensation wizard or manually using Compensation beads (Cat.No.01-2222-41) from Thermofisher Scientific. Acquisition of correct compensation samples was performed without the presence of brightfield or side scatter but both 488nm 405nm and 642nm lasers were utilised at the same intensity value as used during the experimental setup. Acquired files formed compensation matrices in AMNIS IDEAS® 6.2 software. Two separates compensation matrices were generated for optimal and acquisition error settings.

4.2.5.5 - Amnis IDEAS® v6.2 Template

Data analysis was conducted using Amnis IDEAS® software version 6.2 (Merck Millipore, Nottingham, UK). Prior to signal assessment RIF files were converted to compensated image files (CIF) and data analysis files (DAF).

Of the initial RAW cell population collected using brightfield and nuclear parameters single in focus healthy cell population was determined as laid out in section 3.3.3.2. DNA content was then plotted on a histogram, and cells with nuclear intensity greater than $1X10^5$ was the final population used for MN, ɣH2AX, P53 and pH3 assessment.

Using the brightfield channel and DRAQ5™ DNA stain for the assessment of mononucleated MN cells, the cell population was determined my using nuclear mask 3 to distinguish mononucleated cells from cells with multiple nuclei using the spot count feature. This mononucleated population of cells was then used to generate MN data. The designed mask termed Complete final micronucleus mask in combination with spot count feature was used to automatically score the MN response (See section 3.3.3.3 for in-depth description nuclear and MN masking criteria). The automated MN scoring within the mononucleated cells was carried out by attempting to include the criteria designed for slide based scoring (Fenech *et al*., 2003) in the MN mask. Therefore, the MN that were DRAQ5™ positively labelled were accepted for scoring were, circular/oval, 1/3-1/16 the size of the main nuclei and resided within the cytoplasmic boundary. A

minimum of 5000 mononucleated cells were assessed per dose, per replicate to obtain the MN dose response.

For the assessment of BV421 ɣH2AX, AF 488 pH3 and PE P53 fluorescence signal positivity was determined through pixel intensity through the use of stained vs unstained populations, signal separation on scatter graphs and specific signal masking based on nuclear/cytoplasmic localization. Gates were then applied to scatter graphs to extract positively stained cell populations for each of the three biomarkers (see section 3 for boundary cut-offs and mask development). To assess the specific biomarker response per stage of the cell cycle the same gate cut offs were used as the overall population assessment of each of the biomarkers but the populations used were taken from the cell cycle gates placed on the DNA content graph. Once these parameters were established the CIF files were batch processed via the use of an IDEAS® template.

4.2.5.6 – Optimal Data Set Positive Response Criteria

For the optimal data set the fold change responses and statistical analysis were as described in 2.2.6 data assessment section of general methods.

4.3 – Preliminary Results

4.3.1 – Preliminary Dual Biomarker and MN Assessment

The results from the well characterised chemicals, MMS (clastogen) and Carbendazim (aneugen), show a distinct pattern with regards to ɣH2AX and phosphorylated H3 (pH3) signal. Examples of the images obtained during data processing can be seen presented in figure 4.1.

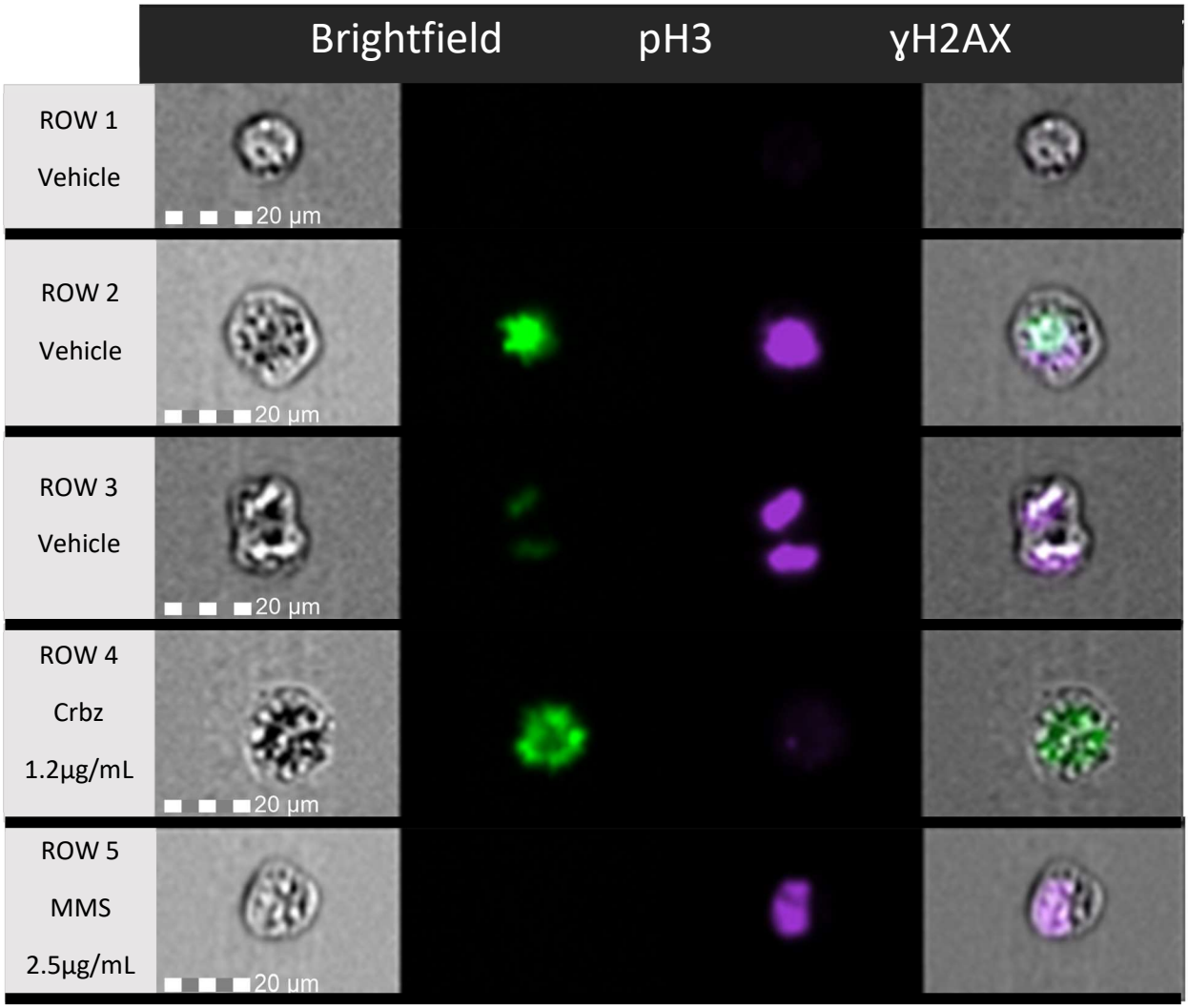

Figure 4.1: Demonstrating images obtained on Amnis FlowSight® at 20x magnification of sample dual stained with pH3 and ɣH2AX AB. Brightfield light microscope image. Composite is an overlay of brightfield and all fluorescent image channels. Row 1 – 3 shows negative control cellls. Row 1 shows images with no AB binding. Row 2 demonstrates cell at beginning of mitosis. Row 3 shows cell in telophase of mitosis. Row 4 images shows 1.2µg/mL Carbendazim dosed cells, with reduction in ɣH2AX. Row 5 images show 2.5µg/mL MMS dosed cells with ɣH2AX signal.

As figure 4.2A, presented in fold change, demonstrates, all concentrations of MMS lead to statistically significant ($p < 0.05$) increases in a dose dependant manner of ɣH2AX signal. Doses 1.25µg/mL to 5.0 µg/mL have a fold change >1.5 fold change. Demonstrating a positive response. The H3 signal decreased dose dependently, a NOGEL was determined to be 2.5µg/mL with a statistically significant decrease of signal at 5.0µg/mL with a <0.7 fold change. The MN scored using FlowsSight® in mononucleated TK6 cells, following exposure to MMS, data shows a dose dependant increase (See figure 4.2B). This is consistent with the dose dependant response generated by ɣH2AX along with previous microscopy based analyses (Verma *et al*., 2017).

A)

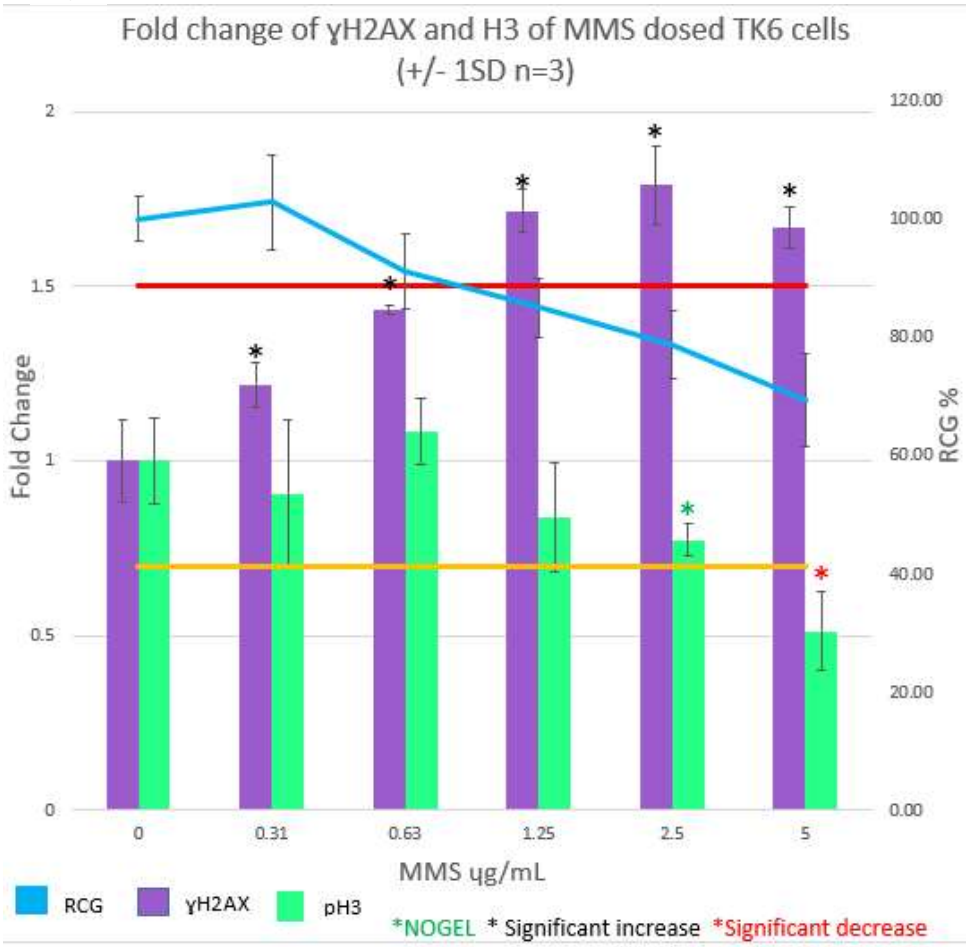

B)

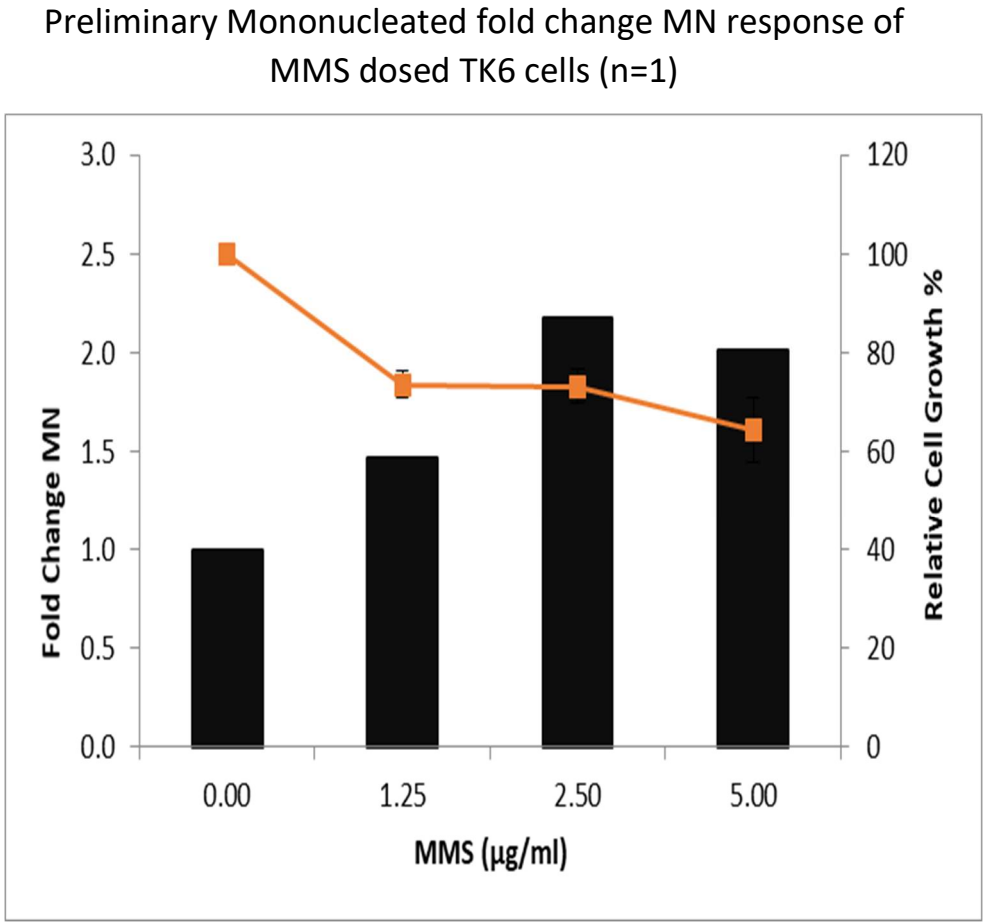

Figure 4.2: Demonstrating biomarker response of set 1 compared to the independent DRAQ5 stained MN response of set 2 spanning similar dose ranges of MMS using the Amnis FlowSight®. Graphs include Relative Cell Growth (RCG) % of treated TK6 cells. A) Induction of γH2AX and pH3 dual marker response to MMS a known clastogen. The red line shows the 1.5 fold change and orange line shows the 0.7 fold change industry standards. B) MN fold change response scored manually from captured images acquired on the Amnis FlowSight®.

As demonstrated in Figure 4.3A, presented in fold change, exposure to Carbendazim results in an increase of phosphorylated H3 signal and corresponding decrease in ɣH2AX signal.

A)

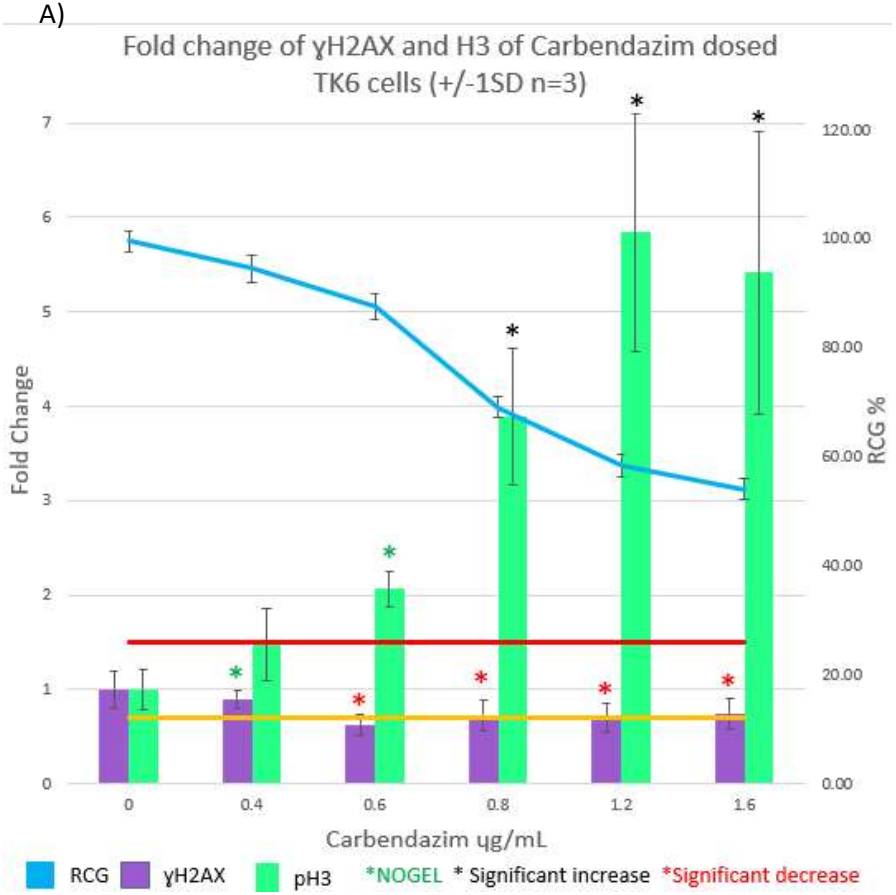

B)

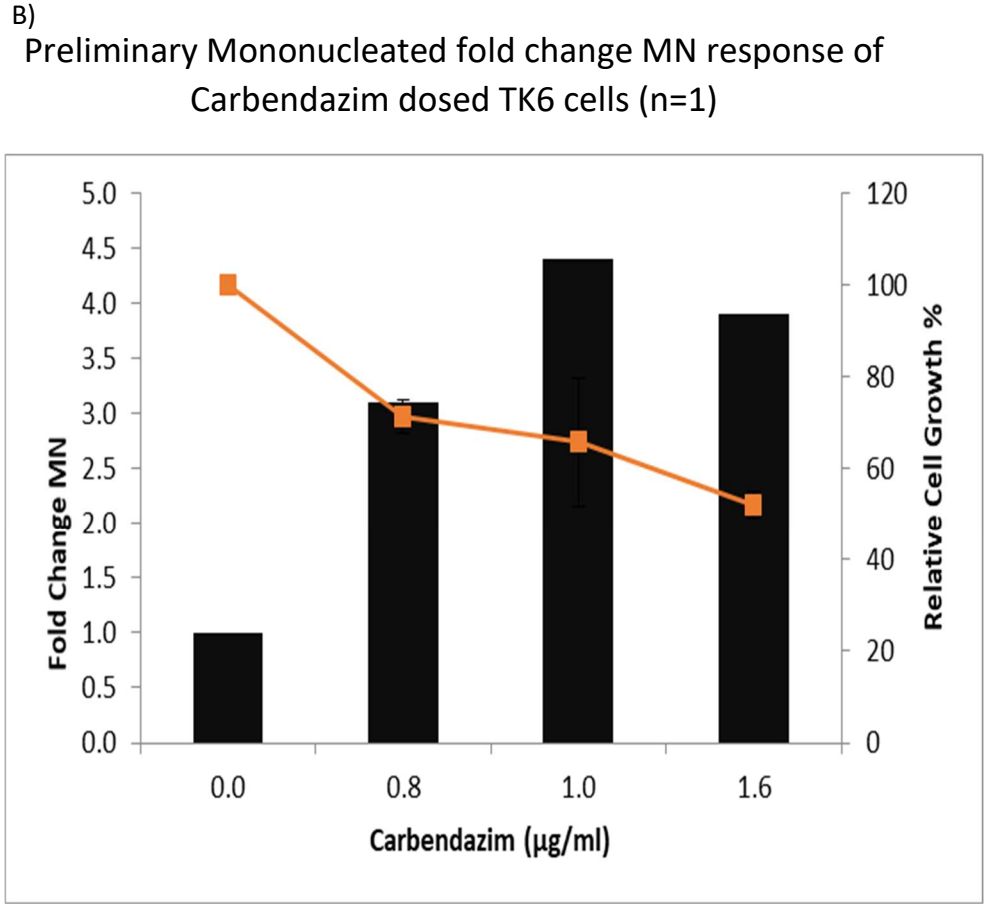

Figure 4.3: Demonstrating biomarker response of set 1 compared to the independent DRAQ5 stained MN response of set 2 spanning similar dose ranges of Carbendazim using the Amnis FlowSight®. Graphs include Relative Cell Growth (RCG) % of treated TK6 cells. A) Induction of ɣH2AX and pH3 dual marker response to Carbendazim a known aneugen. The red line shows the 1.5 fold change and orange line shows the 0.7 fold change industry standards. B) MN fold change response scored manually from captured images acquired on the Amnis FlowSight®.

The pH3 NOGEL was determined to be 0.6µg/mL with a statistically significant increase ($p<0.05$) from 0.8µg/mL. Phosphorylated H3 signal for 0.6µg/mL is considered positive, even though not statistically significant, via a >1.5 fold increase with respect to control values as per industry standard. The NOGEL for ɣH2AX is at 0.4 µg/mL with statistically significant decrease of ɣH2AX from 0.6 µg/mL to the top dose tested. A ɣH2AX positive fold decrease of <0.7was observed at the 0.6 µg/mL dose, however, was not sustained resulting in the 0.8 µg/mL through to 1.6 µg/mL doses being considered as an equivocal decrease. The MN scored with mononucleated TK6 cells using the FlowSight® platform for Carbendazim, shows a dose dependant increase of MN events (See figure 4.3B) consistent with the dose dependant response generated by phosphorylated H3.

4.4 – Optimal Results

4.4.1 – Optimised Multiplex System: ɣH2AX, pH3, P53 MN and Cell Cycle Analysis

In depth assessment of ɣH2AX, P53 & pH3 biomarkers in direct relation to each stage of the cell cycle of the chemicals MMS and Carbendazim. Due to the acquisition error of MMS and Carbendazim the data should be considered preliminary.

4.4.1.1 – MMS: Optimal Staining Sub Optimal Laser Settings (Preliminary Response Data)

Methyl Methane Sulfonate is a well defined genotoxic chemical, its Mode of Action falling under clastogenicity. The following results demonstrate the fold induction of the biomarkers ɣH2AX, P53 and pH3 compared to that of the DMSO vehicle control as well as cell cycle assessment relationships.

Figure 4.4 shows a significant increase of ɣH2AX from the 1.25 µg/mL dose onwards compared to control which also rises above the industry fold change standard for a biologically relevant result. There is a significant increase at all MMS doses for P53 response the response rising above the determined cut off from 1.2 µg/mL onwards. MN response also increases with dose and does so proportionally with ɣH2AX and P53 response. The only MN response that was found to be significant was at 5.0 µg/mL.

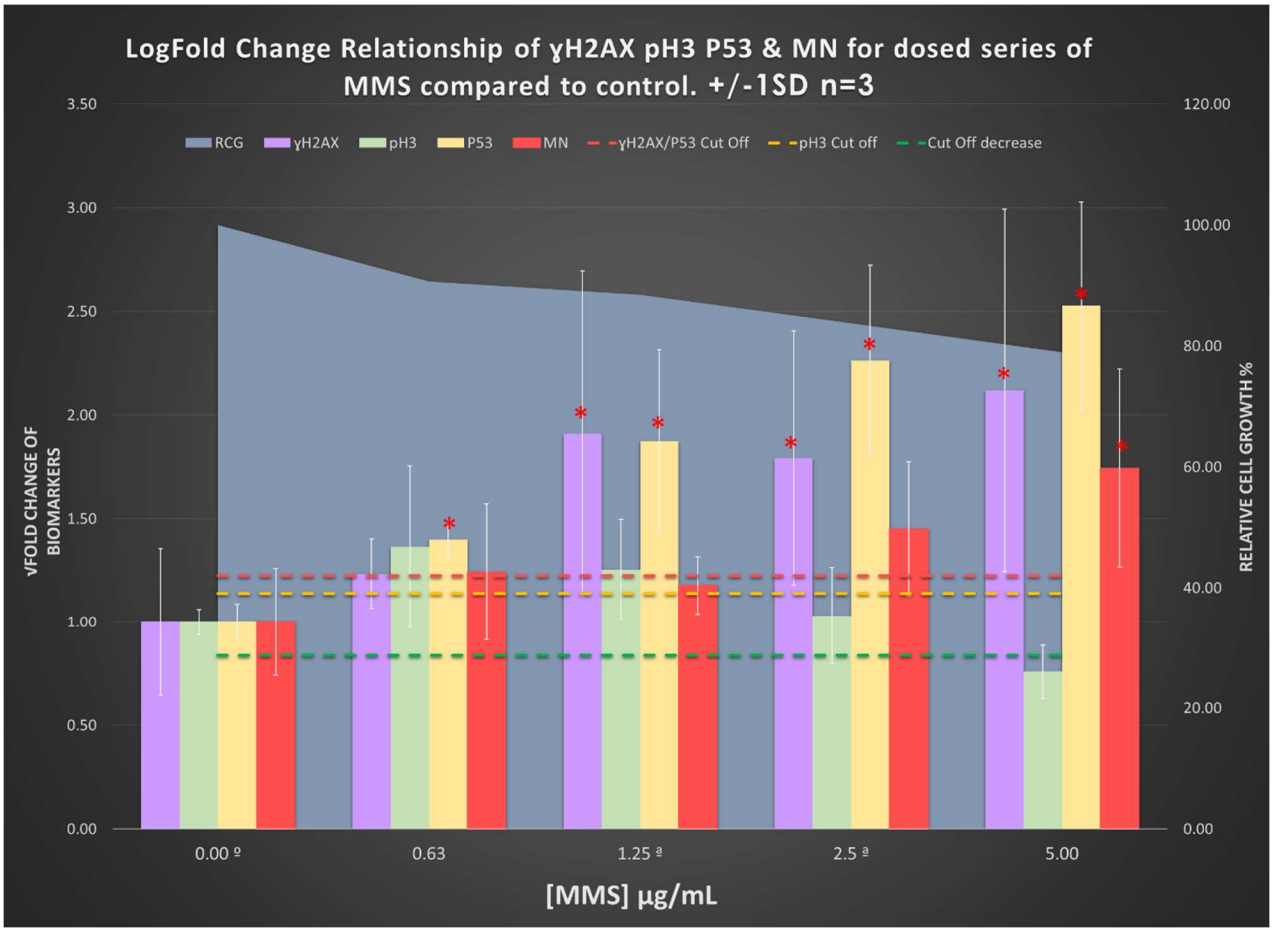

ºVehicle control DMSO
ªAquisition error n=2
**Significant response p value < 0.05* ** Highly Significant Response p value<0.0001*

Figure 4.4: Combination graph showing the square root of raw fold change values of the biomarker responses for γH2AX, pH3, P53 and the Micronucleus (MN) genotoxic endpoint in response to MMS doses. RCG shows the % growth of cell cultures, RCG response decreases in a dose dependant manner. The dashed lines are the fold change cut offs for the biomarkers pH3, P53 and γH2AX. γH2AX response rises above the fold change cut off from 1.25 µg/mL onward and is also statistically significant the same doses. P53 increases with γH2AX in a dose dependant manner and is significant from 0.63 µg/mL onwards. MN gradually increases across all doses but only shows a significant response at 5.00 µg/mL. pH3 response initially increases but then from the peak at 0.63 µg/mL the response decreases until dropping below the fold change decrease cut off at 5.00 µg/mL. No doses for pH3 were significant. There was no dose that was not significant for all biomarkers. γH2AX NGEL was 0.63 µg/mL and MN NOGEL was 2.50 µg/mL.

With the inclusion of the DNA staining, whilst this allows for MN assessment it also allows for cell cycle analysis. Figure 4.5 below demonstrates the percentage of cells found in each portion of the cell cycle. The figure shows that as MMS concentration increases the G1 population decreases and the G2 population increases whilst the synthesis stage decreases initially before increasing. This cell cycle response is consistent with the literature (Bryce *et al*., 2017). When looking at this data in combination with other factors additional patterns begin to emerge. Table 4.1 shows the response for the three biomarkers pH3, ɣH2AX and P53 in relation to cell cycle stage.

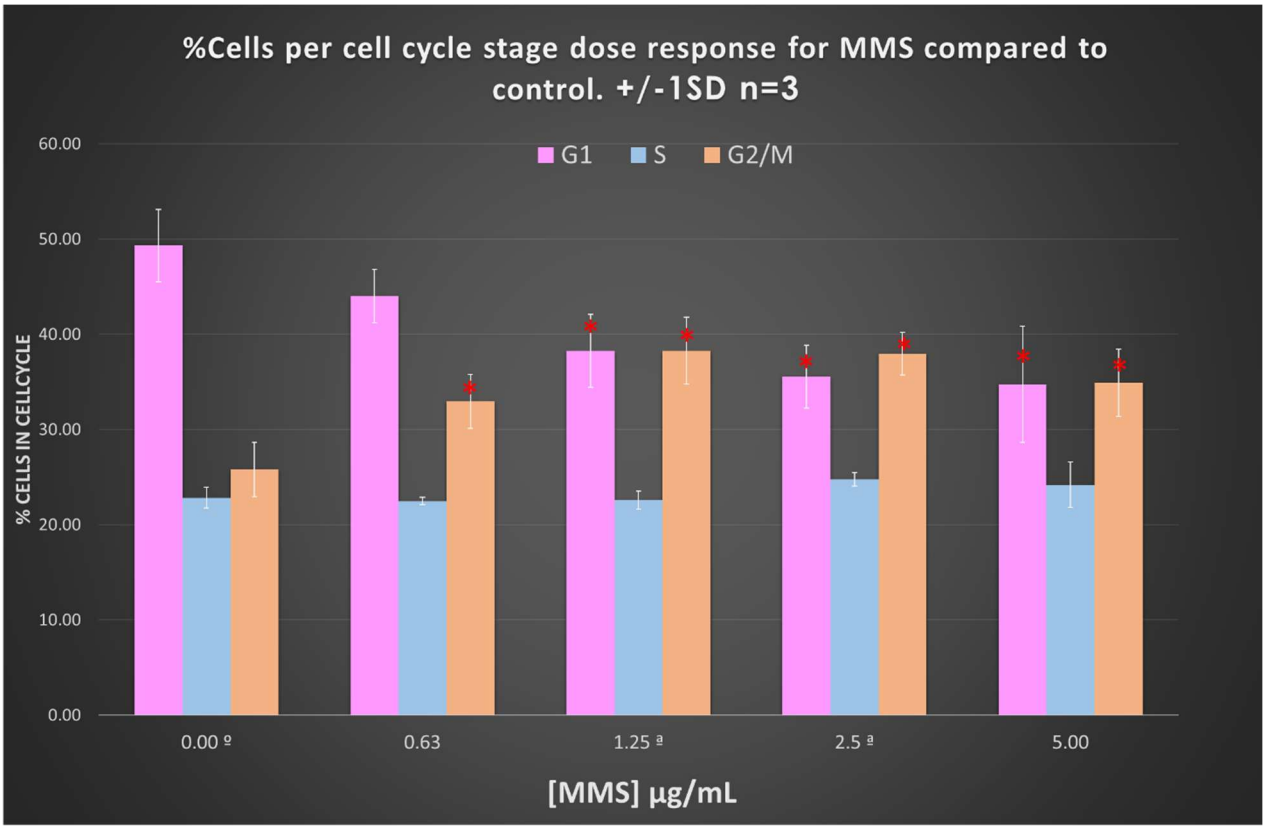

ºVehicle control DMSO
ªAquisition error n=2
**Significant response p value < 0.05* ** Highly Significant Response p value<0.0001*

Figure 4.5: Graph showing percentage of cells found in each portion of the cell cycle in relation to MMS concentration. Statistically significant decrease of cells in G1 phase compared to control was at 1.25 µg/mL and onwards though all doses showed a trend decrease. S phase remained stable across all doses though there is a slight s phase decrease from control at 0.63 and 1.25 µg/mL. G2/M cell populations increase and was significant at all doses.

As the system response occurs all within the same cell the platform allows additional relationship assessment passed that of overall dose response per biomarker. Tables 4.1a and 4.1b contain the fold responses for the assessment of each biomarker in relation to each stage of the cell cycle ±1 standard deviation is displayed, values that are highlighted green have shown a decrease in signal and values highlighted red a increase. Statistical significance is indicated with a Asterix.

Table 4.1a: Fold change average of biomarkers ɣH2AX and P53 in direct relation to the phase of the cell cycle the cell population is in ±1SD for MMS doses.

	Fold change of biomarker in relation to cell cycle																		
MMS (µg/mL)	G1 ɣH2AX	±SD	G1 P53	±SD	S ɣH2AX	±SD	S P53	±SD	G2 ɣH2AX	±SD	G2/M P53	±SD	Proph	±SD	Meta	±SD	Anaph	±SD	H3+ve ɣH2AX -ve	±SD
0.00 º	1.00	0.52	1.00	0.10	1.00	0.48	1.00	0.11	1.00	0.25	1.00	0.19	1.00	0.03	1.00	0.09	1.00	0.43	1.00	0.40
0.63	1.29	0.23	1.16	0.08	1.27	0.25	1.64*	0.08	1.13	0.19	1.62*	0.28	0.98	0.06	1.05	0.20	1.42	0.43	0.96	0.40
1.25 ª	2.10*	0.69	1.47*	0.33	2.03*	0.81	2.22*	0.24	1.67	0.71	2.20*	0.82	0.98	0.05	1.04	0.15	1.36	0.57	1.29	1.09
2.5 ª	2.57*	0.82	1.81*	0.39	1.99*	0.74	2.83*	0.27	1.37	0.45	2.42*	0.82	1.03	0.02	0.87	0.13	1.61	0.78	1.45	0.94
5.00	3.80*	1.78	2.49*	0.30	2.89	1.72	3.08*	0.91	1.29	0.58	2.24*	0.67	0.95	0.03	1.15	0.09	1.72	1.35	2.71	2.16

ºVehicle control DMSO
n=3 ªAcquisition error n=2 *Significant response p value < 0.05* ** Highly Significant Response p value<0.0001
Trend decrease Trend Increase

Table 4.1b: Fold change average of the ratio of Prophase, Metaphase and Anaphase cells populations when compared to control for MMS doses

	Mitosis stage fold change ratio		
MMS (µg/mL)	Prophase:Ananaphase+Metaphase	Metaphase:Prophase	Anaphase:Prophase
0.00 º	1.00	1.00	1.00
0.63	0.94	1.07	1.20
1.25 ª	0.85	1.19	1.13
2.5 ª	0.99	0.96	1.11
5.00	0.85	1.20	1.08

ºVehicle control DMSO
n=3 ªAcquisition error n=2 Trend decrease Trend Increase

The above data has been displayed as a set of scatter graphs for visual assessment of the data. Tables 4.1a and 4.1b have been plotted on a line scatter graph, figures 4.6 and 4.7 respectively.

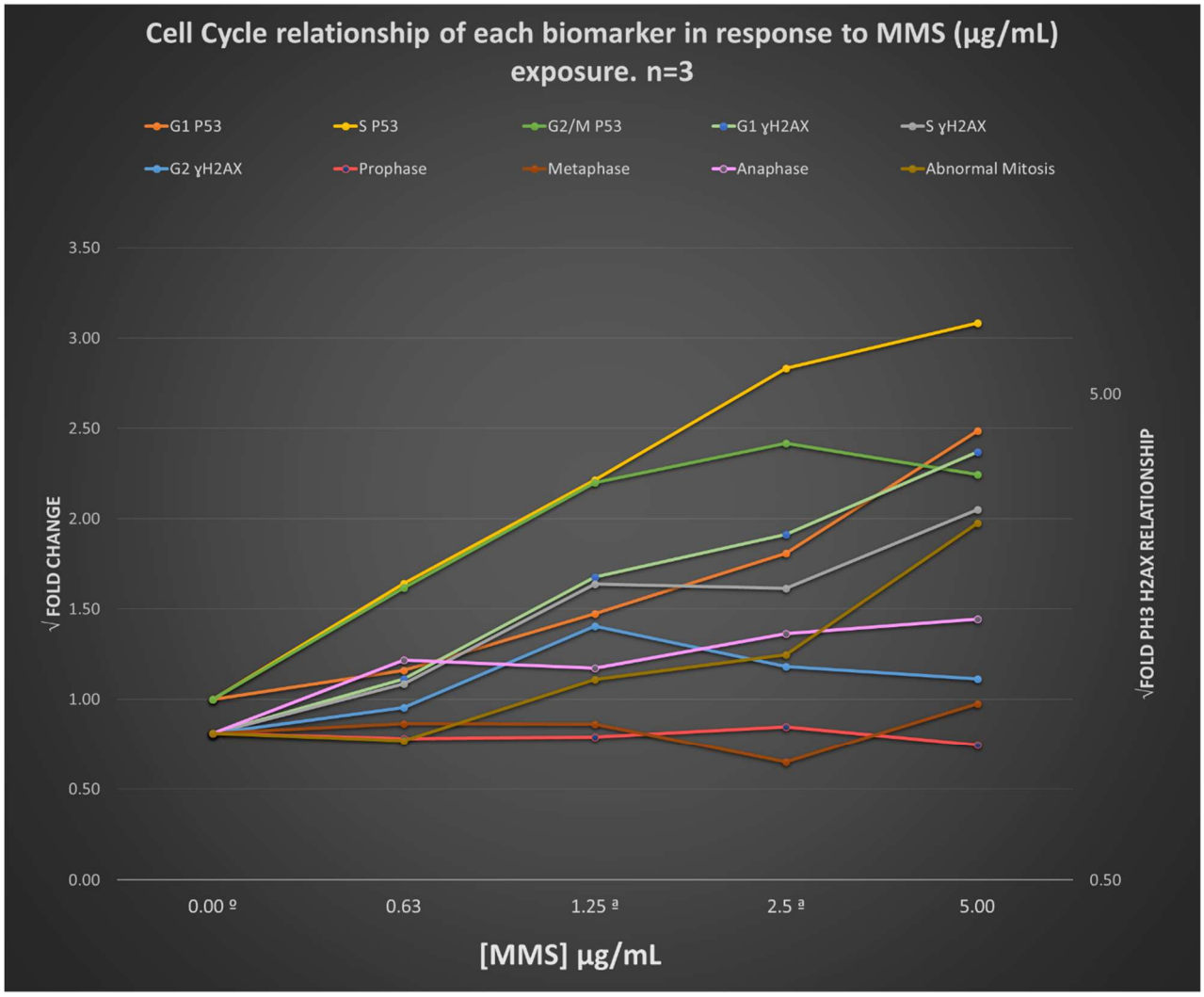

ºVehicle control DMSO ªAcquisition error n=2

Figure 4.6: Line scatter graph visually displaying data in table 4.1a illustrating relationship of each biomarker and cell cycle stage for MMS dose. The abnormal mitosis label refers to H3+ve H2AX-ve cell fluorescence. Primary Y axis shows the P53 response data. Secondary Y axis plots γH2AX and pH3 cell cycle signals and relationship the axis was log scaled. Statistical significance of each response can be found in table 4.1a.

When comparing figure 4.4 displayed results of the individual biomarkers to cell cycle analysis of the biomarkers, increases in the biomarker response for both γH2AX and P53

is observed for all doses. The data trend does show that the ɣH2AX response is highest in G1 phase and lowest in G2 phase whilst P53 response is highest in S phase followed by G2/M phase. This corresponds to the increase of cells in anaphase implying a mitotic arrest of some description which is also confirmed by the increase of abnormal mitotic cells that are positive for pH3 but negative for ɣH2AX response. Whilst cell mitosis ratios as displayed in table 4.1b and figure 4.7 show a limited change in the overall cells in prophase to metaphase and anaphase, a anaphase prophase ratio change effect is demonstrated.

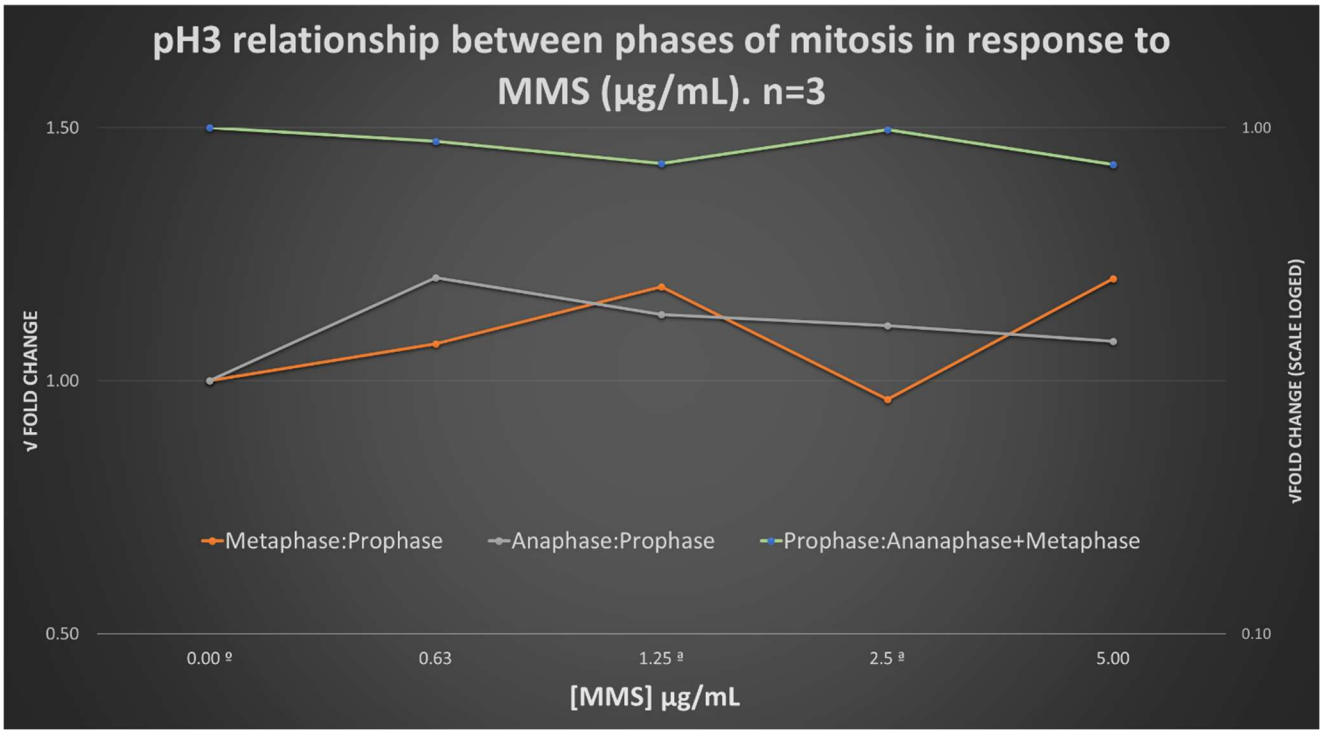

ºVehicle control DMSO ªAquisition error n=2

Figure 4.7: Line scatter graph displaying the ratio of average fold change responses for MMS concentrations (data in table 4.1b). Allowing assessment of proportional changes of the different phases of mitosis to one another. Primary Y axis shows the changes compared to vehicle control of the individual metaphase prophase change, and anaphase prophase change. Secondary Y axis plots the overall prophase response to anaphase and metaphase combined. No statistical analysis was performed, a qualitative trend only was looked at. There was a plateau trend of prophase population to the combined anaphase/metaphase population this was the same for the Anaphase prophase and metaphase prophase responses.

4.4.1.2 - Carbendazim: Optimal Staining Sub Optimal Laser Settings (Preliminary Response Data)

Carbendazim response data for individual biomarkers, their fold change and statistical evaluation are shown in figure 4.8. Followed by cell cycle response in figure 4.9. The response for ɣH2AX is reasonably stable when compared to control, however, there does appear to be an equivocal fold change decrease of ɣH2AX response at 0.6 µg/mL and 0.8 µg/mL for Carbendazim perhaps even showing a slight decrease, this is to be expected as Carbendazim does not induce strand breakage. pH3 signal increases and rises above the pH3 fold cut off value from 0.6 µg/mL onwards and is statistically significant for P53 at the same doses. The highest fold change induction of MN occurred at 1.20 µg/mL and was also statistically significant.

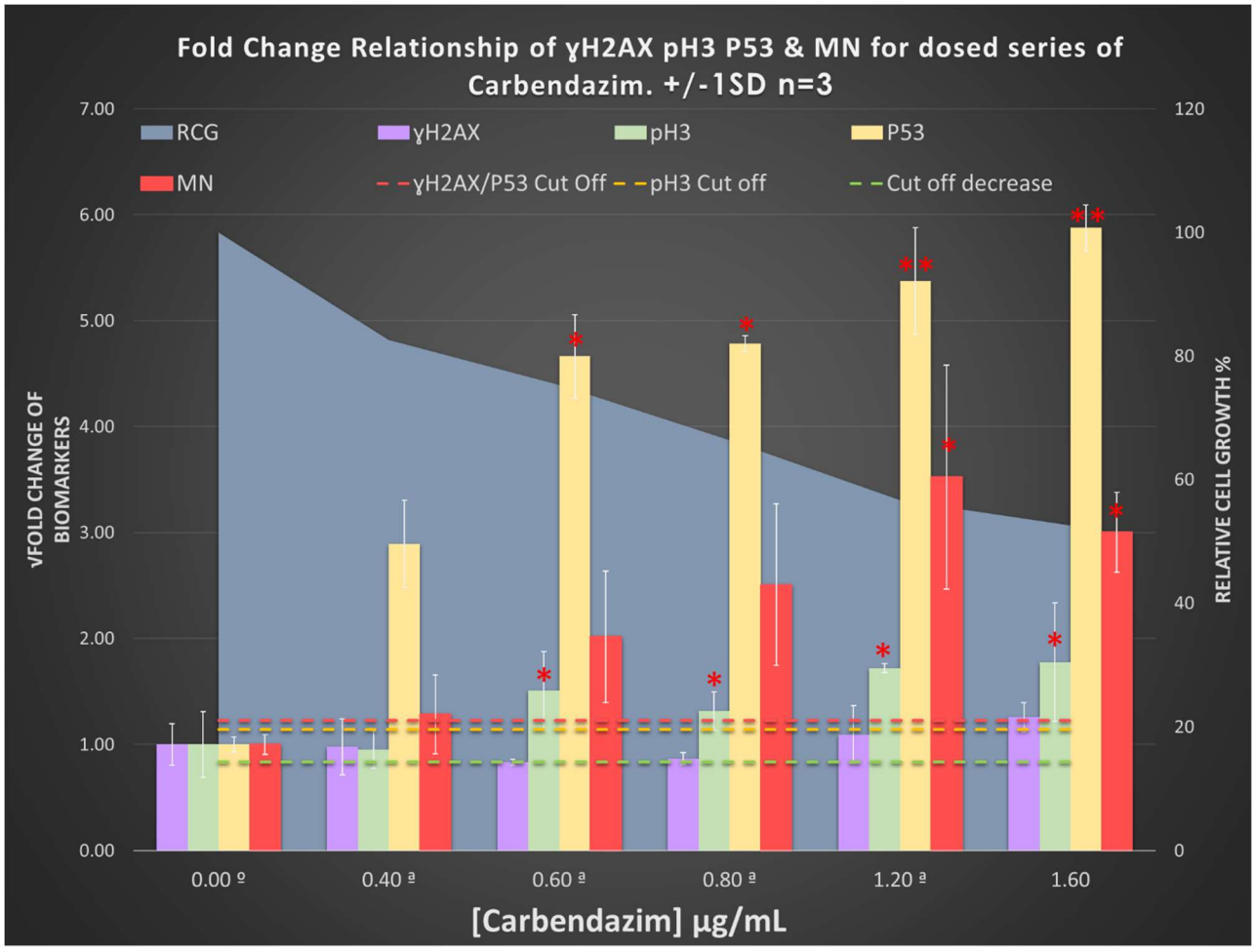

ºVehicle control DMSO
ªAquisition error n=2 **Significant response p value < 0.05** *** Highly Significant Response p value<0.0001*

Figure 4.8: Combination graph showing the square root of raw fold change values of the biomarker responses for γH2AX, pH3, P53 and the Micronucleus (MN) genotoxic endpoint in response to Carbendazim doses. RCG shows the % growth decrease of cell cultures as Carbendazim concentrations increase. The dashed lines are the fold change cut offs for the biomarkers pH3, P53 and γH2AX. This highlights a equivocal response for γH2AX decrease at 0.60 and 0.80 µg/mL. The doses that are statistically significant are indicated with Asterix. The only dose demonstrating NOGEL for all biomarkers is 0.40 µg/mL. The NOGEL for the MN response is at 0.80 µg/mL.

The cell cycle was also able to be assessed and displayed below in figure 4.9. The graph demonstrates that whilst the percentage of cells increases in G1 with dose S percentage decreases and G2/M phase remains reasonably stable when compared to the control cell cycle profile. G1 and G2/M responses are not statistically significant at any dose. S phase responses are significant at all Carbendazim doses.

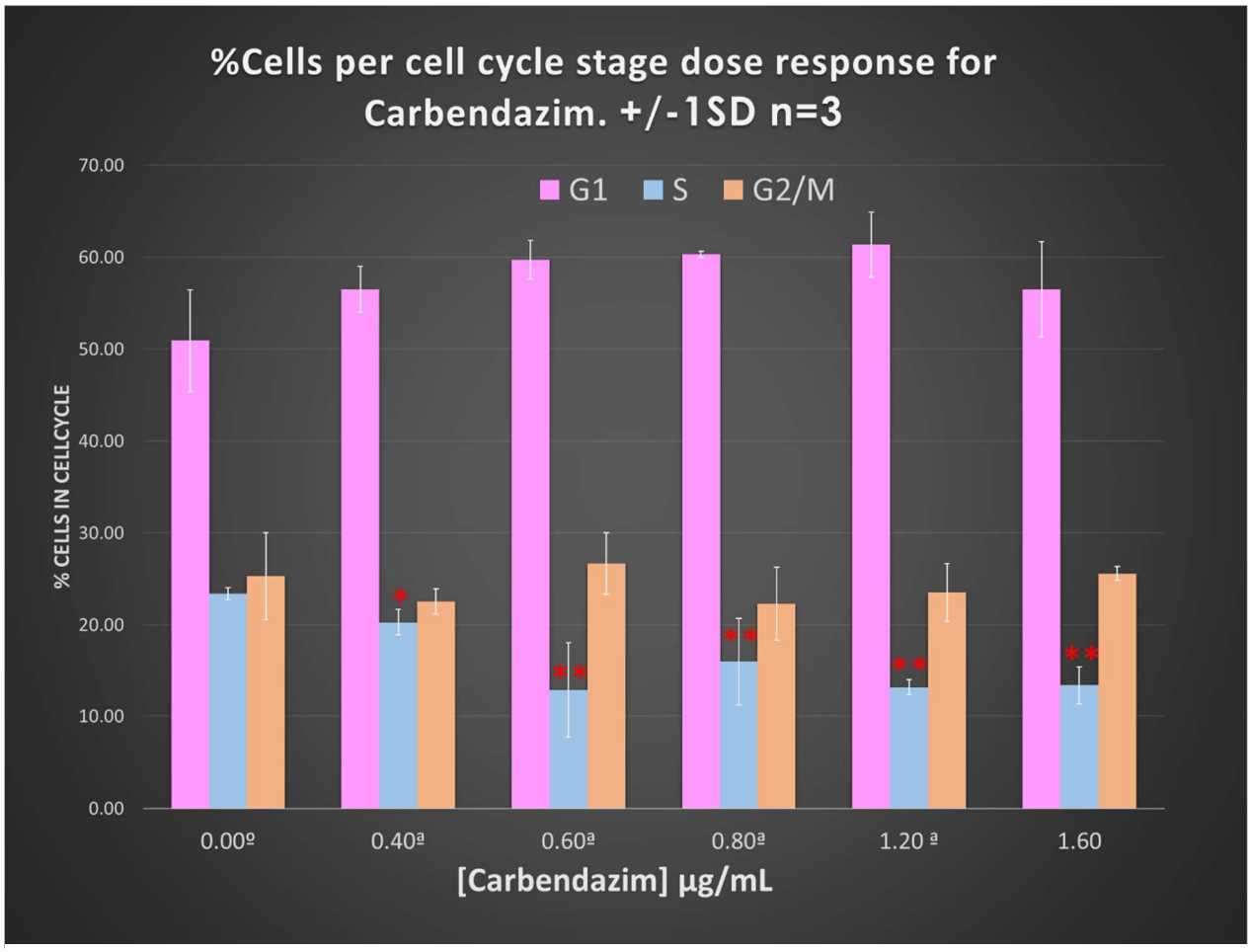

ºVehicle control DMSO
*ªAquisition error n=2 *Significant response p value < 0.05* ** Highly Significant Response p value<0.0001*

Figure 4.9: Graph showing percentage of cells found in each portion of the cell cycle in relation to Carbendazim concentration. Statistically significant decrease of cells in S phase was seen from 0.4 µg/mL onwards. Whilst not significant there was a trend increase of cells present in G1, the decrease toward vehicle control at 1.60 µg/mL is most likely due to increase in cell death as suggested by the RCG plot in figure 4.8. G2/M population remained relatively stable. Response was seen at doses 1.25 µg/mL onwards for G1 and G2/M at all doses. No significant change for S at any dose was observed.

As with MMS having this cell cycle data directly related to biomarker response could prove beneficial in identifying additional trends that lend themselves towards classifying chemicals. The tables 4.2a and 4.2b show these additional end point metrics and statistically significant responses are indicated with a asterix. These tables were then plotted graphically see figure 4.10 and 4.11 below.

Table 4.2a: Fold change average of biomarkers ɣH2AX and P53 in direct relation to the phase of the cell cycle the cell population is in ±1SD for Carbendazim doses

	Fold change of biomarker in relation to cell cycle																		
Crbz (µg/mL)	G1 ɣH2AX	±SD	G1 P53	±SD	S ɣH2AX	±SD	S P53	±SD	G2 ɣH2AX	±SD	G2/M P53	±SD	Proph	±SD	Meta	±SD	Anaph	±SD	H3+ve ɣH2AX -ve	±SD
0.00º	1.00	0.44	1.00	0.06	1.00	0.22	1.00	0.12	1.00	0.05	1.00	0.05	1.00	0.01	1.00	0.03	1.00	0.71	1.00	0.87
0.40º	1.17	0.37	2.62**	0.99	1.13	0.25	2.54	0.83	1.14	0.24	2.19	0.82	0.98	0.04	1.04	0.11	1.37	0.42	0.56	0.42
0.60º	0.92	0.51	4.15**	1.65	0.99	0.18	3.93	1.35	1.05	0.06	3.81*	1.50	0.97	0.02	1.10	0.07	0.97	0.20	1.01	0.61
0.80º	0.66	0.13	4.43**	1.14	0.89	0.12	4.18**	0.89	1.02	0.14	4.05*	1.16	0.95*	0.06	1.15*	0.19	1.06	0.04	2.52	2.00
1.20º	0.94	0.29	5.19**	0.52	1.32	0.39	5.23**	0.52	1.21	0.17	5.26**	0.81	0.92*	0.04	1.23*	0.12	1.25	0.22	2.30	1.43
1.60	1.15	0.20	5.89**	0.13	1.55	0.15	6.04**	0.56	1.32	0.18	6.02**	0.09	0.91*	0.04	1.26*	0.12	1.17	0.09	2.51	1.68

ºVehicle control DMSO
n=3 ºAquisition error n=2 *Significant response p value < 0.05* ** Highly Significant Response p value<0.0001
Trend decrease Trend Increase

Table 4.2b: Fold change average of the ratio of Prophase, Metaphase and Anaphase cells populations when compared to control for Carbendazim

	Mitosis stage fold change ratio		
Crbz (µg/mL)	Prophase:(Ananaphase+Metaphase)	Metaphase:Prophase	Anaphase:Prophase
0.00º	1.00	1.00	1.00
0.40º	0.93	1.06	1.63
0.60º	0.89	1.14	1.18
0.80º	0.88	1.24	1.31
1.20º	0.75	1.36	1.53
1.60	0.73	1.39	1.46

ºVehicle control DMSO
n=3 ºAquisition error n=2 Trend decrease Trend Increase

The ɣH2AX response especially in G1 population decreases and at 0.80µg/mL passed the 0.8 fold change cut off. From 0.80 µg/mL dose onwards levels of ɣH2AX in G1, S and G2 started to increase. The P53 response in relation to the cell cycle is interesting, here P53 at all doses in each of the stages of the cell cycle increase over that of control, all responses being greater than the 1.2 fold change cut off and being significant from 0.40 µg/mL in G1, 0.08 µg/mL in S and 0.06 µg/mL at G2/M. P53 G1 levels are slightly higher than the S and the G2M phases until 1.6 µg/mL where the signal starts to drop below the S and G2M response. From 0.8 µg/mL to the top dose both anaphase and metaphase increases being a greater than the 1.2 fold change cut off. When assessing

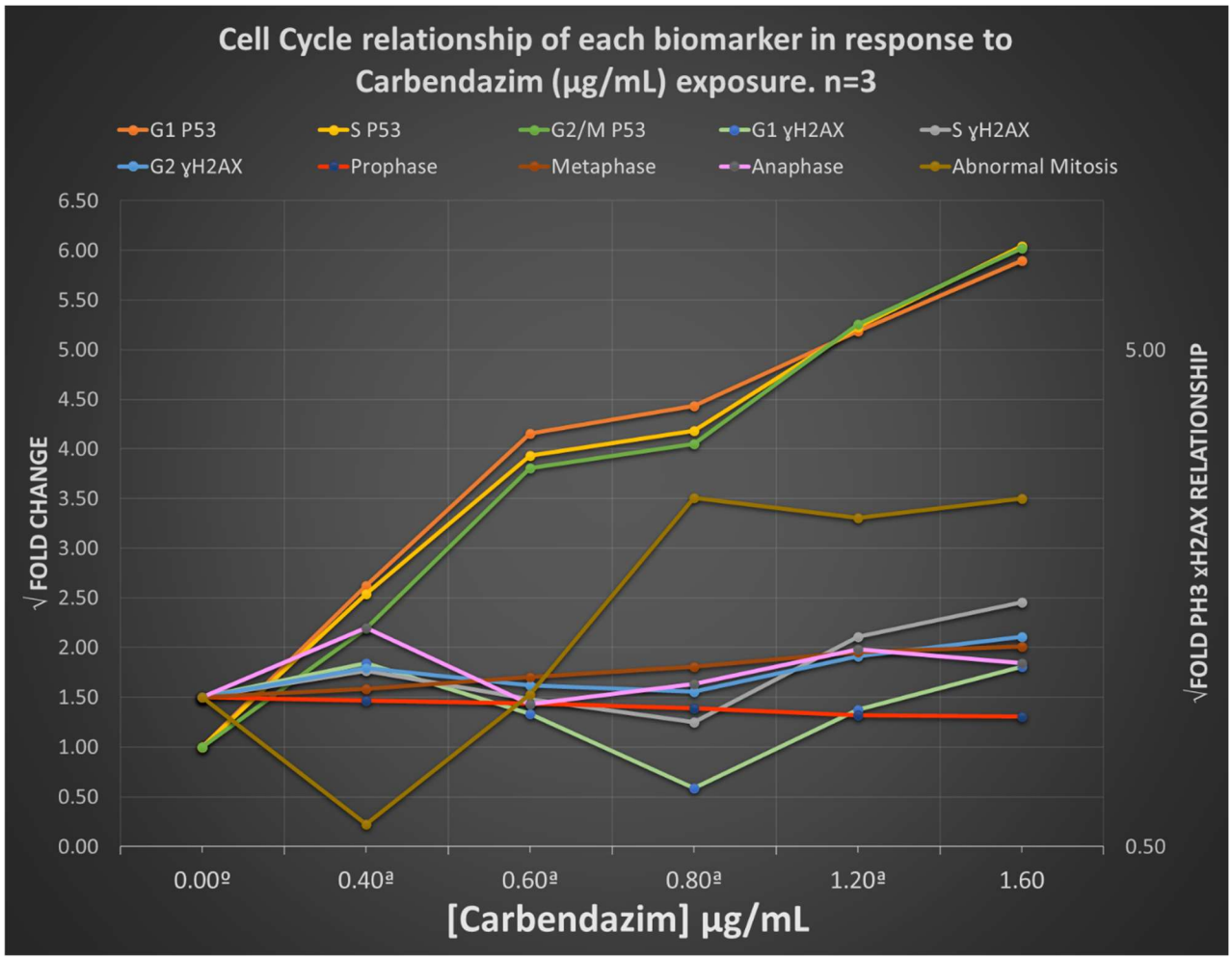

ºVehicle control DMSO
ªAquisition error n=2

Figure 4.10: Line scatter graph visually displaying data in table 4.2a illustrating relationship of each biomarker and cell cycle stage for Carbendazim doses. Primary Y axis shows the P53 response data. Secondary Y axis plots ɣH2AX and pH3 cell cycle signals and relationship on a logged scale. Statistical significance of each response can be found in table 4.2a.

the mitotic stages proportionally against one another as demonstrated by figure 4.11 below

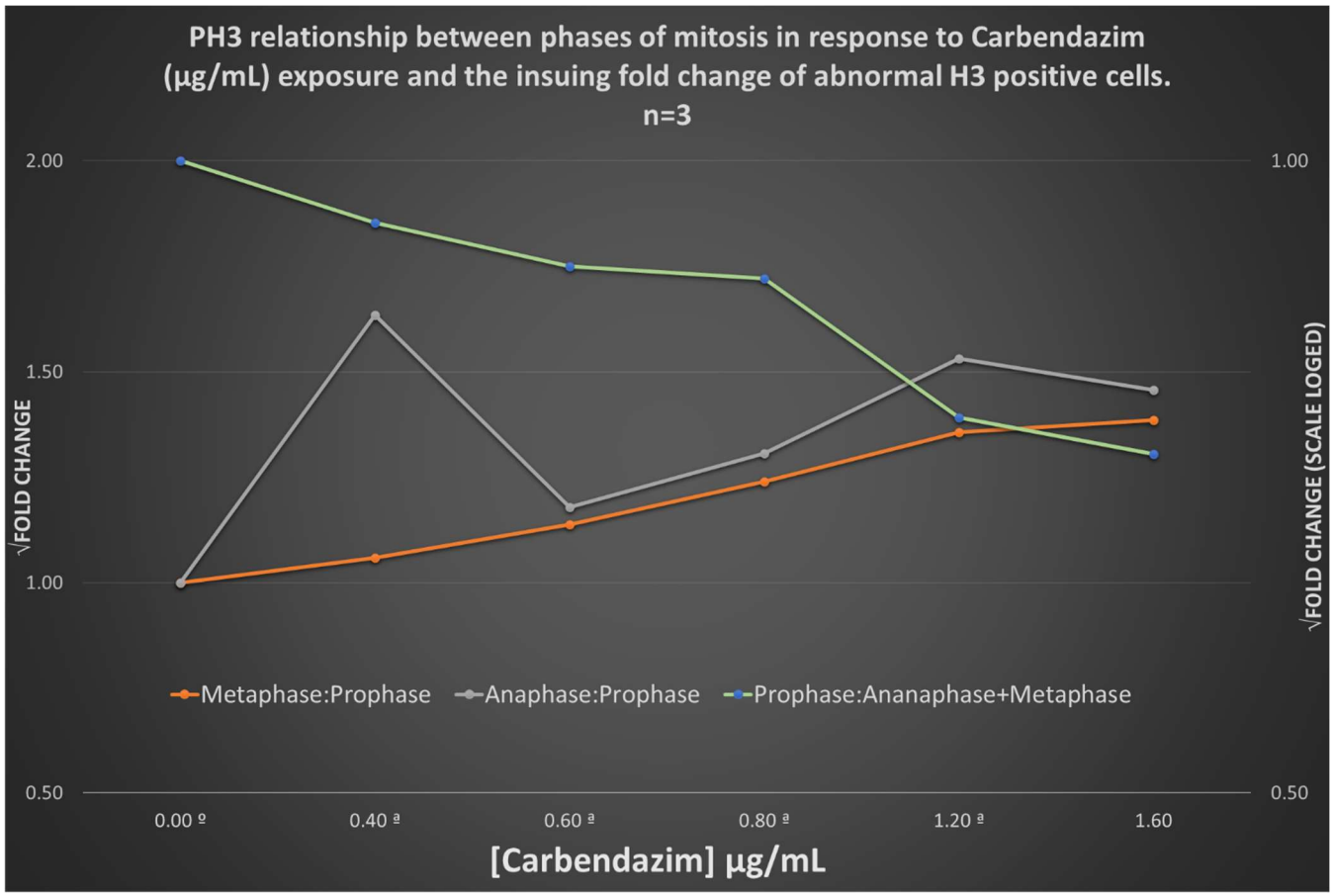

ºVehicle control DMSO
ªAquisition error n=2

Figure 4.11: Line scatter graph displaying the ratio of average fold change responses for Carbendazim concentrations (data in table 4.2b). Allowing assessment of proportional changes of the different phases of mitosis to one another. Primary Y axis shows the changes compared to vehicle control of the individual metaphase prophase change, and anaphase prophase change. Secondary Y axis plots the overall prophase response to anaphase and metaphase combined. No statistical analysis was performed, a qualitative trend only was looked at. There was an overall trend decrease of prophase population to the combined anaphase/metaphase population whilst there was a simultaneous increase of metaphase to prophase and anaphase to prophase cell populations. These occurred in a dose dependant manner.

The ratio of prophase to metaphase and anaphase population decreases as crbz dose increases this is mirrored by a corresponding increase in the anaphase to prophase.

4.5 – Discussion

4.5.1 – Preliminary Data Set: Dual Biomarker and MN Assessment

This preliminary data comparing response of the biomarkers ɣH2AX and pH3 for MoA assessment against separately stained DRAQ5™ cells for MN assessment allows for a initial proof of principle assessment. From the data increases in micronucleus dose responses can be observed, alongside their corresponding respective responses with the MoA markers ɣH2AX and pH3. The data appears to demonstrate the typical responses indicative of MMS acting via a clastogenic MoA and Carbendazim acting through an aneugenic MoA.

For MMS there was a dose dependent increase of ɣH2AX and MN at the same doses where pH3 signal decreasing. The relevant increase in ɣH2AX reflects an increase of cells with DNA strand breaks, at the same concentration as MN, along with there being a decrease of cells in mitosis as demonstrated by the reduction in pH3 signal. From the results generated, MMS appears to cause MN through chromosome breaks, and this is displayed without the need for kinetochore labelling. By contrast the aneugen Carbendazim had the reverse ɣH2AX, pH3 profile at the same concentrations as an increase in MN. The decrease in strand breaks observed, could be linked with mitotic arrest, and the increase in pH3 is in line with the response of known aneugens, particularly when happening at the same concentrations as the increase in MN. This suggests that MN are generated through aneuploidy dominant mechanism.

Use of this dual staining approach on the Amnis® Imaging flow cytometry platform allows for specific image analysis of individual cells, combining the assessment of signal intensity (both ɣH2AX and pH3) per cell and cellular morphology offers additional Mode of Action information alongside the MN assay.

ɣH2AX and pH3 use on the flow cytometry platform have become increasingly popular and the combination of ɣH2AX and pH3 signal results on the Amnis FlowSight® has proven consistent with current literature (Bryce *et al*, 2016; Khoury *et al*, 2016). Combined use of ɣH2AX and pH3 signal in a single sample provides a reduction in experimental variability when compared to separate sample analysis. This process also reduces time of sample preparation, number of samples needing to be assessed and amount of compound required for analysis.

4.5.2 – Optimal Staining Preliminary Data Set

The biomarker response for MMS is consistent with the expected biology as P53 is a DNA damage marker and its increase in line with ɣH2AX increase shows a double check system that confirms the DNA damage response alongside MN induction. Whilst there is an initial increase of pH3 response, above the fold change cut off, at 0.63µg/mL compared to control and the 1.25µg/mL dose is still higher than vehicle control, the pH3 biomarker shows a decreasing trend as the MMS dose increases from 0.63µg/mL. Whilst there is no statistically

significant increase or decrease when compared to that of control, the initial increases of pH3 does rise above the fold change cut off at 0.63 µg/mL and 1.25 µg/mL and then at 5.0 µg/mL does fall below the 0.8 cut off value. This could suggest that MMS at lower doses may have a dual MoA. Similar observations have been made in the literature (Bryce *et al*., 2017; Krishner *et al*., 1992). The large standard deviation bars for the MN response is to be expected due to the variability of MN automated counting as explained in section 3.3.3.3 The accuracy rate of the system is only 57% with a miss rate of around 45%, for chemicals that induce the smaller MN such as MMS due to the largely clastogenic nature of the chemicals MoA the system simply isn't sensitive enough to identify these smaller events especially in the Mono MN assay where the nucleus takes up more of the cell cytoplasm offering more places for the MN to 'hide' behind the nucleus or blend with it depending on cell orientation when passing by the camera. Assessment of the cell cycle alongside the biomarker responses demonstrates a cascade type of event i.e., a increase of ɣH2AX in G1 leads to an upregulation of P53 resulting in a increase of DNA damage response pathway leading to DSB being fixed during S phase. As a result, ɣH2AX response decreases during S phase resulting in the loss of statistically significant responses at G2. A limited decrease of P53 at G2M demonstrates DNA damage is still present after S phase.

Delving further into the cell cycle relationship of fold increases in each stage of the cell cycle, with the highest P53 response being in the S phase followed closely by G2M phase and the highest response being in G1 for ɣH2AX. These responses for ɣH2AX are to be expected as it is a transient DNA damage repair signal, this means when the cell cycle passes through its check points more damaged is detected by the cell and so there is a corresponding increase of ɣH2AX signal as the cell recruits damage repair proteins. Whilst overall there wasn't really a change in pH3 levels there was an increase of anaphase cells and when assessing pH3 response for each prophase, anaphase and metaphase there was a ratio decrease of cells in prophase when compared to the combined metaphase and anaphase population and a ratio increase of anaphase cells. The metaphase ratio did not change.

The chemical Carbendazim works through a aneugenic MoA via microtubule destabilisation (Hummelen *et al*., 1995). A statistically significant response for pH3 induction was found at all doses with the exception of 0.40 µg/mL an indication of aneugenicity (Muehlbauer & Schuler, 2005) The strongest P53 response is in line with the MN response increase, and whilst this is the same for MMS the fold change P53 for MMS did not exceed 3 fold induction. This is to be expected as loss of chromosomes is a more damaging effect on the cell than strand breakages. The higher MN response picked out by the system could also be as a result of the aneugenic MoA, as the MN present in the cell will be of the larger variety therefore stained easier and less able to hide behind the nucleus as is probably the case with MMS above. The MN response is again proportional to the DNA damage P53 signal response and the increase of cells arresting in mitosis. Whilst there is a increase of cells with pH3 you would expect a corresponding increase of G2M cell population rather than G1.

However, all this means is that whilst the percentage population in G2/M has not changed a greater proportion of those cells have arrested in mitosis therefore leading to the increase in pH3 signal. These cells once they eventually pass into G1 a higher proportion will be abnormal resulting in cells that cannot pass the G1, S check point. This therefore explains the decrease in S phase population, as cells are halting at G1 but healthy synthesised cells continue on into G2/M. The increase of ɣH2AX at the different phases of the cell cycle at the higher dose concentrations is most likely due to apoptotic pathway induction which results in the global phosphorylation of ɣH2AX (Moeglin *et al*., 2019; de Feraudy *et al*., 2010).

The P53 cell cycle signal response is line with the cell cycle assessment graph and suggests the most active phase for DNA damage and cell cycle control is actually S phase relative to G1 and G2M when you compare the small cell population. As explained above the lack of ɣH2AX presence in abnormal mitotic pH3 positively stained cells could be a indicator of clastogenicity vs aneugenisity and as the graph displays there is a large fold change in the abnormal mitotic (ɣH2AX -ve H3+ve) response from 0.6 µg/mL onwards. This combined with the individual assessment of prophase, metaphase and anaphase and the ratio responses to one another based on the pH3 response implies the cell cycle is stalling specifically at metaphase/anaphase stages of mitosis, as Carbendazim is suspected to affect spindle stability this affect is reasonable to assume. This proportion trend and over all cell cycle biomarker responses is consistent/similar with another aneugenic spindle poison assessed, Vinblastine (See section 5 below).

There is a overall trend increase of P53 for both the Carbendazim and MMS data set along with a mirrored response of MN induction. The increase of biomarker the biomarker signals pH3 and ɣH2AX respectively for Carbendazim and MMS, are indicative of aneugenic and clastogenic MoA's. These responses are consistent with that found in the literature (Bryce *et al*., 2007, Audbert *et al*., 2010)

4.5.3 – Disparity Between FlowSight® and ImageStream X Mark II®

The above data of the 3 marker and MN genotoxic endpoint combined system shows a trend that consistent with the preliminary development stage data response in section 4.3 above. However, there are some discrepancies for instance the pH3 response in the multi-marker system does not give as definitive a trend decrease from control level for MMS and as large a increase for Carbendazim. This could be due to a few reasons; 1) As the data was collected at different magnifications on separate machines the plane of focus for spectrum detection the machine is able to collect is different. This is demonstrated by figure 4.12 below.

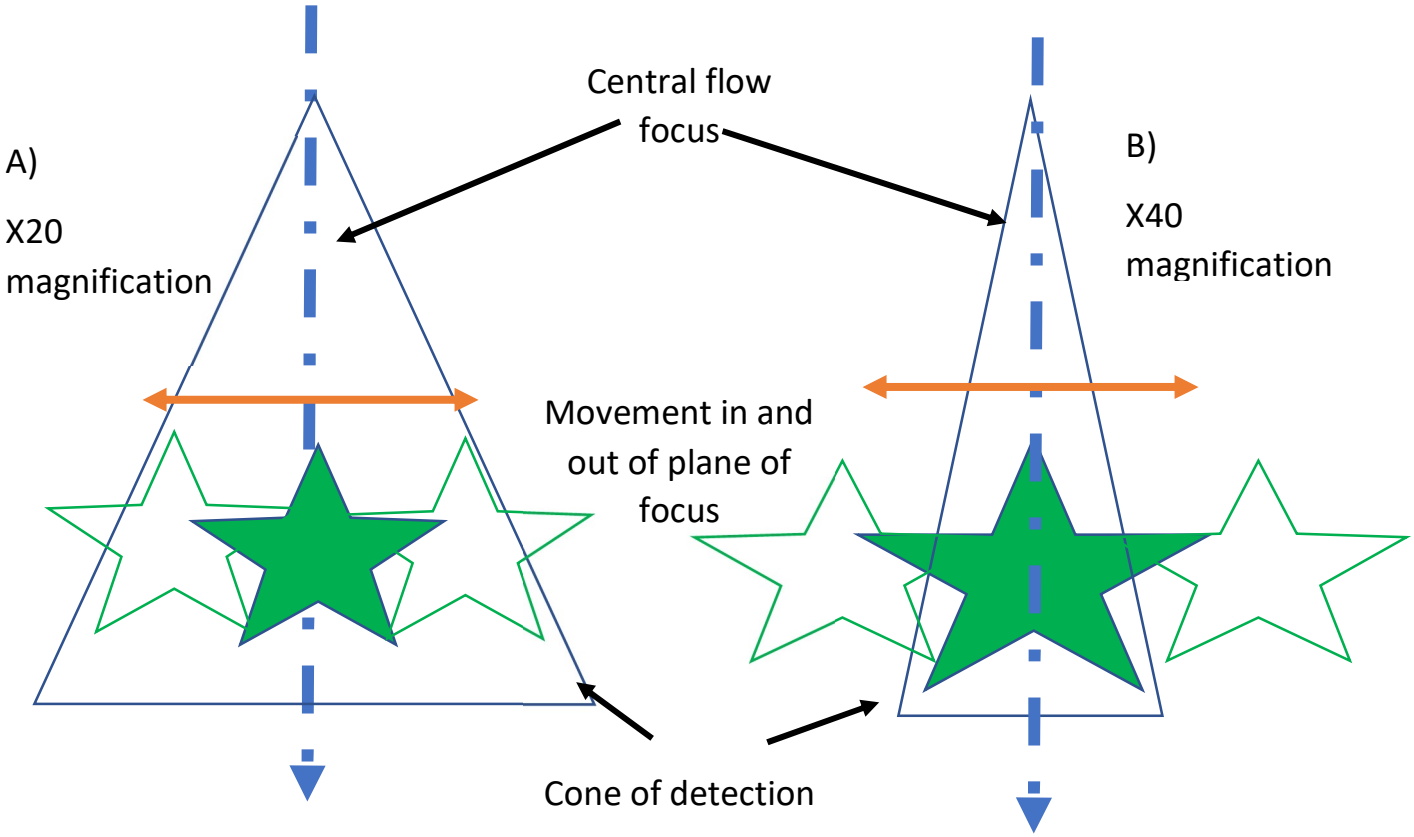

Figure 4.12: Demonstrates the variation in spectrum detection between X20 FlowSight® machine and X40 ISXII. A) Shows that at lower magnification the detector has a greater field of view to both collect more of the spectrum emitted by the fluorophore and has more tolerance for object movement in the focal plane. B) At a higher magnification the cone of detection becomes narrower this means the system has a lower tolerance for movement out of the central plane of focus and less of the available excitation spectrum is detected.

This limitation of the imaging flow system explains why at a lower magnification the pixels available have a higher overall fluorescence intensity causing some saturation even at lower laser powers and optimal staining compared to the higher power settings at the x40 magnification. This means some of the lower intensity pH3 stained cells in the control samples may have been missed by the higher magnification system. Due to this lower end of the population being missed the overall proportional change of the pH3 signal could have been affected.

Whilst there are some discrepancies between the data collected on the FlowSight® and ImageStream X Mark II® the overall trend that ɣH2AX increases for MMS and pH3 increases for Carbendazim whilst the alternate marker plateaus/ does the opposite remains. Furthermore, the data is in line with expected clastogenic aneugenic MoA already reported in the literature (Bryce *et al*., 2007; Bryce *et al*., 2016; Smart *et al*., 2011; Audbert *et al*.,

2010). This also demonstrates that a multiplex system that assesses the biomarker P53 ɣH2AX, pH3 and MN can be achieved simultaneously in the same cell sample without lysing the cells meaning spatial location information is maintained and can be used for further in depth data analysis and mining.

Despite suboptimal laser excitation of the biomarker's identification of MMS as a clastogen and Carbendazim as a aneugen was possible at the 24hr time point. Furthermore, additional cell cycle relationship information was obtained suggesting most likely location of cell cycle arrests and what biomarkers are most prevalent when. Whilst this type of data individually is not necessarily new, assessment in single sample of whole unlysed cells allowing for direct relationship analysis in a high content fashion using the imaging cytometer platform is. This along with the flexibility of including additional mechanistic markers, shows that this platform is well placed for the next generation of genotoxicity testing

Chapter 5 – Results 3: ImageStream Micronucleus Expansion (ISMN-me) assay: Optimal Staining and Laser Acquisition For The Chemicals ARA-C, Vinblastine, Etoposide and Crizotinib.

5.1 - Introduction

As established in section 4.1, the use of ɣH2AX, pH3, P53 and DRAQ5™ in a multiplexing system in TK6 cells is possible and the responses in the model chemicals MMS and Carbendazim are consistent with that in the literature. Figure 5.1 shows the type of images acquired using the multiplex platform that available for analysis.

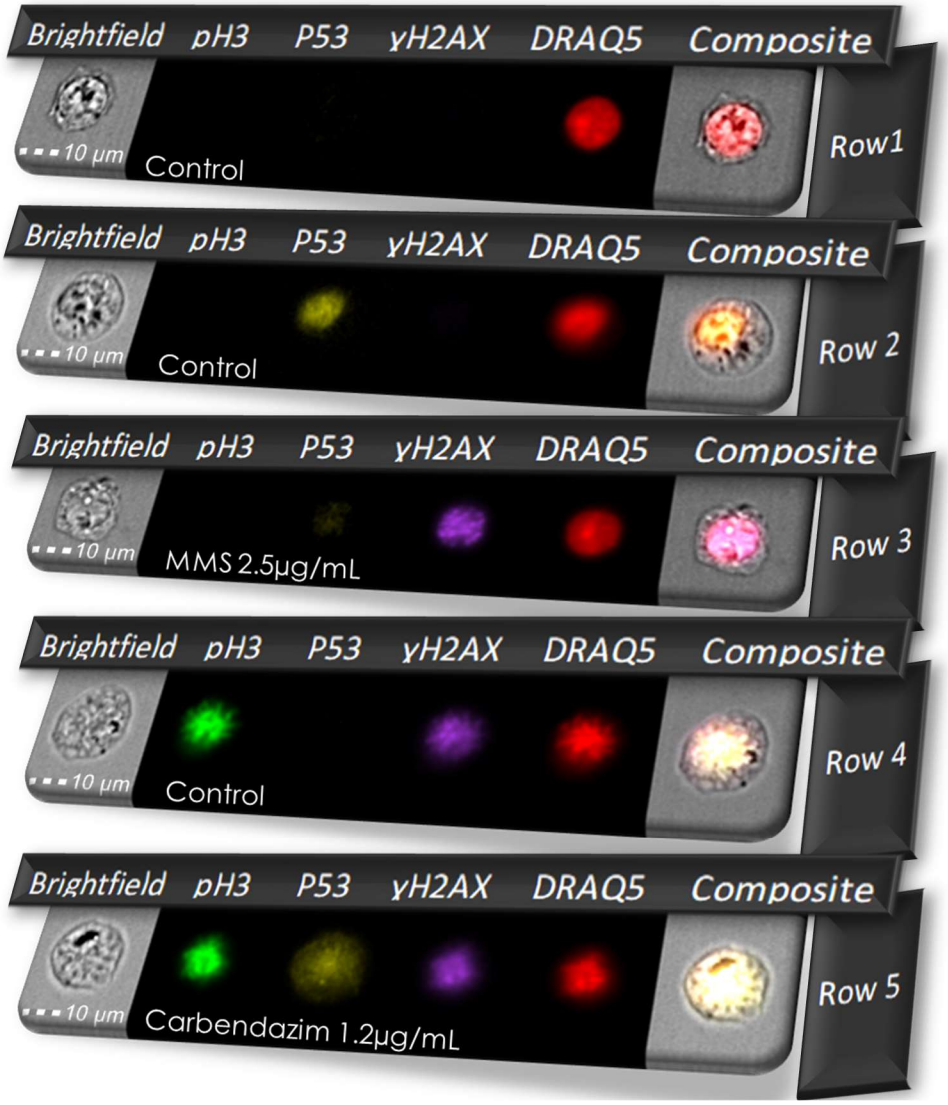

Figure 5.1: Images obtained at x40 magnification on Amnis ImageStream X mark II® demonstrating the combined platform. This allows the assessment of ɣH2AX, pH3, P53 and MN generation simultaneously. Rows 1,2 and 4 show vehicle control biomarker examples. Row 2 shows P53 activation in potentially in response to cell cycle control. Row 4 shows a healthy biomarker response in metaphase. Row 3 demonstrates a typical ɣH2AX response in relation to a clastogen. Row 5 demonstrates a P53 response for a cell in mitosis when exposed to a aneugen.

Assessment of additional chemicals of known classification, mode and mechanism of action is required to further assess this multiplexing platform ability to identify chemicals of varying MoA.

Whilst genotoxic chemicals can be broadly divided into Clastogens and Aneugens as the predominant MoA, the underlying mechanisms are often varied. Taken from the list of ECVAM recommended chemicals for assessment of new *in vitro* genetic toxicology assays, Kirkland *et al*. 2016, the additional chemicals assessed under 24 hour exposure at varying concentrations were, the Aneugens: Crizotinib, which is a tyrosine kinase inhibitor and Vinblastine which binds to tubulin inhibiting microtubule formation (Sahu *et al*., 2013; Kong *et al*., 2018; Alder *et al*., 1991. The Clastogens: Etoposide is a topoisomerase II inhibitor and Cytosine Arabinoside (ARA-C) which is a nucleoside analogue that inhibits DNA synthesis (Kirkland *et al*., 2008; Fenech *et al*., 1994). These chemicals were selected as alternate platforms have assessed them using the biomarkers ɣH2AX, pH3, P53 either individually or in some form of combination (Dertinger *et al.*, 2019; Watters *et al*, 2009; Cheung *et al*, 2015; Khoury *et al*, 2016). Further to this, as each chemical has a different MoA and underlying mechanism the platforms ability to correctly identify MoA and potential variations in biomarker responses can be investigated.

This ImageStream MN multiplex expansion assay, termed ISMN-me assay, initially assesses the traditional response of these DNA damage markers in fold change using both gating and microscopy strategies. Through immunohistological staining with antibodies the following are identified; pH3 providing metaphase cell frequency as a aneugenic flag (Muehlbauer & Schuler, 2005), ɣH2AX identifying clastogenicity based on fluorescence shift within nuclei (Smart *et al*., 2011) and P53 stabilisation as a signal for DNA damage induction (Sun *et al*., 2013; Bernacki *et al*., 2016). Counterstaining the DNA with DRAQ5™ allows for the identification of the MN genotoxic endpoint and cell cycle assessment based on the change of cell population percentage in G1, S and G2/M relative to vehicle control (Fenech *et al*., 2011; Parry & Parry 2006; Avlasevich *et al*., 2011).

This chapter focuses on the ability of ISMN-me to identify dose responses of the DNA damage biomarkers ɣH2AX, pH3, P53 and MN endpoint in fixed permeabilised P53 proficient TK6 cells using ImageStream X Mark II® leading to MoA identification. Given the intact nature of the cells, maintaining the integrity of the cytoplasmic membrane, the platform also investigates cell cycle response relationships for each of the biomarkers, identification of mitotically abnormal cells, as well as biomarker presence within MN. Thus, providing scope for identification of underlying mechanistic flags within the MoAs.

5.2 – Materials & Methods

5.2.1 - Test Article Formulation

Master stock solutions for each chemical were made fresh on the day of the experiment. DMSO (Cas. No. 67-68-5) was the solvent used to generate the dose concentrations and was therefore used as vehicle control. In instances where the chemical would not go into solution gentle warming and vortexing was used.

Methyl Methanesulphonate (MMS), Cas no.: 66-27-3, Carbendazim, Cas no.: 10605-21-7, Crizotinib (Crztb) Cas no.: 877399-52-5, Etoposide (Etop) Cas no.: 33419-42-0, Cytosine β-Darabinofuranoside (ARA-C) Cas no.: 147-94-4 and Vinblastine (Vbstn) Cas no.: 143-67-9 all supplied from Sigma-Aldrich.

Working concentrations for the remaining chemicals were: Crizotinib, 0.00, 0.57, 1.31, 2.25, 4.51 (µg/ml); Etoposide 0.00, 0.01, 0.03, 0.06, 0.13 (µg/ml); ARA-C 0.00, 0.01, 0.03, 0.05, 0.21, 0.41 (µg/ml); Vinblastine, 0.0000, 0.0002, 0.0006, 0.0008, 0.0010, 0.0020 (µg/ml).

To confirm test validity positive controls of MMS and Crbz were used as confirmation of true system activity and response for P53, ɣH2AX and pH3 was ran alongside each of the test article experimental repeats. MMS positive control doses were 2.50 or 5.00 (µg/ml) and Carbendazim positive control doses were 1.20 or 1.60 (µg/ml). Whilst this data was not shown a statistically significant response was obtained when compared to vehicle control relevant to the MoA.

5.2.2 - Cell Culture and Growth Media

Refer to general methods section 2.2.2.

5.2.3 - Treatment Of Cell Cultures

TK6 cells were cultured at $2x10^5$ cells/mL and treated with Crztb, Etop, ARA-C or Vbstn for 1.5-2 cell cycles alongside concurrent positive controls. All incubation steps occurred at 37˚C, 5% (v/v) CO2± 0.5% in air. Please refer to section 2.2.2.1 for further detail.

5.2.4 – ISMN-me Antibody and DNA staining

Antibody master mix was prepared fresh on the day of experiment, 300ul of the antibody master mix was added to each sample and protected from light. After the initial incubation period 100ul of DRAQ5™ was added to each sample for continued incubation. Full details of the staining procedure please see section 2.2.3 of general methods.

5.2.5 – ISMN-me Cell Processing

After the treatment period, cultures were washed then fixed and permeabilised by FACS Lyse. Post fixation samples stained and incubated under agitation whilst protected from

light. Please see section 2.2.3 for full fixation and staining procedures with focus on route B of figure 10 highlighting the optimal workflow.

At the end of the incubation period cells were then transferred to appropriately labelled Eppendorf's and shipped on ice via DHL to: Newcastle Flow Cytometry Core Facility (FCCF), William Leech Building (2nd floor Room M2.099), Newcastle University, NE1 7RU, for subsequently acquisition on the ImageStream X Mark II® imaging platform.

5.2.5.1 - ImageStream Flow Cytometry: ImageStream X Mark II®

Samples were analysed on a Amnis® ImageStream X Mark II® imaging flow cytometer using Amnis® INSPIRE™ software version 6.2 (Merck Millipore, Nottingham UK). Prior to experimental analysis, following the manufacturers instructions for appropriate ImageStream X Mark II® set up and quality control procedures, all system calibrations performed and passed using Amnis® ImageStream SpeedBead calibration reagents (Cat. No. 400041). 100µL aliquots of cell suspension at a concentration of ~$7x10^5$ and no less than ~$4x10^5$ cells/mL were prepared in 1.5mL Eppendorf's for shipment upon arrival at the FCCF facility samples were transferred to a 96 well plate and loaded on the sample port. All samples were excited using 405nm, 488nm 642nm lasers at 120mw, 90mw, 80mw respectively. Laser 785nm was used for side scatter at laser power 5mw. INSPIRE® instrument software acquired cell data at a low velocity 66.0(mm/sec), resulting in 15,000 – 30,000 single cellular events being collected in approximately 45 seconds, and subsequently automatically saved for each experimental replicate. Acquisition of images for pH3, P53, ɣH2AX and DRAQ5™ assessment occurred in: Channel 2, 3, 7 and 11 fluorescence respectively; Channel 1, bright field; Channel 6 side scatter. Whilst these channels were of main interest data was acquired for all 12 channels. Additional detail on INSPIRE® template set up and image acquisition, including laser balancing can be found in section 2.2.4.2.2 and 2.2.4.2.3.

Once data has been collected for all samples, the acquired raw image files (.RIF) data files were analysed using IDEAS® v 6.2 software, compensation matrix and template applied and subsequent, .CIF (compensated image files) and .DAF (Data Analysis Files) were generated.

5.2.5.2 - INSPIRE™ Compensation File Acquisition

Compensation sample files were acquired using the INSPIRE® acquisition compensation wizard or manually using Compensation beads. Acquisition of correct compensation samples was performed without the presence of brightfield or side scatter. Lasers 488nm 405nm and 642nm were utilised at the same intensity value as used during the experimental setup. Acquired files formed compensation matrices in AMNIS IDEAS® 6.2 software. Further detail on the compensation applied to files can be found in section 2.2.4.2.

5.2.5.3 - Amnis IDEAS® v 6.2 Template

Data analysis was conducted using Amnis IDEAS® software version 6.2 (Merck Millipore, Nottingham, UK). Prior to signal assessment RIF files were converted to compensated image files (CIF) and data analysis files (DAF).

Of the initial RAW cell population collected using brightfield and nuclear parameters single in focus healthy cell population was determined as laid out in section 3 DNA content was then plotted on a histogram, and cells with nuclear intensity greater than $1X10^5$ was the final population used for MN, ɣH2AX, P53 and pH3 assessment.

Using the brightfield channel and DRAQ5™ DNA stain for the assessment of mononucleated MN cells, the cell population was determined my using nuclear mask 3 to distinguish mononucleated cells from cells with multiple nuclei using the spot count feature. This mononucleated population of cells was then used to generate MN data. The designed mask termed Complete final micronucleus mask in combination with spot count feature was used to automatically score the MN response (See section 3.3.3.3 for in depth description nuclear and MN masking criteria). The automated MN scoring within the mononucleated cells was carried out by attempting to include the criteria designed for slide based scoring (Fenech *et al*., 2003) in the MN mask. Therefore, the MN that were DRAQ5™ positively labelled were accepted for scoring were, circular/oval, 1/3-1/16 the size of the main nuclei and resided within the cytoplasmic boundary. A minimum of 5000 mononucleated cells were assessed per dose, per replicate to obtain the MN dose response.

For the assessment of BV421, ɣH2AX, AF 488 pH3and PE P53 fluorescence signal positivity was determined through pixel intensity via stained vs unstained populations assessment, signal separation on scatter graphs and specific signal masking based on nuclear/cytoplasmic localization. Gates were then applied to scatter graphs to extract positively stained cell populations for each of the three biomarkers (see section 3 for boundary cut-offs and mask development). To assess the specific biomarker response per stage of the cell cycle the same gate cut offs were used as the overall population assessment of each of the biomarkers but the populations used were taken from the cell cycle gates placed on the DNA content graph. Once these parameters were established the CIF files were batch processed via the use of an IDEAS® template, generation described in section 3 results.

5.2.5.4 - MN Containing Biomarker Signal

Whilst not assessed automatically using the optimised IDEAS® template of the true MN population (confirmed manually) a brief look into presence of either P53 and or ɣH2AX signal is present in distinct MN. This was performed by assessing the P53, ɣH2AX and DRAQ5™ DNA stain channels along with composite overlay of signal images and brightfield. The criteria here was simple, visually do the MN have: DRAQ5 and ɣH2AX

signal; DRAQ5™ and P53; DRAQ5™ with both P53 and ɣH2AX; DRAQ5™ only. This was performed as preliminary assessment as to whether the high content nature combined with imagery allows for assessment of rare cellular events providing additional MoA information.

5.2.5.5 – Data Assessment

Positive response criteria of fold change values and statistical analysis were as described in 2.2.6 data assessment section of general methods.

5.3 – Results: ISMN-me Assay Chemical Assessment

5.3.1 - Etoposide

Etoposide inhibits topoisomerase II and primarily impacts the S and G2 phases of the cell cycle. Ligation of cleaved DNA is inhibited and therefore there is an increase of single and double strand breakage. Figure 5.2 displays the biomarker response and RCG data for Etoposide.

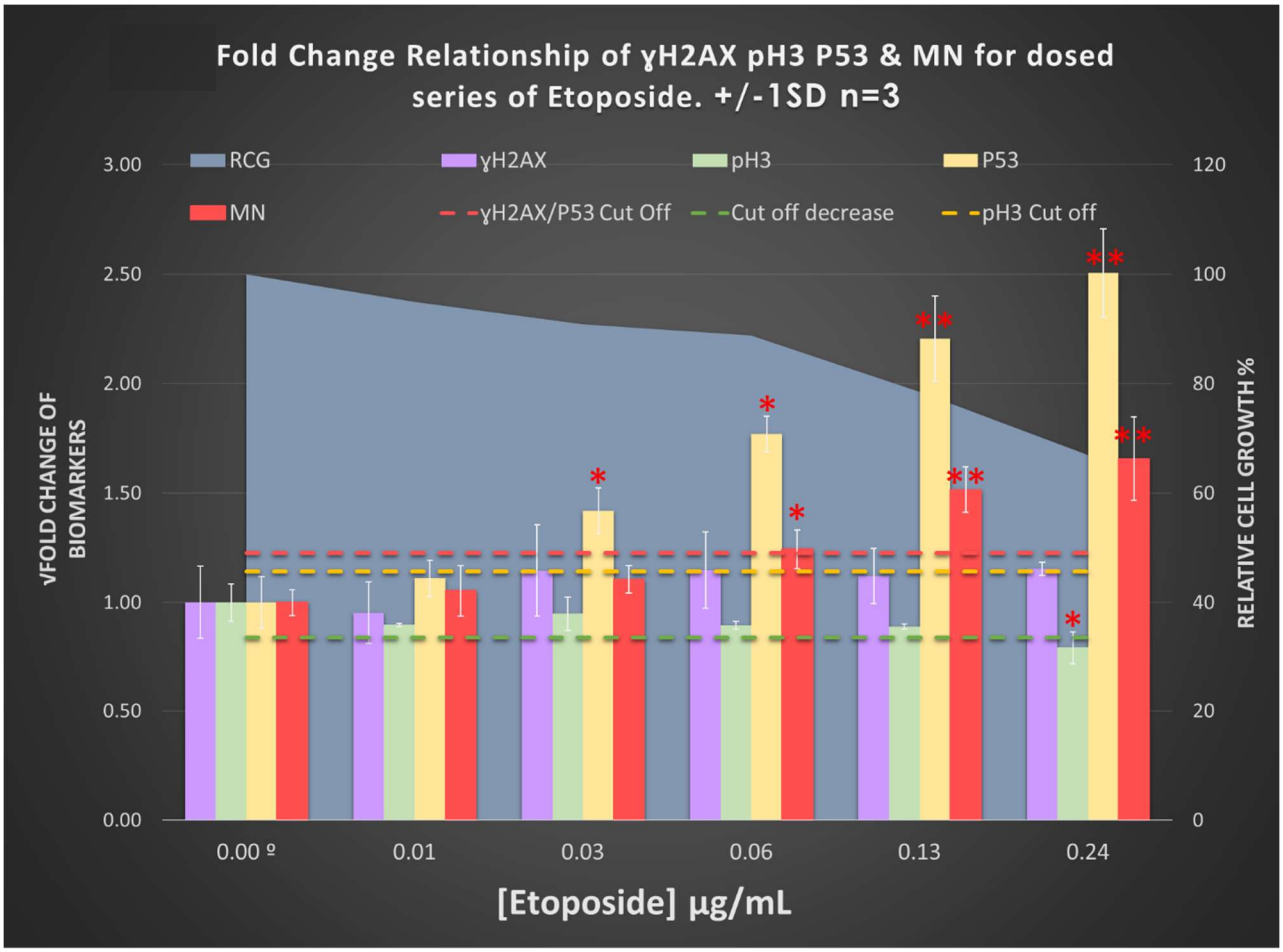

ºVehicle control DMSO
**Significant response p value < 0.05* ** Highly Significant Response p value<0.0001*

Figure 5.2: Combination graph showing the square root of raw fold change values of the biomarker responses for γH2AX, pH3, P53 and the Micronucleus (MN) genotoxic endpoint in response to Etoposide doses. RCG shows the % growth decrease of cell cultures as Etoposide concentrations increase. The dashed lines are the fold change cut offs for the biomarkers pH3, P53 and γH2AX. This highlights the relatively stable pH3 and γH2AX response though there is a slight trend decrease and increase respectively. γH2AX does not on average exceed the fold change cut off and no responses are significant. pH3 shows a statistically significant decrease at 0.24µg/mL and falls below the fold change cut off. The doses that are statistically significant are indicated with a Asterix. The only dose demonstrating NOGEL for all biomarkers is 0.01µg/mL. The NOGEL for the MN response is at 0.03µg/mL.

There is an increase in γH2AX response but the induction does not exceed the 1.2 fold change cut off nor is it statistically significant The NOGEL for P53 was at 0.01 µg/mL with statistical significance and exceeding of the fold change cut off occurring from 0.03 onwards. There is a corresponding increase of MN response, the MN NOGEL being 0.03 µg/mL and being significant from 0.06µg/mL, this is consistent with the expected DNA damage response. There is a steady decrease of pH3 response but statistical significance

and dropping below the 0.8 fold change cut off only occurs at the top Etoposide does, 0.24µg/mL.

The cell cycle response data for 24 hour Etoposide exposure is displayed in figure 5.3 below.

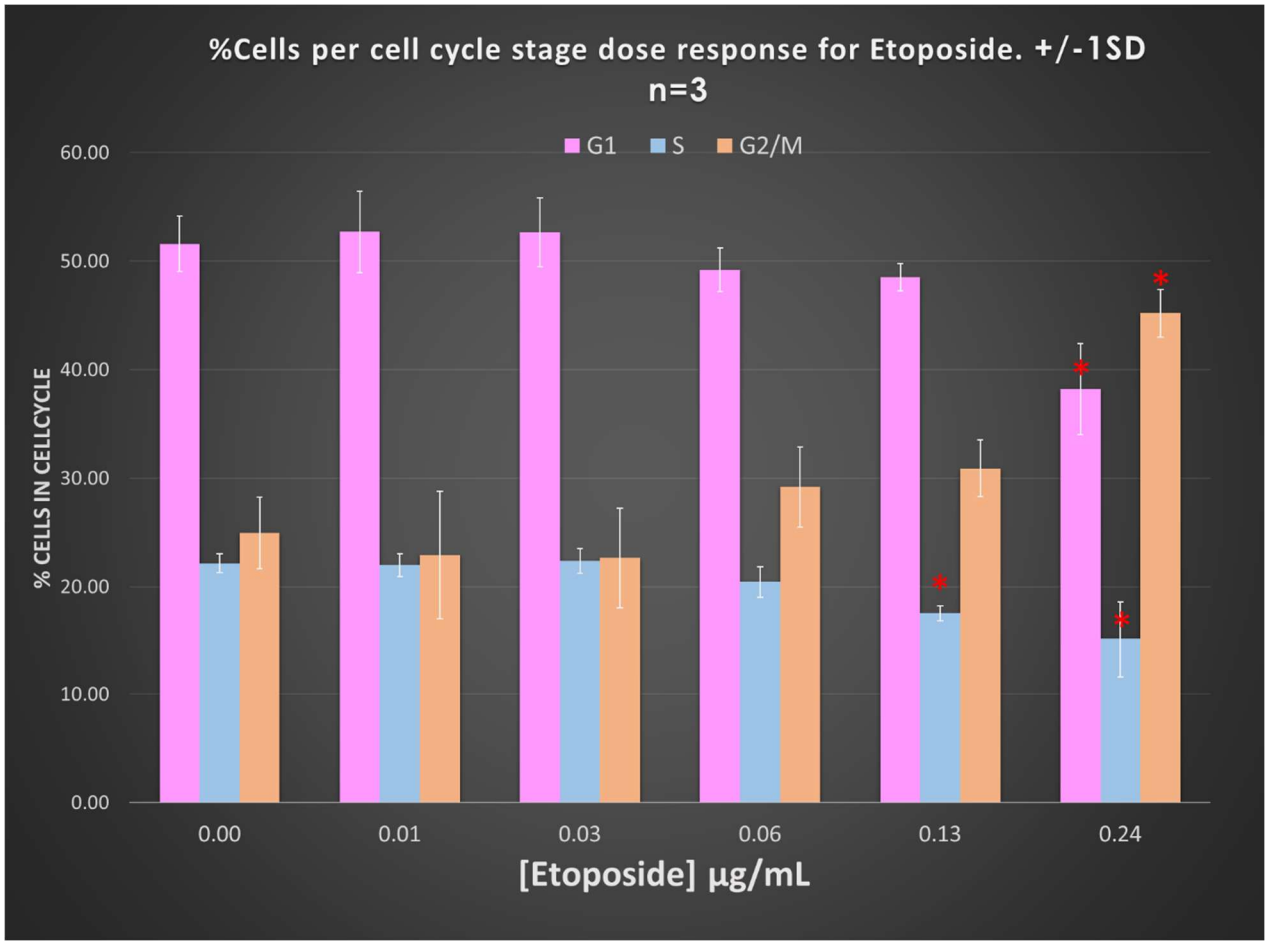

ºVehicle control DMSO
Significant response p value < 0.05 ** Highly Significant Response p value<0.0001

Figure 5.3: Graph showing percentage of cells found in each portion of the cell cycle in relation to Etoposide concentration. Statistically significant decrease of cells in S phase was seen at 0.13 and 0.24 µg/mL over all S phase showing a decreasing trend in relation to dose. A decrease in G1 was observed with significance at 0.24 µg/mL. A steady increase in G2/M population occurred with dose significance occurring at 0.24 µg/mL.

There is a slight decrease of cells in G1 and S from 0.03 onwards and this is proportional to a G2/M increase. All phases of the cell cycle show a statistically significant response at the highest concentration of Etoposide, G1 and S decreasing where G2/M increases relative to control. The decrease in S phase population percentage relative to control is statistically significant from 0.13µg/mL. Table 5.1a and 5.1b show the additional biomarker metrics of

Etoposide response in relation to the cell cycle, this data is also displayed graphically in figures 5.4 and 5.5 respectively.

Table 5.1a: Fold change average of biomarkers ɣH2AX and P53 in direct relation to the phase of the cell cycle the cell population is in ±1SD for Etoposide

	Fold change of biomarker in relation to cell cycle																		
Etop (µg/mL)	G1 ɣH2AX	±SD	G1 P53	±SD	S ɣH2AX	±SD	S P53	±SD	G2 ɣH2AX	±SD	G2/M P53	±SD	Proph	±SD	Meta	±SD	Anaph	±SD	H3+ve ɣH2AX -ve	±SD
0.00 º	1.00	0.08	1.00	0.09	1.00	0.19	1.00	0.21	1.00	0.17	1.00	0.13	1.00	0.04	1.00	0.25	1.00	0.23	1.00	0.00
0.01	1.05	0.21	1.12	0.08	0.97	0.16	1.05	0.15	0.95	0.08	1.19	0.05	0.98	0.01	1.12	0.17	1.28	0.54	1.05	0.08
0.03	1.24	0.18	1.44	0.10	1.22	0.28	1.34	0.17	1.07	0.20	1.48*	0.11	1.00	0.01	1.01	0.07	0.99	0.24	1.00	0.00
0.06	1.18	0.10	1.76*	0.08	1.21	0.18	1.73	0.24	1.04	0.13	1.93**	0.13	0.97	0.01	1.21	0.22	1.28	0.70	1.04	0.07
0.13	1.29	0.05	2.20**	0.10	1.25	0.17	2.03*	0.41	0.95	0.06	2.53**	0.19	0.98	0.02	1.14	0.20	1.16	0.18	1.06	0.10
0.24	1.03	0.10	2.19**	0.26	1.26	0.18	2.66**	0.12	0.93	0.07	2.95**	0.27	0.97	0.02	1.19	0.22	1.27	0.39	1.06	0.11

ºVehicle control DMSO
n=3 *Significant response p value < 0.05* ** Highly Significant Response p value<0.0001
Trend decrease Trend Increase

Table 5.1b: Fold change average of the ratio of Prophase, Metaphase and Anaphase cells populations when compared to control for Etoposide

	Mitosis stage fold change ratio		
Etop (µg/mL)	Prophase:Ananaphase+Metaphase	Metaphase:Prophase	Anaphase:Prophase
0.00 º	1.00	1.00	1.00
0.01	0.85	1.08	1.27
0.03	0.99	0.98	1.06
0.06	0.78	1.18	1.16
0.13	0.83	1.09	1.13
0.24	0.79	1.15	1.21

ºVehicle control DMSO
n=3 ºAquisition error n=2 Trend decrease Trend Increase

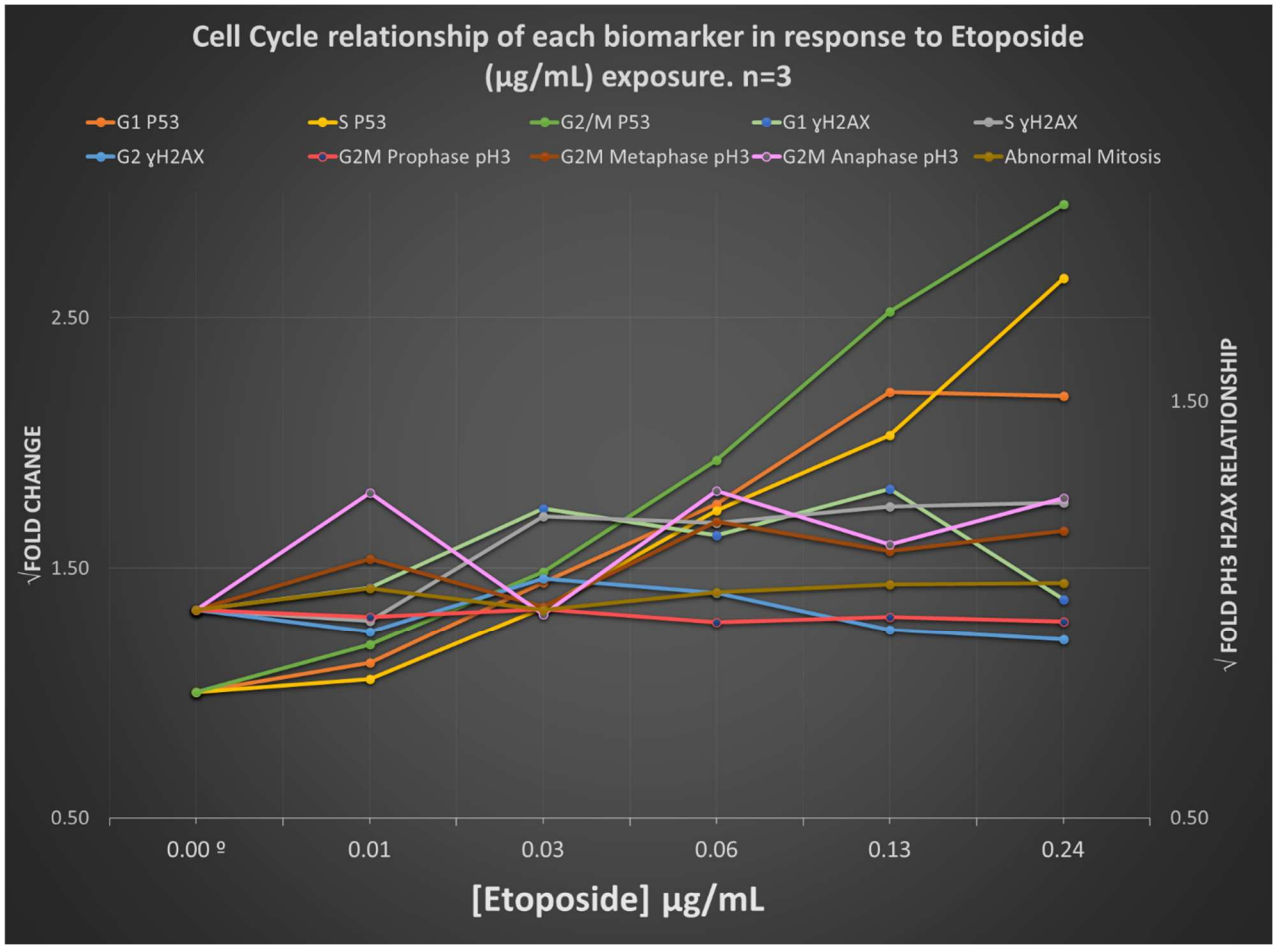

Figure 5.4: Line scatter graph visually displaying data in table 5a illustrating relationship of each biomarker and cell cycle stage for Etoposide. Primary Y axis shows the P53 response data. Secondary Y axis plots γH2AX and pH3 cell cycle signals and relationship. Statistical significance of each response can be found in table 5.1a.

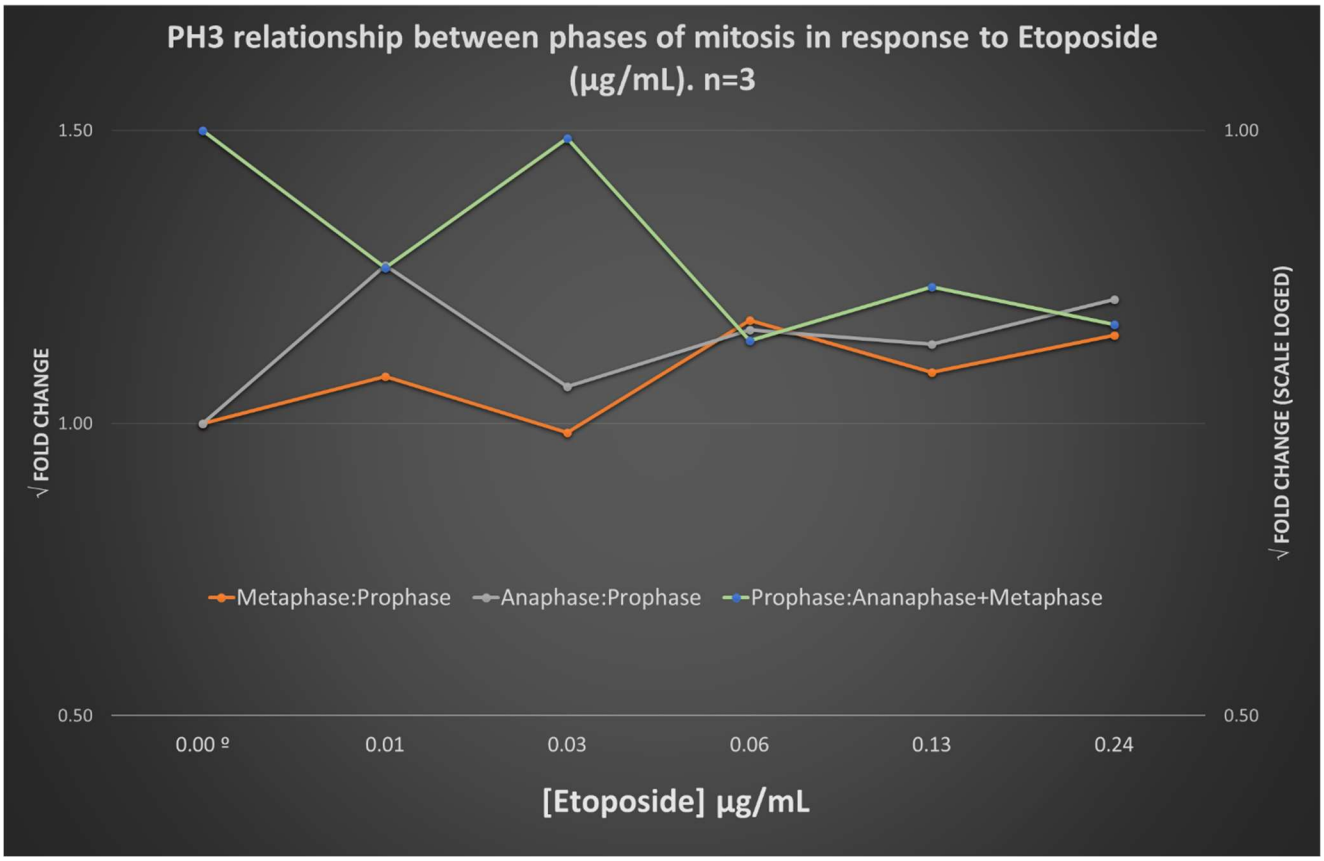

ºVehicle control DMSO

Figure 5.5: Line scatter graph displaying the ratio of average fold change responses (data in table 5.1b) for Etoposide concentrations. Allowing assessment of proportional changes of the different phases of mitosis to one another. Primary Y axis shows the changes compared to vehicle control of the individual metaphase prophase change, and anaphase prophase change. Secondary Y axis plots the overall prophase response to anaphase and metaphase combined. No statistical analysis was performed, a qualitative trend only was looked at. There was a very slight trend decrease of prophase population to the combined anaphase/metaphase population whilst there was a equivalently gentle increase of metaphase to prophase and anaphase to prophase cell populations. These occurred in a dose dependant manner.

Whilst overall levels of ɣH2AX only increase slightly not reaching fold cut off, or presenting significance there are cell cycle response differences, G1 and S phase ɣH2AX signal both increase from 0.03 to 0.13 µg/mL at which point the G1 ɣH2AX then decreases. At 0.24 µg/mL the S phase ɣH2AX increases relative to the decrease of the S phase cell cycle population. The ratios of prophase metaphase and anaphase remain relatively stable compared to control. There is a slight increase of metaphase and anaphase cells but prophase cells remain at a control level. The pH3 positive ɣH2AX negative cells i.e., abnormal mitotic there is no change. The greatest P53 response is at G2/M which is consistent with cell cycle response and suggested G2 effect on the cell cycle, G1 and S phase

P53 levels rise at a consistent rate and are similar in response. However, until 0.24 µg/mL P53 is slightly higher in G1 than S.

Table 5.2 shows MN that were found to have detectible biomarker fluorescence within them.

Table 5.2: Etoposide 0.24µg/mL - Biomarker presence or absence in true MN microscope images obtained on ISXII

Stain present in MN	Total count	% MN Cells
DRAQ5™ only	90	80.4
DRAQ5™ and P53	1	0.9
DRAQ5™ and ɣH2AX	18	16.1
DRAQ5™ P53 and ɣH2AX	3	2.7

n=1, 112 true MN

Table 5.2 looked at a total of 112 true MN events and shows presence of biomarker signal within the MN. 80% of detectible MN had no additional biomarker presence. Even though the overall ɣH2AX signal is not as impactful as would be expected proportionally there are more MN with ɣH2AX signal than P53. To assess the statistical significance of this additional data analysis would be required on the other Etoposide replicates and doses.

5.3.2 - Crizotinib

Crizotnib is a tyrosene kinase inhibitor and more specifically Anaplastic Lymphoma Kinase (ALK) inhibitor. ALK is a major contributor to the DNA damage repair pathway in cells and therefore has a downstream effect on many important regulatory proteins (Gandhi & Janne., 2012). Crizotinib mainly affects P53 response which is demonstrated in figure 5.6 showing that from 2.25 µg/mL the P53 fold change not only rises above the fold change cut off but is also statistically significant. MN response also increases above control levels starting at 2.25 µg/mL which is the same point at which P53 levels pass the fold change cut off. Along with ɣH2AX, pH3 stays at control levels however at the top dose the pH3 response does begin to increase.

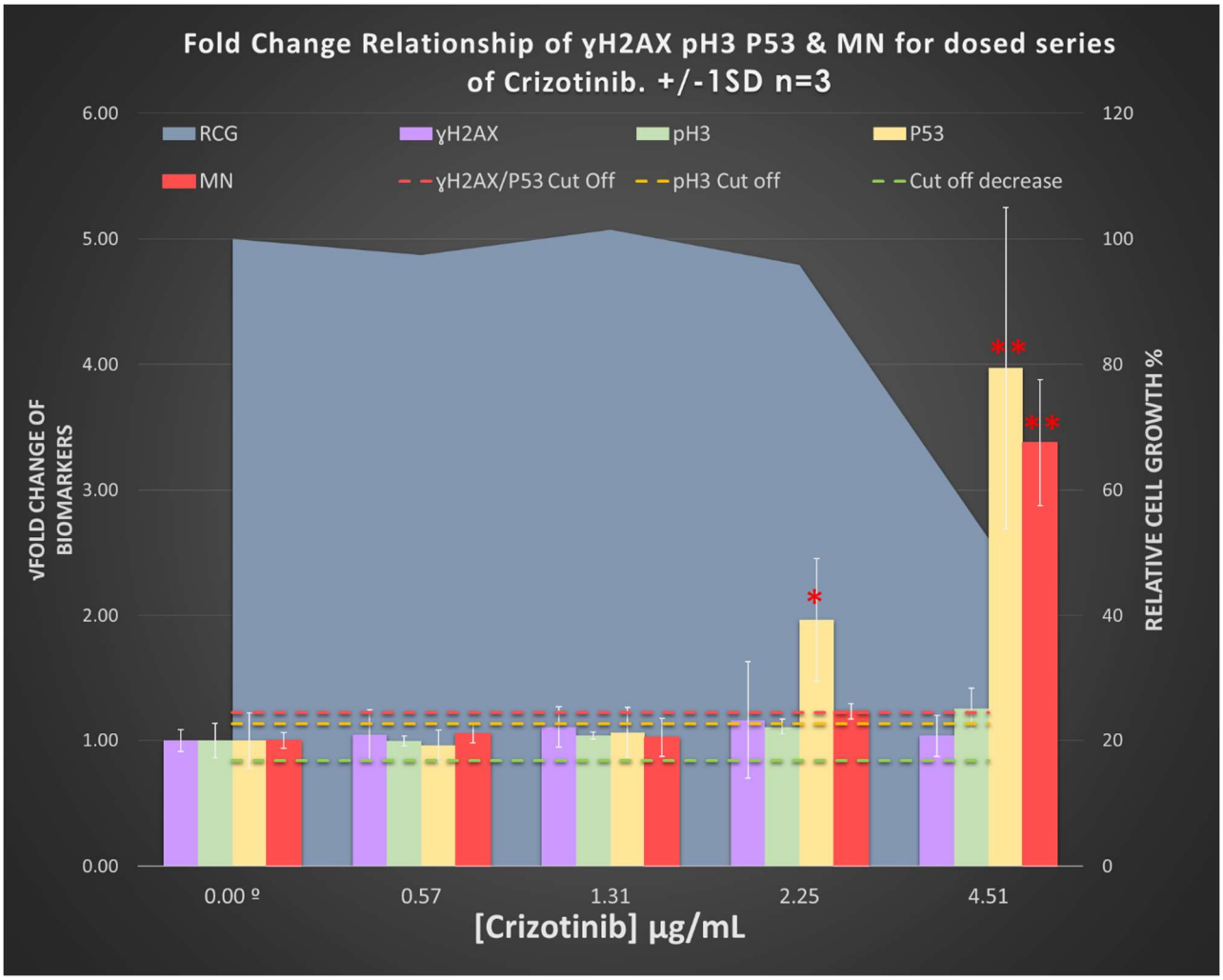

ºVehicle control DMSO
**Significant response p value < 0.05* ** Highly Significant Response p value<0.0001*

Figure 5.6: Combination graph showing the square root of raw fold change values of the biomarker responses for ɣH2AX, pH3, P53 and the Micronucleus (MN) genotoxic endpoint in response to Crizotinib doses. RCG shows the % growth of cell cultures, RCG response stays relatively stable until the top two responses where it drops off. This suggests a more finite dose range between 2.25 and 4.51 µg/mL is required. The dashed lines are the fold change cut off's for the biomarkers pH3, P53 and ɣH2AX. This highlights the relatively stable pH3 and ɣH2AX response, pH3 begins to increase ate 2.25 µg/mL and though not significant the pH3 signal passes the pH3 fold change threshold at 4.51 µg/mL. ɣH2AX does not on average exceed the fold change cut off and no responses are significant. P53 and MN NOGEL is at 1.31 and 2.25 µg/mL respectively. The doses that are statistically significant are indicated with a astrix. The only dose demonstrating NOGEL for all biomarkers is 1.31 µg/mL.

Figure 5.7 displays the cell cycle data of cell cycle stage population percentages. At the lower doses of Crizotinib incubation the cell population percentages are relatively similar.

There is a increase of the G1 population that reaches statistical significance at 2.25 µg/mL and a significant decrease in S phase at the same dose. At the top dose there is a significant decrease of G1 and S phase population and increase of G2/M population relative to control.

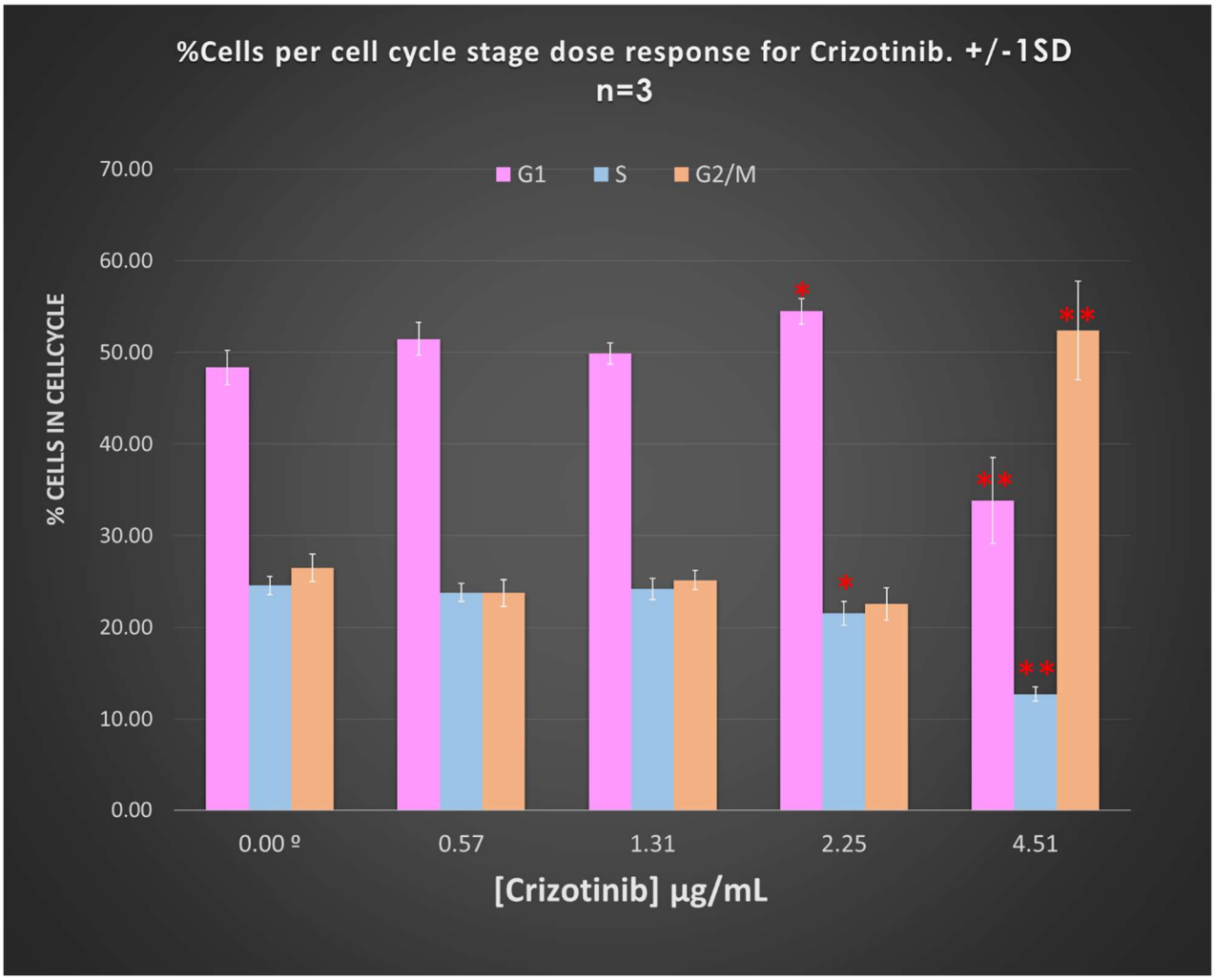

ºVehicle control DMSO
**Significant response p value < 0.05* ** Highly Significant Response p value<0.0001*

Figure 5.7: Graph showing percentage of cells found in each portion of the cell cycle in relation to Etoposide concentration. Statistically significant decrease of cells in S phase was seen at 2.25 and 4.51 µg/mL over all S phase showing a decreasing trend in relation to dose. A statistically significant increase in G1 was seen at 2.25 followed be a statistically significant decrease at 4.51 µg/mL decrease in G1 was observed with significance at 0.24 µg/mL. The reverse is true for G2/M demonstrating a trend to decrease but there being a significant increase at the top dose.

Tables 5.3a and 5.3b look into the cell cycle relationship of the biomarkers. Data displayed in these tables include significance and ±1SD. These data were then plotted on scatter graphs for visual assessment, figures 5.8 and 5.9.

Table 5.3a: Fold change average of biomarkers ɣH2AX and P53 in direct relation to the phase of the cell cycle the cell population is in ±1SD for Crizotinib

	Fold change of biomarker in relation to cell cycle																		
Crztib (µg/mL)	G1 ɣH2AX	±SD	G1 P53	±SD	S ɣH2AX	±SD	S P53	±SD	G2 ɣH2AX	±SD	G2/M P53	±SD	Proph	±SD	Meta	±SD	Anaph	±SD	H3+ve ɣH2AX -ve	±SD
0.00 º	1.00	0.08	1.00	0.17	1.00	0.05	1.00	0.25	1.00	0.09	1.00	0.35	1.00	0.02	1.00	0.14	1.00	0.35	1.00	0.00
0.57	1.21	0.28	0.94	0.16	1.09	0.24	0.97	0.08	1.04	0.18	1.10	0.33	1.00	0.05	1.00	0.26	0.67	0.67	1.11	0.09
1.31	1.25	0.16	1.03	0.15	1.13	0.19	1.07	0.18	1.09	0.13	1.28	0.49	0.99	0.04	1.14	0.19	0.90	0.67	1.00	0.00
2.25	1.32	0.55	1.96*	0.45	1.18	0.57	2.01*	0.38	1.22	0.42	2.16*	0.85	0.97	0.02	1.07	0.30	1.00	0.35	1.09	0.09
4.51	0.82	0.13	3.67**	0.85	0.82	0.08	3.91*	1.26	0.87	0.13	5.29**	2.62	0.99	0.03	1.04	0.36	0.77	0.18	1.09	0.14

ºVehicle control DMSO
n=3 *Significant response p value < 0.05* ** Highly Significant Response p value<0.0001
Trend decrease Trend Increase

Table 5.3b: Fold change average of the ratio of Prophase, Metaphase and Anaphase cells populations when compared to control for Crizotinib

	Mitosis stage fold change ratio		
Crztib (µg/mL)	Prophase:Ananaphase+Metaphase	Metaphase:Prophase	Anaphase:Prophase
0.00 º	1.00	1.00	1.00
0.57	1.07	1.04	0.84
1.31	0.89	1.17	1.07
2.25	1.00	1.10	0.93
4.51	1.12	1.02	0.69

ºVehicle control DMSO
n=3 ºAquisition error n=2 Trend decrease Trend Increase

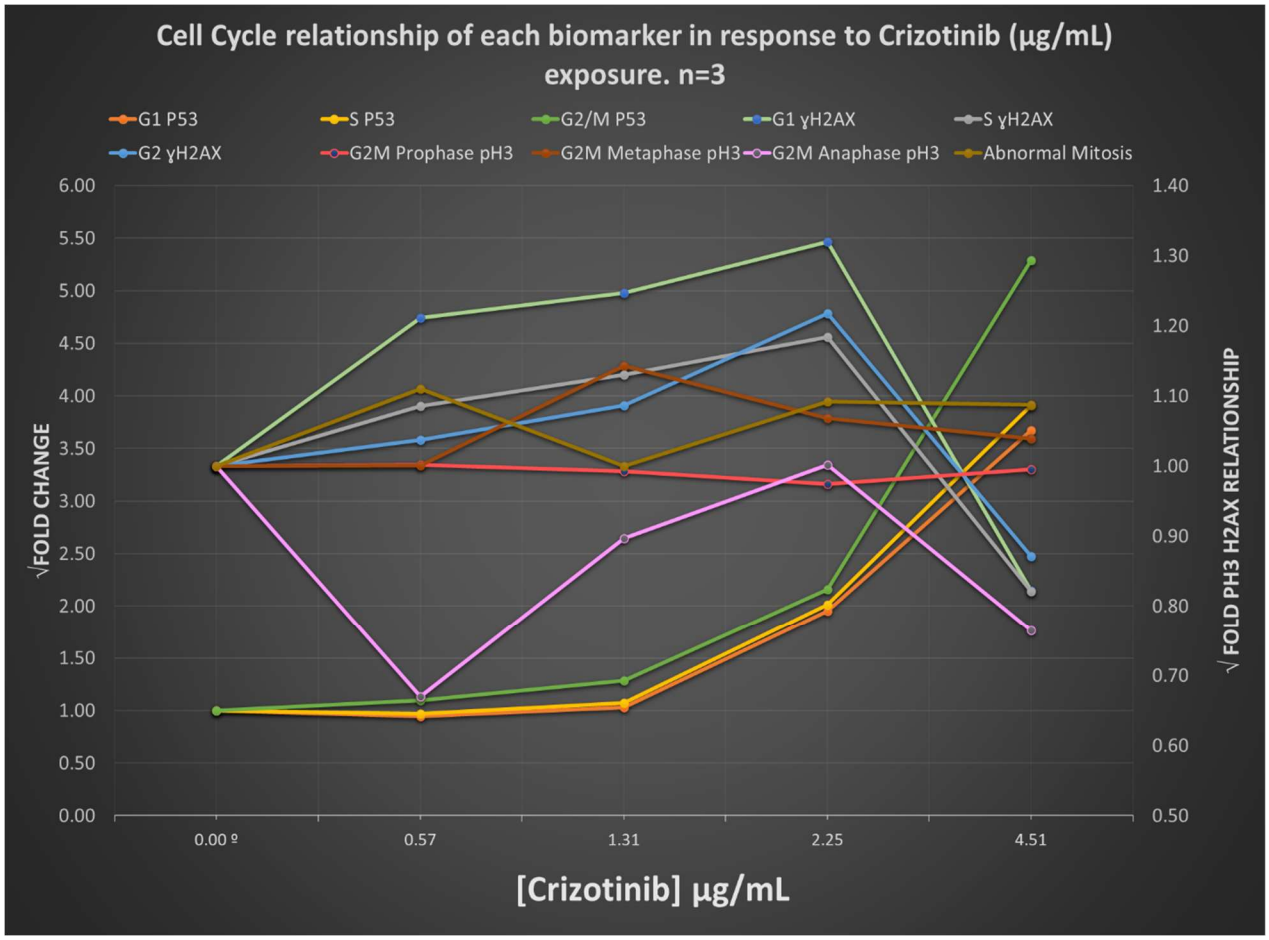

Figure 5.8: Line scatter graph visually displaying data in table 5.3a illustrating relationship of each biomarker and cell cycle stage for Crizotinib. Primary Y axis shows the P53 response data. Secondary Y axis plots ɣH2AX and pH3 cell cycle signals and relationship. Statistical significance of each response can be found in table 5.3a.

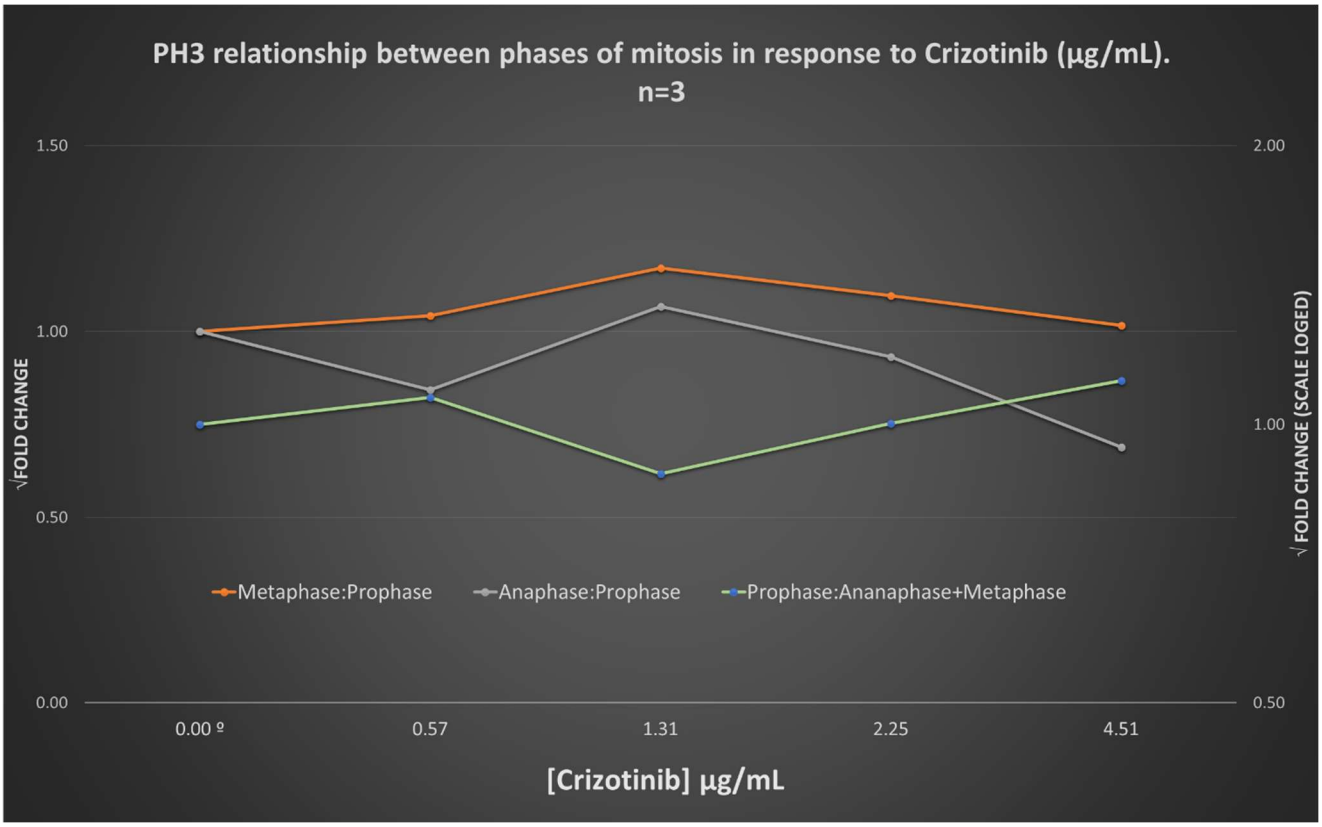

ºVehicle control DMSO

Figure 5.9: Line scatter graph displaying the ratio of average fold change responses (data in table 5.3b) for Crizotinib. Allowing assessment of proportional changes of the different phases of mitosis to one another. Primary Y axis shows the changes compared to vehicle control of the individual metaphase prophase change, and anaphase prophase change. Secondary Y axis plots the overall prophase response to anaphase and metaphase combined. No statistical analysis was performed, a qualitative trend only was looked at. There was a very slight trend decrease of prophase population to the combined anaphase/metaphase population before increasing at 1.31 µg/mL. There was a equivalently gentle increase of metaphase to prophase and anaphase to prophase cell populations followed by decrease at the same does.

Figure 5.8 displaying data from table 5.3a shows a dose response increase for S and G2 ɣH2AX along with metaphase pH3 from control levels until 2.25 µg/mL where the response drops off. Whilst there is a limited overall ɣH2AX response, assessment when breaking the response down into cell cycle reveals there is a fold change induction that is equivocal at 0.57 and 1.31 ug/ml whilst being above the fold change cut off at 2.25 µg/mL for G1 ɣH2AX. Anaphase pH3 fold change levels are lower than control at all doses. Figure 5.9 demonstrates that there is little to no change in the ratio of metaphase to prophase or prophase to metaphase and anaphase but there is a decrease in the ratio of Anaphase to prophase cells when compared to control.

Table 5.4 looked at a total of 496 true MN events and shows presence of biomarker signal within the MN.

Table 5.4: Crizotinib 4.51µg/mL - Biomarker presence or absence in true MN microscope images obtained on ISXII

Stain present in MN	Total count	% MN Cells
DRAQ5™ only	435	87.7
DRAQ5™ and P53	9	1.8
DRAQ5™ and ɣH2AX	51	10.3
DRAQ5™ P53 and ɣH2AX	1	0.2

N=1 True MN total=496

MN containing both ɣH2AX and P53 signal were rare at 0.2%, 10% of MN were found to have ɣH2AX signal. Unlike Etoposide there is a greater percentage of cells with just DRAQ5™ stain and more MN with just P53.

5.3.3 - Vinblastine

Vinblastine Sulfate is a compound used in chemotherapy and is an alkaloid isolated from the Vinca Rosea also known as the periwinkle plant. This compound has a aneugenic Mode of Action disrupting microtubule formation resulting in cell cycle arrest at the M Phase (Gerson *et al.*, 2018). Due to the well characterized nature of this chemical, it is recommended on the ECVAM list of chemicals to assess assays ability to differentiate Mode of Action and assess misleading positive rates (Kirkland *et al*., 2006; Kirkland et al., 2016).

The following figure 5.10 shows the dose response induction of the biomarkers ɣH2AX, pH3 and P53 along with the automated acquisition MN data plotted as a square root fold change when compared to the control response. RCG did not reach cytotoxic levels assessed here even at 0.0020µg/mL

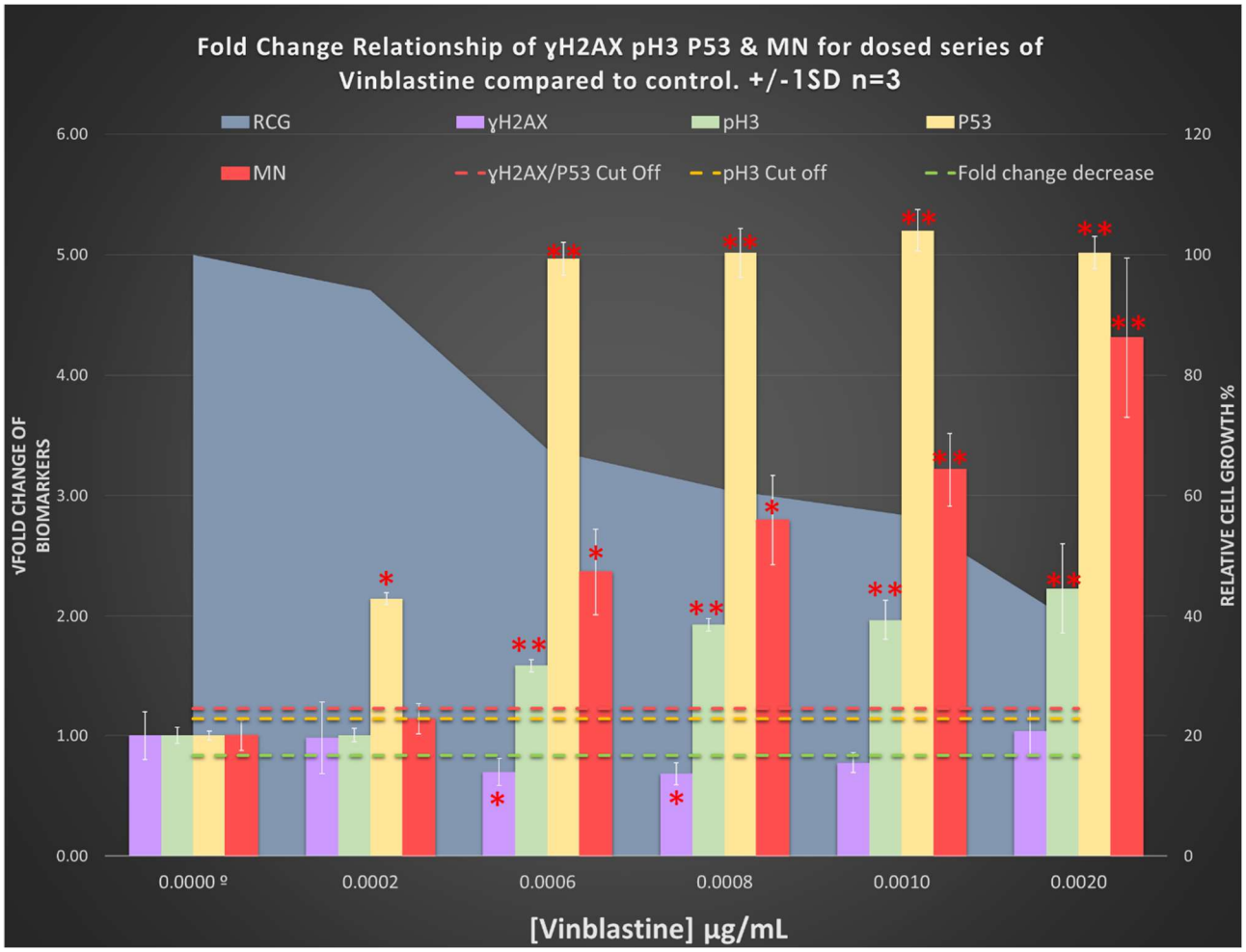

ºVehicle control DMSO

**Significant response p value < 0.05* ** Highly Significant Response p value<0.0001*

Figure 5.10: Combination graph showing the square root of raw fold change values of the biomarker responses for ɣH2AX, pH3, P53 and the Micronucleus (MN) genotoxic endpoint in response to Vinblastine doses. RCG shows the % growth of cell cultures, RCG response decreases in a dose dependant manner. The dashed lines are the fold change cut off for the biomarkers pH3, P53 and ɣH2AX. ɣH2AX response drops below fold change decrease from 0.0006 to 0.0010 µg/mL before increasing to vehicle control levels at 0.0020. ɣH2AX response was significant at 0.0006and 0.0008 µg/mL. P53 was significant at all doses, increasing in a dose dependant manner being above the fold change cut off. pH3 response increased from 0.0006 µg/mL onwards and was both greater than the fold change cut off and significant at theses doses. At the same doses as pH3 MN response also increased and was significant. There was not a NOGEL doses where all biomarkers were not significant. The NOGEL dose for pH3 ɣH2AX and MN was 0.0002 µg/mL.

Figure 5.11 below demonstrates the percentage of cells in each portion of the cell cycle and the ensuing effect of Vinblastine on the cells cycle of TK6 cells. The general trend of the cell cycle phases demonstrated in figure 5.11 are a gradual increase of G1 cell population, a decrease of S phase cells and a consistent G2/M phase response until the top dose of 0.0002 µg/mL. Cell cycle response significance are shown with asterix in figure 5.11.

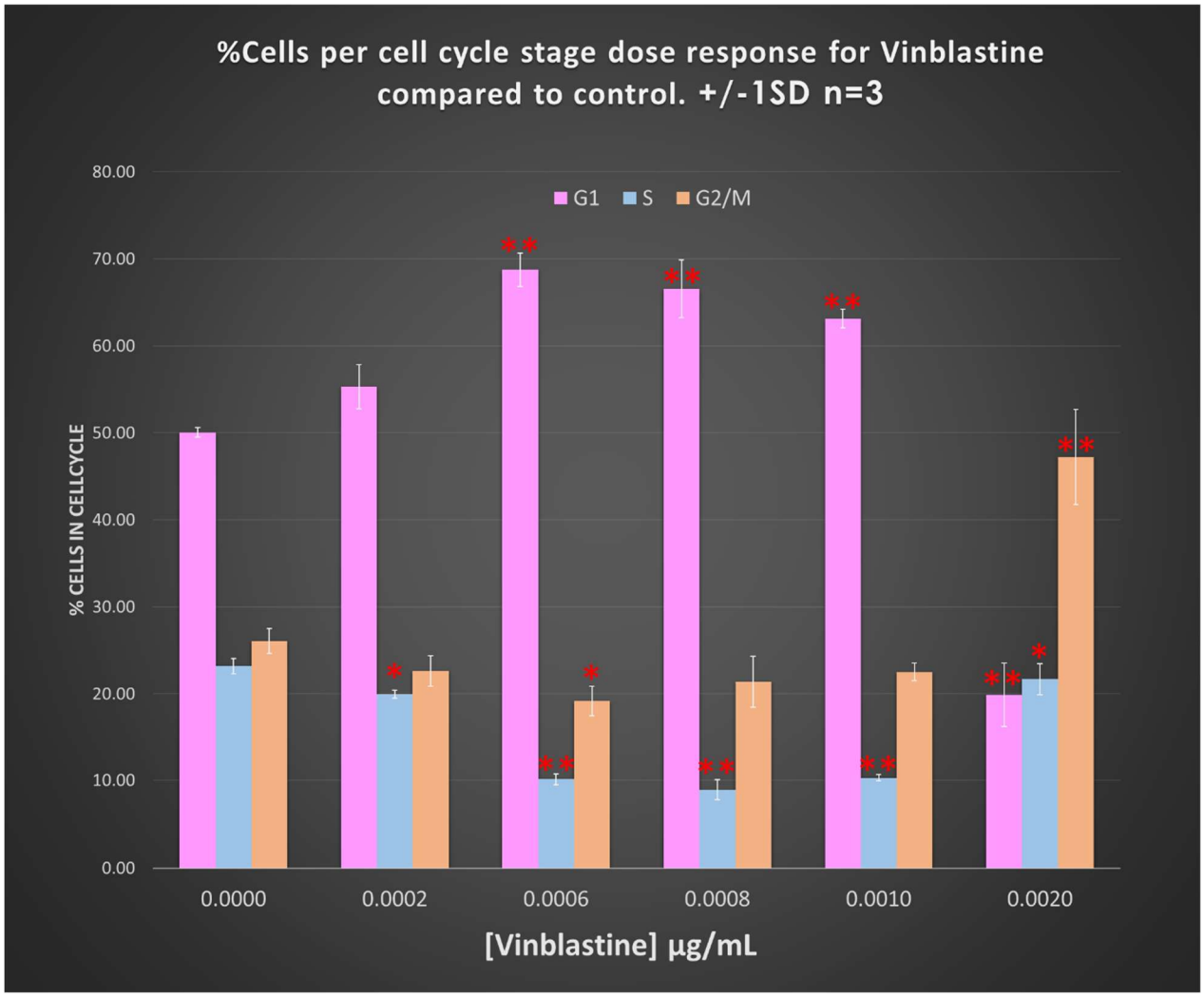

Figure 5.11: Graph showing percentage of cells found in each portion of the cell cycle in relation to Vinblastine concentration. Statistically significant decrease of cells in S phase compared to control was at all doses. From 0.0010 S phase began to increase but was still lower than control S. G2/M cell populations decreases until 0.0006 µg/mL demonstrating a statistically significant decrease, from this point onwards G2/M increased and was significant at 0.0020 µg/mL. G1 response increased and then decreased at the same doses S and G2/M populations decreased then increased. 0.0006 to 0.001 had a significant G1 increase, the top dose then had a significant decrease.

`

The decrease of γH2AX was statistically significant at doses 0.0006 and 0.0008 µg/mL, these same doses and 0.001 µg/mL have a fold decrease of ≤0.8 fold change cut off. Increase of pH3 signal from 0.0006 µg/mL dose onwards exceeding the fold change cut off of 1.1 and showing statistically significant from the same. The P53 marker demonstrates significance at all doses and the increase is proportional with increase pH3 expression and MN generation. Statistical significance is seen for the MN response at al doses with the exception of 0.0002 µg/mL.

Based on the availability of data a more in-depth look into these biomarker responses in relation to one another has been assessed. Tables 5.5a and 5.5b display the fold change data of the individual biomarkers in direct relation to a stage of the cell cycle. Tables 5.5a and 5.5b are graphically visualized in figure 5.12 and 5.13 below.

Table 5.5a: Fold change average of biomarkers γH2AX and P53 in direct relation to the phase of the cell cycle the cell population is in ±1SD for Vinblastine

	Fold change of biomarker in relation to cell cycle																		
Vinbstn (µg/mL)	G1 γH2AX	±SD	G1 P53	±SD	S γH2AX	±SD	S P53	±SD	G2 γH2AX	±SD	G2/M P53	±SD	Proph	±SD	Meta	±SD	Anaph	±SD	H3+ve γH2AX -ve	±SD
0.0000 º	1.00	0.36	1.00	0.04	1.00	0.36	1.00	0.04	1.00	0.15	1.00	0.07	1.00	0.05	1.00	0.23	1.00	0.07	1.00	1.00
0.0002	1.01	0.43	2.16**	0.09	1.13	0.52	2.10*	0.06	1.05	0.24	2.21**	0.07	0.99	0.03	1.05	0.13	1.19	0.23	1.00	1.00
0.0006	0.55*	0.23	4.98**	0.22	1.00	0.38	4.63**	0.09	0.95	0.15	5.57**	0.32	0.97	0.02	1.17	0.18	1.06	0.12	4.55	0.79
0.0008	0.60*	0.25	5.05**	0.27	1.17	0.60	4.65**	0.09	0.91	0.12	5.62**	0.39	1.01	0.02	1.02	0.10	0.68*	0.09	7.93*	2.85
0.0010	0.72	0.22	5.24**	0.16	1.14	0.28	4.82**	0.19	0.96	0.07	5.85**	0.46	1.05	0.03	0.87	0.16	0.54*	0.03	8.18*	3.13
0.0020	1.84*	0.69	5.01**	0.14	1.07	0.50	4.83**	0.24	0.77	0.14	5.67**	0.46	1.12*	0.05	0.26*	0.10	0.21*	0.21	3.79	1.35

ºVehicle control DMSO
n=3 *Significant response p value < 0.05* ** Highly Significant Response p value<0.0001
Trend decrease Trend Increase

Table 5.5b: Fold change average of the ratio of Prophase metaphase and anaphase cells populations when compared to control for Vinblastine

	Mitosis stage fold change ratio		
Vinbstn (µg/mL)	Prophase:Ananaphase+Metaphase	Metaphase:Prophase	Anaphase:Prophase
0.0000 º	1.00	1.00	1.00
0.0002	0.91	1.04	1.18
0.0006	0.84	1.15	1.09
0.0008	1.05	0.99	0.69
0.0010	1.26	0.79	0.51
0.0020	5.63	0.22	0.17

ºVehicle control DMSO
n=3 Trend decrease Trend Increase

Whilst the overall response of γH2AX decreases slightly as shown in figure 5.10 above, further assessment of the biomarker in direct relationship to each stage of the cell cycle was attempted. At G1, γH2AX biomarker decreases significantly from 0.0006 to 0.0010 µg/mL however, there is a statistically significant increase relative to control at 0.0020 µg/mL dose. There was a increase of fold change of γH2AX at the S phase portion of the cell cycle but this response was not statistically significant. The G2 population of cells demonstrate a slight trend decrease in γH2AX signal and the greatest decrease being at the top dose. This fold decrease at 0.0002 µg/ml falling below 0.8 fold change cut off. Cells that are pH3 positive but have reduced γH2AX are termed H3+ve γH2AX -ve in table 5.5a and Abnormal mitosis in figure 5.12. There is a overall trend increase compared to control from 0.0006µg/mL onwards, with statistically significant change of this relationship at 0.0008 and 0.0010µg/mL.

P53 Demonstrates the most obvious response for a mitotic arrest inducing compound. Being statistically significant at all cell cycle phases and dose concentrations. Figure 5.12 shows that the overall nuclear P53 levels in G2/M phase cells has a greater fold change over that of control compared to the G1 phase which in turn has a greater fold change over that of S phase.

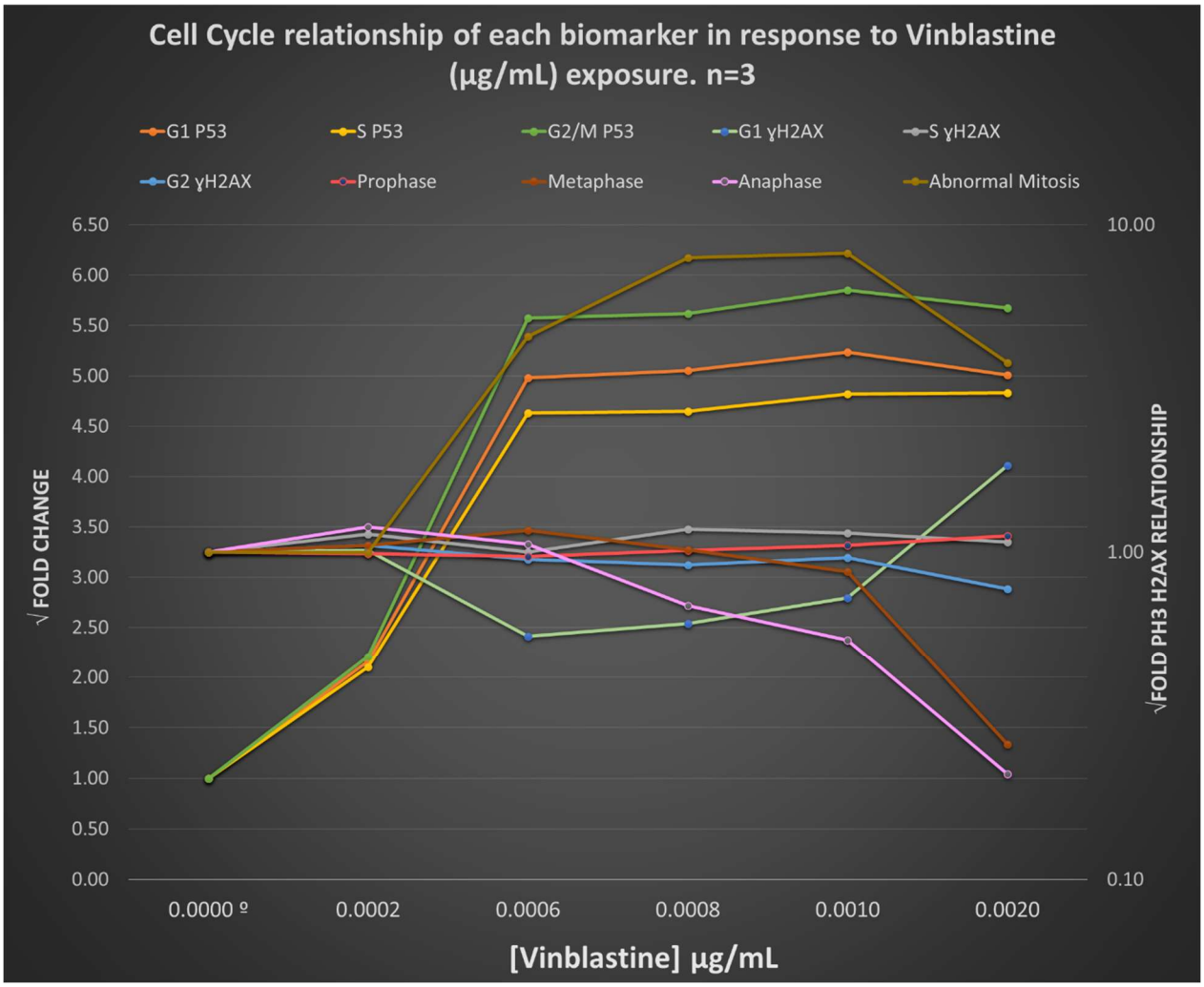

ºVehicle control DMSO

Figure 5.12: Line scatter graph visually displaying data in table 5.5a, illustrating relationship of each biomarker and cell cycle stage for Vinblastine dose concentrations. Primary Y axis shows the P53 response data. Secondary Y axis plots γH2AX and pH3 cell cycle signals and relationship the axis was log scaled. Statistical significance of each response can be found in table 5.5a.

With the exception of the 0.0020 µg/mL Vinblastine concentration where there is a statistically significant increase of cells in prophase, there is no other increase in prophase, metaphase or anaphase population at any of the doses. In metaphase and anaphase, however, there are statistically significant decreases in populations. 0.0008 and 0.0010 µg/mL showed a statistically significant decrease of the anaphase population and at 0.0020 µg/mL both anaphase and metaphase presented a decrease in population that was statistically significant. The ratios of these phases of mitosis can be compared with one another and is displayed graphically in figure 5.13.

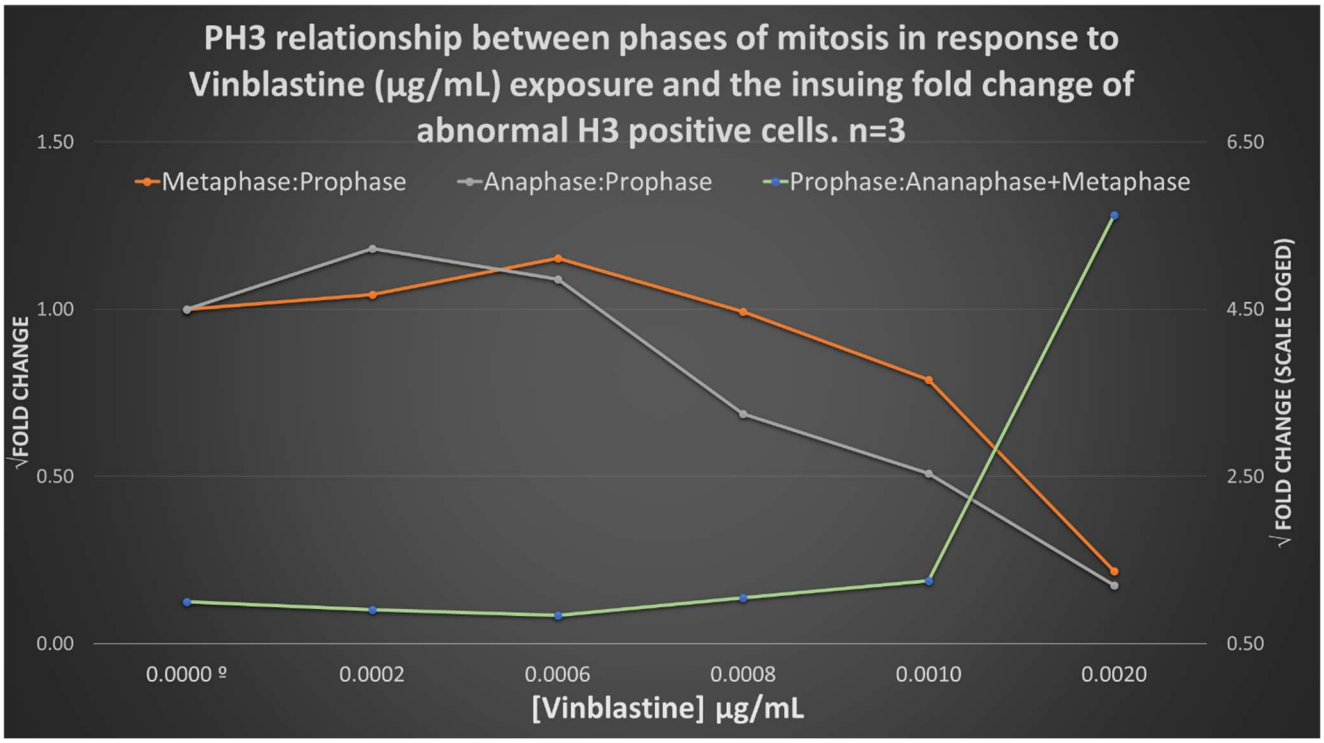

ºVehicle control DMSO

Figure 5.13: Line scatter graph displaying the ratio of average fold change responses (data in table 5.5b) for Vinblastine. Allowing assessment of proportional changes of the different phases of mitosis to one another. Primary Y axis shows the changes compared to vehicle control of the individual metaphase prophase change, and anaphase prophase change. Secondary Y axis plots the overall prophase response to anaphase and metaphase combined. No statistical analysis was performed, a qualitative trend only was looked at. There was a plateau trend of prophase population to the combined anaphase/metaphase population before increasing at 0.0010µg/mL onwards. There was a decrease of metaphase to prophase and anaphase to prophase cell populations. Metaphase:Prophase was lower initially than Anaphase:Prophase at 0.0002 µg/mL at all other doses the trend was higher but still decreasing.

There is an initial fold change increase of the metaphase:prophase and anaphase:prophase ratios at 0.0002 and 0.0006 µg/mL relative to control and a corresponding decrease of the prophase: combined anaphase and metaphase ratio. However, from 0.0008 µg/mL onwards the relationships flip and prophase: combined anaphase and metaphase ratio increase. None of these responses were statistically significant.

For the top dose Vinblastine the additional metric for true MN and presence or absence of either ɣH2AX and or P53 biomarker in the MN can be found in table 5.6.

Table 5.6: Vinblastine 0.002ug/mL - Biomarker presence or absence in true MN microscope images obtained on ISXII

Stain present in MN	Total count	% MN Cells
DRAQ5™ only	44	33.1
DRAQ5™ and P53	66	49.6
DRAQ5™ and ɣH2AX	11	8.3
DRAQ5™ P53 and ɣH2AX	12	9.0

n=1 Total MN 133

In contrast to Etoposide and Crizotinib there is a large percentage of assessed MN with P53 signal more so than DRAQ5™ only. D5 only MN% decreased compared to Etoposide and Crizotinib. An increase in MN with both P53 and ɣH2AX could indicate cells about to enter apoptosis.

5.3.4 - ARA-C

ARA-C specifically affects the synthesis phase of the cell cycle as it acts as a nucleoside analogue i.e., it becomes incorporated into the DNA rather than the correct pyrimidine.

Figure 5.14 shows the biomarker responses for ARA-C. Doses 0.01 through to 0.05 µg/mL had a RCG percentage of 78 – 46.1% respectively, this is in line with regulatory guidelines that biologically relevant responses have a RCG value of above 30%. The doses 0.21 and 0.41 µg/mL had RCG values of 26.1 and 28.9%. In terms of genetic toxicology assessment, it is considered that RCG values of less than 30% any genetic toxicological response is more likely to be as a result of cytotoxicity rather than genotoxicity. When assessing the following data this potential for a cytotoxicity response should be remembered however in lieu of intermediate doses between 0.05 and 0.21 µg/mL the metrics for 0.21 and 0.41 µg/mL are displayed to aid qualitative assessment of the systems ability to distinguish chemical MoA.

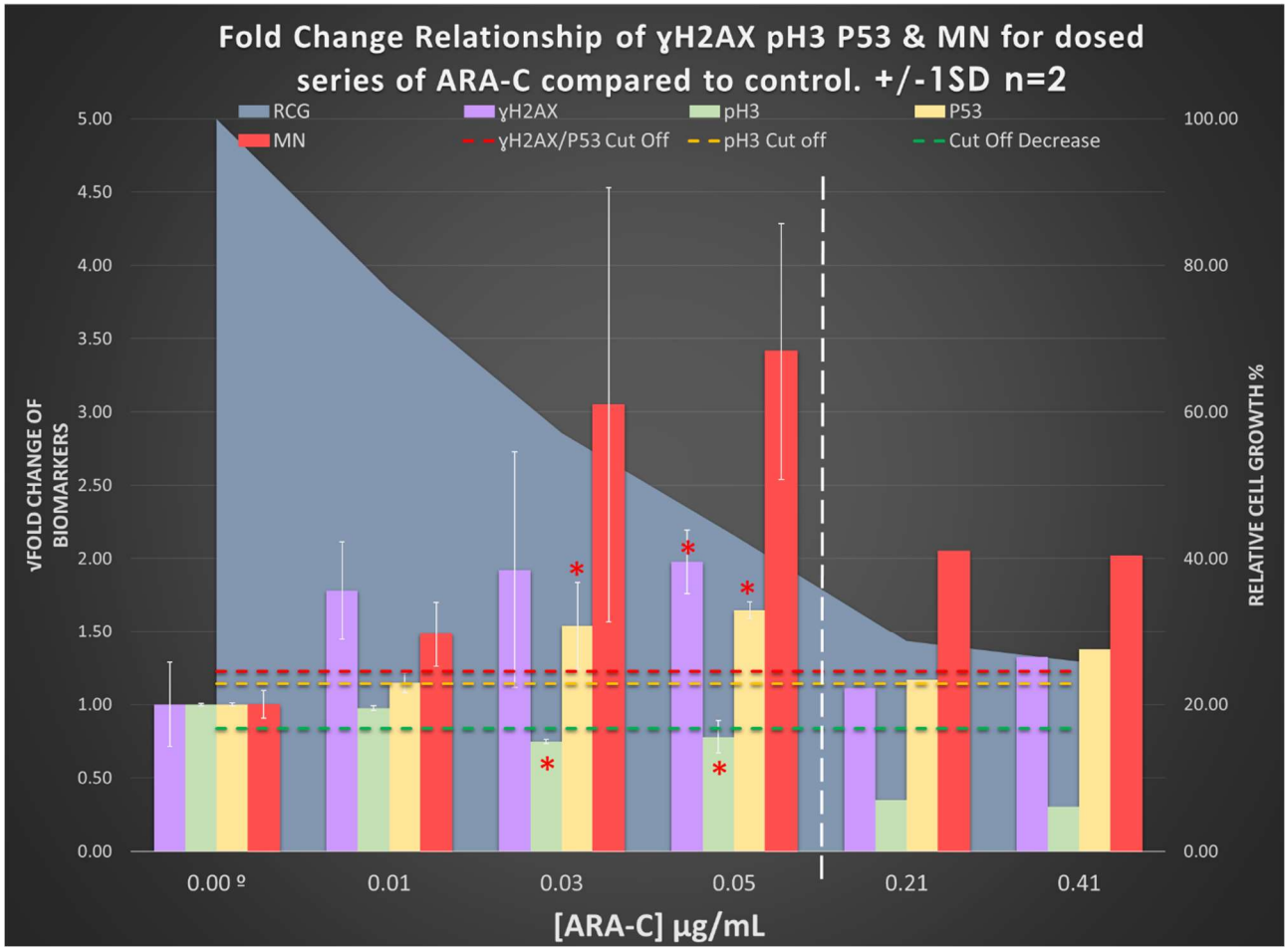

ºVehicle control DMSO
**Significant response p value < 0.05* ** Highly Significant Response p value<0.0001*

Figure 5.14: Combination graph showing the square root of raw fold change values of the biomarker responses for γH2AX, pH3, P53 and the Micronucleus (MN) genotoxic endpoint in response to ARA-C doses. RCG shows the % growth of cell cultures, RCG response drops with increasing ARA-C dose, after the white dashed line the RCG has fallen below 30% as a result only one repeat at the doses 0.21 and 0.41 µg/mL were assessed. This suggests a more finite dose range between 0.05 and 0.21 µg/mL is required. The horizontal dashed lines are the fold change cut offs for the biomarkers pH3, P53 and γH2AX. Statistical significance of 0.21 and 0.41 µg/mL were not performed due to there only being one experimental repeat. pH3 from 0.03 onward drops below the decrease fold change cut off and is significant at 0.03 and 0.05 µg/mL. γH2AX exceed the fold change cut off from 0.01 to 0.05 µg/mL only 0.05 was significant. P53 response was significant at both 0.03 and 0.05 increasing with γH2AX and MN response. The only dose demonstrating NOGEL for all biomarkers is 0.01µg/mL.

The increase of γH2AX at all doses and is above the fold change cut off, being statistically significant from 0.05 µg/mL is consistent with the chemical's MoA. A decrease of pH3 happens at each dose being significant from 0.03 µg/mL dropping below the cut off fold

change decrease value. Fold change for P53 surpasses the suggested cut off and is significant at 0.03 µg/mL. MN increases as dose increases however no response is significant, this could be due to the large SD value at 0.03 µg/mL and 0.05 µg/mL doses.

Figure 5.15 below demonstrates the effect of ARA-C on the cell cycle. G1 population decreases with dose and G2/M population increases whilst S phase stays stable up to 0.05 ug/mL. A statistically significant decrease in G1 and a statistically significant increase in G2/M are observed at 0.05 µg/mL.

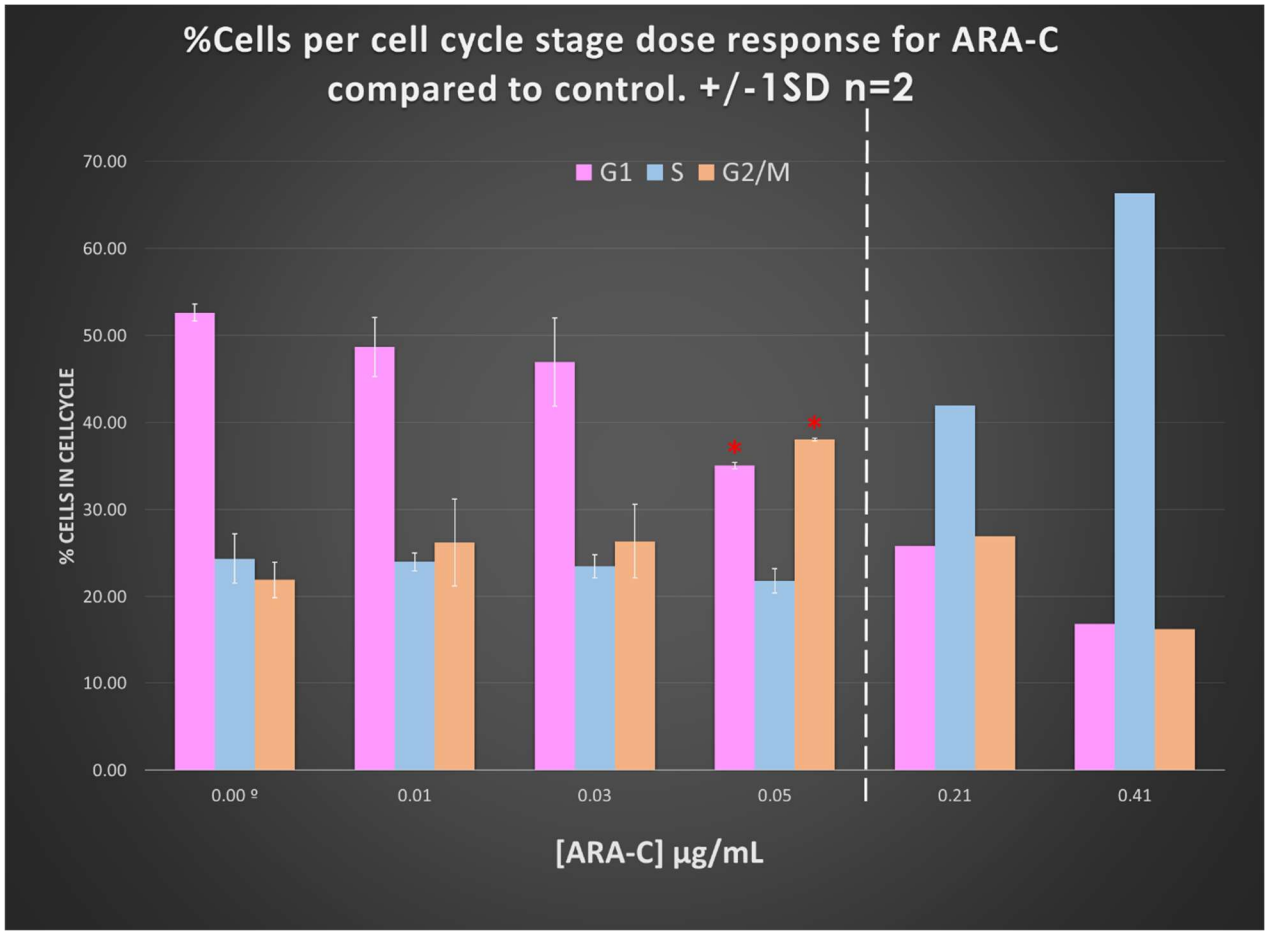

ºVehicle control DMSO
**Significant response p value < 0.05* ** Highly Significant Response p value<0.0001*

Figure 5.15: Graph showing percentage of cells found in each portion of the cell cycle in relation to ARA-C concentration. As the ARA-C concentration increases the G1, S and G2 stages of the cell cycle shift. G1 decreases at all doses including 0.21 and 0.41 µg/mL and is significant at 0.05. Number of S phase cells remain stable up to 0.05ug/mL after this the S phase population increases dramatically. G2/M phase demonstrates the reverse of S phase increasing initially, being significant at 0.05, before decreasing drastically at 0.21 and 0.41 µg/mL doses. The white line indicates the doses where the RCG was below 30%.

Tables 5.7a and 5.7b below show the data for direct cell cycle assessment with biomarker response and statistical significance is demonstrated with an Asterix. Data for 5.7a is also displayed in graphical format in figure 5.16.

Table 5.7a: Fold change average of biomarkers ɣH2AX and P53 in direct relation to the phase of the cell cycle the cell population is in ±1SD for ARA-C

	Fold change of biomarker in relation to cell cycle																		
ARA-C (µg/mL)	G1 ɣH2AX	±SD	G1 P53	±SD	S ɣH2AX	±SD	S P53	±SD	G2 ɣH2AX	±SD	G2/M P53	±SD	Proph	±SD	Meta	±SD	Anaph	±SD	H3+ve ɣH2AX -ve	±SD
0.00 º	1.00	0.44	1.00	0.01	1.00	0.54	1.00	0.04	1.00	0.18	1.00	0.00	1.00	0.07	1.00	0.24	1.00	0.45	1.00	1.00
0.01	2.93*	0.88	1.19	0.07	2.83	1.11	1.12	0.14	1.27	0.08	1.12	0.04	0.92	0.01	1.26	0.12	0.95	0.28	0.52	0.52
0.03	3.98*	2.29	1.59*	0.28	3.15	1.96	1.36*	0.21	1.27	0.43	1.60	0.37	0.88	0.02	1.36*	0.16	0.87	0.25	1.51	0.68
0.05	3.42*	0.75	1.63*	0.18	2.92	0.96	1.46*	0.01	1.27	0.08	1.86*	0.01	0.90	0.08	1.33*	0.27	0.81	0.22	1.73	0.81
0.21¯	1.58		1.10		1.15		1.05		0.96		1.36		1.01		0.92		0.00		2.95	
0.41¯	2.04		1.36		1.38		1.31		1.10		1.52		0.99		1.06		0.00		0.00	

ºVehicle control DMSO
n=2 ¯n=1 *Significant response p value < 0.05* ** Highly Significant Response p value<0.0001
Trend decrease Trend Increase

Table 5.7b: Fold change average of the ratio of Prophase metaphase and anaphase cells populations when compared to control for ARA-C.

	Mitosis stage fold change ratio		
ARA-C (µg/mL)	Prophase:Ananaphase+Metaphase	Metaphase:Prophase	Anaphase:Prophase
0.00 º	1.00	1.00	1.00
0.01	0.62	1.48	1.24
0.03	0.56	1.65	1.17
0.05	0.60	1.58	1.04
0.21¯	0.00	0.00	0.00
0.41¯	0.00	0.00	0.00

ºVehicle control DMSO
n=2 ¯n=1 Trend decrease Trend Increase

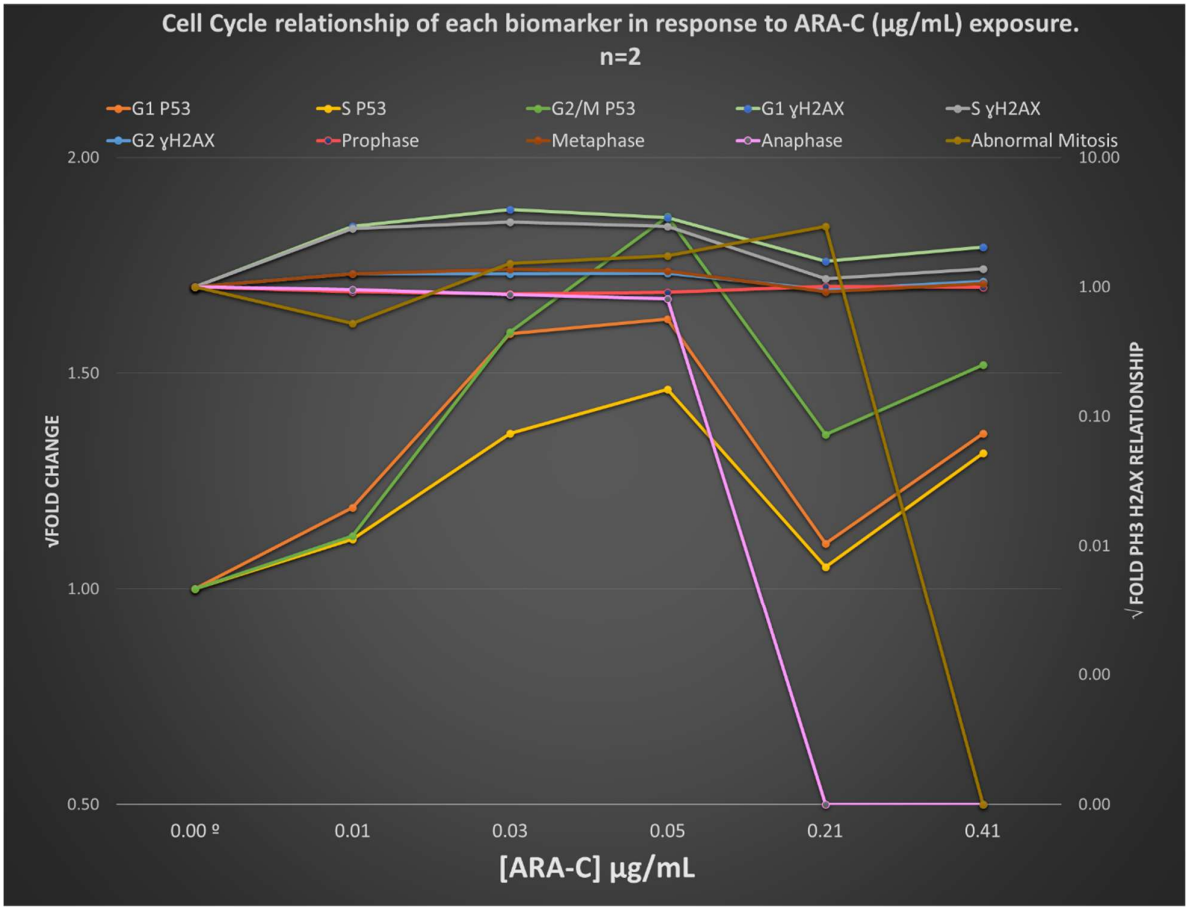

ºVehicle control DMSO

Figure 5.16: Line scatter graph visually displaying data in table 5.7a illustrating relationship of each biomarker and cell cycle stage for ARA-C. Primary Y axis shows the P53 response data. Secondary Y axis plots γH2AX and pH3 cell cycle signals and relationship, the axis scale is logged. Statistical significance of each response can be found in table 5.7a.

The γH2AX response is seen most in the G1 portion of the cell cycle being statistically significant at all doses as seen in table 5.7a. Though no doses were significant for S pahse γH2AX response, there was a trend increase greater than fold change cut off at all doses. Levels of γH2AX increase slightly at the G2 portion of the cell cycle compared to control, this could be due to DSB repair. Whilst pH3 overal has decreased reultining in no change of cells in prophase, a increase of cells in metaphase generating a statistically significant response at doses 0.03 and 0.05 µg/mL and decrease of cells in annaphase. Whilst cells in healthy mitosis decreases, cells that have managed to enter mitosis display abnormal mitotic profile by being positive for pH3 signal but negative for γH2AX signal have increased. At all doses ARA-C seems to have the most impact on P53 at the G2/M phase of the cell cycle . G1 has the next highest P53 activation followed lastly by S phase of the cell cycle. Doses being significant at 0.03 and 0.05µg/mL. Figure 5.17

further demonstrates assessment of Metaphase anaphase and prophase relationship response to ARA-C.

There is a decrease of prophase: combined anaphase and metaphase ratio and a increase of metahase:prophase ratio, there is not much change of the anaphase:prophase ratio this is expected due to the decrease of cell phosphorylated H3 in mitosis.

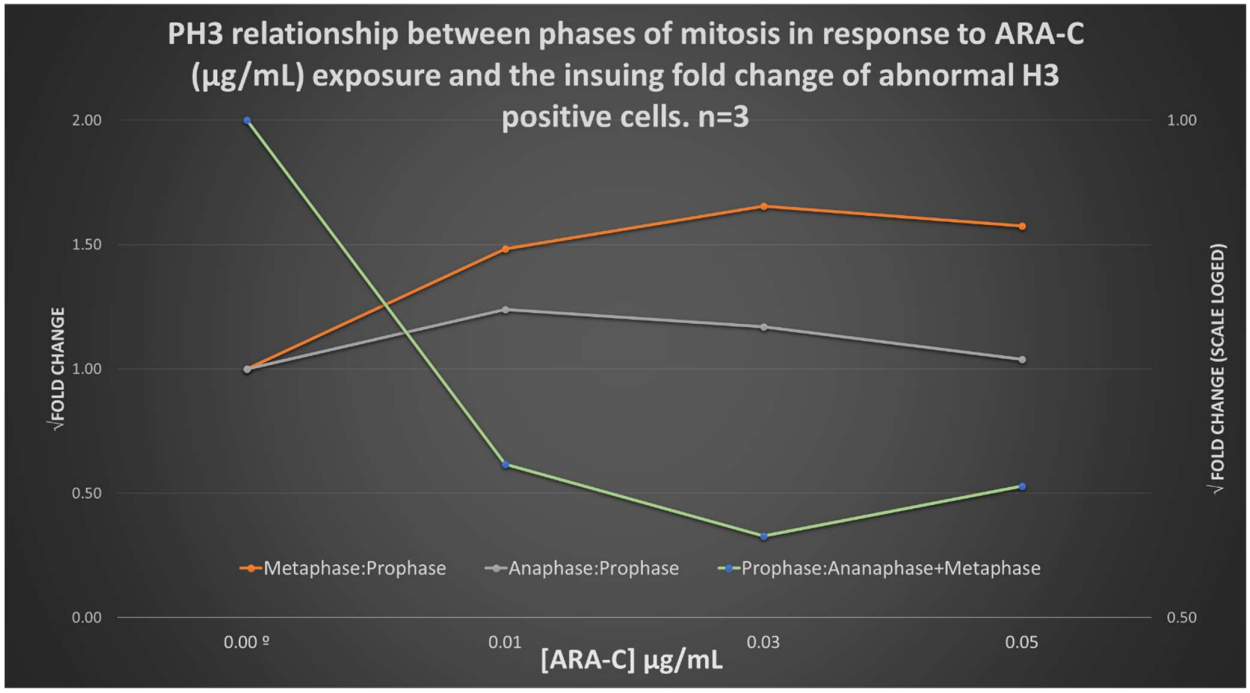

ºVehicle control DMSO

Figure 5.17: Line scatter graph displaying the ratio of average fold change responses (data in table 5.7b) for ARA-C. Allowing assessment of proportional changes of the different phases of mitosis to one another. Primary Y axis shows the changes compared to vehicle control of the individual metaphase prophase change, and anaphase prophase change. Secondary Y axis plots the overall prophase response to anaphase and metaphase combined. No statistical analysis was performed, a qualitative trend only was looked at. There was a trend decrease of prophase population to the combined anaphase/metaphase population before starting to increase at 0.05 µg/mL. There was an increase of metaphase to prophase at all doses and anaphase to prophase cell populations followed a slight increase both starting to decrease at 0.05µg/mL. 0.21 and 0.41 µg/mL doses are not shown due to a lack of anaphase response as shown in table 5.7b.

Table 5.8 looks at biomarker signal presence within the MN.

Table 5.8: ARA-C 0.05ug/mL - Biomarker presence or absence in true MN microscope images obtained on ISXII

Stain present in MN	Total count	% MN Cells
DRAQ5™ only	556	94.9
DRAQ5™ and P53	9	1.5
DRAQ5™ and ɣH2AX	20	3.4
DRAQ5™ P53 and ɣH2AX	1	0.2

N=1 Mn total= 586

Presence of MN with P53 signal are minimal which is consistent with the overall low response of P53 biomarker levels. There is a 3% portion of the MN have ɣH2AX 1.5% that has P53 and 0.2% that have both biomarkers. These responses are relatively low when compared to the other chemicals and their biomarker MN assessment most of the MN present contained no biomarker signal.

5.4 – Discussion

5.4.1 – Etoposide

Etoposide is a topoisomerase II inhibitor, it stabilizes the cleavage topoisomerase II-DNA complex which prevents the sealing of the DNA backbone leading to DSBs (Caldecott *et al*., 1990).

Though there is a slight increase of ɣH2AX the response is not necessarily consistent with the expected larger increase suggested by the initial understanding of the mechanism. Especially as the P53 response indicating DNA damage presence is so strong and is statistically significant from 0.03µg/mL onwards. However, this is consistent with results in the literature, Tamamori-Adaci *et al*., 2018 in the P53 competent H295R cells ɣH2AX response was not detected prior to 72hrs of treatment. The cell cycle responses of ɣH2AX do demonstrate differences (see table 5.1a) the decrease of G1 ɣH2AX signal is likely related to the G1 population decrease. The increase of ɣH2AX at 0.24 µg/mL S phase suggests the beginnings of senescence of S phase checkpoint in relation to ɣH2AX response

Whilst the ɣH2AX response is not necessarily as drastic as expected the decrease of pH3 is consistent with compound effect. Cells are not exiting the G2/M phase of the cell cycle, but cells are continuing to exit the G1 and S phases. The decrease of pH3 population combined with the S/G2 arrest at the 24hr time point is consistent with current literature (Ando *et al*., 2014). P53 response is the best DNA damage indicator at the 24hr time point looked at for Etoposide along with MN response. At 0.24µg/mL, like ɣH2AX, the P53 at S phase increases over that of G1 which again suggests the cell cycle induced affect at higher doses is important and consistent with the biology.

It has been suggested that topoisomerase II inhibiter induced DSB's are marked for repair by the NHEJ pathway as a result, cells containing a DNA repair system, as is the case with TK6's, would confir a threshold level at which this repair system would become overwhelmed (Smart *et al*., 2008; Mao *et al*., 2001; Malik *et al*., 2006). This therefore suggests that at the 24 hour time point chosen combined with the rapid continual repair nature of NHEJ along with the dose concentrations selected results in any initial ɣH2AX response based on immediate DSB's generated on initial introduction of Etoposide would be repaired resulting in the dissipation of the ɣH2AX signal as seen here. It is therefore reasonable to suggest that to truly assess the Etoposide MoA in this system a more finite dose range exceeding 0.5 µg/mL at the 24 hour time point to overwhelm the system tolerance for Etoposide exceeding the DNA damage threshold should be assessed alongside similar doses at a 3-4 hour exposure time point (Smart *et al*., 2008; Lynch *et al*., 2003; Kirkland *et al*., 2010; Wilson *et al*., 2021).

5.4.2 – Cizotinib

Crizotinib inhibits ALK but stabilises the P53 protein resulting in cell cycle arrests (Lev *et al*., 2018). This cell cycle profile and increase of G2/M cell population at the top dose is consistent with literature (Megiorni *et al*., 2015).

Crizotinib on its own does not sufficiently induce double strand breakage to further signal P53 response to induce an apoptotic outcome for the cancer cell, rather it induces cell cycle arrest that could potentially be recovered from, this is why Crizotinib cancer therapies are usually combinatorial (Lev *et al*., 2017). This lack of DSB induction is identified here through lack of ɣH2AX response above that of control levels, this is consistent with aneugenic MoA and with current literature (Dertinger *et al*., 2019). The increase of G1 ɣH2AX is more likely due to the chemical simply inducing stress on the cells and the lack of G1 P53 response at these lower levels of Crizotinib where ɣH2AX has these fold increases implies this is generic background stress response rather than actual induced DNA damage. P53 response is significant at G1, S and G2/M at the same doses 2.25 and 4.51µg/mL.

The lack of pH3 induction that is usually a sign of aneugenicity could be as a result of off target effects on aurora kinases that are used in the phosphorylation of H3 (Kong *et al*., 2018; Dertinger *et al*., 2019; Crosio *et al*., 2002). When assessing the prophase, metaphase, anaphase relationships, pH3 being of less than control levels, when there is no reduction over all in the collective pH3 population, may be a suggestion of slight mitotic arrest at the metaphase portion of the cell cycle. Whilst more in depth analysis would need to be taken, it is a interesting trend to take note of. This suggestion is further backed up by an increase of multinucleated cells (bi, tri and tetra nucleated) examples of which are demonstrated below in figure 5.18 suggesting potential for a non-disjunction event and or blocking of cytokinesis. This observation was also noted and investigated further by Megiorni *et al*., 2015.

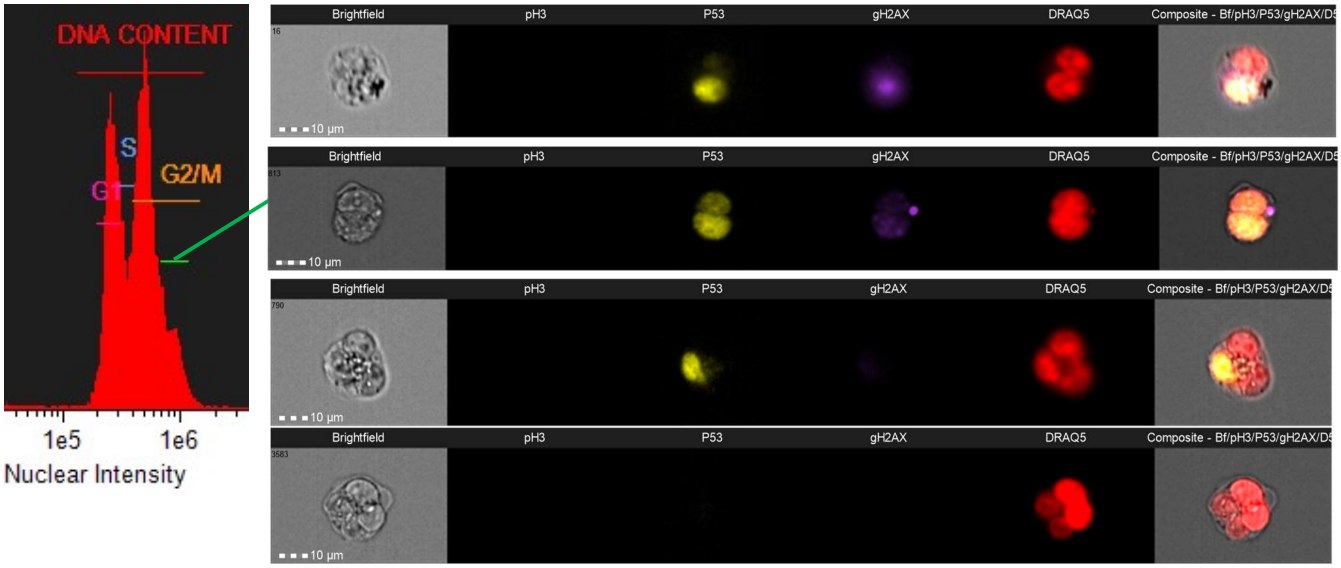

Figure 5.18: Demonstrating multinucleated cells and location within DNA histogram with cell cycle gates and rare events generated by Crizotinib. Image Row 2 shows a binucleate cell with MN containing ɣH2AX signal. Image Row 1 and 3 show a bi and tri nucleated cell with P53 sequestered to only one nucleus.

The limited response of ɣH2AX response variation along with P53 increases confirm Crizotinibs tyrosine kinase inhibition potentially having an effect on the ɣH2AX response pathway whilst re-affirming Crizotinibs stabilisation of the P53 anti tumour molecule.

The lack of activity at the lower doses of Crizotinib, <2.25µg/mL showed no significant changes of biomarker response (figure 5.5) or cell cycle response (figure 5.6) suggests that between the dose concentrations of 2.25 and 4.51 µg/mL a more refined set of interval concentrations should be used to truly elucidate the biomarker and MN dose response. This being said the profile generated by the platform of no ɣH2AX and pH3 dose response whilst being statistically significant for P53 and MN response as seen in figure 5.6 and polyploidisation is consistent with recently reported results (Dertinger *et al*., 2019).

Vinblastine – 5.4.3

Vinblastine binds to tubulin inhibiting mitotic spindle assembly. Based on the data above the dose response of Vinblastine recorded is consistent with that in the literature of a aneugenic profile (Smart *et al*., 2020; Dertinger *et al*., 2019). The response by ɣH2AX for the system is consistent with the expected hypothesis that there would be no or limited increase in ɣH2AX signal detected. The slight increase back to control levels of ɣH2AX at the top dose could be indicative of an increase in cells signalling entry into apoptosis. This is consistent with Carbendazim data suggesting a lack of ɣH2AX increase can be linked to a aneugenic MoA (Bryce *et al*., 2016; Audbert *et al*., 2016). Increase of pH3 signal is now well classified in the literature with being consistent with a aneugenic Mode of Action, here pH3 signal exceeds the fold change cut off of being greater than

1.1 fold. P53 as associated as a marker for DNA damage and cell cycle maintenance increased presence is to be expected and does so proportionally with MN response (Bryce *et al*., 2007; Bryce *et al*., 2016; Audbert *et al*., 2016). P53 stabilization really drives home the activity of the cell at the various checkpoints. The highest response of P53 being in G2/M implies this is where the chemical is having the most impact despite the percentage of cells in G2/M being of a smaller population than G1 at the 0.0010 µg/mL dose and lower. Up until 0.0008µg/mL cell cycle response (figure 5.10) was consistent with literature (Bryce *et al*., 2007). The increase in percentage cells found in G1 is in line with cells that have not quite received enough damage to arrest in G2M but have stalled in cell cycle progression at the G1 checkpoint. An overall decrease of percentage cells in S phase implies that the cells present in S phase whilst reduced are capable of continued cell cycle progress. Unlike Bryce *et al*., 2007 where cytotoxity was a limiting factor, concentrations up to 0.0020 µg/mL were able to be assessed. At the top dose the effect on the cell cycle observed is a large portion of cells in G2/M phase increasing and G1 decreasing. As figure 5.12 demonstrates there is a fold increase of ɣH2AX at 0.0020µg/mL, this increase corresponds with an overall decrease of cell population in the G1 phase. This increase of ɣH2AX signal could be indicative of cells entering apoptosis (figure 5.19) or the Vinblastine chemical at higher doses having a secondary clastogenic effect. It is interesting to note that the overall response of ɣH2AX not having an increase further demonstrates the importance of scrutinising cellular responses compared with one another rather than making sweeping assessments on general trends of biomarkers.

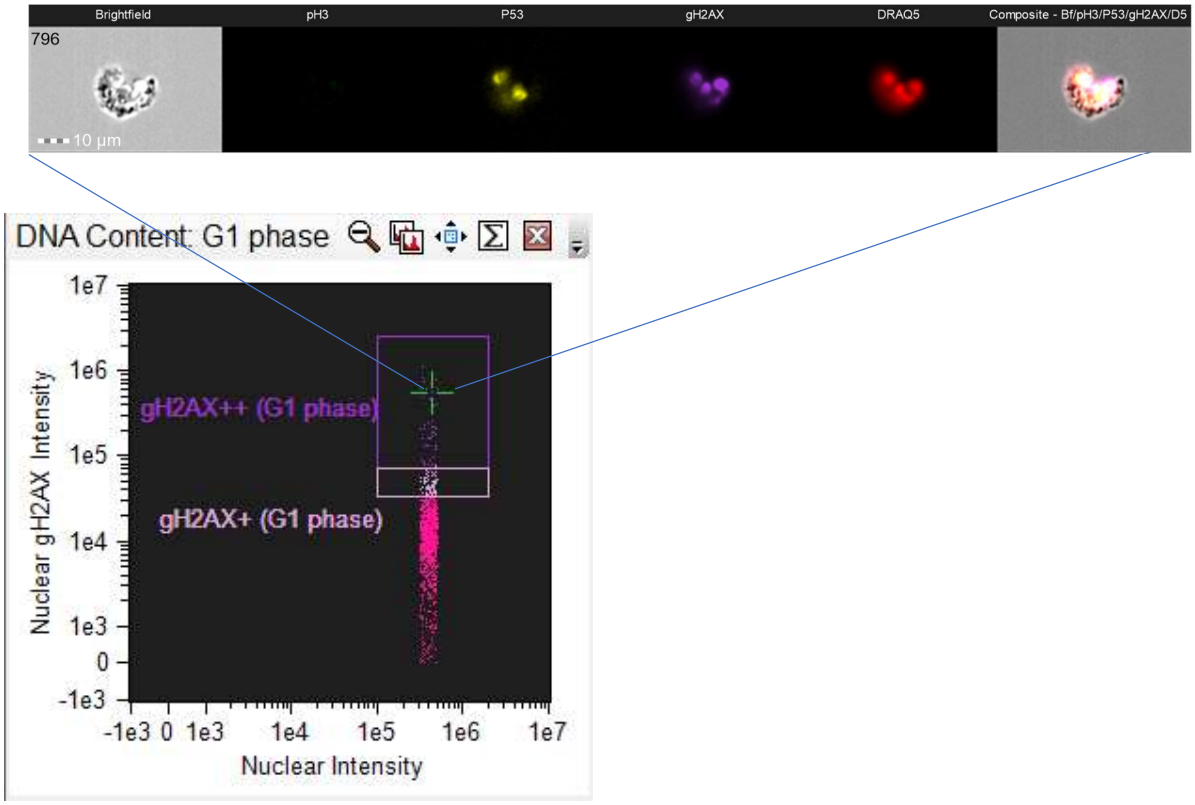

Figure 5.19: Shows the G1 gH2AX response for Vinblastine at the 0.002µg/mL dose and corresponding apoptotic cell image. The scatter point demonstrating apoptosis is in the ++ gate. This is the population of gH2AX being assessed for response metric. The cell image shows this cell is likely apoptotic with its blebbing nucleus.

Though the biology behind ɣH2AX and pH3 is linked and established i.e., during mitosis there is a global phosphorylation of H3 and ɣH2AX and therefore in this context ɣH2AX cannot be relied upon as a marker for DNA damage. There is no reason to say that a change away from the “normal” healthy relationship of pH3 and ɣH2AX should not be considered a potential way to help indicate MoA as previously discussed. Vinblastine clearly demonstrates a dose response increase of abnormally mitotic cells (table 5.5a) suggesting mitosis is a key site of DNA damage activity. This reasoning is not unreasonable to suggest given Vinblastine exposure has been shown to induce chromosome lag and non-disjunction events (Zijno *et al*., 1996; Surrallés *et al*., 1995).

Whilst there is a clear dose dependant statistically significant increase of pH3 signal the relative proportions of cells in prophase, metaphase and anaphase compared to control have not increased with any great effect, but rather decreased. This at first can seem counter intuitive, as surely there should be an increase at the metaphase stage as this is the main step of spindle interaction. However, understanding of the underlying biology explains this decrease of cells at the metaphase/anaphase cell stages. As Vinblastine is a spindle poison the cell essentially stalls before entering into "correct" metaphase so

there ends up being a build-up of cells ready to exit prophase/prometaphase but can not because of the damage to spindle assembly. Therefore, looking at the change proportionally from cells identified as prophase compared to cells in metaphase and anaphase a response can be identified, see figure 5.14, to potentially identify the arresting phase within mitosis i.e., prophase arrest. Whilst this is an interesting observation on the proportional effects of cells in prophase vs metaphase vs anaphase additional spindle poisons would need to be assessed. At this point in time the system as it is cannot explicitly identify the exact stage of influence of the compound past that of generically saying the "compound causes cell cycle arrest at the M phase of the cell cycle" without further assessment.

5.4.4 - ARA-C

ARA-C not only does it become incorporated into the DNA during synthesis which results in double strand breakage (Gerson *et al*., 2018) it also inhibits DNA damage repair through binding of polymerases resulting in inhibition of cell repair at checkpoints outside synthesis phase (Gerson *et al*., 2018). As ɣH2AX is a DSB biomarker a increase in ɣH2AX with a increase of DSB is expected.

As the chemical mainly impacts the S phase of the cell cycle and inhibits polymerases (Momparler, 2013), as the data here suggests this prevents cells from passing into G2 and passing the G2/M checkpoint there is a corresponding decrease of cells with H3 phosphorylation. This suggests that the integrity of the DNA, due to integration of ARA-C, results in a genomic instability that mitosis cannot support, this explains the decrease of cells in G1 population as shown in figure 5.17

Whilst a effect at the lower doses on S phase would be expected initially the effect on the checkpoints and DNA repair mechanisms seem to be larger. This can be explained by cells not passing the G2/M checkpoint due to interferences with polymerase reactions. At the lower doses the repair pathway mechanisms and the inactivation of the chemical to ARA-U (uracil arabinoside) by cytidine deaminase initially helps protect the synthesis portion of the cell cycle (Momparler, 2013). At some point between 0.05 and 0.21µg/mL there is a overwhelming of the synthesis pathway protective mechanisms at which point the expected effect of cell cycle arrest at the s phase of the cell cycle is observed.

As figure 5.16 shows P53 increases with ɣH2AX induction confirms true DNA damage is occurring. Inhibition of the DNA damage repair system at the G2M checkpoint explains this increase of G1 ɣH2AX signal and the increase of S phase ɣH2AX is also explained as the compound induces more double strand breakage as the compound becomes integrated into the DNA. The importance of the G2/M response is highlighted by P53, where at all doses ARA-C induces P53 response the most at the G2/M phase of the cell cycle this could be due to cell cycle arrest at the G2/M checkpoint leading to mitotic catastrophe.

5.4.5 – ISMN-me MoA Overview

Data displayed above indicates the ISMN-me whilst flawed is able to identify differences between the various chemicals assessed. Based on the general consensus in the literature (Bryce *et al*., 2016; Bryce *et al.,* 2017; Khoury *et al*., 2016; Dertinger *et al*., 2018) induction of P53 response is indicative of DNA damage, pH3 increase indicates aneugenictity and ɣH2AX increase indicates clastogenicity and MN generation is proportional to genotoxic potential of a compound. In all instances the ISMN-me assay detected a increase in MN and P53 response. The chemicals MMS, ARA-C and Etoposide display features associated with clastogenicity (increase MN, P53, ɣH2AX and decrease in pH3). The chemicals Vinblastine, Carbendazim and Crizotinib display features associated with aneugenicity (increase MN, P53 pH3 and decrease ɣH2AX). Specific cell cycle biomarker assessment enabled further insights into cell cycle processing of DNA damage response markers. Whilst conclusive decisions cannot be made at this stage about the in depth cell cycle biomarker profile for chemicals of varying chemical classes a acknowledgement that differences of these cell cycle biomarker metrics generate different chemical profiles (even within known MoA groupings) can be detected, see figure 5.20 below.

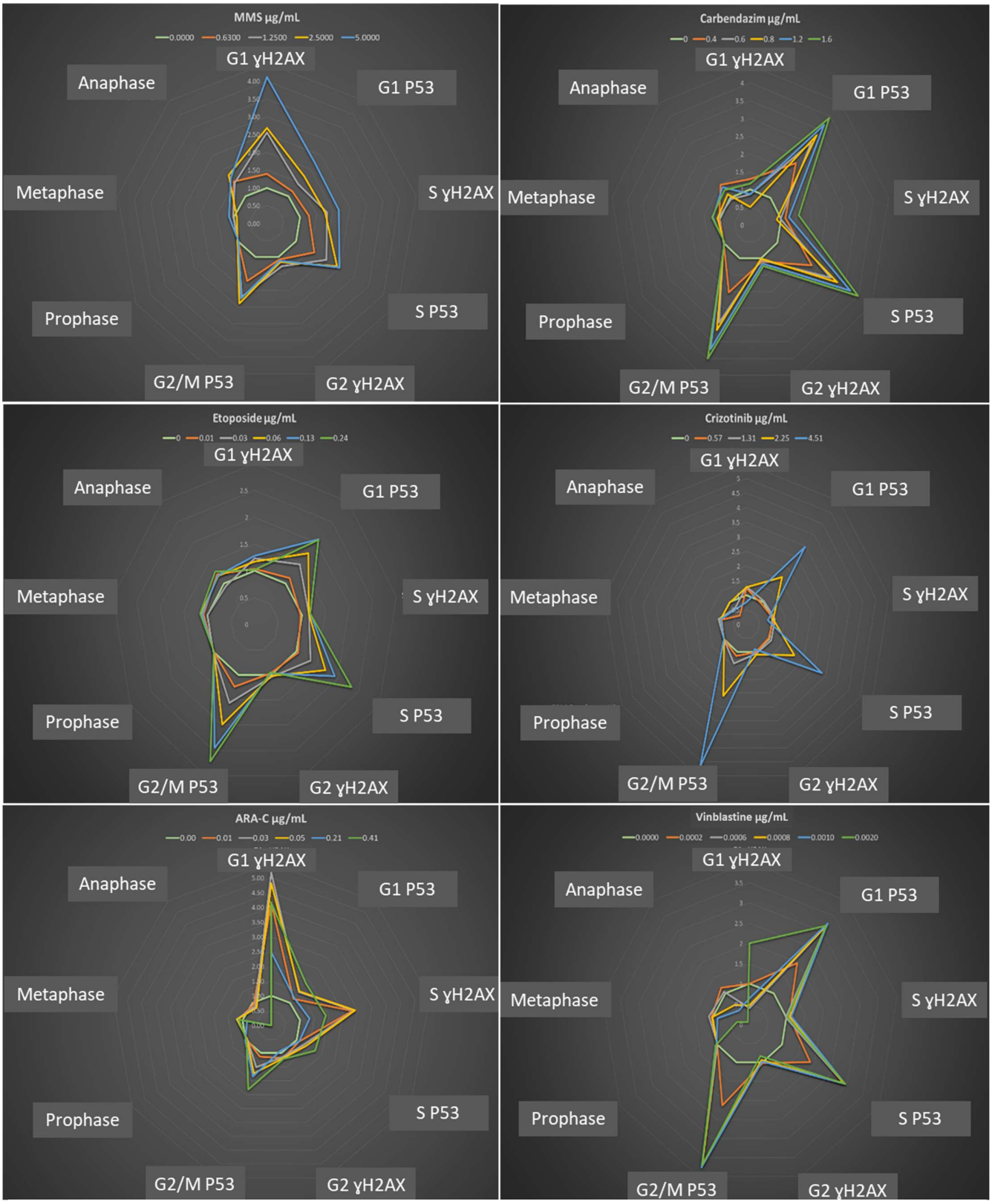

Figure 5.20: Demonstrating qualitatively the overall visual differences of the different genotoxic chemicals assessed. Left panel is known clastogens and right panel known aneugens. Graphs show the plotted square root fold change of biomarkers as radar graphs. Different coloured lines are relative to the dose and points around the edge are metrics assessed excluding MN. Based on shape MMS and ARA-C work via clastogenic MoA. Carbendazim, Crizotinib and Vinblastine via a aneugenic MoA. Etoposide demonstrates features of both aneugenic and clastogenic MoA which has been identified in other studies (Hermine et al., 1997).

The high content nature of the assay allowed for the assessment of rare events such as MN containing P53 and or ɣH2AX signal. Whilst the meaning of these relationships has yet to be investigated fully the ability to assess these events because of microscopy image presences provides an addition angle for MoA assessment. Furthermore, features such as multinucleation in response to chemical presence was also identified as a potential avenue of investigation as demonstrated in figure 5.18. Image analysis also allowed confirmation of potential reasons for clastogenic marker increase in response at higher doses due to apoptotic induction, see figure 5.19. Ability for further data mining of rare cellular events such as P53 translocation to one nucleus in a multinucleated cell (figure 5.18) offer exciting avenues of exploration with deep learning techniques.

Chapter 6 – General Discussion

6.1 – Thesis Overview

Here I demonstrate a simple robust protocol for optimised staining of fixed human lymphoblast p53 proficient TK6 cells with the antibodies; Anti- ɣH2AX, Anti -P53 and Ant-pH3S28 along with DRAQ5™ DNA staining in a whole cell multiplex system that is suitable for analysis via microscopy or imaging flow cytometry. Antibody penetration of the cell and nuclear membrane was demonstrated by qualitative assessment of confocal microscopy Z-Stack imagery that allowed 3D visualisation of nuclear specific antibody binding. Use of the Amnis® FlowSight® and ImageStream X Mark II® platform provided a high content, high throughput acquisition platform with the sensitivity of flow cytometry and accuracy of image analysis. Using both optimal and suboptimal lasers for fluorophore excitation demonstrated that a multiplex system for DNA damage assessment including MN was possible in unlysed cells. IDEAS® 6.2 template generation allowed for batch processing of data samples extracting the following metrics: Cell Cycle, MN, ɣH2AX, P53, pH3, G1 ɣH2AX, G1 P53, S ɣH2AX, S P53, G2 ɣH2AX, G2/M P53, G2M Prophase pH3, G2M Metaphase pH3, G2M Anaphase pH3, Abnormal mitosis (H3+ve ɣH2AX-ve) and shifts in Prophase, Metaphase and Anaphase relationships along with some preliminary data on biomarker signal found within MN. The system found differences in the biomarker metric responses between the chemicals; MMS, Carbendazim, ARA-C, Vinblastine, Etoposide and Crizotinib suggesting potential for chemical MoA elucidation.

6.1.1 – Template Generation and Batch Processing

IDEAS® 6.2 is a intuitive software that is user friendly providing comparable data sets across FlowSight® and ImageStream X Mark II® machines. Template design and batch analysis of data sets filtered user bias while providing high data content outputs that were able to be mined for relevant responses linked with the biology of the antibodies and DNA stain used. However, limitations of this multiplex platform were mainly found in relation to the IDEAS® 6.2 software and masking features. Lack of a automated cell cycle assessment feature hindered the batch processing of data sets requiring manual placement of the cell cycle gates G1 S and G2/M to account for sample variability. On average the masking spot count feature for MN analysis was on only 57% accurate with a 45% miss rate which varied between chemical classes.

6.1.2 – FlowSight® and ImageStream X Mark II®

I have begun to investigate the use of mechanistic markers alongside MN scoring to provide multiplex data analysis. From the data increases in micronucleus dose responses can be observed, alongside their corresponding respective responses within the mechanistic markers ɣH2AX P53 and pH3. The data appears to demonstrate the typical responses indicative of MMS acting via a clastogenic MoA and Carbendazim acting through an aneugenic MoA. Whilst the FlowSight® system did not allow for the four colour stain system to be used the dual marker response with regards to pH3 and ɣH2AX was consistent with the optimised assay response data. Both the FlowSight® dual marker system and ISMN-me allowed MoA assessment to enable high throughput and

high content whole cell analysis, along with computer-based image scoring and archiving.

For MMS there was a dose dependant increase of ɣH2AX and MN at the same doses where H3 signal decreasing. The relevant increase in ɣH2AX reflects an increase of cells with DNA strand breaks, at the same concentration as MN and P53 levels, along with there being a decrease of cells in mitosis as demonstrated by the reduction in pH3 signal. From the results generated, MMS appears to cause MN through chromosome breaks, and this is displayed without the need for kinetochore labelling. By contrast the aneugen Carbendazim had the reverse ɣH2AX, H3 profile at the same concentrations as an increase in MN and P53 response. The decrease in strand breaks observed, could be linked with mitotic arrest, and the increase in H3 is in line with the response of known aneugens, particularly when happening at the same concentrations as the increase in MN. This suggests that MN are generated through aneuploidy dominant mechanism. Furthermore, the greater fold increase of P53 response of Carbendazim compared to MMS could be indicative of the fact MN generation via aneugenicity is more lethal than simply DSB generation.

6.1.3 – ISMN-me Assay

ISMN-me whilst flawed, i.e., accuracy of the MN mask, is able to identify differences between the various chemicals assessed. Based on the general consensus in the literature (Bryce *et al*., 2016; Bryce *et al*., 2017; Koury *et al*., 2016; Dertinger *et al*., 2019) induction of P53 response is indicative of DNA damage, pH3 increase indicates aneugenistity, ɣH2AX increase indicates clastogenicity and MN generation is proportional to genotoxic potential of a compound. In all instances the ISMN-me assay detected a increase in MN and P53 response. The chemicals MMS, ARA-C and Etoposide display features associated with clastogenicity (Increase MN, P53, ɣH2AX and decrease in pH3). The chemicals Vinblastine, Carbendazim and Crizotinib display features associated with aneugenisity (increase MN, P53 pH3 and decrease ɣH2AX). Specific cell cycle biomarker assessment enabled further insights into cell cycle processing of DNA damage response markers. Whilst conclusive decisions cannot be made at this stage about the in depth cell cycle biomarker profile for chemicals of varying chemical classes, an acknowledgement can be made that differences of these cell cycle biomarker metrics generate different chemical profiles (even within known MoA groupings) can be detected. The main drawbacks of the system thus far are actually in relation to limitations of software and data mining to accurately and coherently unlock the available information collected in the data sets.

6.1.4 – Position In Industry

The principal advantage of this assay is the simultaneous detection of DNA damage Mode of Action whilst maintaining the morphological high content localisation information of microscopy, with the high throughput potential of flow cytometry. These qualities of the ISMN-me assay place the platform within industry safety assessment, specifically in genetic toxicology within the drug development pipeline filling a niche not

covered by current MoA genetic toxicology assays (Wilson *et al*., 2021; Dertinger *et al*., 2018).

Use of such a platform for understanding of MoA could result in less late stage attrition and reduction on the abandoning of promising candidates too early. For instance, compounds with a aneugenic MoA can have thresholds of carcinogenic risk established (Elhajouji *et al*., 2011). In terms of clastogens, due to their direct interaction with DNA, this thresholds approach is less accepted however with more in depth MoA data thresholds of safety could be established (Wills et al., 2017). Being able to analyse thousands of cells across multiple samples in mere seconds could provide the quantitative data needed to start making such decisions as well as providing opportunities to interrogate rare event generation as shown in figure 6.1 and potential links to mechanism providing information for Adverse Outcome Pathway generation.

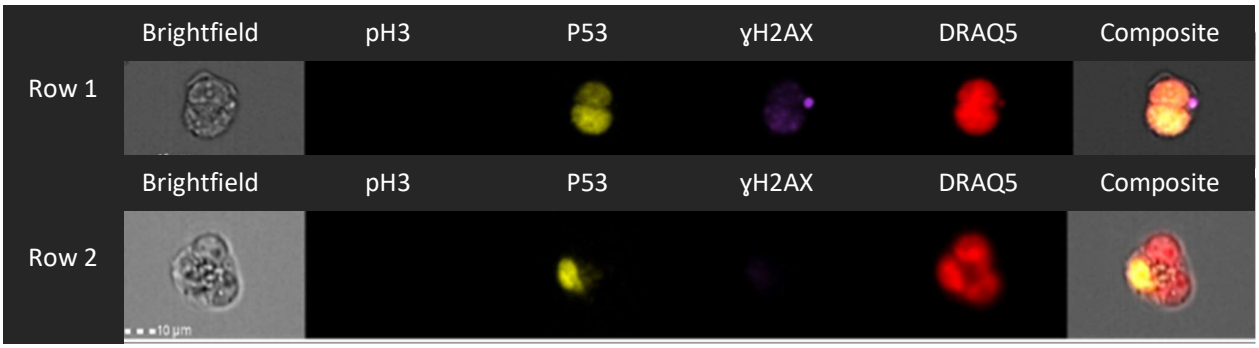

Figure 6.1: Rare event identification. Row 1 shows a binucleated cell with MN containing ɣH2AX signal. Row 2 shows a tetra nucleated cell with P53 signal aggregated to one nucleus.

Adverse Outcome Pathways refer to conceptual steps associated with stress factors that result in a molecular initiating event that can then progress through a series of key events that result in an adverse outcome. This framework of adverse outcome pathway generation relies on existing knowledge and empirical data between upstream and downstream toxicological pathways (Zeiger *et al*., 2015; Sasaki *et al*., 2020). AOP development requires the identification and detection of key events along the pathway, these frameworks can then be used to identify MoA. Thus, MoA's of specific chemicals and their classes can be used to generate hypothetical MoA across compounds that are similar in action and structure. Elucidation of MoA's, using assays such as the one described here, for a small subset of chemicals can potentially inform on a larger chemical space reducing time and resource (Zeiger *et al*., 2015; Derarfield *et al*., 2017; Sasaki *et al*., 2020). The high throughput, high content as well as miniaturisation and automation potential of the ISMN-me assay alongside Artificial Intelligence (AI) imaging classifiers and generation of AOPs could aid in the evolving landscape of next generation genetic toxicology testing strategy as reviewed by Dearfield *et al* 2017 providing a greater pool of information for assessing realistic risk in humans.

Having the ability to generate data on multiple DNA damage markers, as well as provides a template analysis approach for batch processing of acquired image files, the platform provides a reduction in time and resource required for compound assessment. As a result, it not only has the ability to reduce late stage attrition, but also could potentially be used as a screening assay for candidate selection optimisation. An extension of this is the determining of appropriate testing strategies to decrease animal usage, as well as off and on target interrogations. Whilst the IMN-me assay has the potential to be useful in the decision making process within the drug development pipeline, as demonstrated throughout chapters 3, 4 and 5 the complex profiles generated by the biomarkers and imagery information have posed a challenge in the presentation of the data. Use of tools such as Toxicological Prioritization Index (ToxPi) visualisation software for generation of a carcinogenicity scores could go a long way to making this barrage of information easier to digest and draw conclusions from in terms of determining MoA (Chapman *et al*., 2021; Wilde *et al*., 2018). Whilst promising, generation of clean cut 'Yes/No' decision making, that is often relied upon in genetic toxicology with regard to compound progression and regulatory submissions, specifically in relation to biomarker response and best approaches is a topic of debate (Chapman *et al*., 2021; Wheeldon *et al*., 2020; Bryce *et al*., 2018; Dertinger *et al*., 2019; Gollapudi *et al*., 2013; Wilson *et al*., 2021).

6.2 – Conclusion

ɣH2AX, pH3 and P53 use on the flow cytometry platform have become increasingly popular and the combination of Cell Cycle, MN ɣH2AX, pH3 and P53 signal results on the Amnis® FlowSight® (only pH3 and ɣH2AX) and ImageStream X Mark II® has proven consistent with current literature (Bryce *et al*., 2016; Khoury *et al*., 2016). Combined use of Cell Cycle, MN ɣH2AX, pH3 and P53 signal in a single sample containing unlysed cells allows for the direct comparison of DNA damage biomarkers MN and Cell cycle responses of chemicals that directly and indirectly result in DNA damage events. The system provides a reduction in experimental variability when compared to separate sample analysis, reduces time of sample preparation, number of samples needing to be assessed and amount of compound required for analysis. Adaptability for use using auto sampling and 96well plates generates not only a high content assay but a high through put one as well.

Whilst the ISMN-me platform does not necessarily provide the same resolution and qualitative microscopy power of confocal microscopy. The system provides the high content power of flow cytometry with the spatial location of microscopy. Archival of thousands of images allows for continual mining of data sets as understanding of biology evolves and software programmes are updated. The ISMN-me assay is a novel approach to genetic toxicology assessment in the identification of Mode of Action and giving insights into the underlying mechanisms has potential for use as a chemical screening system in the pharmaceutical industry during the drug development pipeline.

During 24hr exposures the ISMN-me system was able to identify differences between aneugenic MoA (inhibiting microtubule formation Vinblastine, microtubule destabilisation Carbendazim and tyrosine Kinase Inhibitor Crizotinib) Clastogen alkylating agent MMS,

nucleoside analogue ARA-C, topoII inhibitor Etoposide MoA. Whilst further work on these chemicals including 3hr exposures in presence and absence of metabolic activation (S9) and additional ECVAM chemical analysis is still needed to confirm the trends seen here, potential for the assay is promising.

Use of this staining approach on the Amnis® Imaging flow cytometry platform allows for specific image analysis of individual cells. Combining the assessment of signal intensity per cell and cellular morphology offers additional MoA information alongside the MN assay. Within this body of work this approach allows for the direct comparison of P53, pH3 and ɣH2AX signals with direct respect to MN results, per cell, as well as direct biomarker cell cycle analysis. The 12 channel system of the platform, provides potential for further expansion of the multiplex assay to add in more mechanistic markers. This platform has the ability to reduce the subjectivity of traditional flow cytometry gating, due to the individual assessment of physical cellular images and additional features offered within the IDEAS® software such as pixel saturation, for each biomarker within each gate. Another significant advantage to this approach, is that it does not require cell lysis, therefore the histone foci and MN are maintained within the boundary of the cell cytoplasmic membrane. This could result in a reduction of misleading positives as providing MN localisation data ensures that each MN and cellular signal is associated with its own cell of origin. Furthermore, access to the cellular images provide additional morphological data which can be mined for additional information. This additional spatial information could aid further chemical categorisation based on mechanism of action in a fast, automated way. The ISMN-me assay has potential to be a powerful tool in helping elucidate chemical MoA.

6.2.1 – Future Work and Developments

ISMN-me assay is at the start of its journey and whilst the first initial steps of optimisation have been completed and feasibility of chemical MoA shown, more work is still required to identify the robustness of the assay and expand its usage into more specific DNA damage and high content image analysis assessment. As optimal machine setting, and gating strategies have been established re-analysis of Carbendazim and MMS need to be performed to confirm preliminary results. Repeats of experiments showing unexpected results i.e., Etoposide, need to be performed along with degradation experiments to identify the robustness of the assay. Having performed the initial 24 hour exposures of six chemicals an additional 3 hour exposure assay arm needs to be performed in the presence and absence of a metabolic activating system. Not only as part of the assay validation criteria, as suggested in the OECD guidelines, but also to assess potential biomarker and cell cycle nuances under a shorter exposure at higher concentrations. Further chemicals from the ECVAM list of model chemicals need to be tested to aid in elucidation of cell cycle biomarker related patterns for different chemical groups and assessment of the assays' sensitivity and specificity in identification of true negative and positive compounds. Initial work has only been performed in the well defined TK6 cell line, assessment of the assay in other cell lines such as the metabolically active HepG2 cell line would further assess the robustness as well as flexibility and transferability of this assay.

Future developments of the assay lie in true miniaturisation of the assay i.e., culturing cells, compound treatments and staining all performed in 96 well plates to aid in assay automation. As the ImageStream has the capacity to accept up to 12 different fluorophores further expansion of the assay is possible. Potential avenues of additional biomarkers to explore could be: Use of an apoptotic marker such as a antibody against cleaved PARP or anti-cleaved caspase 3 for identification of cells that are triggered for cell death; Use of multiple phosphorylated P53 antibodies specific to different phosphorylation events for identification of particular DNA damage responses i.e., reactive oxygen species induced damage; biomarkers for specific DNA damage repair pathway assessment i.e., MGMT, OGG1. Further high content image analysis and re analysis of current data sets using the Deep Flow neural network, developed at Swansea University or IDEAS® 6.3 and Amnis AI software (Wills *et al*., 2021; Rodrigues, *et al*., 2021) for data mining of biomarker metrics, MN responses and cell cycle analysis. Assessment of collected bi-nucleated ISMN-me files and compare analysis and biomarker responses to mononucleated data to assess the impact of Cyto-B on the biomarker responses.

Use of the ISMN-me assay for chemical MoA assessment has barely begun and multiple avenues for further gains in efficiency and precision will come as software and understandings evolve. Suggestions above are just a small sampling of the plethora of possibilities for this platform.

Here I have focused on the imaging flow cytometry platform, however the preparation and staining method of the samples has the adaptability to be moved into other microscopy based platforms allowing for further alignment with the more commonly used microscopy techniques within genetic toxicology. Adding to the tools in the genetic toxicology arsenal allows for the advent of more robust testing, allows for a greater understanding with less time and resource as well as help direct compounds into more appropriate drug projects i.e., oncology. Feed into in silico databases and generation of adverse outcome pathways to aid in animal use reduction. Whilst it is tempting to suggest with the variability of *in vitro* tests and the subjectivity of flow cytometry to simply abandon these Mode and Mechanism of action genetic toxicology assays and their development in favour of the exciting new world toxicogenomics. It is my opinion that advancements in safety science such as toxicogenomics should be used alongside the more traditional genotoxic end points and biomarkers to create a holistic view of the mode and mechanism minutia. Demonstrating the genetic effect and the physical biological response expanding our understanding. “Any fool can know. The point is to understand” Albert Einstein.

References

Abramowitz, M., Spring, K. R., Keller, E., & Davidson, M. W. (2002) Basic Principles of Microscope Objectives. *BioTechniques*. 33(4).

Adler, I. D., Kliesch, U., van Hummelen, P., & Kirsch-Volders, M. (1991). Mouse micronucleus tests with known and suspect spindle poisons: results from two laboratories. *Mutagenesis*, *6*(1), 47–53. https://doi.org/10.1093/mutage/6.1.47

Alberts, B., Johnson, A., Lewis, J., Raff, M., Roberts, K., & Walter, P. (2002). Molecular Biology of the Cell. 4th edition. New York: Garland Science; The Structure and Function of DNA. https://www.ncbi.nlm.nih.gov/books/NBK26821/

Altmeyer, M., & Lukas, J. (2013). To spread or not to spread--chromatin modifications in response to DNA damage. *Current opinion in genetics & development*, 23(2), 156–165. https://doi.org/10.1016/j.gde.2012.11.001

Ames, B. N., Durston, W. E., Yamasaki, E., & Lee, F. D. (1973). Carcinogens are mutagens: a simple test system combining liver homogenates for activation and bacteria for detection. *Proceedings of the National Academy of Sciences of the United States of America*, *70*(8), 2281–2285. https://doi.org/10.1073/pnas.70.8.2281

Amnis part of EMD Millipore. (2015) IDEAS®: Image Data Exploration and Analysis Software User's Manual, Version 6.2.

Applegate, M. L., Moore, M. M., Broder, C. B., Burrell, A., Juhn, G., Kasweck, K. L., Lin, P. F., Wadhams, A., & Hozier, J. C. (1990). Molecular dissection of mutations at the heterozygous thymidine kinase locus in mouse lymphoma cells. *Proceedings of the National Academy of Sciences of the United States of America*, *87*(1), 51–55. https://doi.org/10.1073/pnas.87.1.51

Ashby, J., & Tennant, R. W. (1988). Chemical structure, Salmonella mutagenicity and extent of carcinogenicity as indicators of genotoxic carcinogenesis among 222 chemicals tested in rodents by the U.S. NCI/NTP. *Mutation research*, *204*(1), 17–115. https://doi.org/10.1016/0165-1218(88)90114-0

Audebert, M., Riu, A., Jacques, C., Hillenweck, A., Jamin, E. L., Zalko, D., & Cravedi, J. P. (2010). Use of the γH2AX assay for assessing the genotoxicity of polycyclic aromatic hydrocarbons in human cell lines. *Toxicology letters*, *199*(2), 182–192. https://doi.org/10.1016/j.toxlet.2010.08.022

Avery, O. T., MacLeod, C. M., & McCarty, M. (1944). Studies on the chemical nature of the substance inducing transformation of pneumococcal types: Induction of transformation desoxyribonucleic acid fraction isolated from pneumococcus type III. *The Journal of experimental medicine*, *79*(2), 137–158. https://doi.org/10.1084/jem.79.2.137

Avlasevich, S., Bryce, S., De Boeck, M., Elhajouji, A., Van Goethem, F., Lynch, A., Nicolette, J., Shi, J., & Dertinger, S. (2011). Flow cytometric analysis of micronuclei in mammalian cell cultures: past, present and future. *Mutagenesis*, *26*(1), 147–152. https://doi.org/10.1093/mutage/geq058

Bailly, V., & Verly, W. G. (1988). Possible roles of beta-elimination and delta-elimination reactions in the repair of DNA containing AP (apurinic/apyrimidinic) sites in mammalian cells. *The Biochemical journal*, *253*(2), 553–559. https://doi.org/10.1042/bj2530553

Baldwin, E. L., & Osheroff, N. (2005). Etoposide, topoisomerase II and cancer. *Current medicinal chemistry. Anti-cancer agents*, *5*(4), 363–372. https://doi.org/10.2174/1568011054222364

Barteneva, N., Vorobjev, I., Basiji, D., Lau, A., Wong, T. T. W., Shum, C, H., Wong, K., Tsia, K., Hildebrand, M., Davis, A., Abbriano, R., Pugsley, H., Traller, J., Smith, S., Shrestha, R., Cook, O., Sanchez-Alvarez, E., Manandhar-Shrestha, K., & Alderete, B. (2016). Imaging Flow Cytometry: Methods and Protocols. *Methods in Molecular Biology*, vol. 1389. https://doi.org/10.1007/978-1-4939-3302-0

Bednar, J., Horowitz, R. A., Grigoryev, S. A., Carruthers, L. M., Hansen, J. C., Koster, A. J., & Woodcock, C. L. (1998). Nucleosomes, linker DNA, and linker histone form a unique structural motif that directs the higher-order folding and compaction of chromatin. *Proceedings of the National Academy of Sciences of the United States of America*, *95*(24), 14173–14178. https://doi.org/10.1073/pnas.95.24.14173

Bernacki, D. T., Bryce, S. M., Bemis, J. C., Kirkland, D., & Dertinger, S. D. (2016). γH2AX and p53 responses in TK6 cells discriminate promutagens and nongenotoxicants in the presence of rat liver S9. *Environmental and molecular mutagenesis*, *57*(7), 546–558. https://doi.org/10.1002/em.22028

Besaratinia, A., Synold, T. W., Chen, H. H., Chang, C., Xi, B., Riggs, A. D., & Pfeifer, G. P. (2005). DNA lesions induced by UV A1 and B radiation in human cells: comparative analyses in the overall genome and in the p53 tumor suppressor gene. *Proceedings of the National Academy of Sciences of the United States of America*, *102*(29), 10058–10063. https://doi.org/10.1073/pnas.0502311102

Branda, R. F., O'Neill, J. P., Brooks, E. M., Trombley, L. M., & Nicklas, J. A. (2001). The effect of folate deficiency on the cytotoxic and mutagenic responses to ethyl methanesulfonate in human lymphoblastoid cell lines that differ in p53 status. *Mutation research*, *473*(1), 51–71. https://doi.org/10.1016/s0027-5107(00)00138-x

Bridges, B. A., Dennis, R. E., & Munson, R. J. (1967). Differential induction and repair of ultraviolet damage leading to true revesions and external suppressor mutations of an ochre codon in Escherichia coli B-r WP2. *Genetics*, *57*(4), 897–908. https://doi.org/10.1093/genetics/57.4.897

Bryce, S. M., Bemis, J. C., Avlasevich, S. L., & Dertinger, S. D. (2007). *In vitro* micronucleus assay scored by flow cytometry provides a comprehensive evaluation of cytogenetic damage and cytotoxicity. *Mutation research*, 630(1-2), 78–91. https://doi.org/10.1016/j.mrgentox.2007.03.002

Bryce, S. M., Bernacki, D. T., Bemis, J. C., & Dertinger, S. D. (2016). Genotoxic mode of action predictions from a multiplexed flow cytometric assay and a machine learning approach. *Environmental and molecular mutagenesis*, *57*(3), 171–189. https://doi.org/10.1002/em.21996

Bryce, S. M., Bernacki, D. T., Bemis, J. C., Spellman, R. A., Engel, M. E., Schuler, M., Lorge, E., Heikkinen, P. T., Hemmann, U., Thybaud, V., Wilde, S., Queisser, N., Sutter, A., Zeller, A., Guérard, M., Kirkland, D., & Dertinger, S. D. (2017). Interlaboratory evaluation of a multiplexed high information content in vitro genotoxicity assay. *Environmental and molecular mutagenesis*, *58*(3), 146–161. https://doi.org/10.1002/em.22083

Caldecott, K., Banks, G., & Jeggo, P. (1990). DNA double-strand break repair pathways and cellular tolerance to inhibitors of topoisomerase II. *Cancer research*, *50*(18), 5778–5783.

Cariou, O., Laroche-Prigent, N., Ledieu, S., Guizon, I., Paillard, F., & Thybaud, V. (2010). Cytosine arabinoside, vinblastine, 5-fluorouracil and 2-aminoanthracene testing in the in vitro micronucleus

assay with L5178Y mouse lymphoma cells at Sanofi Aventis, with different cytotoxicity measurements, in support of the draft OECD Test Guideline on In Vitro Mammalian Cell Micronucleus Test. *Mutation research*, *702*(2), 148–156. https://doi.org/10.1016/j.mrgentox.2010.04.005

Chan, K., Resnick, M. A., & Gordenin, D. A. (2013). The choice of nucleotide inserted opposite abasic sites formed within chromosomal DNA reveals the polymerase activities participating in translesion DNA synthesis. *DNA repair*, *12*(11), 878–889. https://doi.org/10.1016/j.dnarep.2013.07.008

Chapman, K. E., Wilde, E. C., Chapman, F. M., Verma, J. R., Shah, U. K., Stannard, L. M., Seager, A. L., Tonkin, J. A., Brown, M. R., Doherty, A. T., Johnson, G. E., Doak, S. H., & Jenkins, G. (2021). Multiple-endpoint in vitro carcinogenicity test in human cell line TK6 distinguishes carcinogens from non-carcinogens and highlights mechanisms of action. *Archives of toxicology*, *95*(1), 321–336. https://doi.org/10.1007/s00204-020-02902-3

Chargaff, E. (1950). Chemical specificity of nucleic acids and mechanism of their enzymatic degradation. *Experientia*, *6*(6), 201–209. https://doi.org/10.1007/BF02173653

Chargaff, E. (1971). Preface to a grammar of biology. A hundred years of nucleic acid research. *Science* (New York, N.Y.), 172(3984), 637–642. https://doi.org/10.1126/science.172.3984.637

Chatterjee, N., & Walker, G. C. (2017). Mechanisms of DNA damage, repair, and mutagenesis. *Environmental and molecular mutagenesis*, *58*(5), 235–263. https://doi.org/10.1002/em.22087

Cheeseman, I. M., & Desai, A. (2008). Molecular architecture of the kinetochore-microtubule interface. *Nature reviews. Molecular cell biology*, *9*(1), 33–46. https://doi.org/10.1038/nrm2310

Chen, L., Nievera, C. J., Lee, A. Y., & Wu, X. (2008). Cell cycle-dependent complex formation of BRCA1.CtIP.MRN is important for DNA double-strand break repair. *The Journal of biological chemistry*, *283*(12), 7713–7720. https://doi.org/10.1074/jbc.M710245200

Cheung, J. R., Dickinson, D. A., Moss, J., Schuler, M. J., Spellman, R. A., & Heard, P. L. (2015). Histone markers identify the mode of action for compounds positive in the TK6 micronucleus assay. *Mutation research. Genetic toxicology and environmental mutagenesis*, *777*, 7–16. https://doi.org/10.1016/j.mrgentox.2014.11.002

Ciccia, A., McDonald, N., & West, S. C. (2008). Structural and functional relationships of the XPF/MUS81 family of proteins. *Annual review of biochemistry*, *77*, 259–287. https://doi.org/10.1146/annurev.biochem.77.070306.102408

Clauson, C., Schärer, O. D., & Niedernhofer, L. (2013). Advances in understanding the complex mechanisms of DNA interstrand cross-link repair. *Cold Spring Harbor perspectives in biology*, *5*(10), a012732. https://doi.org/10.1101/cshperspect.a012732

Cole, J., Arlett, C. F., Green, M. H., Lowe, J., & Muriel, W. (1983). A comparison of the agar cloning and microtitration techniques for assaying cell survival and mutation frequency in L5178Y mouse lymphoma cells. *Mutation research*, *111*(3), 371–386. https://doi.org/10.1016/0027-5107(83)90034-9

Collins, P. L., Purman, C., Porter, S. I., Nganga, V., Saini, A., Hayer, K. E., Gurewitz, G. L., Sleckman, B. P., Bednarski, J. J., Bassing, C. H., & Oltz, E. M. (2020). DNA double-strand breaks induce H2Ax

phosphorylation domains in a contact-dependent manner. *Nature communications*, 11(1), 3158. https://doi.org/10.1038/s41467-020-16926-x

Countryman, P. I., & Heddle, J. A. (1976). The production of micronuclei from chromosome aberrations in irradiated cultures of human lymphocytes. *Mutation research*, *41*(2-3), 321–332. https://doi.org/10.1016/0027-5107(76)90105-6

Crosio, C., Fimia, G. M., Loury, R., Kimura, M., Okano, Y., Zhou, H., Sen, S., Allis, C. D., & Sassone-Corsi, P. (2002). Mitotic phosphorylation of histone H3: spatio-temporal regulation by mammalian Aurora kinases. *Molecular and cellular biology*, *22*(3), 874–885. https://doi.org/10.1128/MCB.22.3.874-885.2002

Dahm, R. (2008). Discovering DNA: Friedrich Miescher and the early years of nucleic acid research. *Human genetics*, *122*(6), 565–581. https://doi.org/10.1007/s00439-007-0433-0

de Feraudy, S., Revet, I., Bezrookove, V., Feeney, L., & Cleaver, J. E. (2010). A minority of foci or pan-nuclear apoptotic staining of gammaH2AX in the S phase after UV damage contain DNA double-strand breaks. *Proceedings of the National Academy of Sciences of the United States of America*, *107*(15), 6870–6875. https://doi.org/10.1073/pnas.1002175107

de Laat, W. L., Jaspers, N. G., & Hoeijmakers, J. H. (1999). Molecular mechanism of nucleotide excision repair. *Genes & development*, *13*(7), 768–785. https://doi.org/10.1101/gad.13.7.768

Dearfield, K. L., Gollapudi, B. B., Bemis, J. C., Benz, R. D., Douglas, G. R., Elespuru, R. K., Johnson, G. E., Kirkland, D. J., LeBaron, M. J., Li, A. P., Marchetti, F., Pottenger, L. H., Rorije, E., Tanir, J. Y., Thybaud, V., van Benthem, J., Yauk, C. L., Zeiger, E., & Luijten, M. (2017). Next generation testing strategy for assessment of genomic damage: A conceptual framework and considerations. *Environmental and molecular mutagenesis*, 58(5), 264–283. https://doi.org/10.1002/em.22045

Decottignies, A. (2013). Alternative end-joining mechanisms: a historical perspective. *Frontiers in genetics*, 4, 48. https://doi.org/10.3389/fgene.2013.00048

Dertinger, S. D., Kraynak, A. R., Wheeldon, R. P., Bernacki, D. T., Bryce, S. M., Hall, N., Bemis, J. C., Galloway, S. M., Escobar, P. A., & Johnson, G. E. (2019). Predictions of genotoxic potential, mode of action, molecular targets, and potency via a tiered multiflow® assay data analysis strategy. *Environmental and molecular mutagenesis*, *60*(6), 513–533. https://doi.org/10.1002/em.22274

Ding, L., Cao, J., Lin, W., Chen, H., Xiong, X., Ao, H., Yu, M., Lin, J., & Cui, Q. (2020). The Roles of Cyclin-Dependent Kinases in Cell-Cycle Progression and Therapeutic Strategies in Human Breast Cancer. *International journal of molecular sciences*, *21*(6), 1960. https://doi.org/10.3390/ijms21061960

Doerig, C., Rayner, J. C., Scherf, A., & Tobin, A. B. (2015). Post-translational protein modifications in malaria parasites. *Nature reviews. Microbiology*, *13*(3), 160–172. https://doi.org/10.1038/nrmicro3402

Doherty A. T. (2012). The in vitro micronucleus assay. *Methods in molecular biology (Clifton, N.J.)*, *817*, 121–141. https://doi.org/10.1007/978-1-61779-421-6_7

Doherty, K. R., Wappel, R. L., Talbert, D. R., Trusk, P. B., Moran, D. M., Kramer, J. W., Brown, A. M., Shell, S. A., & Bacus, S. (2013). Multi-parameter in vitro toxicity testing of crizotinib, sunitinib,

erlotinib, and nilotinib in human cardiomyocytes. *Toxicology and applied pharmacology*, *272*(1), 245–255. https://doi.org/10.1016/j.taap.2013.04.027

Eker, A. P., Quayle, C., Chaves, I., & van der Horst, G. T. (2009). DNA repair in mammalian cells: Direct DNA damage reversal: elegant solutions for nasty problems. *Cellular and molecular life sciences: CMLS*, *66*(6), 968–980. https://doi.org/10.1007/s00018-009-8735-0

Elhajouji, A., Lukamowicz, M., Cammerer, Z., & Kirsch-Volders, M. (2011). Potential thresholds for genotoxic effects by micronucleus scoring. *Mutagenesis*, 26(1), 199–204. https://doi.org/10.1093/mutage/geq089

Elledge, S. J. (1996). Cell cycle checkpoints: preventing an identity crisis. *Science (New York, N.Y.)*, *274*(5293), 1664–1672. https://doi.org/10.1126/science.274.5293.1664

Fekairi, S., Scaglione, S., Chahwan, C., Taylor, E. R., Tissier, A., Coulon, S., Dong, M. Q., Ruse, C., Yates, J. R., 3rd, Russell, P., Fuchs, R. P., McGowan, C. H., & Gaillard, P. (2009). Human SLX4 is a Holliday junction resolvase subunit that binds multiple DNA repair/recombination endonucleases. *Cell*, *138*(1), 78–89. https://doi.org/10.1016/j.cell.2009.06.029

Fenech, M. (2020). Cytokinesis-Block Micronucleus Cytome Assay Evolution into a More Comprehensive Method to Measure Chromosomal Instability. *Genes*, *11*(10), 1203. https://doi.org/10.3390/genes11101203

Fenech, M., & Morley, A. A. (1985). Measurement of micronuclei in lymphocytes. *Mutation research*, *147*(1-2), 29–36. https://doi.org/10.1016/0165-1161(85)90015-9

Fenech, M., & Morley, A. A. (1989). Kinetochore detection in micronuclei: an alternative method for measuring chromosome loss. *Mutagenesis*, 4(2), 98–104. https://doi.org/10.1093/mutage/4.2.98

Fenech, M., Chang, W. P., Kirsch-Volders, M., Holland, N., Bonassi, S., Zeiger, E., & HUman MicronNucleus project (2003). HUMN project: detailed description of the scoring criteria for the cytokinesis-block micronucleus assay using isolated human lymphocyte cultures. *Mutation research*, *534*(1-2), 65–75. https://doi.org/10.1016/s1383-5718(02)00249-

Fenech, M., Kirsch-Volders, M., Natarajan, A. T., Surralles, J., Crott, J. W., Parry, J., Norppa, H., Eastmond, D. A., Tucker, J. D., & Thomas, P. (2011). Molecular mechanisms of micronucleus, nucleoplasmic bridge and nuclear bud formation in mammalian and human cells. *Mutagenesis*, *26*(1), 125–132. https://doi.org/10.1093/mutage/geq052

Fenech, M., Rinaldi, J., & Surralles, J. (1994). The origin of micronuclei induced by cytosine arabinoside and its synergistic interaction with hydroxyurea in human lymphocytes. *Mutagenesis*, *9*(3), 273–277. https://doi.org/10.1093/mutage/9.3.273

Fielder, R. J., Allen, J. A., Boobis, A. R., Botham, P. A., Doe, J., Esdaile, D. J., Gatehouse, D. G., Hodson-Walker, G., Morton, D. B., & Kirkland, D. J. (1992). Report of British Toxicology Society/UK Environmental Mutagen Society Working Group. Dose setting in in vivo mutagenicity assays. *Mutagenesis*, *7*(5), 313–319. https://doi.org/10.1093/mutage/7.5.313

Filby, A., Day, W., Purewal, S., & Martinez-Martin, N. (2016). The Analysis of Cell Cycle, Proliferation, and Asymmetric Cell Division by Imaging Flow Cytometry. *Methods in molecular biology (Clifton, N.J.)*, *1389*, 71–95. https://doi.org/10.1007/978-1-4939-3302-0_5

Filby, A., Perucha, E., Summers, H., Rees, P., Chana, P., Heck, S., Lord, G. M., & Davies, D. (2011). An imaging flow cytometric method for measuring cell division history and molecular symmetry during

mitosis. *Cytometry. Part A: the journal of the International Society for Analytical Cytology*, *79*(7), 496–506. https://doi.org/10.1002/cyto.a.21091

Fischle, W., Wang, Y., & Allis, C. D. (2003). Histone and chromatin cross-talk. *Current opinion in cell biology*, *15*(2), 172–183. https://doi.org/10.1016/s0955-0674(03)00013-9

Foster, I. (2008). Cancer: A cell cycle defect. *Radiography*, 14(2), 144-149. https://doi.org/10.1016/j.radi.2006.12.001

Fousteri, M., & Mullenders, L. H. (2008). Transcription-coupled nucleotide excision repair in mammalian cells: molecular mechanisms and biological effects. *Cell research*, *18*(1), 73–84. https://doi.org/10.1038/cr.2008.6

Fowler, P., Smith, K., Young, J., Jeffrey, L., Kirkland, D., Pfuhler, S., & Carmichael, P. (2012). Reduction of misleading ("false") positive results in mammalian cell genotoxicity assays. I. Choice of cell type. *Mutation research*, *742*(1-2), 11–25. https://doi.org/10.1016/j.mrgentox.2011.10.014

Fukui, K. (2010). DNA mismatch repair in eukaryotes and bacteria. *Journal of nucleic acids*, *2010*, 260512. https://doi.org/10.4061/2010/260512

Galano, A., Tan, D. X., & Reiter, R. J. (2018). Melatonin: A Versatile Protector against Oxidative DNA Damage. *Molecules (Basel, Switzerland)*, *23*(3), 530. https://doi.org/10.3390/molecules23030530

Gandhi, L., & Jänne, P. A. (2012). Crizotinib for ALK-rearranged non-small cell lung cancer: a new targeted therapy for a new target. *Clinical cancer research: an official journal of the American Association for Cancer Research*, *18*(14), 3737–3742. https://doi.org/10.1158/1078-0432.CCR-11-2393

Gatehouse, D. (2012). Bacterial mutagenicity assays: test methods. *Methods in molecular biology (Clifton, N.J.)*, *817*, 21–34. https://doi.org/10.1007/978-1-61779-421-6_2

Gerson, S, L., Caimi, P, F., William, B, M., & Creger, R, J. (2018). Chapter 57 - Pharmacology and Molecular Mechanisms of Antineoplastic Agents for Hematologic Malignancies. (Seventh Edition), Elsevier. Pages 849-912, ISBN 9780323357623. https://doi.org/10.1016/B978-0-323-35762-3.00057-3

Gillet, L. C., & Schärer, O. D. (2006). Molecular mechanisms of mammalian global genome nucleotide excision repair. *Chemical reviews*, *106*(2), 253–276. https://doi.org/10.1021/cr040483f

Gollapudi, B. B., Johnson, G. E., Hernandez, L. G., Pottenger, L. H., Dearfield, K. L., Jeffrey, A. M., Julien, E., Kim, J. H., Lovell, D. P., Macgregor, J. T., Moore, M. M., van Benthem, J., White, P. A., Zeiger, E., & Thybaud, V. (2013). Quantitative approaches for assessing dose-response relationships in genetic toxicology studies. *Environmental and molecular mutagenesis*, 54(1), 8–18. https://doi.org/10.1002/em.21727

Goto, H., Yasui, Y., Nigg, E. A., & Inagaki, M. (2002). Aurora-B phosphorylates Histone H3 at serine28 with regard to the mitotic chromosome condensation. *Genes to cells: devoted to molecular & cellular mechanisms*, *7*(1), 11–17. https://doi.org/10.1046/j.1356-9597.2001.00498.x

Green, M. H., & Muriel, W. J. (1976). Mutagen testing using TRP+ reversion in Escherichia coli. *Mutation research*, *38*(1), 3–32. https://doi.org/10.1016/0165-1161(76)90076-5

Hanawalt, P. C. (2002). Subpathways of nucleotide excision repair and their regulation. *Oncogene*, *21*(58), 8949–8956. https://doi.org/10.1038/sj.onc.1206096

Hans, F., & Dimitrov, S. (2001). Histone H3 phosphorylation and cell division. *Oncogene*, *20*(24), 3021–3027. https://doi.org/10.1038/sj.onc.1204326

Hartmann, A., Agurell, E., Beevers, C., Brendler-Schwaab, S., Burlinson, B., Clay, P., Collins, A., Smith, A., Speit, G., Thybaud, V., Tice, R. R., & 4th International Comet Assay Workshop (2003). Recommendations for conducting the in vivo alkaline Comet assay. 4th International Comet Assay Workshop. *Mutagenesis*, *18*(1), 45–51. https://doi.org/10.1093/mutage/18.1.45

Hartmann, A., Schumacher, M., Plappert-Helbig, U., Lowe, P., Suter, W., & Mueller, L. (2004). Use of the alkaline in vivo Comet assay for mechanistic genotoxicity investigations. *Mutagenesis*, *19*(1), 51–59. https://doi.org/10.1093/mutage/geg038

Hartwell, L. H., & Kastan, M. B. (1994). Cell cycle control and cancer. *Science (New York, N.Y.)*, *266*(5192), 1821–1828. https://doi.org/10.1126/science.7997877

Hartwig, A., Arand, M., Epe, B., Guth, S., Jahnke, G., Lampen, A., Martus, H. J., Monien, B., Rietjens, I., Schmitz-Spanke, S., Schriever-Schwemmer, G., Steinberg, P., & Eisenbrand, G. (2020). Mode of action-based risk assessment of genotoxic carcinogens. *Archives of toxicology*, 94(6), 1787–1877. https://doi.org/10.1007/s00204-020-02733-2

Hashimoto, K., Nakajima, Y., Matsumura, S., & Chatani, F. (2010). An in vitro micronucleus assay with size-classified micronucleus counting to discriminate aneugens from clastogens. *Toxicology in vitro: an international journal published in association with BIBRA*, *24*(1), 208–216. https://doi.org/10.1016/j.tiv.2009.09.006

Hayashi, M., Morita, T., Kodama, Y., Sofuni, T., & Ishidate, M., Jr (1990). The micronucleus assay with mouse peripheral blood reticulocytes using acridine orange-coated slides. *Mutation research*, *245*(4), 245–249. https://doi.org/10.1016/0165-7992(90)90153-b

Hermine, T., Jones, N. J., & Parry, J. M. (1997). Comparative induction of micronuclei in repair-deficient and -proficient Chinese hamster cell lines following clastogen or aneugen exposures. *Mutation research*, *392*(1-2), 151–163. https://doi.org/10.1016/s0165-1218(97)00053-0

Hoeijmakers J. H. (2001). Genome maintenance mechanisms for preventing cancer. *Nature*, *411*(6835), 366–374. https://doi.org/10.1038/35077232

Hoeijmakers, J. H. (2009). DNA damage, aging, and cancer. *The New England journal of medicine*, *361*(15), 1475–1485. https://doi.org/10.1056/NEJMra0804615

Hoeller, D., & Dikic, I. (2009). Targeting the ubiquitin system in cancer therapy. *Nature*, *458*(7237), 438–444. https://doi.org/10.1038/nature07960

Holloman, W. K. (2011). Unraveling the mechanism of BRCA2 in homologous recombination. *Nature structural & molecular biology*, *18*(7), 748–754. https://doi.org/10.1038/nsmb.2096

Huang, X., Kurose, A., Tanaka, T., Traganos, F., Dai, W., & Darzynkiewicz, Z. (2006). Activation of ATM and histone H2AX phosphorylation induced by mitoxantrone but not by topotecan is prevented by the antioxidant N-acetyl-L-cysteine. *Cancer biology & therapy*, *5*(8), 959–964. https://doi.org/10.4161/cbt.5.8.287

ICH S2(R1). 2011. Guidance on Genotoxicity Testing and Data Interpretation for Pharmaceuticals Intended for Human Use. Available at: https://database.ich.org/sites/default/files/S2_R1_Guideline.pdf. Accessed: 30 September 2021

Ichijima, Y., Sakasai, R., Okita, N., Asahina, K., Mizutani, S., & Teraoka, H. (2005). Phosphorylation of histone H2AX at M phase in human cells without DNA damage response. *Biochemical and biophysical research communications*, *336*(3), 807–812. https://doi.org/10.1016/j.bbrc.2005.08.164

Jackson, S. P. (2009). The DNA-damage response: new molecular insights and new approaches to cancer therapy. *Biochemical Society transactions*, *37*(Pt 3), 483–494. https://doi.org/10.1042/BST0370483

Jackson, S. P., & Bartek, J. (2009). The DNA-damage response in human biology and disease. *Nature*, 461(7267), 1071–1078. https://doi.org/10.1038/nature08467

Jenkins, G. J., Zaïr, Z., Johnson, G. E., & Doak, S. H. (2010). Genotoxic thresholds, DNA repair, and susceptibility in human populations. *Toxicology*, *278*(3), 305–310. https://doi.org/10.1016/j.tox.2009.11.016

Jensen, J. C., & Thilly, W. G. (1986). Spontaneous and induced chromosomal aberrations and gene mutations in human lymphoblasts: mitomycin C, methylnitrosourea, and ethylnitrosourea. *Mutation research*, 160(2), 95–102. https://doi.org/10.1016/0027-5107(86)90033-3

Johnson, G. E., Soeteman-Hernández, L. G., Gollapudi, B. B., Bodger, O. G., Dearfield, K. L., Heflich, R. H., Hixon, J. G., Lovell, D. P., MacGregor, J. T., Pottenger, L. H., Thompson, C. M., Abraham, L., Thybaud, V., Tanir, J. Y., Zeiger, E., van Benthem, J., & White, P. A. (2014). Derivation of point of departure (PoD) estimates in genetic toxicology studies and their potential applications in risk assessment. *Environmental and molecular mutagenesis*, *55*(8), 609–623. https://doi.org/10.1002/em.21870

Johnson, R. D., & Jasin, M. (2000). Sister chromatid gene conversion is a prominent double-strand break repair pathway in mammalian cells. *The EMBO journal*, *19*(13), 3398–3407. https://doi.org/10.1093/emboj/19.13.3398

Juan, G., Traganos, F., James, W. M., Ray, J. M., Roberge, M., Sauve, D. M., Anderson, H., & Darzynkiewicz, Z. (1998). Histone H3 phosphorylation and expression of cyclins A and B1 measured in individual cells during their progression through G2 and mitosis. *Cytometry*, *32*(2), 71–77. https://doi.org/10.1002/(sici)1097-0320(19980601)32:2<71::aid-cyto1>3.0.co;2-

Kasai, F., Hirayama, N., & Kohara, A. (2020). TK6 genome profile compared with WIL2-NS: Reference data to improve the reproducibility of genotoxicity studies. Mutation research. *Genetic toxicology and environmental mutagenesis*, 858-860, 503236. https://doi.org/10.1016/j.mrgentox.2020.503236

Kasamoto, S., Masumori, S., & Hayashi, M. (2013). In vivo micronucleus assay in mouse bone marrow and peripheral blood. *Methods in molecular biology (Clifton, N.J.)*, *1044*, 179–189. https://doi.org/10.1007/978-1-62703-529-3_9

Khoury, L., Zalko, D., & Audebert, M. (2016). Complementarity of phosphorylated histones H2AX and H3 quantification in different cell lines for genotoxicity screening. *Archives of toxicology*, *90*(8), 1983–1995. https://doi.org/10.1007/s00204-015-1599-1

King, K. L., & Cidlowski, J. A. (1998). Cell cycle regulation and apoptosis. *Annual review of physiology*, *60*, 601–617. https://doi.org/10.1146/annurev.physiol.60.1.601

Kirkland D. (2010). Evaluation of different cytotoxic and cytostatic measures for the in vitro micronucleus test (MNVit): summary of results in the collaborative trial. *Mutation research*, *702*(2), 139–147. https://doi.org/10.1016/j.mrgentox.2010.02.001

Kirkland, D., Aardema, M., Henderson, L., & Müller, L. (2005). Evaluation of the ability of a battery of three in vitro genotoxicity tests to discriminate rodent carcinogens and non-carcinogens I. Sensitivity, specificity and relative predictivity. *Mutation research*, *584*(1-2), 1–256. https://doi.org/10.1016/j.mrgentox.2005.02.004

Kirkland, D., Kasper, P., Martus, H. J., Müller, L., van Benthem, J., Madia, F., & Corvi, R. (2016). Updated recommended lists of genotoxic and non-genotoxic chemicals for assessment of the performance of new or improved genotoxicity tests. *Mutation research. Genetic toxicology and environmental mutagenesis*, *795*, 7–30. https://doi.org/10.1016/j.mrgentox.2015.10.00

Kirkland, D., Kasper, P., Müller, L., Corvi, R., & Speit, G. (2008). Recommended lists of genotoxic and non-genotoxic chemicals for assessment of the performance of new or improved genotoxicity tests: a follow-up to an ECVAM workshop. *Mutation research*, *653*(1-2), 99–108. https://doi.org/10.1016/j.mrgentox.2008.03.00

Kirkland, D., Pfuhler, S., Tweats, D., Aardema, M., Corvi, R., Darroudi, F., Elhajouji, A., Glatt, H., Hastwell, P., Hayashi, M., Kasper, P., Kirchner, S., Lynch, A., Marzin, D., Maurici, D., Meunier, J. R., Müller, L., Nohynek, G., Parry, J., Parry, E., … White, P. (2007). How to reduce false positive results when undertaking in vitro genotoxicity testing and thus avoid unnecessary follow-up animal tests: Report of an ECVAM Workshop. *Mutation research*, 628(1), 31–55. https://doi.org/10.1016/j.mrgentox.2006.11.008

Kirkland, D., Uno, Y., Luijten, M., Beevers, C., van Benthem, J., Burlinson, B., Dertinger, S., Douglas, G. R., Hamada, S., Horibata, K., Lovell, D. P., Manjanatha, M., Martus, H. J., Mei, N., Morita, T., Ohyama, W., & Williams, A. (2019). In vivo genotoxicity testing strategies: Report from the 7th International workshop on genotoxicity testing (IWGT). *Mutation research. Genetic toxicology and environmental mutagenesis*, 847, 403035. https://doi.org/10.1016/j.mrgentox.2019.03.008

Kirkland, D., Zeiger, E., Madia, F., & Corvi, R. (2014). Can in vitro mammalian cell genotoxicity test results be used to complement positive results in the Ames test and help predict carcinogenic or in vivo genotoxic activity? II. Construction and analysis of a consolidated database. *Mutation research. Genetic toxicology and environmental mutagenesis*, *775-776*, 69–80. https://doi.org/10.1016/j.mrgentox.2014.10.006

Kong, Y., Bender, A., & Yan, A. (2018). Identification of Novel Aurora Kinase A (AURKA) Inhibitors via Hierarchical Ligand-Based Virtual Screening. *Journal of chemical information and modeling*, *58*(1), 36–47. https://doi.org/10.1021/acs.jcim.7b00300

Krajewska, M., Fehrmann, R. S., de Vries, E. G., & van Vugt, M. A. (2015). Regulators of homologous recombination repair as novel targets for cancer treatment. *Frontiers in genetics*, *6*, 96. https://doi.org/10.3389/fgene.2015.00096

Krejci, L., Altmannova, V., Spirek, M., & Zhao, X. (2012). Homologous recombination and its regulation. Nucleic acids research, 40(13), 5795–5818. https://doi.org/10.1093/nar/gks270

Lavin, M. F., & Gueven, N. (2006). The complexity of p53 stabilization and activation. *Cell death and differentiation*, *13*(6), 941–950. https://doi.org/10.1038/sj.cdd.4401925

Lev, A., Deihimi, S., Shagisultanova, E., Xiu, J., Lulla, A. R., Dicker, D. T., & El-Deiry, W. S. (2017). Preclinical rationale for combination of crizotinib with mitomycin C for the treatment of advanced colorectal cancer. *Cancer biology & therapy*, *18*(9), 694–704. https://doi.org/10.1080/15384047.2017.136432

Levene, P. A. (1919). The structure of yeast nucleic acid. IV. Ammonia hydrolysis. *Journal of Biological Chemistr*y, 40, 415–424.

Levy, J. A., Virolainen, M., & Defendi, V. (1968). Human lymphoblastoid lines from lymph node and spleen. *Cancer*, *22*(3), 517–524. https://doi.org/10.1002/1097-0142(196809)22:3<517::aid-cncr2820220305>3.0.co;2-a

Li, X., & Heyer, W. D. (2008). Homologous recombination in DNA repair and DNA damage tolerance. Cell research, 18(1), 99–113. https://doi.org/10.1038/cr.2008.1

Liber, H. L., & Thilly, W. G. (1982). Mutation assay at the thymidine kinase locus in diploid human lymphoblasts. *Mutation research*, *94*(2), 467–485. https://doi.org/10.1016/0027-5107(82)90308-6

Lieber, M. R. (2010). The mechanism of double-strand DNA break repair by the nonhomologous DNA end-joining pathway. *Annual review of biochemistry*, *79*, 181–211. https://doi.org/10.1146/annurev.biochem.052308.093131

Lim, J. H., Catez, F., Birger, Y., West, K. L., Prymakowska-Bosak, M., Postnikov, Y. V., & Bustin, M. (2004). Chromosomal protein HMGN1 modulates histone H3 phosphorylation. *Molecular cell*, *15*(4), 573–584. https://doi.org/10.1016/j.molcel.2004.08.006

Lindahl, T. (1993). Instability and decay of the primary structure of DNA. *Nature*, *362*(6422), 709–715. https://doi.org/10.1038/362709a0

Lindahl, T., & Barnes, D. E. (2000). Repair of endogenous DNA damage. *Cold Spring Harbor symposia on quantitative biology*, *65*, 127–133. https://doi.org/10.1101/sqb.2000.65.127

Lloyd, M., & Kidd, D. (2012). The mouse lymphoma assay. *Methods in molecular biology (Clifton, N.J.)*, *817*, 35–54. https://doi.org/10.1007/978-1-61779-421-6_3

Lodish, H., Berk, A., Matsudaira, P., Kaiser, C. A., Krieger, M., Scott, M. P., Zipursky, S. L., & Darnell J. (2004). Molecular Biology of the Cell, p963. WH Freeman: New York, NY. 5th ed.

Lodish, H., Berk, A., Zipursky, S. L., Matsudaira, P., Baltimore, D., & Darnell, J. (2000). Molecular Cell Biology. 4th edition. New York: W. H. Freeman; Section 4.1, Structure of Nucleic Acids. Available from: https://www.ncbi.nlm.nih.gov/books/NBK21514/

Lord, C. J., & Ashworth, A. (2012). The DNA damage response and cancer therapy. *Nature*, *481*(7381), 287–294. https://doi.org/10.1038/nature10760

Lovell, D. P., Thomas, G., & Dubow, R. (1999). Issues related to the experimental design and subsequent statistical analysis of in vivo and in vitro comet studies. *Teratogenesis, carcinogenesis, and mutagenesis*, *19*(2), 109–119.

Lynch, A., Harvey, J., Aylott, M., Nicholas, E., Burman, M., Siddiqui, A., Walker, S., & Rees, R. (2003). Investigations into the concept of a threshold for topoisomerase inhibitor-induced clastogenicity. *Mutagenesis*, *18*(4), 345–353. https://doi.org/10.1093/mutage/geg003

Ma, Y., Kanakousaki, K., & Buttitta, L. (2015). How the cell cycle impacts chromatin architecture and influences cell fate. *Frontiers in genetics*, *6*, 19. https://doi.org/10.3389/fgene.2015.00019

MacGregor, J. T., Casciano, D., & Müller, L. (2000). Strategies and testing methods for identifying mutagenic risks. *Mutation research*, 455(1-2), 3–20. https://doi.org/10.1016/s0027-5107(00)00116-0

Mahajan, K., & Mahajan, N. P. (2015). Cross talk of tyrosine kinases with the DNA damage signaling pathways. *Nucleic acids research*, *43*(22), 10588–10601. https://doi.org/10.1093/nar/gkv1166

Malik, M., Nitiss, K. C., Enriquez-Rios, V., & Nitiss, J. L. (2006). Roles of nonhomologous end-joining pathways in surviving topoisomerase II-mediated DNA damage. *Molecular cancer therapeutics*, *5*(6), 1405–1414. https://doi.org/10.1158/1535-7163.MCT-05-0263

Mao, Y., Desai, S. D., Ting, C. Y., Hwang, J., & Liu, L. F. (2001). 26 S proteasome-mediated degradation of topoisomerase II cleavable complexes. *The Journal of biological chemistry*, *276*(44), 40652–40658. https://doi.org/10.1074/jbc.M104009200

Maron, D. M., & Ames, B. N. (1983). Revised methods for the Salmonella mutagenicity test. *Mutation research*, *113*(3-4), 173–215. https://doi.org/10.1016/0165-1161(83)90010-9

Mazin, A. V., Mazina, O. M., Bugreev, D. V., & Rossi, M. J. (2010). Rad54, the motor of homologous recombination. *DNA repair*, *9*(3), 286–302. https://doi.org/10.1016/j.dnarep.2009.12.006

McClendon, A. K., & Osheroff, N. (2007). DNA topoisomerase II, genotoxicity, and cancer. *Mutation research*, *623*(1-2), 83–97. https://doi.org/10.1016/j.mrfmmm.2007.06.009

Megiorni, F., McDowell, H. P., Camero, S., Mannarino, O., Ceccarelli, S., Paiano, M., Losty, P. D., Pizer, B., Shukla, R., Pizzuti, A., Clerico, A., & Dominici, C. (2015). Crizotinib-induced antitumour activity in human alveolar rhabdomyosarcoma cells is not solely dependent on ALK and MET inhibition. *Journal of experimental & clinical cancer research : CR*, *34*, 112. https://doi.org/10.1186/s13046-015-0228-4

Moeglin, E., Desplancq, D., Conic, S., Oulad-Abdelghani, M., Stoessel, A., Chiper, M., Vigneron, M., Didier, P., Tora, L., & Weiss, E. (2019). Uniform Widespread Nuclear Phosphorylation of Histone H2AX Is an Indicator of Lethal DNA Replication Stress. *Cancers*, *11*(3), 355. https://doi.org/10.3390/cancers11030355

Moll, U. M., & Petrenko, O. (2003). The MDM2-p53 interaction. *Molecular cancer research : MCR*, *1*(14), 1001–1008.

Momparler, R. L. (2013). Optimization of cytarabine (ARA-C) therapy for acute myeloid leukemia. *Experimental hematology & oncology*, *2*, 20. https://doi.org/10.1186/2162-3619-2-20

Moore, M. M., Clive, D., Hozier, J. C., Howard, B. E., Batson, A. G., Turner, N. T., & Sawyer, J. (1985). Analysis of trifluorothymidine-resistant (TFTr) mutants of L5178Y/TK+/- mouse lymphoma cells. *Mutation research*, *151*(1), 161–174. https://doi.org/10.1016/0027-5107(85)90194-0

Moore-Brown, M. M., Clive, D., Howard, B. E., Batson, A. G., & Johnson, K. O. (1981). The utilization of trifluorothymidine (TFT) to select for thymidine kinase-deficient (TK-/-) mutants from L5178Y/TK+/- mouse lymphoma cells. *Mutation research*, *85*(5), 363–378. https://doi.org/10.1016/0165-1161(81)90227-2

Morimoto, S., Tsuda, M., Bunch, H., Sasanuma, H., Austin, C., & Takeda, S. (2019). Type II DNA Topoisomerases Cause Spontaneous Double-Strand Breaks in Genomic DNA. *Genes*, *10*(11), 868. https://doi.org/10.3390/genes10110868

Mortelmans, K., & Riccio, E. S. (2000). The bacterial tryptophan reverse mutation assay with Escherichia coli WP2. *Mutation research*, *455*(1-2), 61–69. https://doi.org/10.1016/s0027-5107(00)00076-2

Mortelmans, K., & Zeiger, E. (2000). The Ames Salmonella/microsome mutagenicity assay. *Mutation research*, *455*(1-2), 29–60. https://doi.org/10.1016/s0027-5107(00)00064-6

Muehlbauer, P. A., & Schuler, M. J. (2005). Detection of numerical chromosomal aberrations by flow cytometry: a novel process for identifying aneugenic agents. *Mutation research*, *585*(1-2), 156–169. https://doi.org/10.1016/j.mrgentox.2005.05.002

Nag, S., Qin, J., Srivenugopal, K. S., Wang, M., & Zhang, R. (2013). The MDM2-p53 pathway revisited. *Journal of biomedical research*, *27*(4), 254–271. https://doi.org/10.7555/JBR.27.20130030

Nimonkar, A. V., Genschel, J., Kinoshita, E., Polaczek, P., Campbell, J. L., Wyman, C., Modrich, P., & Kowalczykowski, S. C. (2011). BLM-DNA2-RPA-MRN and EXO1-BLM-RPA-MRN constitute two DNA end resection machineries for human DNA break repair. *Genes & development*, *25*(4), 350–362. https://doi.org/10.1101/gad.2003811

Norbury, C., & Nurse, P. (1992). Animal cell cycles and their control. *Annual review of biochemistry*, *61*, 441–470. https://doi.org/10.1146/annurev.bi.61.070192.002301

Nowak, S. J., & Corces, V. G. (2004). Phosphorylation of histone H3: a balancing act between chromosome condensation and transcriptional activation. *Trends in genetics : TIG*, *20*(4), 214–220. https://doi.org/10.1016/j.tig.2004.02.007

OECD. (2016), *Test No. 474: Mammalian Erythrocyte Micronucleus Test*, OECD Guidelines for the Testing of Chemicals, Section 4, OECD Publishing, Paris, https://doi.org/10.1787/9789264264762-en.

OECD. (2016), *Test No. 487: In Vitro Mammalian Cell Micronucleus Test*, OECD Guidelines for the Testing of Chemicals, Section 4, OECD Publishing, Paris, https://doi.org/10.1787/9789264264861-en.

OECD. (2017), *Overview on genetic toxicology TGs*, OECD Series on Testing and Assessment, No. 238, OECD Publishing, Paris, https://doi.org/10.1787/9789264274761-en.

OECD. (2014), *Test No. 487: In Vitro Mammalian Cell Micronucleus Test*, OECD Guidelines for the Testing of Chemicals. Section 4. Paris: OECD Publishing, pp. 1-26

OECD. (2010) Guideline for the Testing of Chemicals. *In Vitro* Mammalian Cell Micronucleus Test. 487, in *In Vitro* Micronucleus Test.

Olive, P. L., Banáth, J. P., & Durand, R. E. (1990). Heterogeneity in radiation-induced DNA damage and repair in tumor and normal cells measured using the "comet" assay. *Radiation research*, *122*(1), 86–94.

Otto, T., & Sicinski, P. (2017). Cell cycle proteins as promising targets in cancer therapy. *Nature reviews. Cancer*, *17*(2), 93–115. https://doi.org/10.1038/nrc.2016.138

Ozawa, K. (2008). Reduction of phosphorylated histone H3 serine 10 and serine 28 cell cycle marker intensities after DNA damage. *Cytometry. Part A : the journal of the International Society for Analytical Cytology*, *73*(6), 517–527. https://doi.org/10.1002/cyto.a.20559

Padalino, G., El-Sakkary, N., Liu, L. J., Liu, C., Harte, D., Barnes, R. E., Sayers, E., Forde-Thomas, J., Whiteland, H., Bassetto, M., Ferla, S., Johnson, G., Jones, A. T., Caffrey, C. R., Chalmers, I., Brancale, A., & Hoffmann, K. F. (2021). Anti-schistosomal activities of quinoxaline-containing compounds: From hit identification to lead optimisation. European journal of medicinal chemistry, 226, 113823. Advance online publication. https://doi.org/10.1016/j.ejmech.2021.113823

Panier, S., & Boulton, S. J. (2014). Double-strand break repair: 53BP1 comes into focus. Nature reviews. Molecular cell biology, 15(1), 7–18. https://doi.org/10.1038/nrm3719

Parry, J. M., & Parry, E. M. (2006). The use of the in vitro micronucleus assay to detect and assess the aneugenic activity of chemicals. *Mutation research*, *607*(1), 5–8. https://doi.org/10.1016/j.mrgentox.2006.04.007

Patterson, J. O., Swaffer, M., & Filby, A. (2015). An Imaging Flow Cytometry-based approach to analyse the fission yeast cell cycle in fixed cells. *Methods (San Diego, Calif.)*, *82*, 74–84. https://doi.org/10.1016/j.ymeth.2015.04.026

Perrone, S., Lotti, F., Geronzi, U., Guidoni, E., Longini, M., & Buonocore, G. (2016). Oxidative Stress in Cancer-Prone Genetic Diseases in Pediatric Age: The Role of Mitochondrial Dysfunction. *Oxidative medicine and cellular longevity*, *2016*, 4782426. https://doi.org/10.1155/2016/4782426

Petruseva, I. O., Evdokimov, A. N., & Lavrik, O. I. (2014). Molecular mechanism of global genome nucleotide excision repair. *Acta naturae*, *6*(1), 23–34.

Pierce, B. A. (2012). Genetics: A conceptual approach. New York: W.H. Freeman. 4th ed.

Podhorecka, M., Skladanowski, A., & Bozko, P. (2010). H2AX Phosphorylation: Its Role in DNA Damage Response and Cancer Therapy. *Journal of nucleic acids*, *2010*, 920161. https://doi.org/10.4061/2010/920161

Poehlmann, A., & Roessner, A. (2010). Importance of DNA damage checkpoints in the pathogenesis of human cancers. *Pathology, research and practice*, *206*(9), 591–601. https://doi.org/10.1016/j.prp.2010.06.006

Poetsch, A. R. (2020). The genomics of oxidative DNA damage, repair, and resulting mutagenesis. *Computational and structural biotechnology journal*, *18*, 207–219. https://doi.org/10.1016/j.csbj.2019.12.013

Poulos, R. C., Olivier, J., & Wong, J. (2017). The interaction between cytosine methylation and processes of DNA replication and repair shape the mutational landscape of cancer genomes. *Nucleic acids research*, *45*(13), 7786–7795. https://doi.org/10.1093/nar/gkx463

Punatar, R. S., Martin, M. J., Wyatt, H. D., Chan, Y. W., & West, S. C. (2017). Resolution of single and double Holliday junction recombination intermediates by GEN1. *Proceedings of the National Academy of Sciences of the United States of America*, 114(3), 443–450. https://doi.org/10.1073/pnas.1619790114

Rass, U., Compton, S. A., Matos, J., Singleton, M. R., Ip, S. C., Blanco, M. G., Griffith, J. D., & West, S. C. (2010). Mechanism of Holliday junction resolution by the human GEN1 protein. *Genes & development*, *24*(14), 1559–1569. https://doi.org/10.1101/gad.585310

Riches, L. C., Lynch, A. M., & Gooderham, N. J. (2008). Early events in the mammalian response to DNA double-strand breaks. *Mutagenesis*, *23*(5), 331–339. https://doi.org/10.1093/mutage/gen039

Rodrigues M. A. (2018). Automation of the in vitro micronucleus assay using the Imagestream® imaging flow cytometer. *Cytometry. Part A : the journal of the International Society for Analytical Cytology*, *93*(7), 706–726. https://doi.org/10.1002/cyto.a.23493

Rodrigues, M. A., Beaton-Green, L. A., Wilkins, R. C., & Fenech, M. F. (2018). The potential for complete automated scoring of the cytokinesis block micronucleus cytome assay using imaging flow

cytometry. *Mutation research. Genetic toxicology and environmental mutagenesis*, *836*(Pt A), 53–64. https://doi.org/10.1016/j.mrgentox.2018.05.003

Rodrigues, M. A., Probst, C. E., Zayats, A., Davidson, B., Riedel, M., Li, Y., & Venkatachalam, V. (2021). The in vitro micronucleus assay using imaging flow cytometry and deep learning. *NPJ systems biology and applications*, *7*(1), 20. https://doi.org/10.1038/s41540-021-00179-5

Sahu, A., Prabhash, K., Noronha, V., Joshi, A., & Desai, S. (2013). Crizotinib: A comprehensive review. *South Asian journal of cancer*, *2*(2), 91–97. https://doi.org/10.4103/2278-330X.110506

Sarrif, A. M., Bentley, K. S., Fu, L. J., O'Neil, R. M., Reynolds, V. L., & Stahl, R. G. (1994). Evaluation of benomyl and carbendazim in the in vivo aneuploidy/micronucleus assay in BDF1 mouse bone marrow. *Mutation research*, *310*(1), 143–149. https://doi.org/10.1016/0027-5107(94)90018-3

Sasaki, J. C., Allemang, A., Bryce, S. M., Custer, L., Dearfield, K. L., Dietz, Y., Elhajouji, A., Escobar, P. A., Fornace, A. J., Jr, Froetschl, R., Galloway, S., Hemmann, U., Hendriks, G., Li, H. H., Luijten, M., Ouedraogo, G., Peel, L., Pfuhler, S., Roberts, D. J., Thybaud, V., … Schuler, M. (2020). Application of the adverse outcome pathway framework to genotoxic modes of action. *Environmental and molecular mutagenesis*, *61*(1), 114–134. https://doi.org/10.1002/em.22339

Sasaki, Y. F., Sekihashi, K., Izumiyama, F., Nishidate, E., Saga, A., Ishida, K., & Tsuda, S. (2000). The comet assay with multiple mouse organs: comparison of comet assay results and carcinogenicity with 208 chemicals selected from the IARC monographs and U.S. NTP Carcinogenicity Database. *Critical reviews in toxicology*, *30*(6), 629–799. https://doi.org/10.1080/10408440008951123

Schafer K. A. (1998). The cell cycle: a review. *Veterinary pathology*, *35*(6), 461–478. https://doi.org/10.1177/030098589803500601

Schmid W. (1975). The micronucleus test. *Mutation research*, *31*(1), 9–15. https://doi.org/10.1016/0165-1161(75)90058-8

Sclafani, R. A., & Holzen, T. M. (2007). Cell cycle regulation of DNA replication. *Annual review of genetics*, *41*, 237–280. https://doi.org/10.1146/annurev.genet.41.110306.130308

Sebesta, M., Burkovics, P., Juhasz, S., Zhang, S., Szabo, J. E., Lee, M. Y., Haracska, L., & Krejci, L. (2013). Role of PCNA and TLS polymerases in D-loop extension during homologous recombination in humans. *DNA repair*, *12*(9), 691–698. https://doi.org/10.1016/j.dnarep.2013.05.001

Shi, J., Bezabhie, R., & Szkudlinska, A. (2010). Further evaluation of a flow cytometric in vitro micronucleus assay in CHO-K1 cells: a reliable platform that detects micronuclei and discriminates apoptotic bodies. *Mutagenesis*, *25*(1), 33–40. https://doi.org/10.1093/mutage/gep040

Shivji, M. K., Podust, V. N., Hübscher, U., & Wood, R. D. (1995). Nucleotide excision repair DNA synthesis by DNA polymerase epsilon in the presence of PCNA, RFC, and RPA. *Biochemistry*, *34*(15), 5011–5017. https://doi.org/10.1021/bi00015a012

Singh, N. P., McCoy, M. T., Tice, R. R., & Schneider, E. L. (1988). A simple technique for quantitation of low levels of DNA damage in individual cells. *Experimental cell research*, *175*(1), 184–191. https://doi.org/10.1016/0014-4827(88)90265-0

Skopek, T. R., Liber, H. L., Penman, B. W., & Thilly, W. G. (1978). Isolation of a human lymphoblastoid line heterozygous at the thymidine kinase locus: possibility for a rapid human cell mutation

assay. *Biochemical and biophysical research communications*, *84*(2), 411–416. https://doi.org/10.1016/0006-291x(78)90185-7

Smart, D. J., Ahmedi, K. P., Harvey, J. S., & Lynch, A. M. (2011). Genotoxicity screening via the γH2AX by flow assay. *Mutation research*, *715*(1-2), 25–31. https://doi.org/10.1016/j.mrfmmm.2011.07.001

Smart, D. J., Halicka, H. D., Schmuck, G., Traganos, F., Darzynkiewicz, Z., & Williams, G. M. (2008). Assessment of DNA double-strand breaks and gammaH2AX induced by the topoisomerase II poisons etoposide and mitoxantrone. *Mutation research*, *641*(1-2), 43–47. https://doi.org/10.1016/j.mrfmmm.2008.03.005

Smart, D. J., Helbling, F. R., Verardo, M., Huber, A., McHugh, D., & Vanscheeuwijck, P. (2020). Development of an integrated assay in human TK6 cells to permit comprehensive genotoxicity analysis in vitro. *Mutation research. Genetic toxicology and environmental mutagenesis*, *849*, 503129. https://doi.org/10.1016/j.mrgentox.2019.503129

Stracker, T. H., & Petrini, J. H. (2011). The MRE11 complex: starting from the ends. Nature reviews. *Molecular cell biology*, 12(2), 90–103. https://doi.org/10.1038/nrm3047

Sun, B., Ross, S. M., Trask, O. J., Carmichael, P. L., Dent, M., White, A., Andersen, M. E., & Clewell, R. A. (2013). Assessing dose-dependent differences in DNA-damage, p53 response and genotoxicity for quercetin and curcumin. *Toxicology in vitro: an international journal published in association with BIBRA*, *27*(6), 1877–1887. https://doi.org/10.1016/j.tiv.2013.05.015

Sun, J. M., Chen, H. Y., Espino, P. S., & Davie, J. R. (2007). Phosphorylated serine 28 of histone H3 is associated with destabilized nucleosomes in transcribed chromatin. *Nucleic acids research*, *35*(19), 6640–6647. https://doi.org/10.1093/nar/gkm737

Surrallés, J., Catalán, J., Creus, A., Norppa, H., Xamena, N., & Marcos, R. (1995). Micronuclei induced by alachlor, mitomycin-C and vinblastine in human lymphocytes: presence of centromeres and kinetochores and influence of staining technique. *Mutagenesis*, 10(5), 417–423. https://doi.org/10.1093/mutage/10.5.417

Takeiri, A., Matsuzaki, K., Motoyama, S., Yano, M., Harada, A., Katoh, C., Tanaka, K., & Mishima, M. (2019). High-content imaging analyses of γH2AX-foci and micronuclei in TK6 cells elucidated genotoxicity of chemicals and their clastogenic/aneugenic mode of action. *Genes and environment: the official journal of the Japanese Environmental Mutagen Society*, *41*, 4. https://doi.org/10.1186/s41021-019-0117-8

Thomas, A. D., Fahrer, J., Johnson, G. E., & Kaina, B. (2015). Theoretical considerations for thresholds in chemical carcinogenesis. *Mutation research. Reviews in mutation research*, *765*, 56–67. https://doi.org/10.1016/j.mrrev.2015.05.001

Thybaud, V., Aardema, M., Clements, J., Dearfield, K., Galloway, S., Hayashi, M., Jacobson-Kram, D., Kirkland, D., MacGregor, J. T., Marzin, D., Ohyama, W., Schuler, M., Suzuki, H., Zeiger, E., & Expert Working Group on Hazard Identification and Risk Assessment in Relation to In Vitro Testing (2007). Strategy for genotoxicity testing: hazard identification and risk assessment in relation to in vitro testing. *Mutation research*, 627(1), 41–58. https://doi.org/10.1016/j.mrgentox.2006.10.003

Tocris Biotechne. (2015) Cancer Research: Product Guide. 3:1-63

Tomkova, M., & Schuster-Böckler, B. (2018). DNA Modifications: Naturally More Error Prone?. *Trends in genetics : TIG*, *34*(8), 627–638. https://doi.org/10.1016/j.tig.2018.04.005

Tyson, J. J., Csikasz-Nagy, A., & Novak, B. (2002). The dynamics of cell cycle regulation. *BioEssays : news and reviews in molecular, cellular and developmental biology*, *24*(12), 1095–1109. https://doi.org/10.1002/bies.10191

Skopek, T. R., Liber, H., L., Penman, B. W., Thilly, W. G. & Hoppe, H. (1981). U.S. patent number 4,302,535 [Application Number 06/079,549] was granted by the patent office on 1981-11-24 for assay for mutagenesis in heterozygous diploid human lymphoblasts. This patent grant is currently assigned to Massachusetts Institute of Technology. Invention is credited to Henry Hoppe IV, Howard L. Liber, Bruce W. Penman, Thomas R. Skopek, William G. Thilly.

Van Hummelen, P., Elhajouji, A., & Kirsch-Volders, M. (1995). Clastogenic and aneugenic effects of three benzimidazole derivatives in the in vitro micronucleus test using human lymphocytes. *Mutagenesis*, *10*(1), 23–29. https://doi.org/10.1093/mutage/10.1.23

Venter, J. C., Adams, M. D., Myers, E. W., Li, P. W., Mural, R. J., Sutton, G. G., Smith, H. O., Yandell, M., Evans, C. A., Holt, R. A., Gocayne, J. D., Amanatides, P., Ballew, R. M., Huson, D. H., Wortman, J. R., Zhang, Q., Kodira, C. D., Zheng, X. H., Chen, L., Skupski, M., … Zhu, X. (2001). The sequence of the human genome. *Science (New York, N.Y.)*, *291*(5507), 1304–1351. https://doi.org/10.1126/science.1058040

Verma, J. R., Harte, D., Shah, U. K., Summers, H., Thornton, C. A., Doak, S. H., Jenkins, G., Rees, P., Wills, J. W., & Johnson, G. E. (2018). Investigating FlowSight® imaging flow cytometry as a platform to assess chemically induced micronuclei using human lymphoblastoid cells in vitro. *Mutagenesis*, *33*(4), 283–289. https://doi.org/10.1093/mutage/gey021

Verma, J. R., Rees, B. J., Wilde, E. C., Thornton, C. A., Jenkins, G., Doak, S. H., & Johnson, G. E. (2017). Evaluation of the automated MicroFlow® and Metafer™ platforms for high-throughput micronucleus scoring and dose response analysis in human lymphoblastoid TK6 cells. *Archives of toxicology*, *91*(7), 2689–2698. https://doi.org/10.1007/s00204-016-1903-8

Vermeulen, K., Van Bockstaele, D. R., & Berneman, Z. N. (2003). The cell cycle: a review of regulation, deregulation and therapeutic targets in cancer. *Cell proliferation*, *36*(3), 131–149. https://doi.org/10.1046/j.1365-2184.2003.00266.x

Walsh, C. P., & Xu, G. L. (2006). Cytosine methylation and DNA repair. *Current topics in microbiology and immunology*, *301*, 283–315. https://doi.org/10.1007/3-540-31390-7_11

Watson, J. D., & Crick, F. H. (1953). The structure of DNA. *Cold Spring Harbor symposia on quantitative biology*, *18*, 123–131. https://doi.org/10.1101/sqb.1953.018.01.020

Watters, G. P., Smart, D. J., Harvey, J. S., & Austin, C. A. (2009). H2AX phosphorylation as a genotoxicity endpoint. *Mutation research*, *679*(1-2), 50–58. https://doi.org/10.1016/j.mrgentox.2009.07.007

Wheeldon, R. P., Bernacki, D. T., Dertinger, S. D., Bryce, S. M., Bemis, J. C., & Johnson, G. E. (2020). Benchmark Dose Analysis of DNA Damage Biomarker Responses Provides Compound Potency and Adverse Outcome Pathway Information for the Topoisomerase II Inhibitor Class of Compounds. *Environmental and molecular mutagenesis*, 61(4), 396–407. https://doi.org/10.1002/em.22360

Wiencke, J. K. (2002). DNA adduct burden and tobacco carcinogenesis. *Oncogene*, *21*(48), 7376–7391. https://doi.org/10.1038/sj.onc.1205799

Wilde, E. C., Chapman, K. E., Stannard, L. M., Seager, A. L., Brüsehafer, K., Shah, U. K., Tonkin, J. A., Brown, M. R., Verma, J. R., Doherty, A. T., Johnson, G. E., Doak, S. H., & Jenkins, G. (2018). A novel, integrated in vitro carcinogenicity test to identify genotoxic and non-genotoxic carcinogens using human lymphoblastoid cells. *Archives of toxicology*, 92(2), 935–951. https://doi.org/10.1007/s00204-017-2102-y

Wills, J. W., Johnson, G. E., Battaion, H. L., Slob, W., & White, P. A. (2017). Comparing BMD-derived genotoxic potency estimations across variants of the transgenic rodent gene mutation assay. *Environmental and molecular mutagenesis*, 58(9), 632–643. https://doi.org/10.1002/em.22137

Wilson, A., Grabowski, P., Elloway, J., Ling, S., Stott, J., & Doherty, A. (2021). Transforming early pharmaceutical assessment of genotoxicity: applying statistical learning to a high throughput, multi end point in vitro micronucleus assay. *Scientific reports*, *11*(1), 2535. https://doi.org/10.1038/s41598-021-82115-5

Woodworth, A. M., & Holloway, A. F. (2017). The Role of Epigenetic Regulation in Transcriptional Memory in the Immune System. *Advances in protein chemistry and structural biology*, *106*, 43–69. https://doi.org/10.1016/bs.apcsb.2016.09.002

Xia, F., Wang, X., Wang, Y. H., Tsang, N. M., Yandell, D. W., Kelsey, K. T., & Liber, H. L. (1995). Altered p53 status correlates with differences in sensitivity to radiation-induced mutation and apoptosis in two closely related human lymphoblast lines. *Cancer research*, *55*(1), 12–15.

Zeiger E. (1987). Carcinogenicity of mutagens: predictive capability of the Salmonella mutagenesis assay for rodent carcinogenicity. *Cancer research*, *47*(5), 1287–1296.

Zeiger, E., Gollapudi, B., Aardema, M. J., Auerbach, S., Boverhof, D., Custer, L., Dedon, P., Honma, M., Ishida, S., Kasinski, A. L., Kim, J. H., Manjanatha, M. G., Marlowe, J., Pfuhler, S., Pogribny, I., Slikker, W., Stankowski, L. F., Jr, Tanir, J. Y., Tice, R., van Benthem, J., … Thybaud, V. (2015). Opportunities to integrate new approaches in genetic toxicology: an ILSI-HESI workshop report. Environmental and molecular mutagenesis, 56(3), 277–285. https://doi.org/10.1002/em.21923

Zeiss, C. (2010) Zen 2010: LSM 710, LSM 780 , LSM 710 NLO, LSM780 NLO and ConfoCor 3, Zhang, Y., Xia, M., Jin, K., Wang, S., Wei, H., Fan, C., Wu, Y., Li, X., Li, X., Li, G., Zeng, Z., & Xiong, W. (2018). Function of the c-Met receptor tyrosine kinase in carcinogenesis and associated therapeutic opportunities. *Molecular cancer*, *17*(1), 45. https://doi.org/10.1186/s12943-018-0796-y

Zhang, F., Fan, Q., Ren, K., & Andreassen, P. R. (2009). PALB2 functionally connects the breast cancer susceptibility proteins BRCA1 and BRCA2. *Molecular cancer research: MCR*, *7*(7), 1110–1118. https://doi.org/10.1158/1541-7786.MCR-09-0123

Zhou, C., Li, Z., Diao, H., Yu, Y., Zhu, W., Dai, Y., Chen, F. F., & Yang, J. (2006). DNA damage evaluated by gammaH2AX foci formation by a selective group of chemical/physical stressors. *Mutation research*, 604(1-2), 8–18. https://doi.org/10.1016/j.mrgentox.2005.12.004

Zijno, A., Leopardi, P., Marcon, F., & Crebelli, R. (1996). Analysis of chromosome segregation by means of fluorescence in situ hybridization: application to cytokinesis-blocked human lymphocytes. *Mutation research*, 372(2), 211–219. https://doi.org/10.1016/s0027-5107(96)00141-8

Supplement 1

MN Masks 1, 2 and 3 step wise generation

MN MASK 1

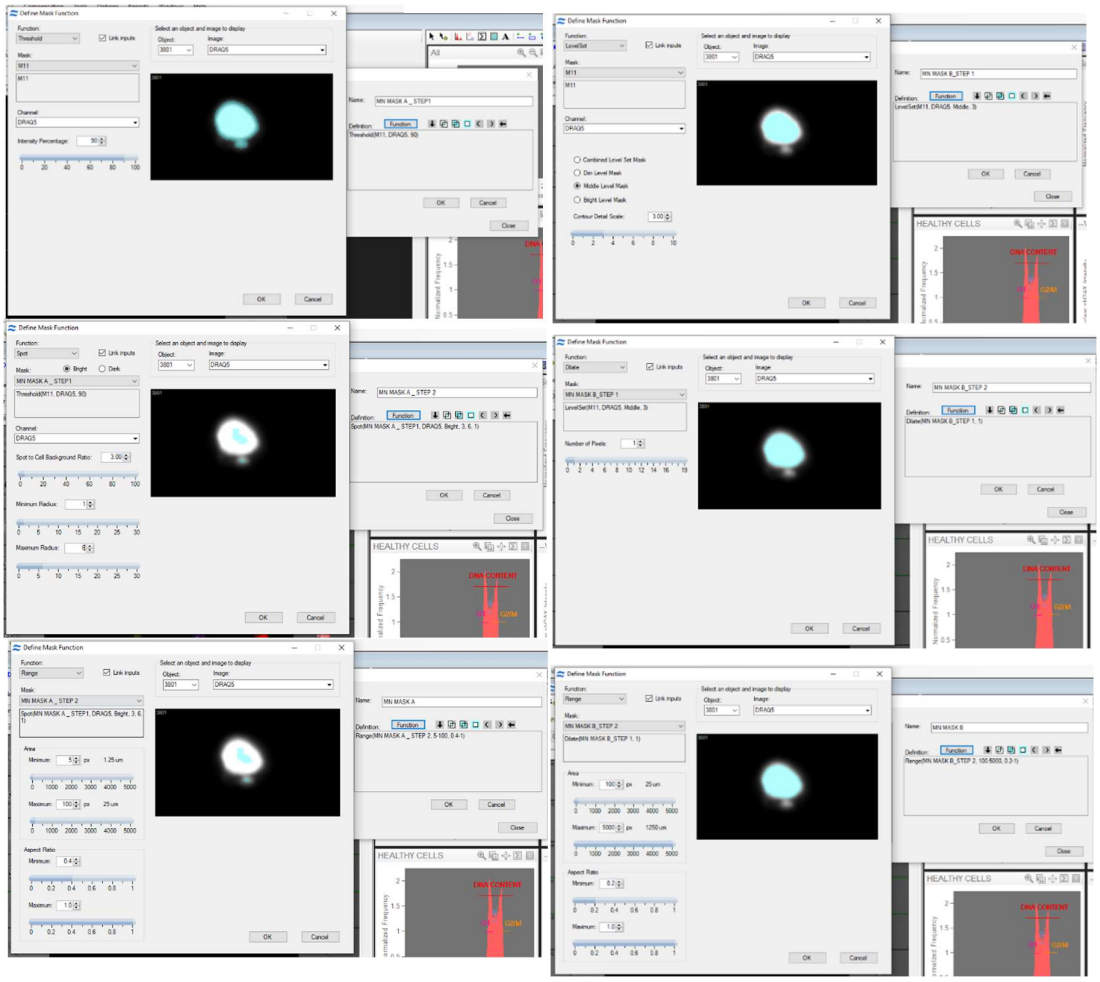

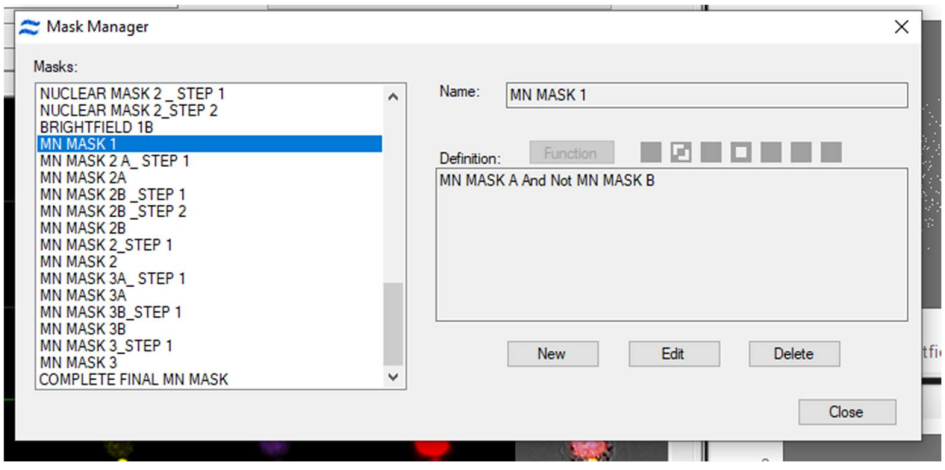

MN Mask 2

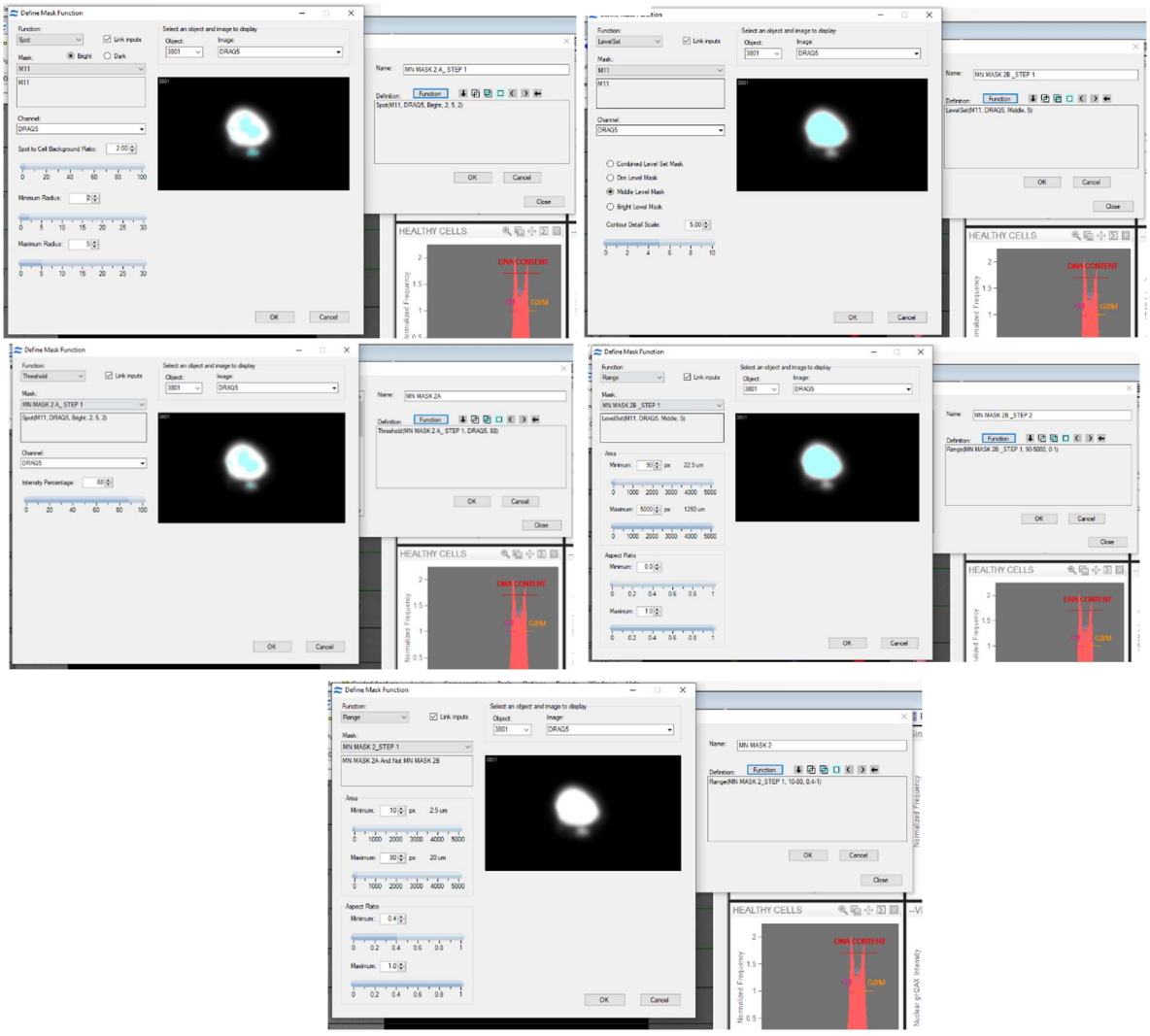

MN Mask 3

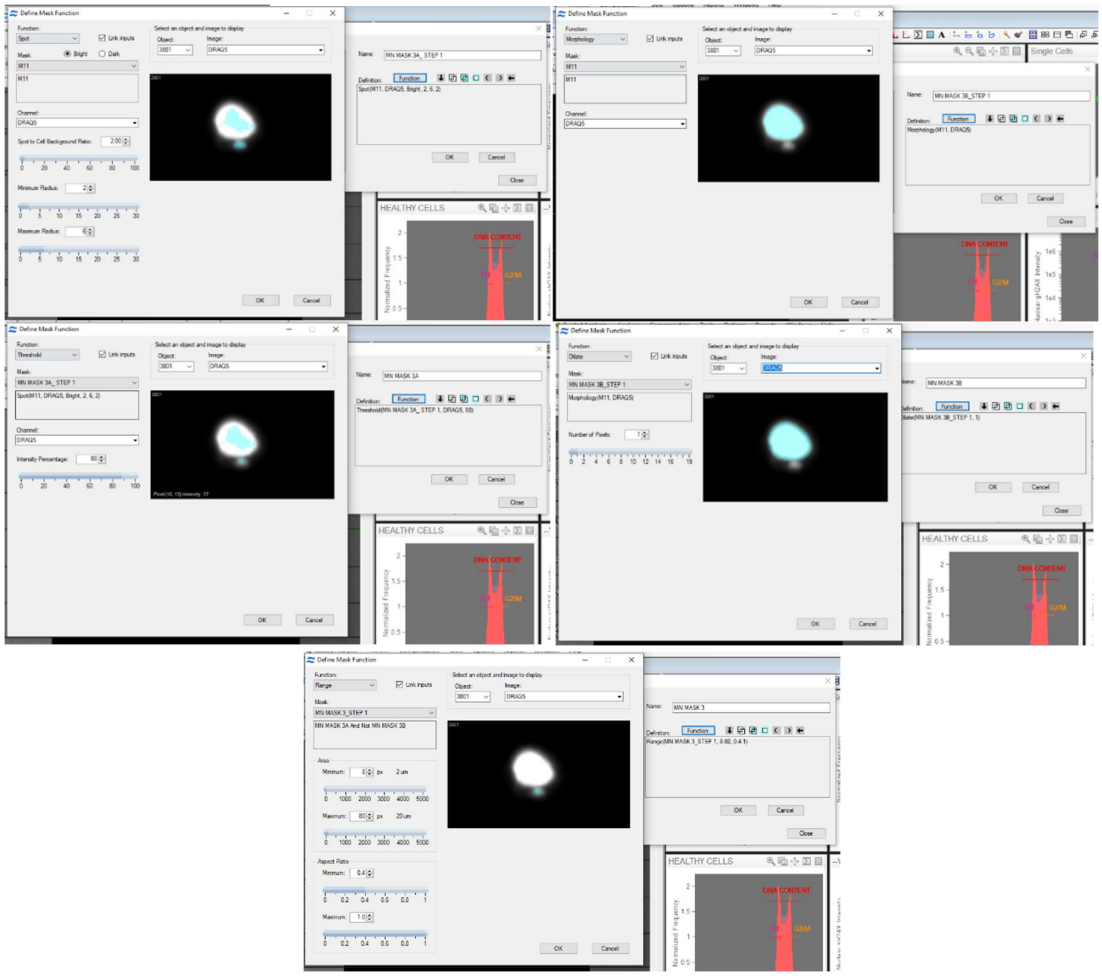

Supplement 2

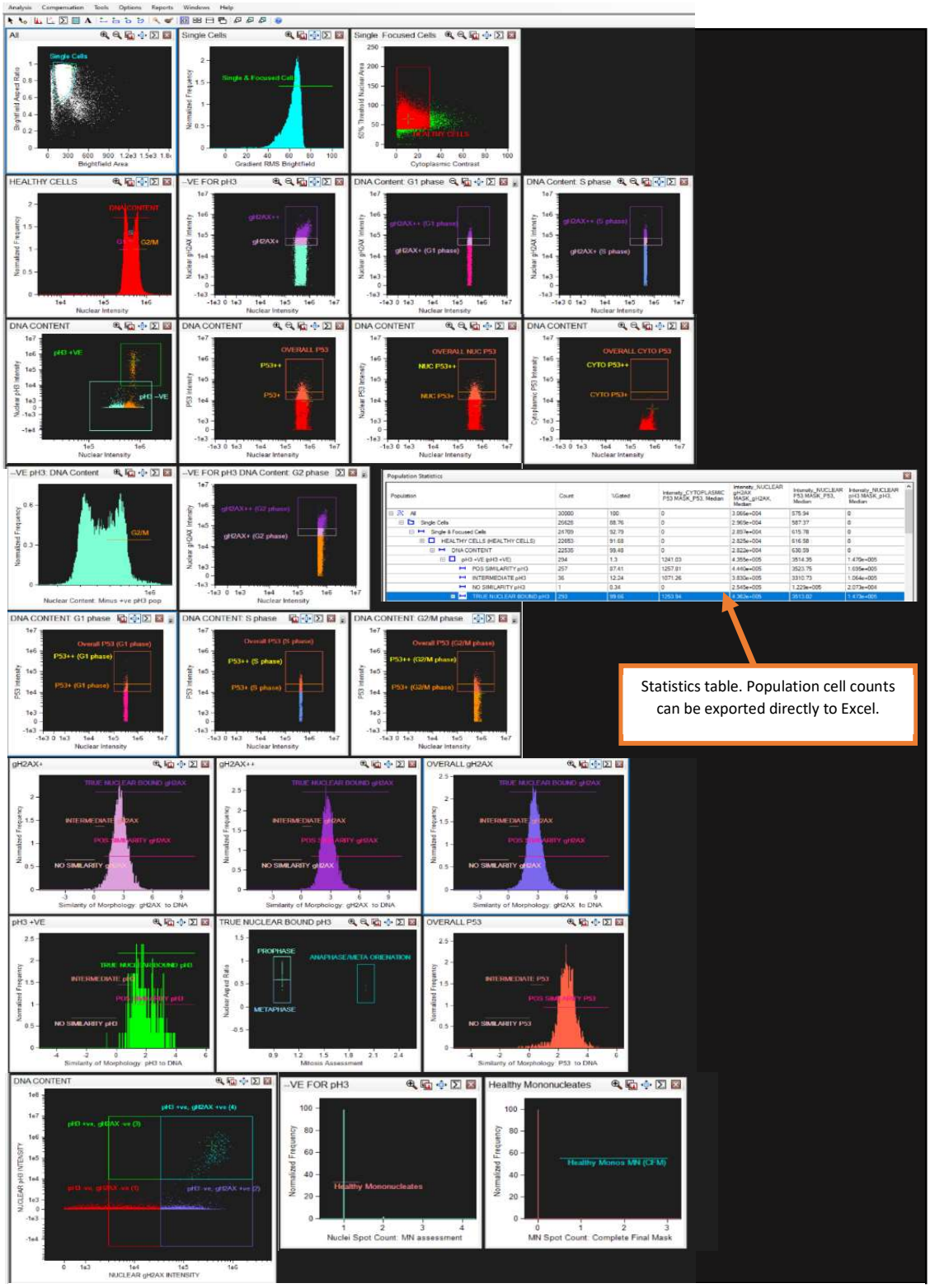

A overview of the work analysis area of the optimised template used to analyse all ISMN-me X40 data.